AD-A275 521

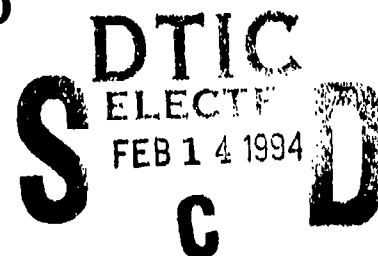|| |||| ||| ||| ||| |||| || |||

PL-TR-93-2215

CBSD: THE CELESTIAL BACKGROUND SCENE DESCRIPTOR

J. P. Kennealy
P. V. Noah
E. F. Tedesco
R. M. Cutri
S. F. Dermott

Mission Research Corporation
One Tara Blvd
Nashua, NH 03062-2801

January 1993

Final Report
April 1988 - January 1993

PHILLIPS LABORATORY
Directorate of Geophysics
AIR FORCE MATERIEL COMMAND
HANSCOM AIR FORCE BASE, MA 01731-3010

94-04895

|| ||| ||| ||| ||| |||| |||

9 4 2 10 2ſ 9

This technical report has been reviewed and is approved for publication

STEPHAN D. PRICE
Contract Manager

STEPHAN D. PRICE
Branch Chief

ROGER VAN TASSEL
Division Director

This report has been reviewed by the ESC Public Affairs Office (PA) and is releasable to the National Technical Information Service (NTIS).

Qualified requestors may obtain additional copies from the Defense Technical Information Center. All others should apply to the National Technical Information Service.

If your address has changed, or if you wish to be removed from the mailing list, or if the addressee is no longer employed by your organization, please notify PL/TSI, Hanscom AFB, MA 01731-3010. This will assist us in maintaining a current mailing list.

Do not return copies of this report unless contractual obligations or notices on a specific document requires that it be returned.

REPORT DOCUMENTATION PAGE

Public reporting burden for this collection of information is estimated to average 1 hour per response, including the time for reviewing instructions, searching existing data sources, gathering and maintaining the data needed, and completing and reviewing the collection of information. Send comments regarding this burden estimate or any other aspect of this collection of information, including suggestions for reducing this burden, to Washington Headquarters Services, Directorate for Information Operations and Reports, 1215 Jefferson Davis Highway, Suite 1204, Arlington, VA 22202-4302, and to the Office of Management and Budget, Paperwork Reduction Project (0704-0188), Washington, DC 20503

1. AGENCY USE ONLY (Leave blank)	2. REPORT DATE January 1993	3. REPORT TYPE AND DATES COVERED Final Report (Apr 1988–Jan 1993)

4. TITLE AND SUBTITLE

CBSD: The Celestial Background Scene Descriptor

6. AUTHOR(S)

J. P. Kennealy, P. V. Noah, E. F. Tedesco, R. M. Cutri, and S. F. Dermott

5. FUNDING NUMBERS

PE: 63220C
PR S321 TA 18 WU AC

Contract F19628-88-C-0014

7. PERFORMING ORGANIZATION NAME(S) AND ADDRESS(ES)

Mission Research Corporation
One Tara Blvd
Nashua, NH 03062-2801

8. PERFORMING ORGANIZATION REPORT NUMBER

9. SPONSORING/MONITORING AGENCY NAME(S) AND ADDRESS(ES)

Phillips Laboratory
29 Randolph Road
Hanscom AFB, MA 01731-3010

Contract Manager: Stephan Price/GPOB

10. SPONSORING/MONITORING AGENCY REPORT NUMBER

PL-TR-93-2215

11. SUPPLEMENTARY NOTES

12a. DISTRIBUTION/AVAILABILITY STATEMENT

Approved for public release;
Distribution unlimited

12b. DISTRIBUTION CODE

13. ABSTRACT (Maximum 200 words)

This report documents the Celestial Background Scene Descriptor (CBSD) program which is a suite of models to simulate the radiance of astronomical sources. The models simulate the contribution of the celestial background in the wavelength regime 2 to 30 μm with a positional accuracy of 2 arcseconds. The output of the models are tables and images suitable for use in sensor simulation. The CBAMP model calculates the thermal radiance and scattered light for the solar system objects including the Sun, Moon, the planets, the Galilean Satellites, 4559 numbered asteroids, and 9643 unnumbered asteroids. The solar system dust cloud (Zodiacal light) model CBZODY uses a Lorentzian out of plane dust density distribution to derive a number density from which the emitted and scattered radiances are computed. The stellar point sources model, CBPNTS, is a "fast" running scene generator version of the Air Force/NASA/Ames statistical point source model SKY. The sky is divided into 899 regions with size inversely proportional to stellar density. In addition, there are 87 different spectral classes, including 82 classes of stars, two classes each of planetary and reflection nebulae, and one of compact HII regions. The nature of the galactic infrared cirrus is discussed.

14. SUBJECT TERMS

Sun, Moon, Stars, Galaxy, Zodiacal Light, Planet, Minor Planet, Asteroid, Infrared, Cirrus, Point Sources, Scattering

15. NUMBER OF PAGES 228

16. PRICE CODE

17. SECURITY CLASSIFICATION OF REPORT	18. SECURITY CLASSIFICATION OF THIS PAGE	19. SECURITY CLASSIFICATION OF ABSTRACT	20. LIMITATION OF ABSTRACT
Unclassified	Unclassified	Unclassified	None

TABLE OF CONTENTS

LIST OF FIGURES

2 THE CBSD ZODIACAL EMISSION MODULE

3 THE CBSD POINT SOURCE BACKGROUND MODULE

4 THE CBSD ASTEROIDS, SUN, MOON, AND PLANETS MODULE

5 THE INFRARED CIRRUS

6 THE COMPOSITE IMAGE MODULE

APPENDIX A: IMAGE PROJECTIONS

LIST OF TABLES

2 THE CBSD ZODIACAL EMISSION MODULE

4 THE CBSD ASTEROIDS, SUN, MOON, AND PLANETS MODULE

5 THE INFRARED CIRRUS

6 THE COMPOSITE IMAGE MODULE

APPENDIX B: CBSD HEADER FORMAT

1.0   INTRODUCTION

Astronomical sources of infrared radiation provide a spectrally, spatially, and even temporally complex infrared background against which surveillance and reconnaissance systems must operate. The general nature and detailed character of this celestial background define the limits of system performance. Tradeoffs between detector size and number, magnitude of data processing, and the size and location of possible outage regions are forced by the intensity and structure of this background. An accurate description of the background at the wavelengths, sensitivities, and spatial resolutions projected for these systems is needed for design and performance analysis.

Although real data is certainly preferred to computer modeled results, such data simply does not exist at the specific wavelengths, sensitivity levels, and spatial finesse contemplated for surveillance systems.

Therefore, development of a capability for generation of computer-synthesized celestial background scenes was mandated. This type of modeling capability must, however, rely on empirical information that does exist, and the computer-modeled scenes must be consistent with relevant experimental data.

1.1   Relevant Data Products

Developing such a scene generation capability is simple in concept, but complex to carry out. First, all available data relevant to the problem must be assembled and reviewed. IRAS (the Infra-Red Astronomical Satellite) has now become the major source of infrared astronomical data and processed data products, although the earlier AFGL ZIP (*Zodiacal Infrared Program*) and Two Micron Survey data remain valuable.

IRAS was a joint NASA/U.K./Netherlands experiment to survey the sky in four broad spectral bands centered at 12, 25, 60 and 100 μm. The 12 and 25 μm focal plane elements were approximately the same size, ~45" in the in-scan direction and ~4.5' in cross-scan extent. Two arrays, each with seven of these detectors, covered the cross-scan field in each color. These redundant arrays were offset in-scan by ~15.1'. The far infrared detectors were larger; at 60 μm they were roughly 1.5' by ~5', while the 100 μm detector width was 3'. The IRAS experiment provided redundant coverage for >95% of the sky during a 10 month mission in 1983.

The Sky Flux Plates (images binned into 2 arc-min pixels), the Point Source Catalog (PSC), and the Zodiacal Observation History Files (ZOHF) are certainly the most familiar IRAS all-sky data products. Much more recently, the *"Infrared Sky Survey Atlas"* (ISSA) has been partially released. The ISSA plates are characterized by a slightly improved 1.5 arc-min pixel size. In addition, the pervasive striping artifacts, which were so objectionable in the original Sky Flux Plates, have been reduced -- but not nearly as much as had been originally anticipated.

The earliest version of the CBSD was based upon re-processed IRAS Sky Flux Plates, where the IRAS images were de-striped, "de-waved," and mosaicked into larger scenes by the original CBSD team (MRC/Nashua, Boeing Aerospace, & the University of Arizona). From

the outset, this was a stopgap effort, strictly to get something useful into the hands of users as quickly as possible.

Although the many problems encountered during this data re-processing tended to emphasize the limited utility of Sky Flux Plates for CBSD purposes, the University of Arizona continued on with the re-processing in order to produce the best possible data base for morphological studies of the IR cirrus. In many ways, their re-processed Sky Flux Plates are still of superior utility to even the new ISSA data.

It was recognized from the outset that the longer-term and more system-relevant CBSD effort would be the development and distribution of physically sound backgrounds models. Physical and/or phenomenological models for the various celestial background components can be developed from analyses of the global properties of observations and detailed studies of the astrophysical processes which give rise to the IR emission. These component models can be used to either extend the image data, for instance by spectrally interpolating on a pixel by pixel basis, or to generate a new scene from first principles.

MRC/Nashua and its current contract team (the Boeing Aerospace Company, the University of Arizona, and the University of Florida), in conjunction with the Air Force Phillips Laboratory, have now developed the first such Celestial Background Scene Descriptor (CBSD) set of models.

The following sections discuss the impacts the celestial background has on surveillance system performance, the data base pertinent to the problem and its most serious deficiencies and, finally, the requirements for a scene descriptor and the process of its development.

1.2 The Major Components of the Celestial Background

The infrared celestial background may be divided into four major components for analysis and modeling purposes. These categories are:

- Zodiacal Dust in the Solar System
- Galactic Point Sources
- Moving Solar System Objects.
- Spatially Structured Sources of Emission

Each of these categories is phenomenologically different from the others. Each will have a different impact on surveillance systems and each must be treated differently by the CBSD.

1.2.1 The Diffuse Zodiacal Background

The diffuse zodiacal background, arising from both scattering and thermal re-emission of sunlight by dust in the solar system, provides the ultimate limiting background for system performance. Because the earth is immersed in the zodiacal dust cloud close to the median plane, the zodiacal background is pervasive and detectable at all viewing angles by any earth-orbiting sensor. There are also distinct bands of zodiacal dust, arising from relatively

recent collisions between large asteroids in the main asteroid belt, circling the sky close to $i=0$ on the ecliptic plane.

Photon noise from the zodiacal emission begins to dominate other sources of detector noise above an irradiance of ~10^{-10} watt/cm^2/µm/sr in an instrument with detectors sized to the diffraction limit of the optics and a 10^{-17} watt/Hz$^{-\frac{1}{2}}$ detector NEP. Such a brightness level is reached for viewing angles less than 40-50° from the sun. IRAS made very few measurements away from a solar elongation angle of 90° and none outside the range of 60 - 120°. A model must be relied upon to get continuous descriptions of the zodiacal background. Chapter 2 of this report fully describes the CBSD zodiacal background module and its extensive validation with IRAS (and other) data.

1.2.2 The Galactic Point Source Background

The galactic point source background is dominated by stars and those HII regions, molecular clouds, and external galaxies so distant as to be effectively point sources at system-specified resolution. The distribution of infrared point sources is neither uniform across the sky nor random in a specified region. At a sensitivity of 10^{-20} watt/cm^2/µm, the number of point sources above detection threshold can be thousands per square degree along the galactic plane.

Such high densities will impact on-board satellite data processing. Since these high-densities are mainly confined to specific regions, a possible solution is to avoid those areas which have densities greater than that able to be handled by the data processing. However, even the extent of those areas above a given threshold is uncertain in the data, bounded only by the confusion limit of the IRAS survey at >25 sources/deg^2.

Chapter 3 of this report describes the CBSD statistical point source background module, its validation, and the NASA/Ames SKY model upon which it is based.

1.2.3 Moving Solar System Objects

Moving objects in the solar system and granularity in the zodiacal background create a temporally and spatially varying form of clutter. If, as is very likely, there is zodiacal granularity due to inhomogeneous distributions of dust in the asteroid belt, then systems will detect a parallax for this component and the phenomenon will vary with aspect and time of observation.

Asteroids, comets and remnants of cometary dust trails constitute non-inertial targets with effective temperatures of 160-260K. IRAS detected as many as 100,000 asteroids not seen before, as well as several score unexpected cometary dust trails. The planets (and their satellites) are moving objects known to be bright in the infrared.

Chapter 4 of this report fully describes the highly tested CBSD asteroids, sun, moon, and planets module. Not described here is a highly preliminary cometary dust trail module, still too embryonic to be distributable.

1.2.4 Spatially Structured Sources of Emission

The existence of "infrared cirrus," whose all-pervasive nature was first observed by IRAS, is now quite widely known. Although rather faint at wavelengths shorter than ~25-30 μm, the cirrus is, nevertheless, the most morphologically spectacular spatially structured source of emission. Because intensive studies of the cirrus have only begun to be undertaken during the past few years, neither the underlying phenomenology or the morphology is yet well enough understood to be reliably modeled. However, in conjunction with the CBSD development program, Drs. Roc Cutri and Frank Low at the University of Arizona have been carrying out some of the leading research in this area. This work is described in some considerable detail in Chapter 5, and we believe strongly that this work will be key to the eventual development of a CBSD cirrus module.

2   THE CBSD ZODIACAL EMISSION MODULE.

2.0   INTRODUCTION.

The CBSD Zodiacal Emission Model code (CBZODY) simulates the contribution of infrared radiation from the solar system dust cloud to the 2 - 30μm infrared celestial background (IRCB). This emission dominates the diffuse IR background over most of this wavelength region (scattering of sunlight by the zodiacal dust becomes an important contribution to the background for wavelengths λ < 4μm). The most prominent feature of the zodiacal light is the smooth emission seen over the entire sky with the apparent brightness dropping by a factor of roughly 3 between the ecliptic plane and the ecliptic poles at a solar elongation (e) of 90°. Figure 2-1 shows typical Infrared Astronomical Satellite (IRAS) scans in all four bands. Infrared and optical studies suggest that the zodiacal dust cloud is a disk-like structure slightly inclined to the Earth's orbital plane ($i \approx 2°$) with an ascending node Ω estimated to be between 40° - 110°. Because the plane of the dust cloud is inclined with respect to the Earth's orbit and neither the cloud nor the Earth's orbit are circularly symmetric about the Sun, the relative geometry of the Earth, Sun, and dust cloud depends on the Earth's orbital position. Therefore, the apparent zodiacal contribution to the IR sky varies with time and position on the sky.
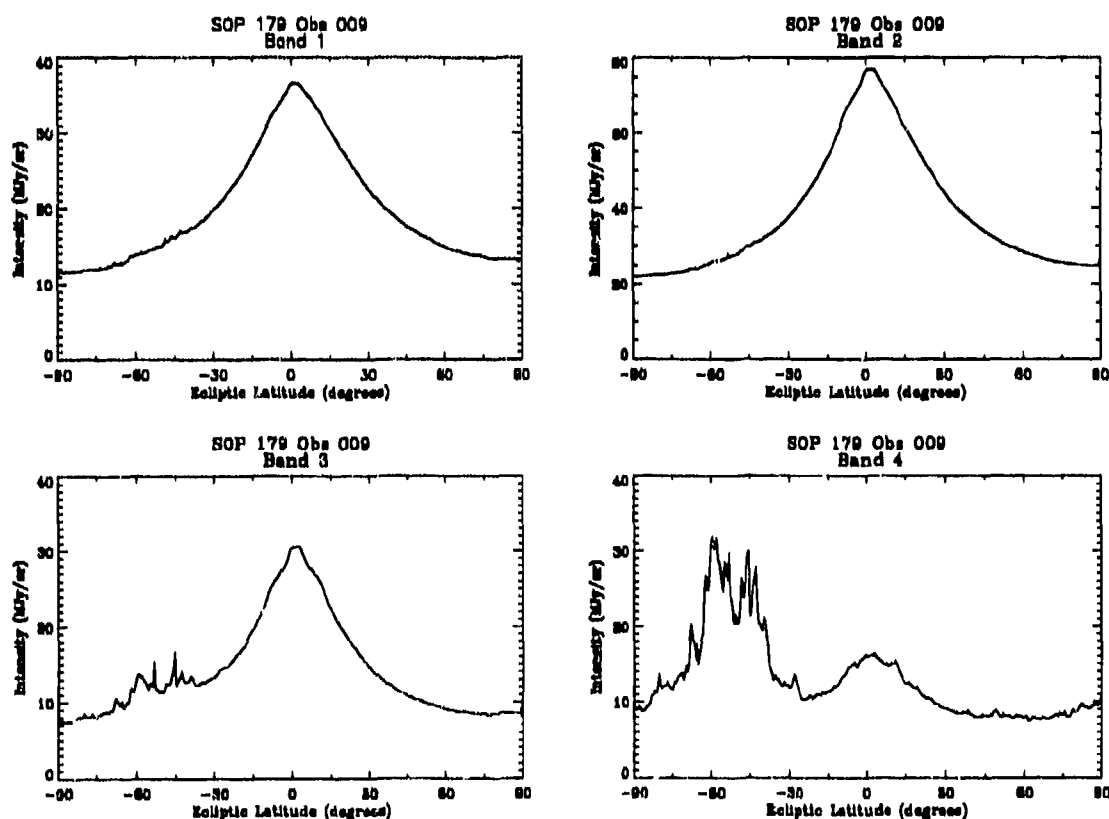
Figure 2-1. The four IRAS bands (12μm, 25μm, 60μm, and 100μm) showing the contribution of the Zodiacal emission. Each data point represents a 0.5° square patch of sky These patches begin at the North ecliptic pole and end at the South ecliptic pole. The galactic plane lies between ecliptic latitudes of -30° to -90° at the ecliptic longitude of the scan shown here.

5

In addition to the zodiacal cloud emission, analyses of observations from IRAS have revealed narrow bands of emission which occur in symmetric pairs above and below the zodiacal cloud symmetry plane ($i \approx 1°$ - $10°$ for the most prominent bands). These structures contain several percent of the peak zodiacal brightness (Sykes *et al.* 1989). The bands are thought to be emission from tori of dust particles associated with different families of asteroids. Observations of both diffuse and banded emission are consistent with dynamical models of dust originating from solar system objects, most likely periodic comets and asteroids.

Shortly after the discovery of the IRAS solar system dust bands, Dermott *et al.*, (1984) suggested that the bands may be related to the prominent Hirayama asteroid families formed by collisions in the asteroid belt. Dermott *et al.*, (1985) also suggested that the geometry of the dust bands is determined by the gravitational perturbations of the planets and showed how these perturbations could be calculated. However, the latter work did not include the effects of Poynting-Robertson light drag. In 1985-6, Dermott's group (then at Cornell University) wrote software for subtracting the dust bands from the broad-scale zodiacal background using Fourier methods. In 1986-7, they used the IRAS Zodiacal Observation History File (ZOHF) (IRAS Explanatory Supp., 1988) to show that the ecliptic latitudes of the dust band peaks vary with ecliptic longitude, as they had previously predicted. They also showed that the central dust band is split, and that the separation of the peaks is consistent with an origin associated with the Themis family (Dermott *et al.*, 1986). (The two most prominent Hirayama families are the Eos and Themis families. They had previously suggested that the "ten-degree" bands are associated with Eos.) They also determined the inclination and nodal longitude of the plane of symmetry of the zodiacal cloud with respect to the ecliptic and presented evidence that the Sun is not at the center of symmetry cloud, again as they had previously predicted.

CBZODY simulates both the diffuse zodiacal dust cloud and dust band contributions to the Infrared celestial background with simple physical models of the dust number density distribution and the dust emission spectrum based on available scientific data and current theories of solar system dust phenomena. The use of simple physical models instead of phenomenological descriptions of observations, or complex dynamical models, enables CBZODY to predict the zodiacal contribution to the IRCB at geometries and wavelengths where observations are limited or non-existent, while minimizing the number of parameters and computation time used to model the IRCB. This makes CBZODY a valuable tool to plan strategies for future observations, and to test, improve, and compare models of the zodiacal dust complex.

6

2.1   CBZODY CAPABILITIES.

CBZODY simulates observations of the zodiacal thermal emission brightness density in Janskys/steradian (Jy/sr) for user-specified spectral filter, sky region, date, and Universal Time (UT) of observation. The observer's latitude, longitude, and mean altitude above sea level are required inputs which provide the parallactic view of the dust. Sky regions are gnomonic projections of the sky in equatorial coordinates similar to the IRAS Skyflux plates.

The wavelength-dependent volume emissivity (ε_v) of the model dust particle population as a function of heliocentric distance (D) is tabulated in an ASCII file. Using code and data supplied by Reach (1988) we have generated an emissivity table which depends on the detailed properties of the dust particle population (spatial variations in particle composition, structure, size distribution) and is based on an analysis of emissivity of dust near the Earth's orbit using IRAS broad-band colors.

2.2   CBZODY MODEL OF THE ZODIACAL DUST COMPLEX.

CBZODY describes the zodiacal dust complex as a multi-component system consisting of a diffuse cloud of dust distributed throughout the inner solar system and several (currently three) pairs of dust bands nominally associated with specific asteroid families (Eos, Koronis, and Themis).   Each component's dust particle population characteristics are assumed homogeneous throughout space which does not account for differences in dust characteristics between the different families asteroidal families or different distributions at different heliocentric distances. The dust band model will be discussed in Section 2.3.

Figure 2-2 gives the geometry of a line-of-sight (LOS). The line-of-sight is broken into a series of volume elements. Each volume element contributes to the total radiance along the line-of-sight. Each volume element is also considered to be optically thin, i.e., there is no significant absorption by the dust along the line-of-sight.   In Figure 2-2 the Z axis is perpendicular to the ecliptic plane and the Z' axis is perpendicular to the symmetry plane. The CBZODY model for the dust cloud number-density distribution is azimuthally symmetric about its plane of symmetry. Therefore, a single volume element is completely described by cylindrical coordinates at constant azimuth (R, z'). Where R is the distance of the dust particle from the Sun projected onto the symmetry plane and z' is the out-of-plane distance of the dust. In Figure 2-2 the observer is located at heliocentric ecliptic rectangular coordinates (X, Y, Z), or in heliocentric spherical coordinates (L, B, d). The dust lies in the zodiacal dust cloud whose symmetry plane is specified by its inclination angle (i) and ascending node (Ω) with respect to the ecliptic plane. In geocentric spherical ecliptic coordinates the line-of-sight can be given in the coordinates pair (λ, b) [not shown on the figure] from which we obtain the observer's line-of-sight elongation angle, e, from the Sun:

$$e = \cos^{-1}\left[\cos b \cdot \cos(\lambda - \lambda_{Sun})\right] - 180° \tag{2-1}$$

where λ_{Sun} is the geocentric ecliptic coordinates of the Sun's position and is determined from the VSOP87 theory as described in Section 4.

A single volume element is specified by its distance from the observer, r, and elongation angle, e. We define the vector along the line-of-sight in heliocentric rectangular coordinates as:

$$
\begin{aligned}
x &= r \cdot \cos\lambda \cdot \cos b + X \\
y &= r \cdot \sin\lambda \cdot \cos b + Y \\
z &= r \cdot \sin b + Z
\end{aligned}
\tag{2-2}
$$

We can transform the ecliptic coordinates into the symmetry plane coordinates by utilizing the rotation matrix:

$$
\mathbf{R} = \begin{pmatrix}
\cos\Omega & \sin\Omega & 0 \\
-\cos i \cdot \sin\Omega & \cos i \cdot \cos\Omega & \sin i \\
\sin i \cdot \sin\Omega & -\sin i \cdot \cos\Omega & \cos i
\end{pmatrix}
\tag{2-3}
$$

8
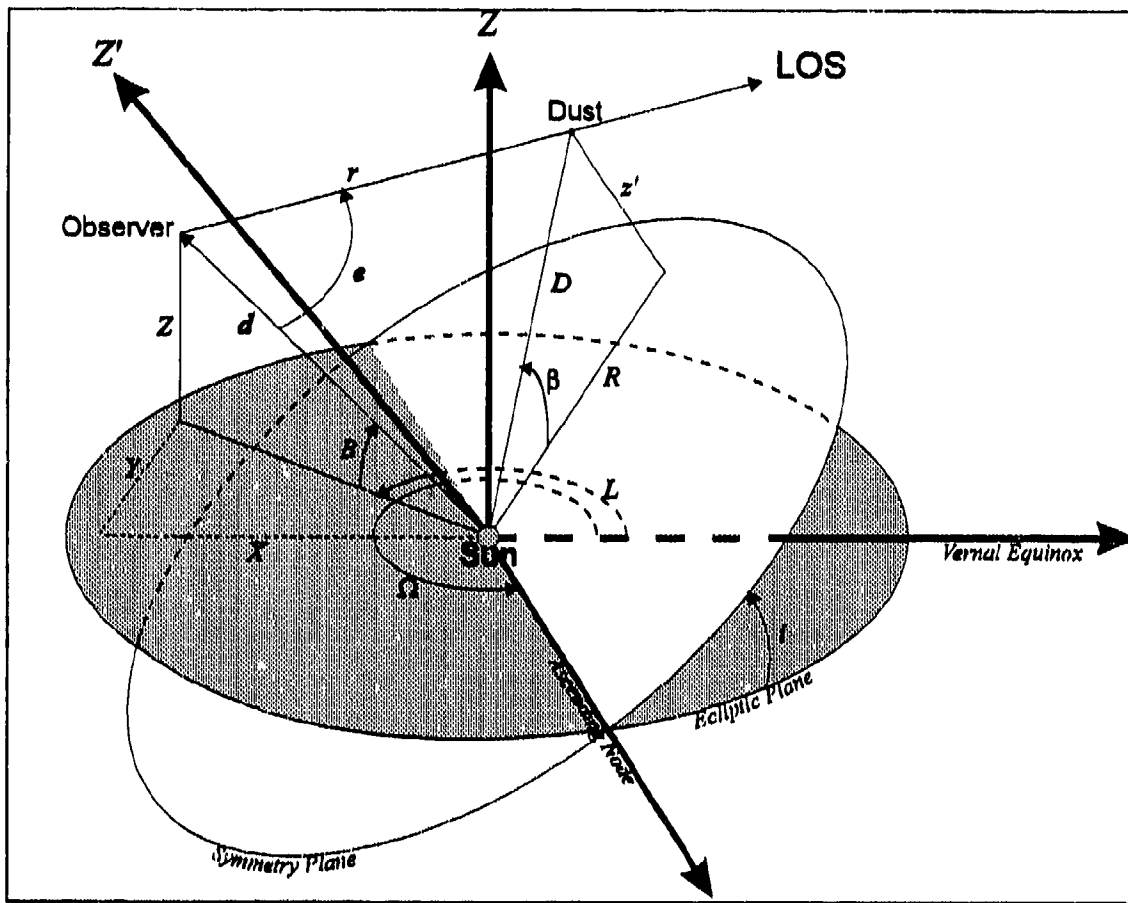
Figure 2-2. Geometry of the Line-of-sight and observer and dust coordinates (not to scale).

from which we get the heliocentric rectangular coordinates of the volume element with respect to the symmetry plane:

$$\begin{pmatrix} x' \\ y' \\ z' \end{pmatrix} = \mathbf{R} \begin{pmatrix} x \\ y \\ z \end{pmatrix} \tag{2-4}$$

The in-symmetry-plane distance to the dust is just:

$$R = \sqrt{x'^2 + y'^2} \tag{2-5}$$

And the dust's heliocentric distance is given by:

$$D = \sqrt{\left(R^2 + z'^2\right)} \tag{2-6}$$

9

We also define β as the heliocentric latitude measured from the symmetry plane of the dust cloud.

$$\beta = \tan^{-1}\left(\frac{z'}{R}\right)$$

(2-7)

The total radiance along the LOS is given by the sum of the radiance of all volume elements along the LOS:

$$L = \sum_j L_j$$

(2-8)

j = number of points along LOS

The number of integration points along the LOS is set by the elongation of the LOS from the Sun since the highest density is seen near the Sun. We have defined a LOS within 15° of the Sun to have 50 integration points. From 15° to 25° degrees there are 40 points. From 25° to 35° there are 30 points, and beyond 35° degrees we use 20 integration points. No integration is performed if the LOS intersects the surface of the Sun. This produces a "hole" of zero intensity with the intent that the zodiacal image be summed with the Sun, Moon, Planets image from CBAMP (Section 4).

CBZODY uses a Gaussian-Quadrature integration scheme where the number of integration points along the LOS defines the number of quadrature points. The zodiacal dust limits are defined from 0.05 AU, near the dust sublimation distance, to 6.00 AU, the farthest extent of most known asteroids. First, for each LOS, we take the distance of the outer edge of the dust cloud as seen from the observer, l, as the endpoint of the LOS integration with the start point at the observer. The end-point is defined as:

$$l = d \cdot \cos e + \sqrt{d^2 \cdot \cos^2 e - d^2 + R_{max}^2}$$

(2-8)

where, R_{max}, is the maximum heliocentric extent of the dust shell and is equal to 6.00 AU.

Then, at any volume along the LOS, we calculate the radiance as:

$$L_j = N \cdot \left[N_0 \cdot \varepsilon_v + S_0 \cdot \sigma\right]$$

(2-9)

where we define:

N = Dust density model,
N_0 = Dust density at 1 AU ≈ $2 \cdot 10^{-17}$ particles/cm^3,
ε_v = Volume emissivity at distance R,
S_0 = Normalized dust scattering function, and
σ = Scattering efficiency.

The dust density model $N{=}N(R, z)$ is traditionally separated into the product of two functions, a radial and an out of plane distribution (Leinert 1975):

$$N(R,z) = N(D,\beta) = f(D) \cdot f(\beta)$$ (2-10)

Where the in-plane dust density distribution is defined as:

$$f(D) = D^{-v}$$ (2-11)

The value of the power index, v, in the function $f(D)$ is a matter of some controversy. The in plane dust density is very sensitive to the value of v. Values less than 0.1 are noticeable in the fits to the data. Leinert et al. (1981) and Roser and Staude (1978), and Giese, et al. (1986) use $v=1.3$ as determined by the optical data from the Helios satellite. Duel and Wolstencroft (1988) find $v=1.1\pm0.1$ based on analysis of IRAS data. Also using IRAS data, Good (1988, unpublished IPAC report) finds a value of $v=1.803\pm0.014$. Murdock and Price (1985) state that $v=1$ is the best-fit power-law model for Zodiacal Infrared Project (ZIP) IR rocket observations in the ecliptic plane, but that the fit is not satisfactory over the entire range of solar elongation ($e = 22° - 180°$). However, we have analyzed the ZIP data using the current version of CBZODY and will comment on the results later.

The simplest dynamical model of the dust cloud hypothesizes that solar radiation drag in the form of the Poynting-Robertson effect and corpuscular drag from the solar wind causes dust particles to spiral inward from solar system sources (comets and/or asteroids) on time-scales of 10^4 to 10^5 years. This drag force preserves orbital inclination, reduces the eccentricity of orbits, and tends toward a steady-state $v = 1$ radial dust density distribution for a constant source of dust. These properties are independent of particle size and composition as long as Poynting-Robertson drag is the dominant perturbing force on the Sun's central gravitational field. However, particles from the same source will be segregated by composition and size because of the differing rates of infall, and dust populations are expected to evolve as a result of collisions and solar heat-induced structural changes.

A number of models have been proposed for the latitudinal density distribution $f(\beta)$. Duel and Wolstencroft (1988) use a modified fan model, Giese et al. (1986) use an exponential. In CBZODY we use a latitudinal function which is similar in form to a Lorentzian:

$$f(\beta) = \frac{\Gamma^2}{(\Gamma^2 + \tan^2 \beta)}$$ (2-12)

or in cylindrical coordinates:

$$f(R,z') = \left[1 + \left(\frac{z'}{\Gamma \cdot R}\right)^2\right]^{-1}$$ (2-13)

where Γ, which we call the scale height, is the value of $\tan(\beta)$ corresponding to the half-width-half-max (HWHM) for $f(\beta)$, i.e. $\Gamma \approx z_{HWHM}$ when $R = 1$ AU.

11

Figure 2-3 gives a cross sectional view of the modeled dust density distribution. The plane shown contains the Sun and is normal to the Sun-Vernal Equinox vector. The entire extent of the dust cloud in the model is 6 AU and the circle seen in the figure has a radius of 6 AU. To give a sense of scale, the positions of the planets Earth, Mars, and Jupiter are indicated by their symbols and define the ecliptic plane. White in the figure has the highest density and black the lowest. Note, that we find the highest dust density near the Sun and in the ecliptic plane. Over the poles of the Sun the dust density is greatly reduced. The dust then forms a toroidal ring about the Sun very nearly in the ecliptic. Figure 2-4 shows three line plots taken from the data of Figure 2-3 showing the dust density as a function of distance from the Sun or from the ecliptic. The top plot shows the density in the plane of the ecliptic and has the highest density. The shape of the distribution is r^{-1} since the latitudinal component is constant in the plane. Likewise, the bottom plot is also r^{-1} since the latitudinal component is nearly constant for this slice. For the middle plot, taken perpendicular to the ecliptic and at the Earth's orbit, the shape takes the form of the Lorentzian-like profile, however, it is still heavily influenced by the r^{-1} component.
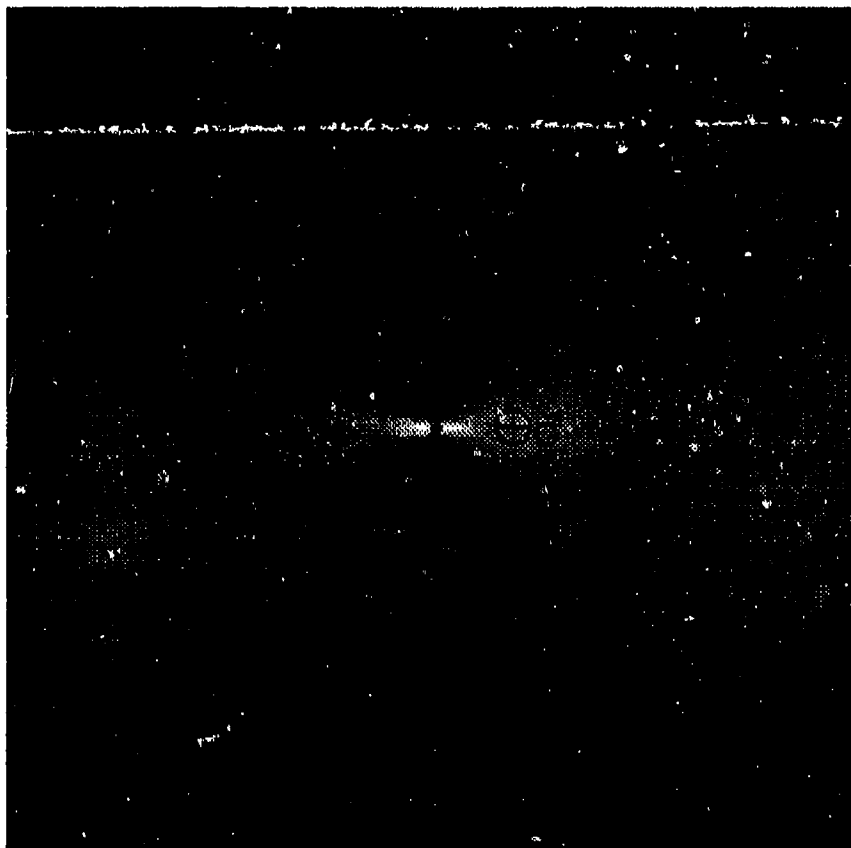
⊕ Earth

♂ Mars

♃ Jupiter

Figure 2-3. Cross section of the dust distribution perpen   ular to the Vernal Equinox and through the Sun.

12
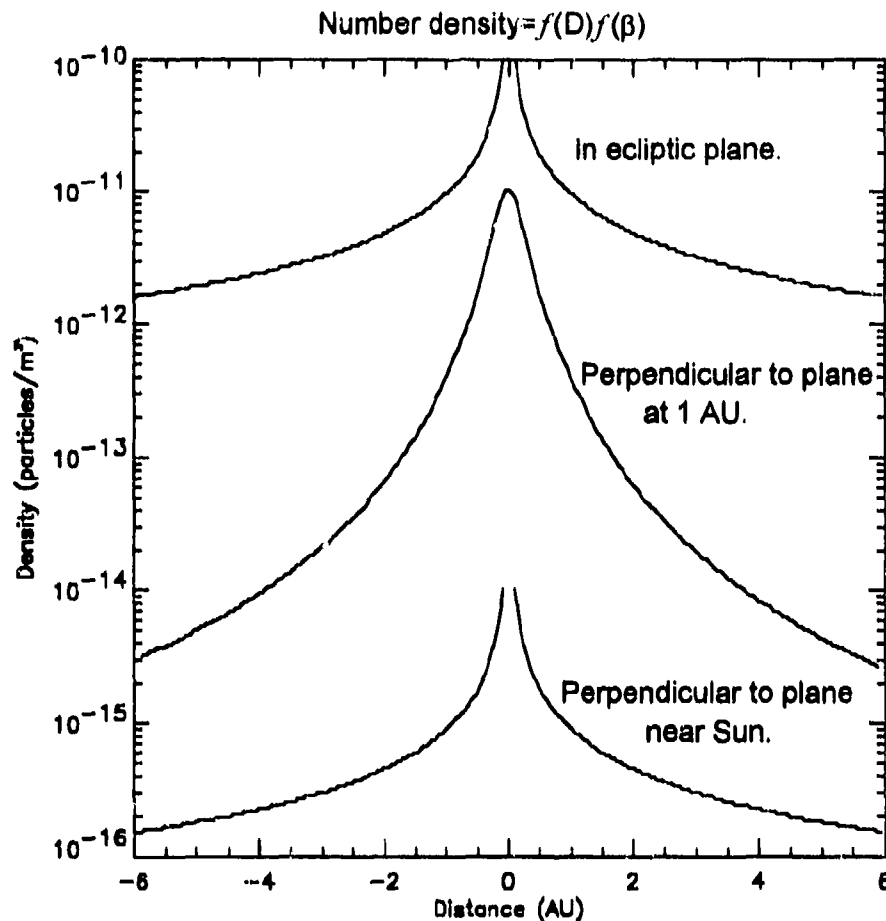
Figure 2-4. Sectional views of the dust density distribution for three slices, top, along the ecliptic, middle, perpendicular to the ecliptic at Earth's orbit, and bottom, perpendicular to the ecliptic near the Sun.

The Lorentzian-like density distribution shares properties of both the classical ellipsoidal and fan models of previous optical and IR studies (see Giese *et al.*, 1986; Giese and Kneißel, 1989 for reviews). The fan model provides a consistent fit over a wide range of solar elongation, but it fails to fit well at all latitudes because of its unphysical cusp in the symmetry plane (Rowan-Robinson *et al.*, 1990). The ellipsoidal model roughly fits the data at 90° solar elongation, although a lack of brightness at intermediate latitudes has been noted in zodiacal light studies (Giese *et al.*, 1986). The CBZODY Lorentzian model has constant density contours which retain the successful features of the fan model while removing the unphysical cusp. Figure 2-5 shows a best fit to the IRAS data along with the residual plot.

SOP 179 Obs 009
Band 1
Best Fit

SOP 179 Obs 009
Band 1
Relative Residuals
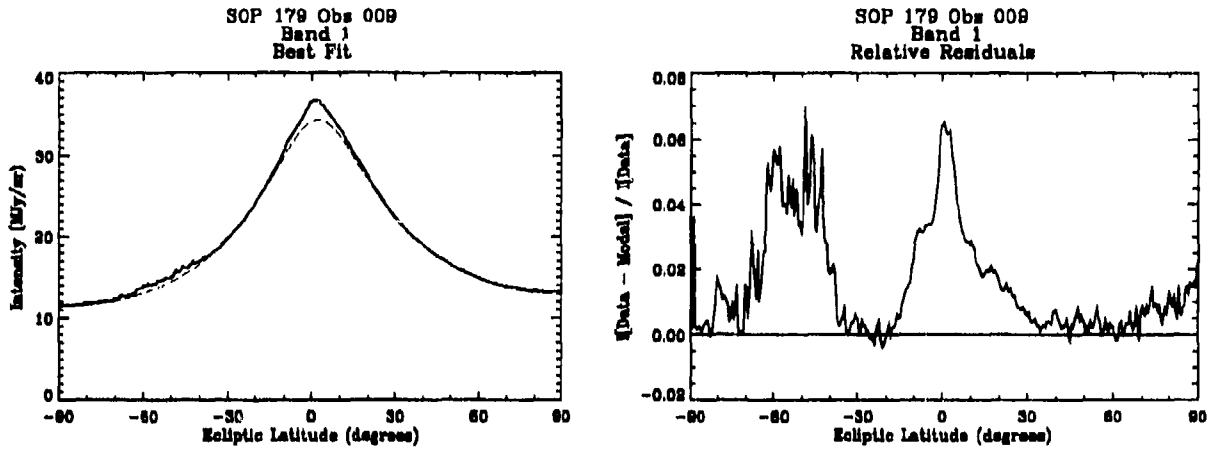
Figure 2-5. A best fit to the IRAS ZOHF scan using a non-linear least squares algorithm. The galactic plane is between ecliptic latitudes of -40° and -90°. The residuals show the Lorentzian-like fit to be well under 2% outside of the galactic plane region. The band region (20° to -20°) is only around 7% since no band model was incorporated in this fit.

The volume emissivity, ε_v, is defined as the amount of energy a unit volume of material emits per second per unit solid angle in the frequency range v to $v + dv$ (Lang 1980, p. 27). The total intensity along a line of sight is:

$$I_v = \int_0^l \varepsilon_v \cdot e^{-\alpha_v x} dx \qquad (2\text{-}14)$$

where:

l = the line of sight distance to the dust cloud outer limit,

α_v = the absorption coefficient per unit length, and

ε_v = Volume emissivity.

The absorption coefficient can also be considered an extinction coefficient and is the combination of the amount of energy absorbed by the dust and the energy scattered out of the line of sight (Gray 1976, p. 106). For the zodiacal light calculations the absorption is essentially zero and is taken to be identically zero. The volume emissivity of an ensemble of particles is calculated by integrating over the size distribution and summing over all constituents (Reach 1988):

$$\varepsilon_v = \sum_i \int da \frac{dn^{(i)}}{da} B_v(T^{(i)}(a)) Q_{abs}^{(i)}(a, v) \qquad (2\text{-}15)$$

where the size distribution:

$$da \frac{dn^{(i)}}{da} \qquad (2\text{-}16)$$

14

is the number density of particles composed of material i with radius between a and $a+da$. The solution for the temperature T is found from the condition of radiative equilibrium (Reach 1988):

$$\int F_v \cdot Q_{abs}^{(i)}(a,v)dv = \int B_v(T^{(i)}(a)) \cdot Q_{abs}^{(i)}(a,v)dv \tag{2-17}$$

where:

F_v = the solar flux,

$Q_{abs}^{(i)}(a,v)$ = the absorption cross section, in units of the geometric cross section, for particles of material type i, and

$B_v(T)$ = the black body function at the dust temperature T.

The temperature of the grains may be solved for via:

$$T = 278° K \left[\frac{\overline{Q}_{Sun}}{\overline{Q}(T)} \right]^{\frac{1}{4}} D^{-\frac{1}{2}} \tag{2-17}$$

where Q_{Sun} is the absorption efficiency averaged over the solar spectrum, $Q(T)$ is the absorption efficiency averaged over a blackbody spectrum at temperature T, and D is the distance of the grain from the Sun in AU. The solution for the temperature is usually done by iteration. The absorption efficiency, Q_{abs}, is defined such that the cross section for absorption of a photon of wavelength λ by a spherical particle of radius a is $\pi a^2 Q_{abs}^{(i)}(a,\lambda)$. The solution for Q_{abs} is based on Mie theory (Van de Hulst 1957, Kerker 1969, and Bohren and Huffman 1983). First, define the dimensionless parameter x as:

$$x = \frac{2\pi a}{\lambda} \tag{2-18}$$

and a complex index of refraction m as:

$$m = n - ik \tag{2-19}$$

For x much less than 1, the absorption efficiency may be expanded into a power series (van de Hulst 1957, Section 14.21). Reach (1988) used the improved solution of Wiscombe (1980) whenever:

$$|m|x < 0.01 \tag{2-20}$$

For intermediate values of x, Reach (1988) calculated the absorption efficiency from the Mie coefficients of van de Hulst (1957, Sections 9.22 and 9.32).

15

Figure 2-6 gives the absorption efficiency for dust near the Earth's orbit (1 AU) for astronomical silicate particles of radius 0.1μm, 1μm, 10μm, and 100μm. The volume emissivity used in CBZODY consists of a single material: astronomical silicates. There are no known samples of materials that can be identified as astronomical silicates. Instead they are a construction based on both laboratory and infrared astronomical measurements. The laboratory data consists of spectral emission of olivine, however, the 9.7μm and 18μm features are too narrow when compared with infrared measurements of the Trapezium. Therefore, the spectrum of astronomical silicate consists of measurements of olivine with the infrared absorption features constrained by the Trapezium observations (Draine and Lee, 1984). As such, astronomical silicates most closely resemble silicates with graphite impurities, the so-called "dirty silicates". Important to note in Figure 2-6 is the absorption feature between 10μm and 20μm. Particles smaller than 1μm show an enhanced absorption at small heliocentric distances, i.e., high temperature. The absorption curve of larger particles is dominated by the real part of the index of refraction, since these particles are optically thick both at the wavelength of the spectral feature and in the surrounding continuum. If the distribution of particles does not contain particles smaller than 1μm or if the particles are located beyond about 3 AU, the 10μm feature will not be present in the spectrum.
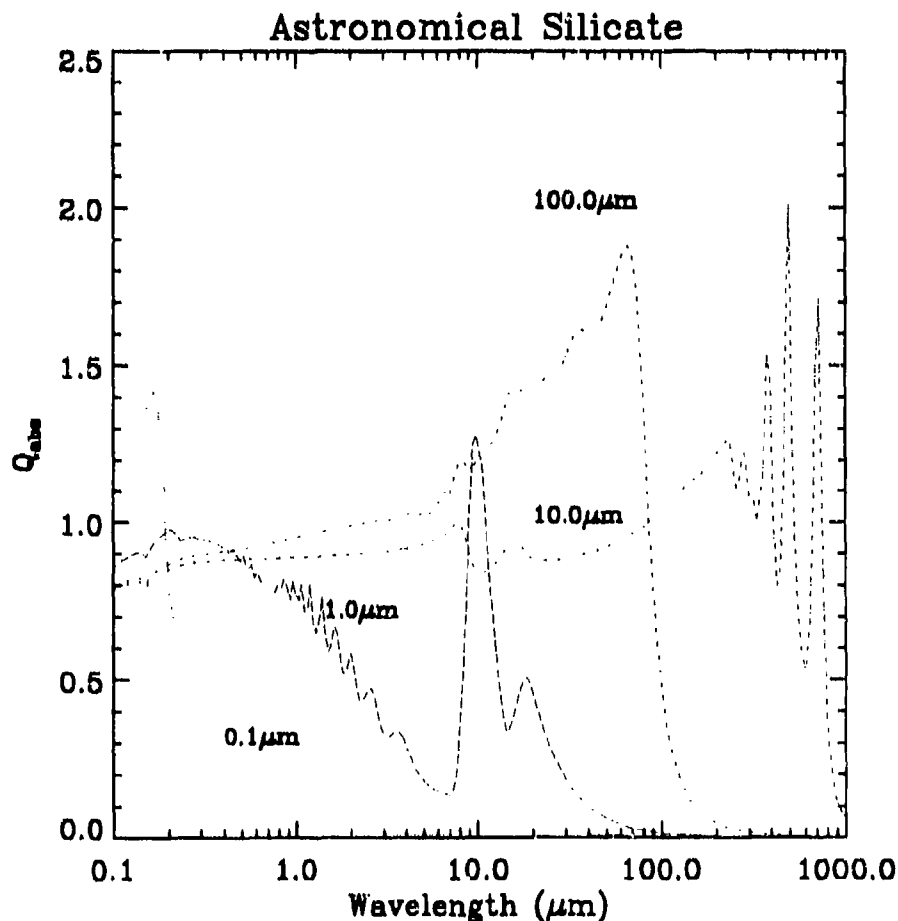
Figure 2-6. A plot of Q_{abs} for four different particle sizes.

16

Figure 2-7 gives the temperature distribution for astronomical silicate as a function of particle size for 3 distances from the Sun, 0.05 AU, 1.00 AU, and 3.30 AU. We see from Figure 2-7 that the assumption of a closest heliocentric distance from the Sun of 0.05 AU is not realistic for the entire particle density distribution. The perihelion distance should be set at the sublimation temperature of the dust. Figure 2-7 indicates that the maximum temperature of the dust at a given distance depends on the particle size. Therefore, we may need a different perihelion distance depending on the size of the particle.

The model for the volumetric emissivity, ϵ_v, of the dust assumes that the dust population is physically homogeneous throughout the solar system (same size distribution, same composition). This is not realistic, but is a reasonable simplifying assumption in the absence of sufficient data. The dynamics of the dust are expected to be size and composition dependent (Poynting-Robertson drag, radiation pressure, secular planetary perturbations), as is the evolution of the dust particle population (collisions, solar heating). However, the effects of any inhomogeneities may be reduced by the near-earth domination of LOS brightness, particularly near the ecliptic poles. In-plane brightness may be more dependent on spatial variations of dust particle properties because of the slow fall-off of emissivity with distance (see below). Also, studies suggest that particles of a small range of sizes will dominate the IR emission (Reach, 1988; Gustafson, 1990) (size $\approx$ 0.1-100µm for typical particle size distributions and compositions). More sophisticated models of spatial variations of particle properties are probably not justified by available data, but can be added to CBZODY through the volume emissivity database file to study the sensitivity of CBZODY to these unknown properties of the dust.
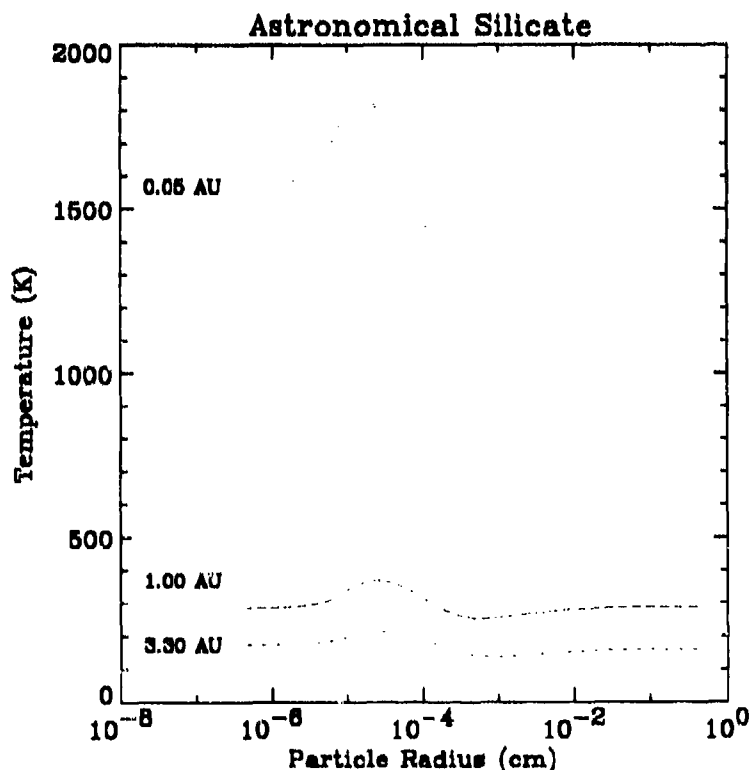
Figure 2-7. Temperature profiles for astronomical silicate at three different distances from the Sun as a function of particle size.

17

The volume emissivity is pre-computed and given in an external file SILEMS.DAT. The database contains 291 spectral data points from 1 to 30µm in steps of 0.1µm computed at 33 different distances. Each spectral point has a mass distribution from 10^{-18} gm to 1 gm., or a particle radius of 0.0045 to 4500 µm. Reach (1988) assumed a particle density of 2.5 gm/cm³, the value determined by Lamy, Grün, and Perrin (1987) from the *Giotto* and *Vega-2* missions to Comet Halley. The 33 heliocentric distances are defined as:

$$\log(D_i) = \log(r_{min}) + (i-1) \cdot \left[\frac{\log(r_{max}) - \log(r_{min})}{N-1} \right] \tag{2-21}$$

$i = 1, N$ and $N = 33$

r_{min} = minimum solar distance of dust shell = 0.05 AU

r_{max} = maximum solar distance of dust shell = 6.00 AU

To calculate the volume emissivity at any given distance a 4-point cubic spline is used to interpolate between the tabulated values.

Figure 2-8 gives the volume emissivity spectra used in CBZODY for three heliocentric distances, 0.05 AU, 1.00 AU, and 3.30 AU. The peak shifts to longer wavelength for increased distance following the temperature profile.

The CBZODY zodiacal model also includes the effects of solar scattering by the dust in terms of the scattering efficiency and measures the amount of energy scattered into the observer's field of view. The scattering efficiency, σ, is defined as:

$$\sigma = [P_0(\cos\phi) + 1.30539 \cdot P_1(\cos\phi) + 1.30144 \cdot P_2(\cos\phi)] \cdot \Omega_{Sun} \cdot F_{Sun} \tag{2-22}$$

where:

$P_n(\cos\phi)$ = Legendre Polynomials,

Ω_{Sun} = Solid angle of Sun from the distance of the dust,

and the band limited solar flux is defined as:

$$F_{Sun} = \int_{\lambda_1}^{\lambda_2} f_\lambda \cdot B_\lambda(T) d\lambda \tag{2-23}$$

with

f_λ = filter response function (normalized to 1),

$B_\lambda(T)$ = Blackbody radiance at dust temperature T.

18
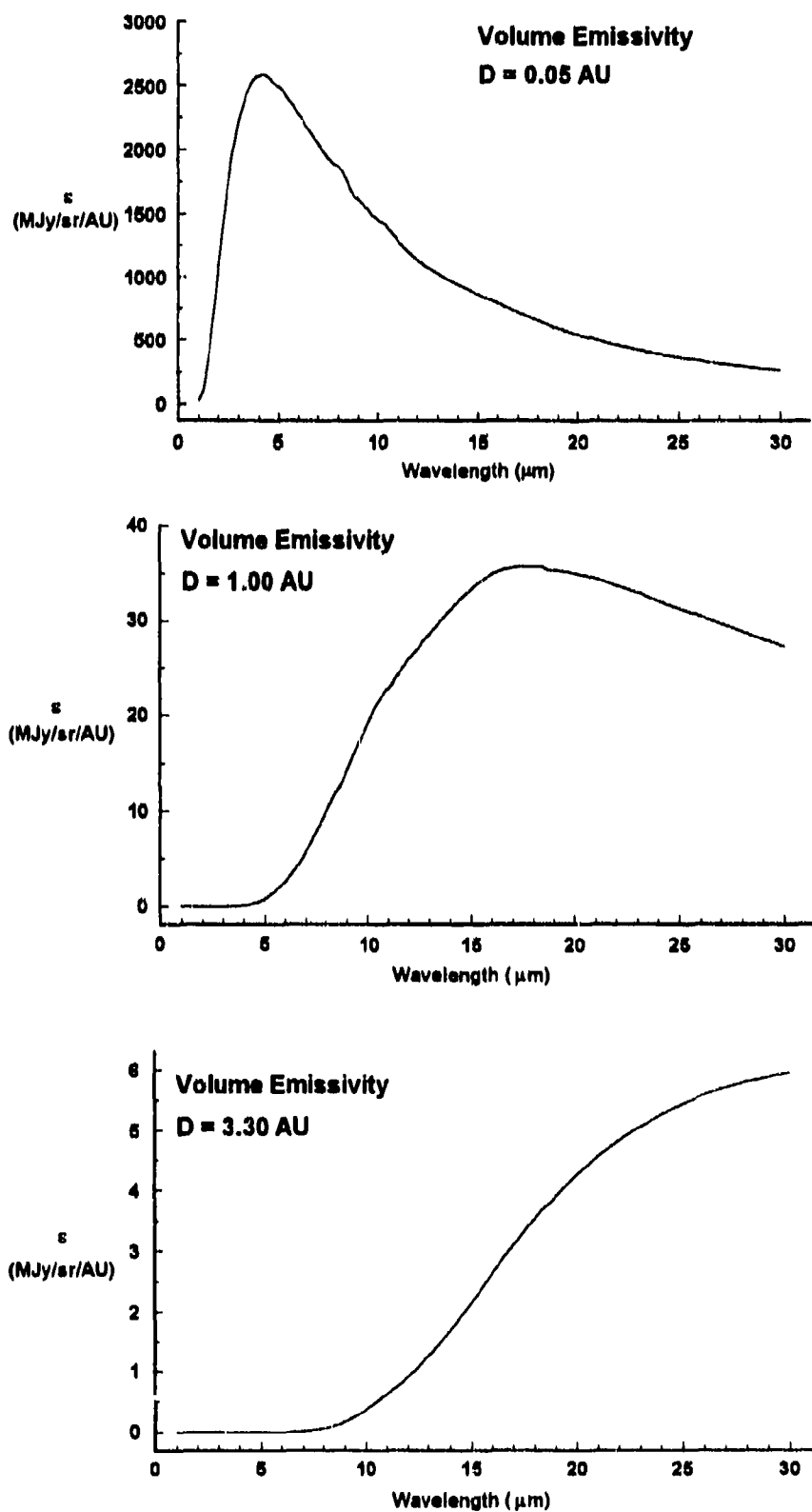
Figure 2-8. Volume emissivity spectra for three different heliocentric distances, top, 0.05 AU, middle, 1.00 AU and bottom, 3.30 AU.

where we have used the scattering phase function of Murdock and Price (1985). The scattering angle, ϕ, is defined as:

$$\cos\phi = \frac{x \cdot h_1 + y \cdot h_2 + z \cdot h_3}{D} \qquad (2\text{-}24)$$

$(h_1, h_2, h_3) =$ Geocentric unit vector along LOS,

$(x, y, z) =$ vector of the dust heliocentric distance

Finally, the normalized dust scattering can be broken down into:

$$S_0 = \frac{N_{\text{eff}} \cdot r_{\text{dust}}^2 \cdot A}{4} \qquad (2\text{-}25)$$

where:

$r_{\text{dust}} =$ Dust radius $\approx 3\mu m$,

$N_{\text{eff}} =$ Dust effective density $\approx 6.4 \cdot 10^{-22}$ particles / cm^3,

$A =$ dust Bond albedo.

In addition, the CBZODY model is a multi-plane model. That is, the characteristics of the dust cloud can be specified by two sets of parameters. The relevant parameters are:

Γ_1, Γ_2	Scale height of the inner and outer dust planes,
Ω_1, Ω_2	ascending node of the inner and outer dust planes,
i_1, i_2	inclination of the inner and outer dust planes,
N_{01}, N_{02}	Normalization density of the inner and outer dust planes, and
Λ	the break point between planes.

The break point Λ is the transition point between planes. The model takes the two planes as discontinuous. Figure 2-9 gives a schematic showing the two planes and their associated parameters.
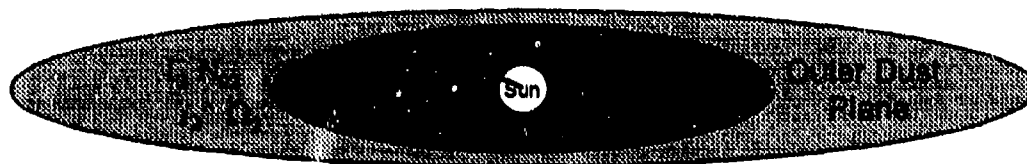
Figure 2-9. Schematic showing parameters associated with the multi-plane model. The figure only shows symmetry planes and not the 3-dimensional extent of the cloud.

Figures 2-10 and 2-11 give nine spectra representing different lines of sight as seen from the Earth. The spectra in Figure 2-10 have units of MJy/sr and Figure 2-11 have units of W/cm^2/μm/sr. Note that the vertical scales used vary corresponding to the wide range in total intensity. Note also how the peak of the spectra shift to longer wavelengths as the elongation angle of observation increases due to a proportionate increase in the contribution from cooler dust at greater heliocentric distance. In Figure 2-11 notice that shortward of 4μm

we see an increase in total intensity due to the effect of scattering of solar radiation for elongations > 10°. The scattering is not evident in Figure 2-10 since it is not a logarithmic scale like Figure 2-11.

The two plane model has not been thoroughly tested and all results are so far preliminary. Figure 2-12 presents the residuals from a fit using both the one-plane and two-plane models. This particular scan has a solar elongation of 60°. For Figure 2-12b the break point between planes was set at 1.00 AU. The residuals clearly shows a decrease in the residual at both ends of the fit. Also, in Figure 2-12a a small oscillation can be seen which is greatly reduced using a second plane. While the nature of the second zodiacal plane can not be commented on, the data do show some evidence that a second plane does exist when using the Lorentzian-like out of plane density distribution.
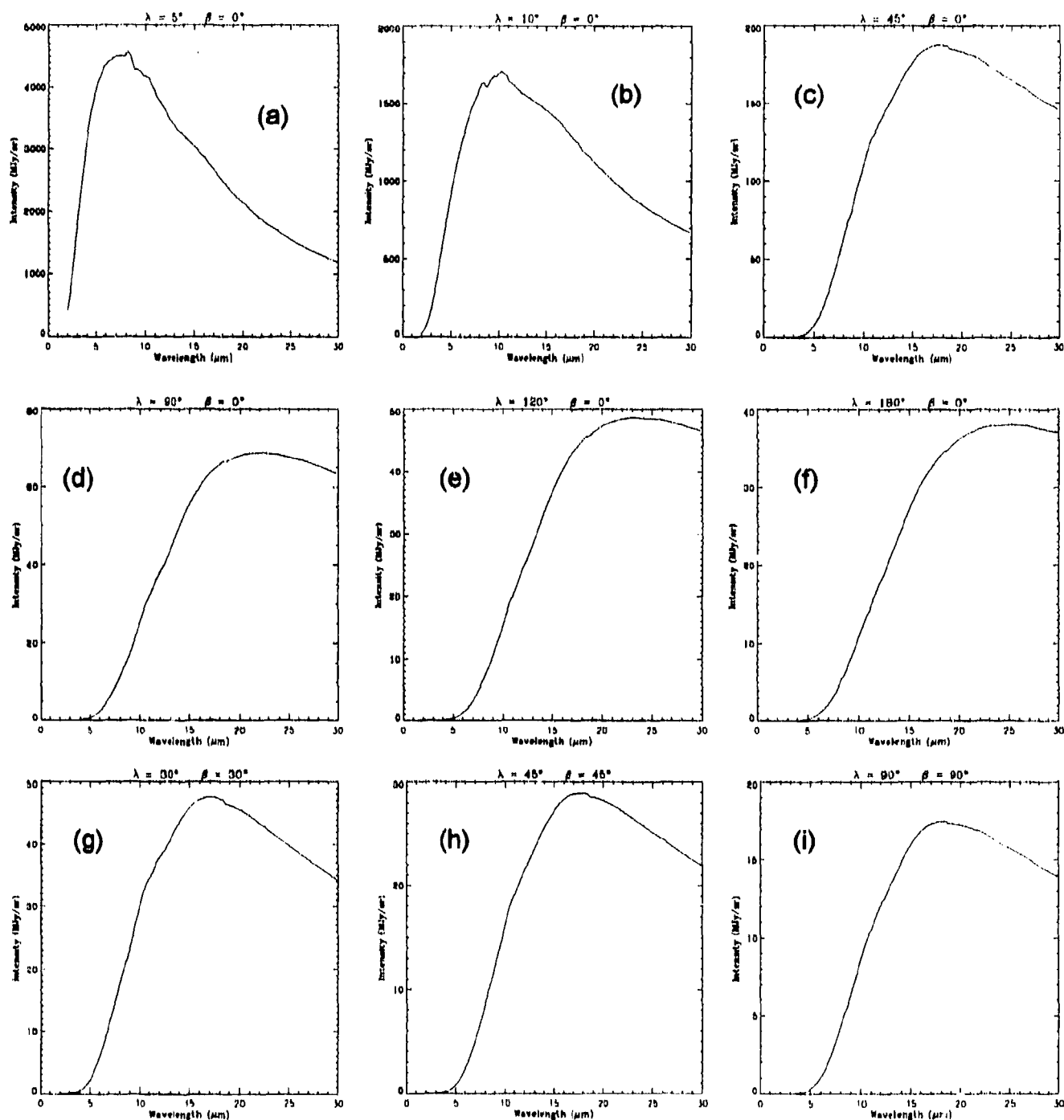
Figure 2-10. Nine views of the spectrum of the Zodiacal light given in ecliptic coordinates, (λ, β) and in units of MJy/sr: (a) 5° away from the Sun in the ecliptic plane. (b) 10° away from the Sun in the ecliptic plane. (c) 45° away from the Sun in the ecliptic plane. (d) along the direction of Earth's orbit. (e) 120° away from the Sun in the ecliptic plane. (f) At the antisolar point. (g) $\lambda=30°$ $\beta=30°$. (h) $\lambda=45°$ $\beta=45°$. (i) The North Ecliptic pole.

22
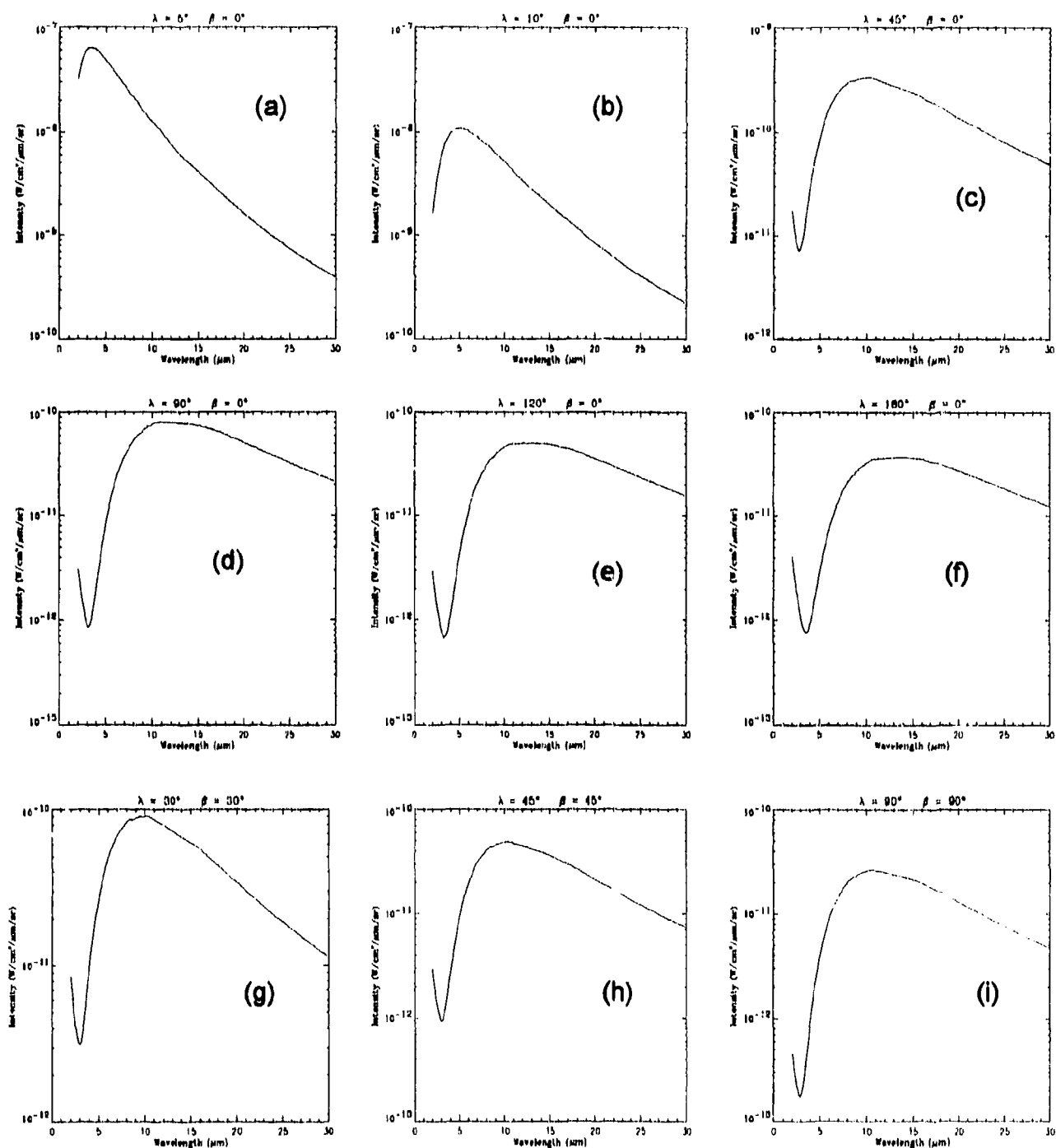
Figure 2-11. Nine views of the spectrum of the Zodiacal light given in ecliptic coordinates, (λ, β) and in units of $W/cm^2/\mu m/sr$: (a) $5°$ away from the Sun in the ecliptic plane. (b) $10°$ away from the Sun in the ecliptic plane. (c) $45°$ away from the Sun in the ecliptic plane. (d) along the direction of Earth's orbit. (e) $120°$ away from the Sun in the ecliptic plane. (f) At the antisolar point. (g) $\lambda=30°$ $\beta=30°$. (h) $\lambda=45°$ β $=45°$. (i) The North Ecliptic pole.

23

SOP 426 Obs 028
Band 1
Relative Residuals

(a) Single Plane Model
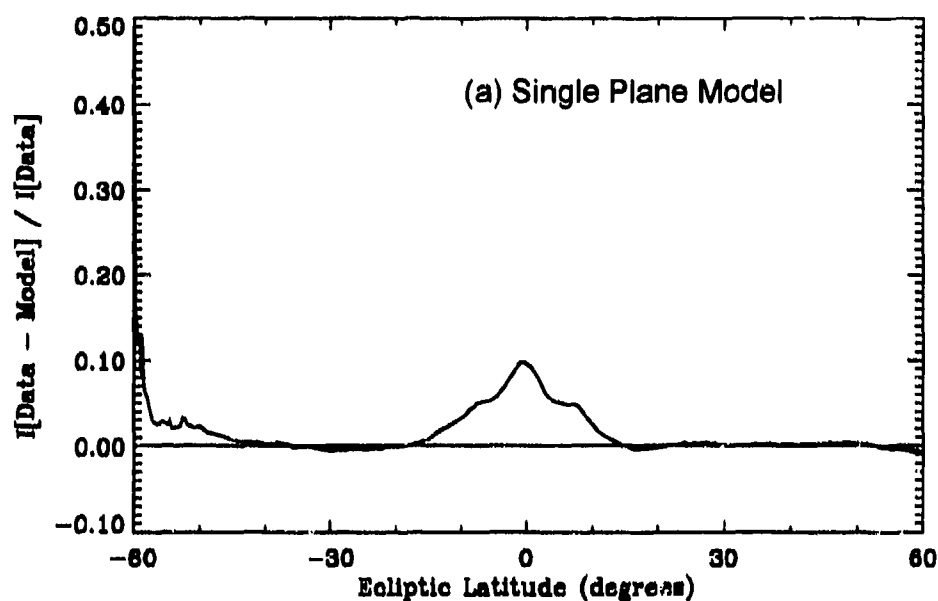
SOP 426 Obs 028
Band 1
Relative Residuals
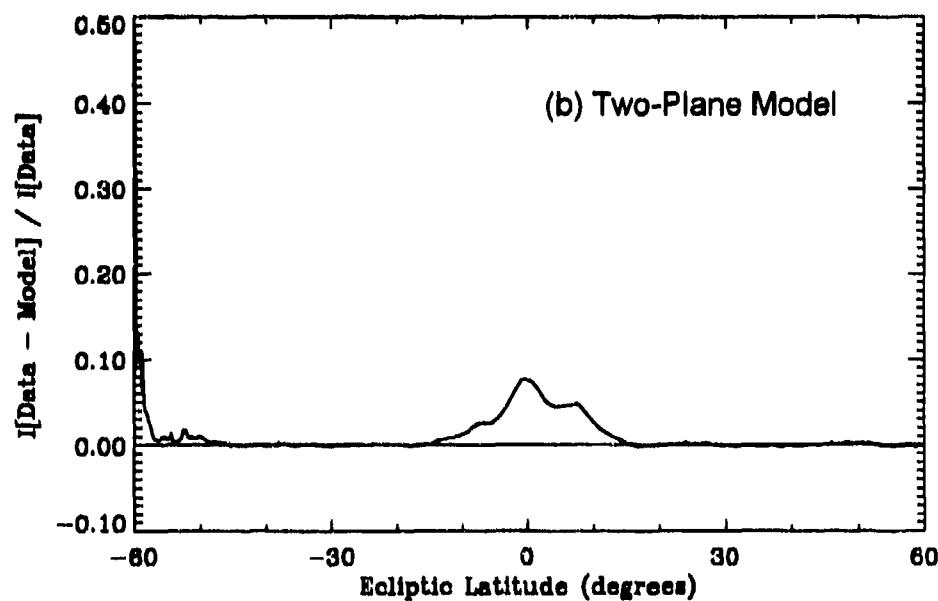
(b) Two-Plane Model

Figure 2-12. Comparison of the effectiveness of the two-plane model. Note that in (a), the single plane model, a small oscillation is clearly visible in the residual. This oscillation is not as strong when a second plane (b) is introduced with a break point of 1.00 AU.

2.3 THE DUST BAND MODEL.

The dust bands appear as several pairs located above and below the plane of the ecliptic. Three pairs of bands are well resolved (Sykes 1986) with possibly 4 additional pairs discernible (Sykes 1988). The bands are now believed to be a result of the distribution of an ensemble of particles in similar orbits with a common inclination but with a uniform distribution of ascending nodes. When seen in cross-section the orbital distribution is a torus about the Sun. The band pairs are produced because an individual particle spends most of its time at its extreme distance from the ecliptic (Figure 2-13). A particle will spend little time near the ecliptic since its velocity component is largest here. Seen from the observer, who is inside the orbit of the dust, the torus is most heavily populated on the edges, labeled Northern and Southern Band in Figure 2-13.
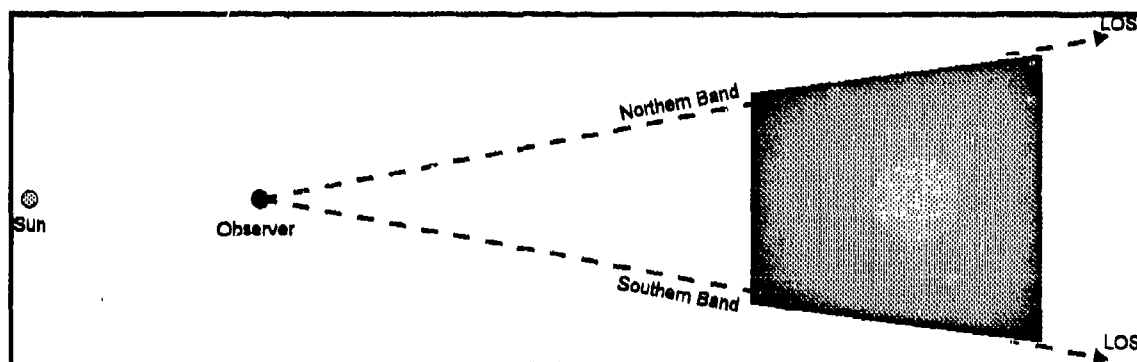
Figure 2-13. Schematic showing how the dust bands are produced from a toroidal dust distribution.

The CBZODY model includes the contribution of the three most prominent bands. These bands are believed due to the break up of asteroids in the Themis, Eos, and Koronis asteroid families (Dermott 1984, Sykes 1986,1988).

Sykes (1989, 1990) has produced an analytical model of the spatial distribution of dust. The particle number density is:

$$\rho(r,\beta) = R(r) \cdot \Theta(\beta) \tag{2-26}$$

where r is the heliocentric distance and β is the heliocentric latitude with respect to the symmetry plane. The two functional forms are:

$$R(r) = \frac{C_r}{r^2 a} \cdot \left(\frac{r}{2a-r}\right)^{\frac{1}{2}} \cdot \left\{1 + \frac{a^2(1-e^2)^2}{e^2 r^2 - \left[a(1-e^2)-r\right]^2}\right\}^{\frac{1}{2}} \tag{2-27}$$

$$\Theta(\beta) = \frac{1}{2\pi^2} \cdot \frac{1}{\sqrt{\left(\cos^2 \beta - \cos^2 i\right)}} . \tag{2-28}$$

where a is the semimajor axis, e is the eccentricity, i is the inclination and C_r is a normalization constant. This density is only good within the limits:

$$a(1-e) \le r \le a(1+e)$$
$$-i \le \beta \le i$$

(2-29)

The CBZODY model does not include the calculation of density for each volume element, instead the emission from each pair of dust bands is modeled as a thin, Sun-centered, toroidal ribbon with a radius equal to the perihelion distance of the asteroid family associated with the band pair. The circular symmetry and infinitesimal thickness allows each pair of bands to be described by a 1-D surface brightness profile in heliocentric latitude about the dust band symmetry plane. The profile is generated from a projection of Sykes' (1990) 3-D dust band model convolved with a Gaussian distribution of inclinations consistent with those of the nominal asteroid family. 251 latitudinal elements are used to construct the band profiles. The current normalizations represent best-guesses consistent with high-pass filtered IRAS observations in the 25μm band. Note that such a normalization scheme is only semi-quantitative, and that final normalization will be determined by a self-consistent fit to IRAS observations together with the CBZODY dust cloud model. A gray-body emissivity spectrum with temperature characteristic of the associated asteroid family is assumed. The characteristics of the three bands are given in Table 2-1.

Table 2-1. The orbital and emission properties of the dust bands used in CBZODY from Sykes.

	Themis	Koronis	Eos
Latitudinal Limits	2°.5	2°.5	12°.5
Ascending Node	97°.8	96°.1	97°.1
Inclination	1°.22	1°.16	1°.19
Perihelion	2.657 AU	2.734 AU	2.801 AU
Effective Optical Depth	$2.5 \ 10^{-8}$	$7.5 \ 10^{-8}$	$4.0 \ 10^{-8}$
Effective scattering Albedo	0.07	0.17	0.09
Temperature	164°K	156°K	159°K

The flux from the bands can be calculated in a similar way to the zodiacal cloud. For a given line of sight, integrate the contribution from all the volume elements. The density for each volume element is found by doing a spline interpolation of the database. Then, the total emission is taken as the sum of the thermal plus scattered light. The thermal emission is just:

$$L_{Thermal} = \tau_{eff} \cdot S \cdot \rho(r,\beta)$$

(2-30)

where τ_{eff} is the effective optical depth given in Table 2-1 and ρ, is the dust density. S is the band limited thermal emission from a Blackbody at the dust temperature, also from Table 2-1, and equal to:

$$S = \frac{\int_{\lambda_1}^{\lambda_2} B_\lambda(T) \cdot \phi(\lambda)\, d\lambda}{\int_{\lambda_1}^{\lambda_2} \phi(\lambda)\, d\lambda}$$

(2-31)

where:

$B_\lambda(T)$ = Blackbody function,
T = Dust effective temperature,
$\phi(\lambda)$ = bandpass response function,
λ_1 = bandpass short wavelength cutoff, and
λ_2 = bandpass long wavelength cutoff.

The scattered light is defined as:

$$L_{Scattered} = \frac{1}{4\pi} \cdot \tau_{eff} \cdot \alpha \cdot \rho(r,\beta) \cdot \frac{\sigma(r,\cos\gamma)}{|\cos\gamma|}$$

(2-32)

where α is the dust band albedo given in Table 2-1, σ is the scattering coefficient, and γ is the scattering angle defined as:

$$\cos\gamma = -\frac{x \cdot g_x + y \cdot g_y + z \cdot g_z}{r}$$

(2-33)

where (x, y, z) are the heliocentric ecliptic coordinates of the volume element at heliocentric distance r and (g_x, g_y, g_z) are the geocentric ecliptic coordinates of the volume element.

The scattering efficiency, σ, is defined as in Section 2.2:

$$\sigma = [P_0(\cos\varphi) + 1.30539 \cdot P_1(\cos\varphi) + 1.30144 \cdot P_2(\cos\varphi)] \cdot \Omega_{Sun} \cdot F_{Sun}$$

(2-34)

where the $P_n(\cos\phi)$ are the Legendre Polynomials, Ω_{Sun} is the solid angle of the Sun as seen from the dust, and F_{Sun} is the band limited emission from the Sun and defined as:

$$F_{Sun} = \frac{\int_{\lambda_1}^{\lambda_2} B_\lambda(T_{Sun}) \cdot \phi(\lambda)\, d\lambda}{\int_{\lambda_1}^{\lambda_2} \phi(\lambda)\, d\lambda}$$

(2-35)

where the Solar effective temperature, T_{Sun} is taken to be 5770°K.

The scattering phase function is that of Murdock and Price (1985). This integration is done for all three band pairs and the line of sight may cross all three bands.

27

2.4   A DYNAMICAL DUST DENSITY MODEL.

Through previous work under NASA's Astrophysics Data Program and NASA's Planetary Geology and Geophysics Program, a group at the University of Florida, led by Dr. Stanley Dermott, has developed various sophisticated tools that allow an ambitious approach to modeling and interpreting the observed structure of the zodiacal cloud. The Dermott *et al.* approach is to start with a postulated source of particles and then describe:

1. The orbital evolution of these particles using equations of motion that include Poynting-Robertson light drag, light pressure and gravitational perturbations by the planets.
2. The collisional evolution of the particles and the variation of their size-frequency distribution with heliocentric distance.
3. The thermal and optical properties of the particles and their variation with particle size.

The orbital evolution of the particles has been accounted for by a secular perturbation theory that incorporates the effects of both gravitational forces due to the planets and Poynting-Robertson light drag. This theory allows the calculation of the forced inclinations and nodes of the particles as they spiral in towards the Sun (Dermott *et al.*, 1992a) and accounts for the observed ecliptic inclination and node of the zodiacal cloud. Work has commenced on the combined collisional and orbital evolution of the dust particles (Durda *et al.*, 1992; Gustafson *et al.*, 1992) and on the determination of their thermal and optical properties (Gustafson, 1992). A computer code (SIMUL) has been written that calculates the distribution of flux produced by any particular distribution of dust particle orbits (Dermott and Nicholson, 1989).

SIMUL reproduces the exact viewing geometry of the IRAS telescope, allows for the eccentricity of the Earth's orbit, and calculates the distribution of flux produced by any particular distribution of dust particle orbits. The result is a model for the variation with ecliptic latitude (and longitude) of the brightness observed at a given wavelength as the line of sight of the telescope sweeps through a model cloud at a constant elongation angle. With SIMUL, they can mimic exactly the IRAS observational geometry and compare the model fluxes directly with the observations.

SIMUL has been used to produce model profiles of the dust bands based on the observed orbital elements of the Hirayama asteroid families and compare these model profiles with the corresponding IRAS observations. The agreement with IRAS observations was good but it was found that the observed profiles were more rounded and broader than the model profiles. The latitudinal separation of the peaks of the model bands associated with the Eos family were also shown to be a few degrees greater than the observed separation of the 10° bands (Dermott *et al.*, 1988). The above discrepancies do not detract from the Hirayama asteroid family model. On the contrary, they showed on the basis of detailed modeling (demonstrating the power of the SIMUL code) that the discrepancies may be evidence that some of the smaller particles (radii ~ 100µm) formed in the asteroid belt, spiral in toward the Sun due to Poynting-Robertson light drag. The resulting dispersion in the *forced* orbital elements experienced by these particles could account for both the rounded dust band profiles and the reduction in the latitudinal separation of the dust band peaks (Dermott *et al.*, 1988).

Durda *et al.*, (1992) and Gustafson *et al.*, (1992) calculated how the area of dust associated with a model Hirayama family decays with time. The calculation was for particles from 1 mm

through the largest asteroidal sizes and described the stochastic break-up of asteroid fragments. Extensions to 1µm will be made using the full-scale code incorporating the effects of radiation forces and covering a full $4.5 \cdot 10^9$ years of collisional evolution. They have already reported results for calculations spanning the first $3 \cdot 10^7$ years of evolution.

The dust production rate becomes more stochastic with time following a relatively smooth decrease in area as the small particles created directly from the break-up of the parent body are destroyed. The spikes in the dust production are due to the breakup of small to intermediate size asteroids. While the observable volume of an asteroidal family may remain fairly constant and well-defined, the total dust area associated with the family during that time may vary by an order of magnitude or more. The magnitude of the spikes is highly sensitive to the exponent q in the power-law size distribution of the collision fragments. The spikes are subdued for values of q less than or equal to the collisional equilibrium value of 1.837.

The shape of the dust-bands and their appearance under varying viewing geometries can be accounted for in detail, based on calculations using single-sized particles from the major Hirayama families and the SIMUL code. The surface area associated with each family was adjusted to fit the observations at 114°.68 elongation angle and the same particle distributions were then used at all elongation angles except those at 65°.68. At this elongation angle the contribution by one family near 10° inclination had to be readjusted. This may be evidence that the dust from that family has not yet reached the inner solar system. The near perfect fit to the observations is strong evidence that the solar system dust bands are due to the Hirayama families and that the dust from these families is transported to the Earth by PR-drag. To obtain a split central dustband at 114°.68 elongation without also generating a marked split at an elongation angle of 65°, SIMUL demonstrates that a majority of the flux must be produced by particles between the orbits of the Earth and Mars.

The success in modeling and interpreting the shape of the dust bands is remarkable, but the use of single-size dust particles is oversimplified and is not commensurate with the level of modeling that they are now capable of. They have developed codes to calculate the dust distribution of colliding particles subject to radiation forces (ACE) and also ways to convert the size distributions into effective surface areas as a function of heliocentric distance. Because the orbital evolution of dust particles depends on their size (or more accurately; the ratio of solar radiation pressure to gravitational pull, i.e. ß), any dynamically correct model of the zodiacal emission must use an estimate of the emitted fluxes as a function of particle size (or ß). The flux depends on the dust's temperature and infrared emission efficiencies. We adopt the Murdock and Price (1985) empirically-determined scattering properties with a wavelength independent mean emissivity of 0.7 and scattering function given by a sum of Legendre Polynomials. The particle temperature at a given heliocentric distance is calculated based on radiative equilibrium with the solar radiation field and re-emission into empty (cold) space. The emitted flux at any wavelength is then given by the Planck function at that temperature times the efficiency factor for the emissivity (0.7).

2.5   AN IMPROVED DUST BAND MODEL.

We have found that the thin ribbon model of the dust bands underestimates by a factor of 2 - 3 the dust cloud model residuals, but that the qualitative structure of the band model appears consistent with the residuals. The dust bands need a better model development. Our approach to this task is based on the following considerations:

1. The dust bands have regular shapes that vary markedly, but systematically, with elongation angle, wavelength, and the ecliptic longitude of the Earth.
2. The sources of these dustbands are collision products in the main asteroid belt, that is, the prominent Hirayama asteroid families.
3. The orbital and collisional evolution of particles derived from these sources can be modeled, largely from first principles. Adjustment of remaining parameters (for example, the effective area of dust associated with a given asteroid family) leads to a sound physical model for the distribution of particle orbits that satisfies the observed dustband profiles. This physical model can then be used to predict the amplitude, shape and location of the dustbands for observing conditions for which, at present, there are no observational data.

All the dustband profiles in a given lune can be summed to give a composite profile that corresponds to an elongation angle of 90° for that particular range of longitudes of the Earth. It is found that the latitudes of the peaks of these composite profiles vary sinusoidally with ecliptic longitude, reflecting the fact that the dustbands are inclined to the ecliptic because of the forced inclinations imposed on their orbits by the gravitational perturbations of the planets. These sinusoidal variations can be removed by a second transformation. The resultant corrected profiles are shown in Figure 2-14.
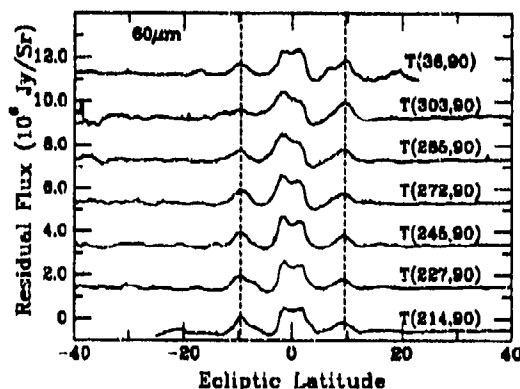
Figure 2-14. The average profile seen in each lune obtained using linear corrections to remove parallax and latitude variations and adding all the profiles in a given lune. The numbers in parentheses on each profile are, respectively, the ecliptic longitude of the Earth and the elongation angle (a constant 90° in this figure).

Figure 2-14 shows that the shape of the profiles varies markedly with the ecliptic longitude of the Earth, even for a constant elongation angle of 90°. (The effect of parallax has been removed by a linear transformation.) This is most easily seen by comparing the amplitudes of the "ten-degree" bands at an ecliptic longitude of 214° with those at 303°. In the lower

profile the amplitude of the band at -10° is much larger than that at +10°, while for the upper profile the magnitudes of these amplitudes are reversed.

Thus, the profiles of the dustbands vary markedly with (i) wavelength (Figure 2-1), (ii) ecliptic longitude of the Earth, and (iii) elongation angle. These variations are smooth and systematic and can be described by comparatively simple means. The more extreme variations that are produced at more extreme elongation angles are shown in Figure 2-15.
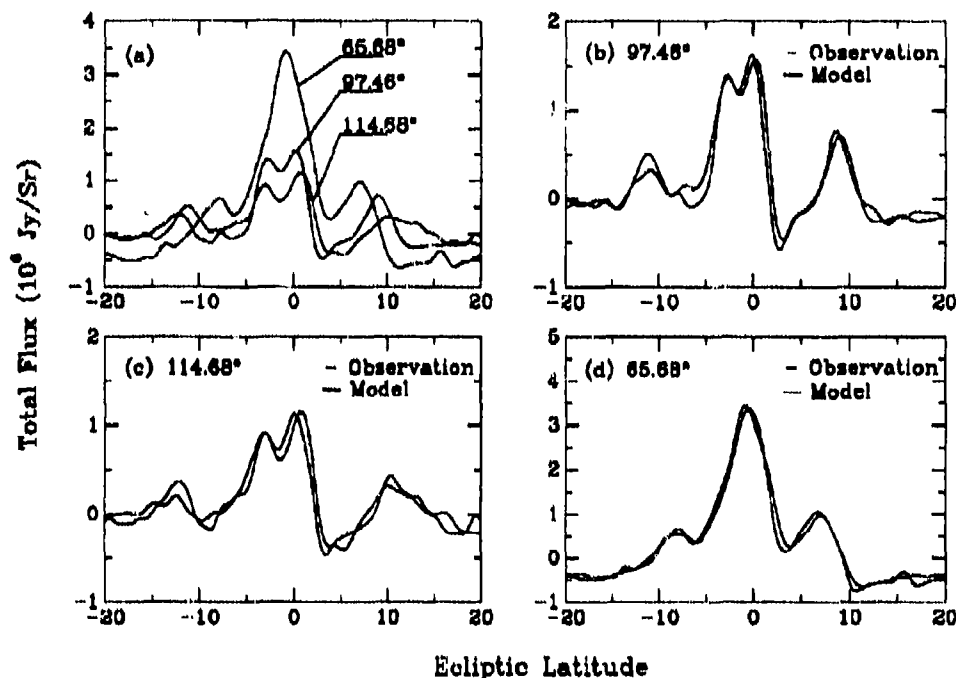
Figure 2-15. (a) IRAS observations of the solar system dustbands at a wide range of elongation angles obtained by filtering out the zodiacal cloud background using Fourier methods. Comparisons of these observations with model profiles based on the prominent Hirayama asteroid families obtained using the SIMUL code are shown in (b), (c), and (d).

In 1984, Dermott et al. (1984) suggested that the solar system dust bands discovered by IRAS are produced by the gradual comminution of the asteroids in the major Hirayama asteroid families. The confirmation of this hypothesis involved:

(1) The development of a new secular perturbation theory that includes the effects of Poynting-Robertson light drag on the evolution of the dust particle orbits;

(2) The production of a new high resolution Zodiacal History File by IPAC (the Infrared Processing and Analysis Center at Caltech);

(3) The development of the SIMUL code: a three-dimensional numerical model that allows the calculation of the thermal flux produced by any particular distribution of dust particle orbits.

With these tools we have been able to develop a new approach to modeling the zodiacal cloud. This approach is based on describing the orbital evolution of interplanetary dust particles from source to sink. We start with a postulated source of particles, in this case

31

particles derived from the prominent Hirayama families, and then describe the orbital evolution of these particles due to Poynting-Robertson drag, using equations of motion that include light pressure and gravitational perturbations. Once the structure of the cloud has been specified in terms of (a) the distribution of the elements of the dust particle orbits, (b) the distribution of the particles on those orbits, and (c) the thermal properties of the particles, we need a means of viewing the model cloud and comparing the predicted fluxes with the observations. We have constructed a three-dimensional numerical model (the SIMUL model) that calculates the distribution of flux produced by any particular distribution of dust particle orbits. This model reproduces the exact viewing geometry of the IRAS telescope and allows for the eccentricity of the Earth's orbit. The result is a model for the variation with ecliptic latitude of the brightness observed in a given wavelength as the line of sight of the telescope sweeps through the model cloud at a constant elongation angle.

IRAS observed the solar system dust bands over a wide range of viewing geometries. Using models based on single-sized particles of radii 3.4μm originating in the major Hirayama asteroid families, plus our calculations of the forced orbital elements of these size particles as a function of heliocentric distance and the SIMUL code, we are able to account for the shapes, amplitudes and ecliptic latitudes of the dust bands (Dermott et al., 1992a). Note, we have shown by calculation that particles of radii about 3.4μm are responsible for most of the thermal flux detected by IRAS at 25μm.

The elongation angles used by IRAS ranged from about 65 to 115 degrees, although most data were obtained with angles in the range 80 to 100 degrees. The mission lasted ten months and covered most, but not all, ecliptic longitudes. To demonstrate our methods, we chose three particular IRAS observations that cover a wide range of elongation angles, e. These are: (1) SOP 452 Obs 22, e = 114.68°, (2) SOP 392 Obs 29, e = 97.46°, and (3) SOP 446 Obs 42, e = 65.68°. The background profiles for these observations were calculated using the CBZODY model. For each observation, the background profile obtained from CBZODY was subtracted from the total IRAS signal to obtain a residual signal which we refer to as the dustband. The three dustbands in the IRAS 25μm band are shown in Figures 2-16, 2-17, and 2-18, while the same dustbands as viewed in the IRAS 12μm band are shown in Figures 2-22, 2-23, and 2-24 --- the dustbands in these six figures are the solid lines.
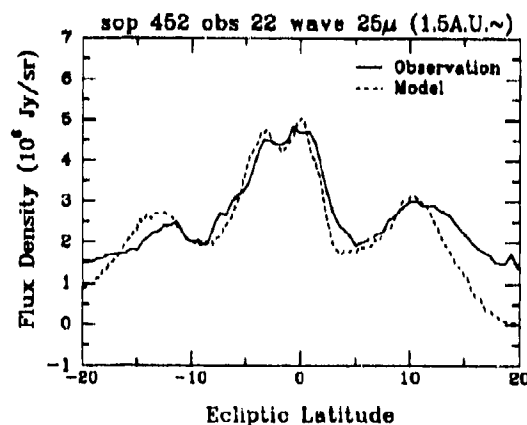
Figure 2-16. Comparison of Model and Observation for SOP 452, Obs 22, e = 114°.68 at 25μm when the dust is allowed to fall to 1.5 AU.
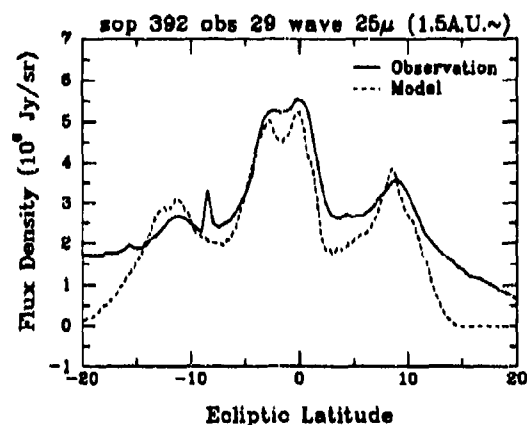
Figure 2-17. Comparison of Model and Observation for SOP 392, Obs 29, $e = 97°.46$ at 25μm when the dust is allowed to fall to 1.5 AU.
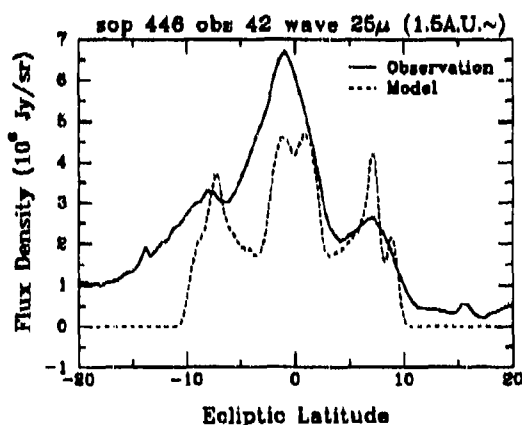
Figure 2-18. Comparison of Model and Observation for SOP 446, Obs 42, $e = 65°.68$ at 25μm when the dust is allowed to fall to 1.5 AU.
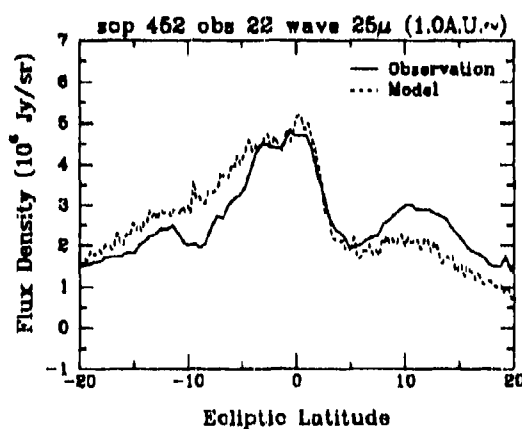
Figure 2-19. Comparison of Model and Observation for SOP 452, Obs 22, $e = $ 114°.68 at 25μm when the dust is allowed to fall to 1.0 AU.
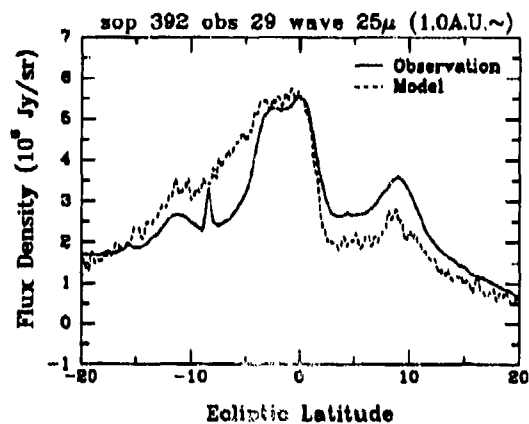
Figure 2-20. Comparison of Model and Observation for SOP 392, Obs 29, $e = 97°.46$ at 25μm when the dust is allowed to fall to 1.0 AU.
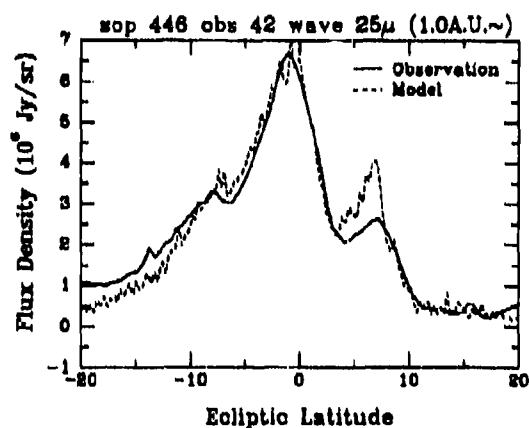
Figure 2-21. Comparison of Model and Observation for SOP 446, Obs 42, $e = 65°.68$ at 25μm when the dust is allowed to fall to 1.0 AU.
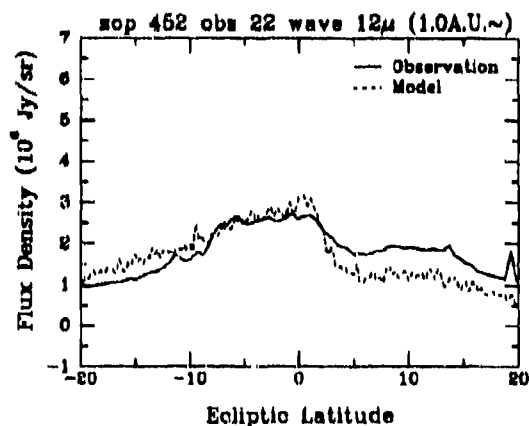
Figure 2-22. Comparison of Model and Observation for SOP 452, Obs 22, $e = 114°.68$ at 12μm when the dust is allowed to fall to 1.0 AU.

34
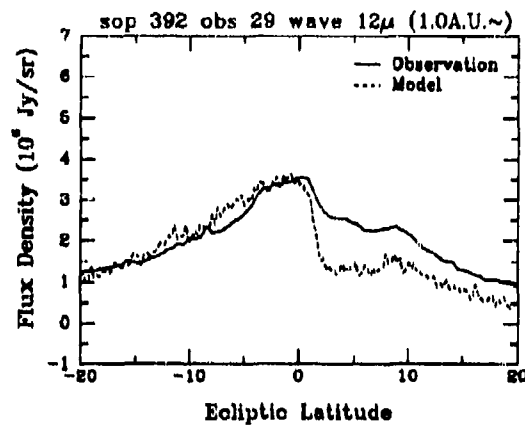
Figure 2-23 Comparison of Model and Observation for SOP 392, Obs 29, $e = 97°.46$ at 12μm when the dust is allowed to fall to 1.0 AU.
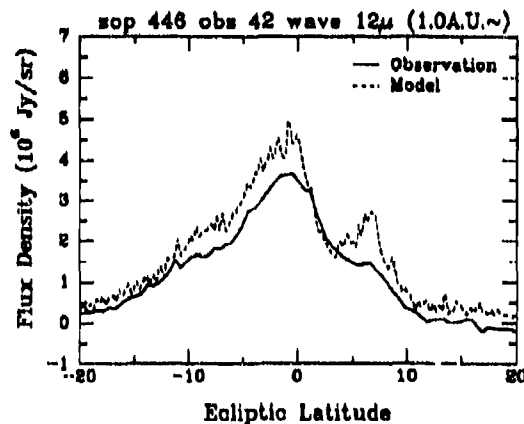
Figure 2-24. Comparison of Model and Observation for SOP 446, Obs 42, $e = 65°.68$ at 25μm when the dust is allowed to fall to 1.0 AU.

We modeled these dustbands using five Hirayama asteroid families, allowing that the effective area of the dust associated with each family is a free parameter to be found by trial and error. The *proper* orbital elements of the families are shown in Table 2-2 (Milani, 1992). The semimajor axis a shown in Table 2-2 refers to the source family. However, we assume that the orbits of the particles decay due to Poynting-Robertson light drag and that the orbits are distributed between the source and some minimum orbital radius, a_{min}, as determined by the rate of orbital decay (this is consistent with the way CBZODY models the background cloud). The other proper elements (e and i) and their dispersions were obtained from the asteroids observed in the various families.

Table 2-2: Proper Elements and Effective Areas of the Families Used in the Model (Milani, 1992).

Family	Area 10^9 km²	a	δa	e	δe	i deg	δi deg
Eos	0.7	3.015	0.006	0.071	0.008	10.2	0.3
Themis	0.32	3.136	0.025	0.152	0.009	1.42	0.3
Koronis	0.23	2.875	0.018	0.049	0.006	2.12	0.3
Nysa/Hertha	0.48	2.450	0.030	0.168	0.014	2.98	0.3
#126/127/128	1.4	2.787	0.006	0.154	0.010	8.43	0.3

The *forced* orbital elements were obtained by calculation using equations of motion that include gravitational perturbations, light pressure and Poynting-Robertson light drag. The details of these calculations are not given here (see Dermott *et al.* 1992b). To demonstrate in this report that it is absolutely essential to follow the orbital evolution of the dust particles from their source to the orbit of the Earth, we present two sets of results.

Set 1. $a_{min} = 1.5$ A.U.: Here we show the results of allowing the orbits of the particles to decay, but we only include in our model those orbits outside 1.5 A.U. The results are shown in Figures. 2-16, 2-17, and 2-18. By adjusting the areas associated with the families, it is possible to find good fits for the observations at large elongation angles, for which all of the flux is coming from particles outside the orbit of the Earth --- see Figures 2-16 and 2-17. However, this model fails for small elongation angles for which a good fraction of the flux comes from particles in the vicinity of the Earth --- see Figure 2-18. Note, that when the elongation angle is small, it is observed that the central dustband is not split. With this set of orbital elements, all the model dustbands show a distinct central split. This is not a good model.

Set 2. $a_{min} = 1.0$ A.U.: Here we show the results of allowing the orbits of the particles to decay to the orbit of the Earth. With this set of orbits, it is possible to find a solution that satisfies the observations over the whole range of elongation angles. The comparisons of the model with the observations are shown in Figures 2-19, 2-20, and 2-21. The fits are very encouraging. The areas associated with the various families that were used to obtain these fits are shown in Table 2-2. We have used the same model, with no adjustment of parameters, to calculate the predicted flux in the IRAS 12μm band. Comparisons of the predictions with the observations are shown in Figures. 2-22, 2-23, and 2-24. Again the fit is fairly good.

The discrepancies between the model and the observations are shown in Figures. 2-25 through 2-30. What stands out in these figures are marked asymmetries between the fluxes predicted from the model and the observations --- the discrepancies tend to be positive for positive latitudes and negative for negative latitudes. Our model can certainly be improved. In fact, we know how it can be improved. However, we consider that it is also possible that the asymmetries arise, in part, from deficiencies in the background model and that this model also needs improvement.
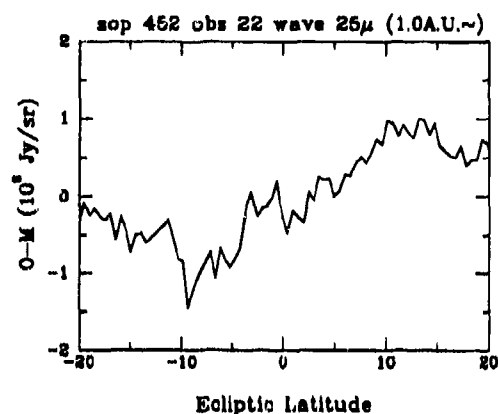
Figure 2-25. Residual plot, in the sense observation minus model, of SOP 452 obs 22, $e = 114°.68$ at $25\mu m$ for an infall distance of 1 AU.
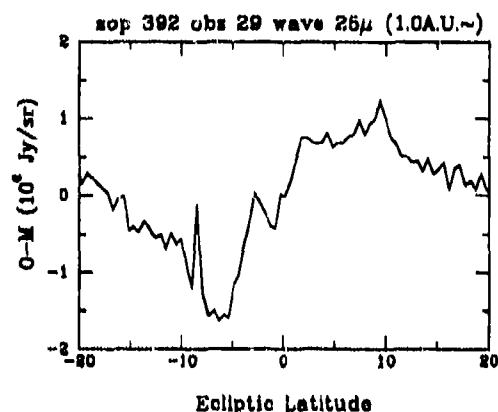
Figure 2-26. Residual plot, in the sense observation minus model, of SOP 392 obs 29, $e = 97°.46$ at $25\mu m$ for an infall distance of 1 AU.
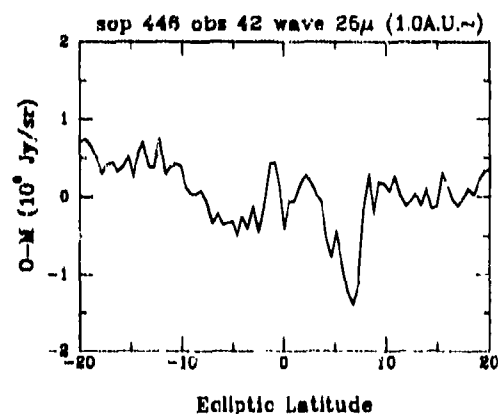
Figure 2-27. Residual plot, in the sense observation minus model, of SOP 446 obs 42, $e = 65°.68$ at $25\mu m$ for an infall distance of 1 AU.

sop 452 obs 22 wave 12μ (1.0A.U.~)
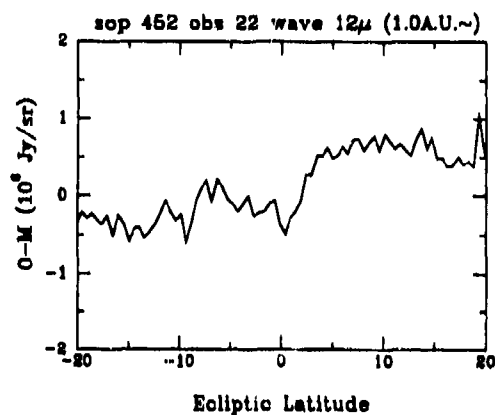
Figure 2-28. Residual plot, in the sense observation minus model, of SOP 452 Obs 22, e = 114°.68 at 12μm for an infall distance of 1 AU.

sop 392 obs 29 wave 12μ (1.0A.U.~)
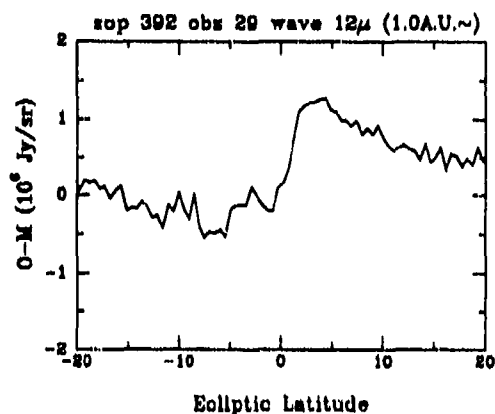
Figure 2-29. Residual plot, in the sense observation minus model, of SOP 392 Obs 29, e ≈ 97°.46 at 12μm for an infall distance of 1 AU.

sop 446 obs 42 wave 12μ (1.0A.U.~)
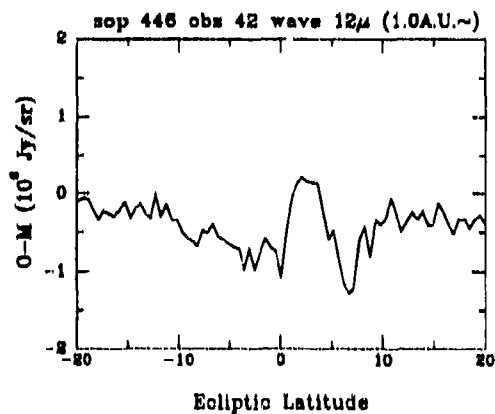
Figure 2-30. Residual plot, in the sense observation minus model, of SOP 446 Obs 42, e = 65°.68 at 12μm for an infall distance of 1 AU.

The above results describe a distribution of orbits. To incorporate these results into the MRC CBZODY model we had to transform this orbit distribution into a three-dimensional "number density" description, that is, we had to find a three-dimensional description of the variation of the "effective area per unit volume". This has been done. We have also written a code that performs a line of sight integration to check that our "number density" description is correct. This has also been done. The results are shown in Figures 2-31, 2-32 and 2-33. There are only minor differences between the two sets of results.
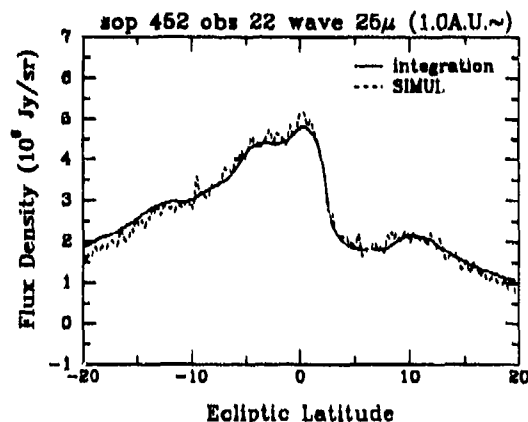
Figure 2-31. Comparison of the complete SIMUL model results to the number density description to be used in CBZODY of SOP 452 Obs 22, $e = 114°.68$ at 25μm for an infall distance of 1 AU.

Figure 2-32. Comparison of the complete SIMUL model results to the number density description to be used in CBZODY of SOP 392 Obs 29, $e = 97°.46$ at 25μm for an infall distance of 1 AU.

39

Figure 2-33. Comparison of the complete SIMUL model results to the number density description to be used In CBZODY of SOP 446 Obs 42, $e = 65°.68$ at $25\mu m$ for an Infall distance of 1 AU.

1. We have demonstrated that we can find a distribution of orbits derived from the prominent Hirayama asteroidal families that gives a model for the dustbands that satisfies the observations over the total range of elongation angles employed by IRAS.

2. We have demonstrated that it is absolutely essential to follow the orbital evolution of these particles from source to sink.

3. We have demonstrated that our model fits the observations to within about 1 MJy/sr or better. The peak flux in the IRAS $25\mu m$ band is about 80 MJy/sr. Thus, our model, when used in conjunction with CBZODY, is already good at the 1 or 2 percent level over the range of elongation angles (60° - 120°) observed by IRAS.

4. The distribution of dust particle orbits used to model the dustbands has been transformed to a three-dimensional distribution of number density (the units are actually effective cross-sectional area per unit volume). All possible cross-sectional area contributions from all the dust particles are computed and recorded in a three-dimensional array.

5. Using this "number density" distribution, a line-of-sight integration is performed for the specified SOP's (days of the year) and elongation angles to produce a smooth plot of the thermal flux in a given band as a function of ecliptic latitude.

6. Comparisons of the dustband profiles obtained (a) from SIMUL and (b) with the corresponding number density model are shown in Figures. 2-31, 2-32, and 2-33. The two sets of curves are nearly identical.

2.6 MODEL FITTING AND VALIDATION.

IRAS observations have been used to verify that the CBZODY model of the zodiacal emission satisfactorily simulates the zodiacal complex. This is accomplished by finding the best-fit, in a least squares sense, model to a well-understood subset of the IRAS data, verifying that the model yields acceptable residuals for this data, and examining the residuals for a larger set of the IRAS data to guide further refinements of the model. Other observations, for example, the Zodiacal Infrared Project (ZIP), have been useful for evaluating the model fit at a wider range of solar elongations.

The IRAS low-resolution ZOHF scans have been used to derive best-fit parameters for the CBZODY dust cloud model. The ZOHF consists of processed one-dimensional scans of the sky binned into approximately $0.5° \times 0.5°$ pixels in all four IRAS bands (effective wavelengths $\lambda_e \approx$ 12, 25, 60, 100μm). Only the 12 and 25μm bands are being used for fitting, since contamination from galactic sources becomes a problem at 60μm and dominates the sky at 100μm. However, the 60 and 100μm bands still contain useful color information, particularly in some relatively uncontaminated scans through the galactic anticenter.

Single scans can be used to put some constraints on the half-width Γ and normalization N_0 of the model density distribution, but the zodiacal emission must be observed throughout the Earth's orbit to determine the ascending node and inclination of the dust cloud symmetry plane. Since the emission varies with elongation, the initial fit uses scans at a single value of elongation ($e = 90°$) from a fairly uniform sampling of points on the Earth's orbit (18 positions over approximately 6 months). At each orbital position, the most nearly pole-to-pole scans were selected (typically ±1°). The use of $e = 90°$ scans minimizes the variation of heliocentric distance D along the LOS, hence minimizing the sensitivity of best-fit estimates of Ω, i, and Γ to radial gradients in dust density and volumetric emissivity. The $e = 90°$ scan sample can be complemented by $e = 80°$ and $100°$ samples with similar 6-month coverage of the Earth's orbit at some cost in coverage near the ecliptic poles. Note that the scan sample will not be uniform in the sense that the near-galactic plane regions excluded from scan fits varies with Earth's orbital position. The effects on coverage of ecliptic latitude resulting from this masking out of the galactic plane should be considered in the analysis of fit results.

It is possible to do a best-fit to any of the IRAS ZOHF scans and obtain a reasonable residual. However, it is important to avoid having every single ZOHF scan fit uniquely. What is more useful is a single set of parameters that fit all data to some accuracy. This has been done and Table 2-3 presents the parameters used when fitting any IRAS data. The default parameter set supplied in the file cbzparms.dat has a default Offset of 0.0 MJy/sr. This is recommend for any non-IRAS data. Figure 2-34 shows the same ZOHF scan as Figure 2-5 only now using the parameter set given in Table 2-3. The total error is still under 10%, but that the zodiacal cloud component is fit less well and is not as flat as in Figure 2-5.

The Normalization Density defined in the default parameter set of Table 2-3 does not fit Zodiacal Infrared Project (ZIP) data. The best fit to the ZIP data consists of the set of values given in Table 2-4. It is not possible to determine the Ascending Node, Inclination, or Scale Height from these in plane data sets. Differences between the ZIP data and IRAS data calibration may account for the differences in Normalization density. Price (1988) reports that the simple D^{-1} model employed did not fit well at large solar elongations ($e > 120°$). They underestimated the flux by 30% at these elongations. Using CBZODY we find that the above parameters fit the data to within a few percent. We have found that the large solar

41

elongations are fit well by CBZODY due to the contribution of the bands. The fits without the band contribution are similar to the Price (1988) fits underestimating the flux by 30%. Table 2-5 gives the file cbzparms.dat supplied with the CBZODY distribution. In the file one can see that the code is possible of a two-plane dust density distribution. The default break point is set to 0.001 AU, inside the Sun, causing the model to always work like a single-plane model.

Table 2-3. Set of general parameters used for all IRAS ZOHF data.

Power Index = ν	1.0
Normalization = N_o	$1.73 \cdot 10^{-17}$ particles/cm^3
HWHM = Γ	0.26
Inclination = i	2.13°
Ascending node = Ω	80.°
IRAS Band 1 Offset	4.45 MJy/sr
IRAS Band 2 Offset	0.95 MJy/sr
Dust Albedo = A	0.3
Dust Effective Density = N_{eff}	$6.4 \cdot 10^{-22}$ particle/cm^3

Table 2-4: Parameters used to fit the ZIP data. Γ, Ω, and i can not be determined from the ZIP data alone.

	12μm	20μm
Power Index = ν	1.0 ± 0.2	1.0 ± 0.2
Normalization = N_o (10^{-17} particles/cm^3)	1.3 ± 0.2	0.8 ± 0.2
Offset	0.0 MJy/sr	0.0 MJy/sr

The IRAS extreme solar elongation scans test the validity of the best-fit model beyond $e = 80°$ - 100°. These scans provide some constraint on the radial power-law index of the density distribution, but this dependence is difficult to separate from radial variations in dust particle properties. The radial density variations are probably better constrained by the wide range of solar elongations observed in ZIP data.

The IRAS 12 and 25μm band observations differ in sensitivity due to contributions to the LOS emissivity integral from different regions of the zodiacal dust complex. The dust temperature near the Earth is estimated at $T_{dust} \approx 250°K$ - 300°K (peak blackbody brightness wavelength $\lambda_{peak} \approx 12\mu m$), and $T_{dust} \propto D^{-1/2}$. As D increases from 1 to 4 AU, λ_{peak} will increase from 12 to 25μm. Therefore, the dust volumetric emissivity at $\lambda = 12\mu m$ will drop more quickly with D > 1 AU than at $\lambda = 25\mu m$ ($12\mu m < \lambda_{peak} < 25\mu m$). The net result is that the 12μm band will be relatively more sensitive than the 25μm band to LOS brightness integral contributions from near-Earth dust, and that the 25μm band will be relatively more sensitive to dust outside the Earth's orbit, particularly dust near $D \approx 4$ AU.

The current dust band model is very qualitative, and it would only confuse the issue to fit the dust cloud and bands simultaneously to the near ecliptic plane data. However, it is in this region that a modified lower envelope fit to the scans would be of use. It is highly undesirable to have the dust cloud model brightness densities exceed the observed brightness here, but we really don't know exactly what the true dust bands look like. Spatial

42

frequency filtering shows distinct bands, but will miss any fairly smooth dust band structures which do appear evident in high resolution scans (perhaps a large number of low brightness bands with a range of inclinations). Rather than having our very uncertain dust band model drive the dust cloud model fit in this region, we can simply reject any dust cloud model which overestimates the observed near-plane brightness density. If the dust cloud model can simultaneously fit scan data away from the ecliptic plane without overestimating in-plane brightness density, then it will be reasonable to fit the dust band model to the observed residuals. This will yield a more accurate normalization for the dust band emission than currently available.
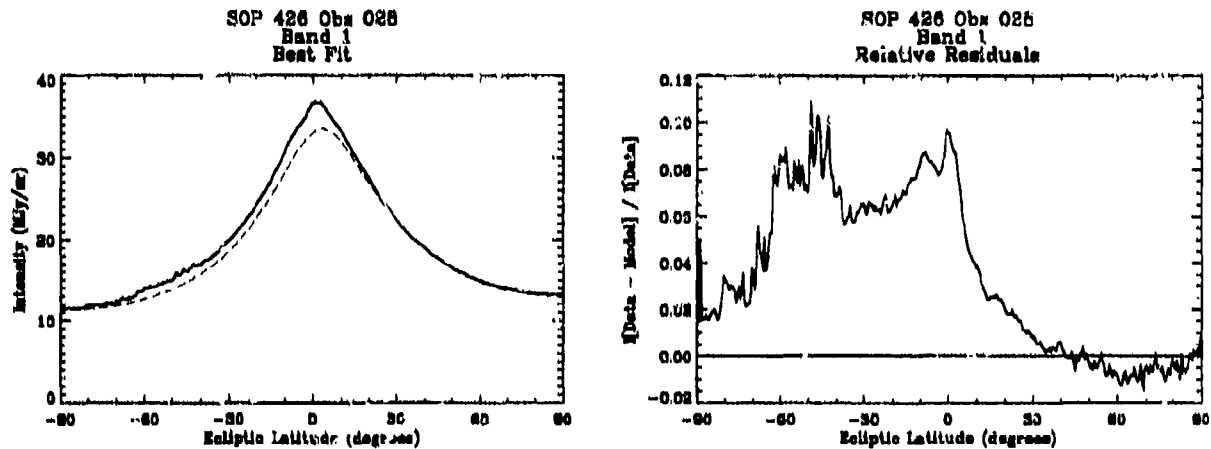
Figure 2.34. The same ZOHF scan as Figure 2-5 but now using the general parameters of Table 2-3.

Comparison of the current best-fit dust cloud model residuals with the dust band model reveals that the location and qualitative features of the dust band model are consistent with the residuals in scans where the dust cloud model is doing a good job of subtracting the true dust cloud emission. However, the overall normalization of the dust band model appears to be a factor of 2 - 3 too low at 25µm and perhaps lower at 12µm. This is not surprising considering the qualitative nature of the model.

Figure 2-35 shows a different perspective of the zodiacal cloud. This image is for an observer in the plane of the ecliptic and 15 AU from the Sun.
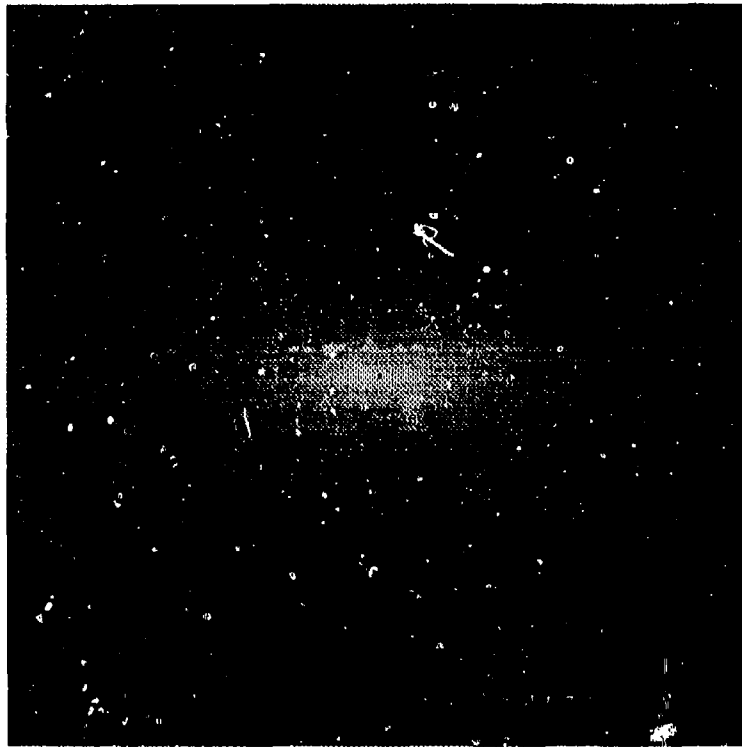
Figure 2-35. Appearance of the entire zodiacal cloud to an observer 15 AU from the Sun and in the plane of the ecliptic.

Table 2-5. The file cbzparms.dat supplied with the CBZODY distribution.

```
nu          -- power index
1.0
hwhm1       -- hwhm inner dust plane
0.26
hwhm2       -- hwhm outer dust plane
0.26
znode1      -- ascending node inner dust plane
80.
znode2      -- ascending node outer dust plane
80.
zincl1      -- inclination inner dust plane
2.13
zincl2      -- inclination outer dust plane
2.13
break1      -- break point between planes
0.001
n0thm1      -- Normalization density, inner plane
1.73
n0thm2      -- Normalization density, outer plane
1.73
n0a2        -- scattering normilization
6.4d-22
albedo      -- dust albedo
0.3
offset      -- DC offset
0.00
```

2.7   CBZODY USER'S MANUAL.

2.7.0   INTRODUCTION.

The current version of CBZODY is Version 5.56, 3 March 1993.

There are six operational modes for the current CBZODY. These are:

1)   Produce a gnomonic projection image of size nxm where n and m are specified by the user (example input MKGNOM.INP),

2)   Produce an intensity along a single line of sight, also capable of reading a list (example input MK1LOS.INP),

3)   Read an IRAS ZOHF and run the model for the same pointing directions (example input SOP426.BAT).

4)   Produce a spectra between two wavelengths (example input MKSPEC.INP).

5)   Produce a Mollweide projection of the entire sky of size nxm where n and m are specified by the user (example input MKMOLL.INP).

6)   Produce a "best fit" to the IRAS data scan using non-linear least squares (example input NLSOP426.BAT).

2.7.1   INSTALLATION.

To install CBZODY copy all files from the distribution media (tape, floppy disk, etc.) into a subdirectory. This subdirectory may have any name and the rest of the document assumes the subdirectory name of cbzody.

For the IBM compatible PC an executable file cbzody.exe is included and the user can skip the compiling steps. For other platforms the user must follow the following steps. CBZODY has been written in ANSI standard FORTRAN, however, not all compilers use the same system for defining OPEN statements and a few other differences exist as well. We have identified as many differences between systems as we can and have written the code to allow easy configuration. There are four FORTRAN files distributed with CBZODY, these are:

CBZ1.FOR,
CBZ2.FOR,
N2PORTA.FOR, and
N2PORTB.FOR.

The file CBZ1.FOR contains the main body of the CBZODY code. CBZ2.FOR contains the machine specific routines, and the N2PORT files are a set of routines for non-linear least squares fitting of data.

STEP 1: In the file CBZ1.FOR is a parameter called SLASH. This parameter sets up naming conventions for the output data files. On PC and compatibles the SLASH parameter is set to backslash, '\', corresponding to directory naming conventions. For UNIX systems the SLASH parameter must be set to '/', the forward slash. Roughly on lines 45 are two parameter statements. Comment out the one not used by your system and be sure the slash character used by your system has no comment.

STEP 2: The file CBZ2.FOR contains all of the machine or compiler specific routines. These are INPUT, IMOPEN, D1MACH, R1MACH, and I1MACH. The first two correspond to I/O functions and the last three set parameters used by the non-linear least squares fitting routines. They identify the largest and smallest significant numbers. Comment out the lines not used by your system. If you system requires different calls you will have to make these changes yourself. All efforts will be made to include system configurations as soon as they are known.

STEP 3: Compile the four files using your native FORTRAN compiler. To aide PC users a file called CBZ32.MAK has been included which contains the calls for the 32-bit version of the Lahey FORTRAN compiler. To aide SUN/UNIX users a makefile has been included. These files may require changes for other systems.

STEP 4: Edit the file IDIRNAME to match the subdirectory name where your source and data files are stored. A sample file for PC user's has been included. A sample UNIX IDIRNAME file would contain:

/files2/pauln/cbzody/

STEP 5: Create a subdirectory called CBZ by

md cbz

for PC users, or

mkdir cbz

for UNIX users. For UNIX systems this must be lower case.

STEP 6: Copy the file MK1LOS.INP to CBZODY.INP and run the code by typing

CBZODY 4

If the program runs without errors then two files are created, CBZODY.OUT which echoes back times and coordinates and RADLIST.DAT which contains the intensities for the sample points in the input file.

All inputs are read from a file called CBZODY.INP or the command line. The following examples describe each of the possible CBZODY options along with sample inputs.

2.7.2 GNOMONIC PROJECTION OPTIONS.

This option creates images with a gnomonic projection (see Appendix A.2) as specified in the input file CBZODY.INP. The images can be any size up to 2048x2048. However, the code always assumes square pixels. To run the model for a gnomonic projection type:

cbzody #

where:

> \# = blank -- run both the cloud and band models;
> \# = 1   -- run both the cloud and band models,
> \# = 2   -- run only the cloud model,
> \# = 3   -- run only the band model,
> \# = 12 -- run both the cloud and band models using the "fast" model,
> \# = 13 -- run only the cloud model using the "fast" model,
> \# = 14 -- run only the band model using the "fast" model.

The "fast" model refers to a technique to reduce execution time but retain a significant part of the accuracy of CBZODY. The method is to calculate, for the cloud intensity, a reduced grid of points. The new grid is taken to b, for the zodiacal cloud intensity, a reduced grid of points. The new grid is taken to be as 1/10 of the original grid size. These points are evenly spaced throughout the image. The rest of the grid is obtained by using a bi-linear interpolation scheme. The zodiacal cloud emission varies slowly over most images and the results should be within 5% of the extended calculations. The bands are calculated by calculating a single cross ecliptic raster at twice the number of pixels. The band image is seen as constant across any ecliptic latitude. Again, a bi-linear interpolation is performed to fill out the rest of the image.

All images will be stored in a file named

> c:\cbzody\cbz\cbz55img.xxx

where xxx represents a numbering sequence from 000 to 999. The full path must exist, the code will not create subdirectories. All images have a 256 byte header.

Sample input for gnomonic projections (MKGNOM.INP):

LINE 1)	256 256	number of pixels in x and y directions
LINE 2)	12	central wavelength in microns
LINE 3)	4,8,1992	day, month, year of observation
LINE 4)	13,5,2.56	hour, minute, second of observation
LINE 5)	71.1,42.5	observers latitude and longitude on the earth's surface degrees. Latitude +90 is N, -90 is south. Longitude -180 to +180 where positive is West of Greenwich.
LINE 6)	0.00	Observer altitude above mean sea level, meters
LINE 7)	0.06667	pixels size, degrees/pixel
LINE 8)	15.	Longitude of center of image, degrees
LINE 9)	0.	Latitude of center of image, degrees
LINE 10)	1	Coordinate system of lines 8 and 9. If the input is -1 the system is Sun centered ecliptic. A 0 is ecliptic and +1 means the system is equatorial and the inputs are RA and Dec.

47

2.7.3   LINE OF SIGHT OPTION.

To run a line of sight type:

        cbzody 4

An output file is produced with the name RADLIST.DAT. Five columns are output. The first are the pointing direction in ecliptic coordinates, degrees. The next are the total (cloud + bands), cloud, and band intensities in MJy/sr.

Sample input for line of sight (MK1LOS.INP):

LINE 1)	256 256	Number of pixels in x and y directions (ignored).
LINE 2)	12	Central wavelength in microns.
LINE 3)	4,8,1992	Day, month, year of observation.
LINE 4)	13,5,2.56	Hour, minute, second of observation.
LINE 5)	71.1,42.5	Observers latitude and longitude on the earth's surface degrees. Latitude +90 is N, -90 is south. Longitude -180 to +180 where positive is West of Greenwich.
LINE 6)	0.00	Observer altitude above mean sea level, meters.
LINE 7)	0.06667	Pixels size, degrees/pixel.
LINE 8)	225.	Ecliptic longitude, degrees, 0 to 360.
LINE 9)	0.	Ecliptic latitude, degrees -90 to +90.
LINE 10)	1	Repeat flag, 0=end of data, 1=read new lines 8 and 9.
LINE 11)	230.	Ecliptic longitude, degrees, 0 to 360.
LINE 12)	0.	Ecliptic latitude, degrees -90 to +90.
LINE 13)	0	Repeat flag, 0=end of data, 1=read new lines 8 and 9.

2.7.4   IRAS DATA FILES.

To run a IRAS ZOHF type:

        cbzody # sop obs 'filename' band

            # = 5   -- run both the cloud and band models
            # = 15   -- run only the cloud model

where:

        sop = SOP of IRAS ZOHF file
        obs = Obs number in the SOP
        'filename' = filename (quotes required) of the SOP file
        the format is the same as the ZOHF data tapes
        band = IRAS band number, 1 (12 microns) or 2 (25 microns)

The input file CBZODY.INP is not used in this mode. The output is a file called CBZODY.OUT. There are seven columns. The first two are the ecliptic coordinates of the stare point in degrees (from the ZOHF). The third column is the orbital inclination, degrees

48

(from the ZOHF). Column four is the IRAS data in MJy/sr. Column five is the model data in MJy/sr. Column six is always 1.0. Column seven is the residual (data - model) in MJy/sr.

A sample IRAS data file is provided in the DATA directory, S426V3.1 along with a batch file (SOP426.BAT) which runs one of the scans.

The sample input (SOP426.BAT) is:

```
cbzody 5 426 17 's426v3.1' 1
```

2.7.5 SPECTRA.

It is possible to use CBZODY to generate spectra for a single line of sight. To implement this option type:

```
cbzody 6
```

An output file is produced with the name RADLIST.DAT. Four columns are output. The first is the wavelength in microns. The next are the total (cloud + bands), cloud, and band intensities in MJy/sr.

The sample input file (MKSPEC.INP) contains:

LINE 1)	256 256	Number of pixels in x and y directions (ignored).
LINE 2)	12	Central wavelength in microns (ignored).
LINE 3)	4,8,1992	Day, month, year of observation.
LINE 4)	13,5,2.56	Hour, minute, second of observation.
LINE 5)	71.1,42.5	Observers latitude and longitude on the earth's surface degrees. Latitude +90 is N, -90 is south. Longitude -180 to +180 where positive is West of Greenwich.
LINE 6)	0.00	Observer altitude above mean sea level, meters.
LINE 7)	0.06667	Pixels size, degrees/pixel.
LINE 8)	2. 30. 0.1	Starting wavelength, ending wavelength, wavelength step size all in microns.
LINE 9)	90.	Sun centered (differential) ecliptic longitude in degrees.
LINE 10)	0.	Ecliptic latitude in degrees.

2.7.6 MOLLWEIDE PROJECTION OPTIONS.

To generate an image using a Mollweide all sky projection use:

```
cbzody #
```

where:

```
# = 7    -- run both the cloud and band models
# = 8    -- run only the cloud model
# = 9    -- run only the band model
```

49

All images will be stored in a file named

cbz55img.xxx

where xxx represents a numbering sequence from 000 to 999 stored in the cbz subdirectory as specified by IDIRNAME.

The sample input to make a Mollweide projection (MKMOLL.INP) is:

LINE 1)	512 256	Number of pixels in x and y directions. The projection will look best with a 2:1 aspect ratio.
LINE 2)	12	Central wavelength in microns.
LINE 3)	4,8,1992	Day, month, year of observation.
LINE 4)	13,5,2.56	Hour, minute, second of observation.
LINE 5)	71.1,42.5	Observers latitude and longitude on the earth's surface degrees. Latitude +90 is N, -90 is south. Longitude -180 to +180 where positive is West of Greenwich.
LINE 6)	0.00	Observer altitude above mean sea level, meters.
LINE 7)	0.06667	Pixels size, degrees/pixel.
LINE 8)	15.	Longitude of center of image, degrees.
LINE 9)	0.	Latitude of center of image, degrees.
LINE 10)	1	Coordinate system of lines 8 and 9. If the input is -1 the system is Sun centered ecliptic. A 0 is ecliptic and +1 means the system is equatorial and the inputs are RA and Dec.

2.7.7 IRAS NON-LINEAR LEAST SQUARE FITS.

To use a non-linear least squares fitting routine the input is:

cbzody # sop obs 'filename' band

where:

= 10   Fit all ten parameters, these parameters are the inner and outer plane inclinations, inner and outer plane ascending node, inner and outer plane normalization density at 1 AU, inner and outer plane HWHM at 1 AU in terms of tan(beta), a DC offset, and the power density law where 1.0 is Poynting-Robertson light drag.

= 11   Fit only nine parameters, the excluded parameter is the power density law.

= 16   Fit only seven parameters, the excluded parameters are the power density law and the normalizations density one and two plane models included.

50

and:

sop = SOP of IRAS ZOHF file
obs = Obs number in the SOP
'filename' = filename (quotes required) of the SOP file the format is the same
as the ZOHF data tapes
band = IRAS band number, 1 (12μm) or 2 (25μm).

The input file CBZODY.INP is not used in this mode. The output is a file called CBZODY.OUT. There are seven columns. The first two are the ecliptic coordinates of the stare point in degrees (from the ZOHF). The third column is the orbital inclination, degrees (from the ZOHF). Column four is the IRAS data in MJy/sr. Column five is the model data in MJy/sr. Column six represents a weight function. The region 15 degrees above and below the ecliptic plane is always excluded because of dust band contamination to the cloud emission. Likewise the region 12 degrees away from the galactic plane is excluded. In this column a 0.0 represents a region excluded from fitting while a 1.0 represents a region included. Column seven is the residual (data - model) in MJy/sr. In addition, CBZODY.OUT reports the results for the ten parameters at the beginning of the file. The same header to CBZODY.DAT is provided in a file called DATA. This file does not have the scan data or model fits. It is provided to allow a hard copy.

A sample IRAS data file is provided in the DATA directory, S426V3.1 along with a batch file (NLSOP426.BAT) which runs one of the scans.

cbzody 11 426 17 's426v3.1' 1

2.7.8 FLOATING POINT OUTPUT.

Like other CBSD component modules, CBZODY allows for the generation of a floating point (4-byte) image. Normal operation is to produce a byte (8-bit) image. To force a floating point output use any of the command line inputs with a negative number:

CBZODY -1
CBZODY -4
etc.

2.7.9 DATA FILES INCLUDED WITH CBZODY.

Eleven data files are included on the CBZODY distribution. These are:

silems.dat	volumetric emissivity spectrum vs. distance database
themis.dat	Themis dust band latitudinal surface brightness profiles and cubic spline interpolation coefficients.
eos.dat	Eos dust band latitudinal surface brightness profiles and cubic spline interpolation coefficients.
koronis.dat	Koronis dust band latitudinal surface brightness profiles and cubic spline interpolation coefficients.
filter.dat	Example bandpass filter data file.

iband1.dat   IRAS filter band 1 (12 microns)
iband2.dat   IRAS filter band 2 (25 microns).
earth.dat   Periodic terms for Earth's orbit
cbzparms.dat Dust cloud parameters
deltaat.dat   Julian dates of leap seconds
s426v3.1   Sample IRAS data records (ZOHF Version 3.1, SOP 426).

2.8 SAMPLE OUTPUT.

The first test is a comparison to the IRAS Sky Flux plates. Figure 2-36 gives an IRAS image, Plate 096, from HCON2, Band 2, centered on RA 1^h and Dec $0°$. The data shown in the plate was acquired early in July of 1983. Figure 2-37 show the CBSD simulation of the same region for a date of 1 July 1983. It is important to note that the original data suffers from extensive stripping due to non-uniformity in detectors. Table 2-6 is the input file used to generate Figure 2-37.
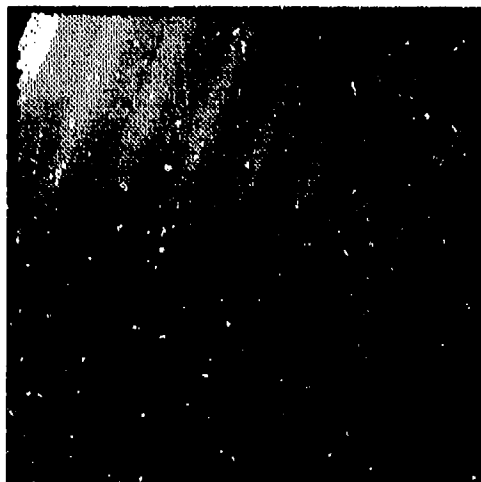
Figure 2-36. IRAS SkyFlux plate of the region 1^h and $0°$.
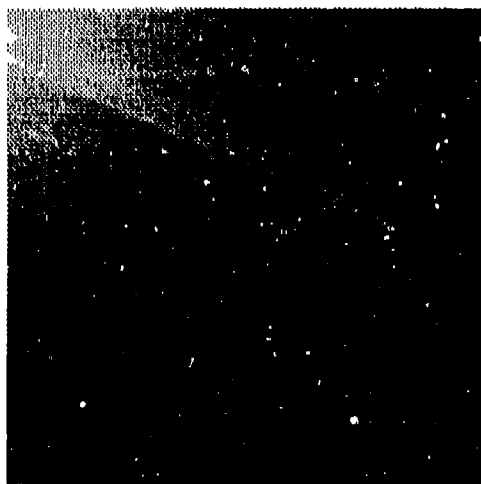
Figure 2-37. CBZODY model output of the same region as Figure 2-36.

53

Table 2-6. CBZODY.INP input file used to generate Figure 2-37:

```
256 256
25.
1,7,1983
0,0,0.0
0.,0.0
900000.
0.066667
15.00
0.0
1
```

The next example is the Mollweide all sky projection. Figure 2-38 shows the entire sky in Sun-centered ecliptic coordinates. Note the parallax effects are prominent when viewing the dust bands. The Sun is the single pixel at the center of the field. The solar intensity is scaled to be the same as the brightest dust pixel in the rest of the image. The 12 solar radius dust free cavity is clearly visible in the image with dust visible along the line of sight and beyond the Sun. Table 2-8 gives the input file used to generate this image. Note that this image is actually a composite. To bring out the structure of the bands CBZODY was run a second time using the band only option. The bands then have a multiplicative factor of 100 applied. The composite program is described in Section 6

Figure 2-38. An all sky projection in Sun-centered ecliptic coordinates.

Table 2-7. Input file used for Figure 2-38.

```
512,256
20.
21,3,1983
0,0,0.0
1.98166666,-167.4533333
0.
0.703125
0.0
0.0
-1
```

Table 2-8 is the input file used to generate a set of single line of sight radiance values. In the file three separate lines of sight are sampled in Sun centered ecliptic coordinates. Table 2-9 gives the results of the run sent to the output file RADLIST.DAT. These also are the same lines of sight as shown in Figures 2-9 and 2-10.

Table 2-6. Input file for the single line of sight test case.

```
256 256
12.
1,11,1992
0,0,0
0.,0.
0.
0.05
0.00000
0.00000
1
10.00000
0.00000
1
30.00000
0.00000
1
45.00000
0.00000
1
90.00000
0.00000
1
120.00000
0.00000
1
180.00000
0.00000
1
30.00000
30.00000
1
45.00000
45.00000
1
90.00000
90.00000
0
```

Table 2-9. Output file RADLIST.DAT for the cases in Table 2-8.

```
Ascending Node =    80.000
Inclination    =     2.130
Power Index    =     1.000
Scale Factor   =     0.260
Normalization  =     1.730
Offset         =     0.000
Lat.      Long.     Total       Cloud       Bands
   0.000     0.000 7.6271E-01 0.0000E+00 7.6271E-01
   0.000    10.000 1.6405E+03 1.6398E+03 6.8976E-01
   0.000    30.000 3.1283E+02 3.1222E+02 6.0805E-01
   0.000    45.000 1.4809E+02 1.4750E+02 5.9578E-01
   0.000    90.000 3.9843E+01 3.9110E+01 7.3284E-01
   0.000   120.000 2.5453E+01 2.4631E+01 8.2245E-01
   0.000   180.000 1.8537E+01 1.7775E+01 7.6269E-01
  30.000    30.000 3.6883E+01 3.6883E+01 0.0000E+00
  45.000    45.000 2.1329E+01 2.1329E+01 0.0000E+00
  90.000    90.000 1.2598E+01 1.2598E+01 0.0000E+00
```

2.9   REFERENCES

Bohren, C.F. and Huffman, D.F. (1983). *Absorption and Scattering of Light by Small Particles*, (New York: Wiley).

Dermott,S. F. P. D. Nicholson, J. A. Burns and J. R. Houck. (1984) *Nature*, **312**, 505

Dermott, S.F., P. D. Nicholson, J. A. Burns and J. R. Houck. (1985). IAU Colloquium #85, *Properties and Interaction of Interplanetary Dust* (eds. R. H. Giese and P. Lamy) (D. Reidel Pub. Co.) p395.

Dermott,S.F., P. D. Nicholson, and B. Wolven. (1986) In *Asteroids, Comets and Meteors, II* (eds. C-I. Lagerkvist and H. Rickman), Uppsala, p583.

Dermott, S.F., P. D. Nicholson, Y. Kim, B. Wolven and E. Tedesco. (1988). In *Comets to Cosmology* (ed. A. Lawrence), (Berlin: Springer-Verlag,), p3.

Dermott,S.F., P. D. Nicholson, R. S. Gomes and R. Malhotra. (1990) *Adv. Space Res.* **10**, (1)165.

Dermott, S. F., Gomes, R. S., Durda, D. D., Gustafson. B. Å. S., Jayaraman, S., Xu, Y. L., and Nicholson. P. D. (1992a) *Chaos, Resonance, and Collective Dynamical Phenomena in the Solar System*, (ed. S. Ferraz-Mello), p333.

Dermott, S. F., Durda, D. D., Gustafson, B. Å. S., Jayaraman, S., Y. L. Xu, R. S. Gomes, and P. D. Nicholson. (1992b) In *Asteroids, Comets and Meteors 1991*, (eds. A.W. Harris and E. Bowell), Flagstaff, p153.

Dermott, S. F. and Nicholson, P.D. (1989), In *Highlights of Astronomy*, **8**, p259.

Deul, E. R., and Wolstencroft, R. D. (1988). *Astron. Astrophys.*, **196**, 277.

Draine, B. T. and Lee, H. M. (1984), *Ap. J.*, **285**, 89.

Durda, D. D., Dermott,S. F., and Gustafson B. Å. S. (1992). In *Asteroids, Comets and Meteors 1991*, (eds. A.W. Harris and E. Bowell), Flagstaff, p161.

Giese, R. H., and Kneißel, B. (1989). *Icarus*, **81**, 369.

Giese, R. H., Kneißel, B., and Rittich U. (1986). *Icarus*, **68**, 395.

Good, J. (1988). Unpublished IPAC Report.

Gray, D. F. (1972) The Observation and Analysis of Stellar Photospheres (New York: Wiley).

Gustafson, B. Å. S. (1990), In Fall 1990 IRCB Review Meeting Minutes.

Gustafson, B. Å. S. (1992) Submitted to *Icarus*.

Gustafson, B. Å. S., E. Grün, S. F. Dermott, and D. D. Durda. (1992) In *Asteroids, Comets and Meteors 1991*, (eds. A.W. Harris and E. Bowell), Flagstaff, p223.

IRAS Catalogs and Atlases, Explanatory Supplement. (1988), ed. C. Beichman, G. Neugebauer, H. J. Habing, P. E. Clegg, and T. J. Chester, (Washington, D.C.: GPO).

Kerker, M. (1969). *The Scattering of Light and other Electromagnetic Radiation*, (New York: Academic Press).

Lamy, P.L., Grün, E., and Perrin, J.M. (1987). *Astron. Astrophys.*, **187**, 767.

Lang, K.R. (1980). *Astrophysical Formulae*, (New York: Spriner-Verlag).

Lienert, C. (1975). *Space Sci.Rev.*, **15**, 281.

Leinert, C., Richter, I., Pitz, E., and Plank, N. (1981). *Astron. Astrophys.*, **103**, 177.

Milani, A. (1992). Private communication to S. Dermott.

Murdock, T. L., and Price, S. D. (1985). *Astron. J.*, **90**, 375.

Price, S.D. (1988). *Optical Eng.*, **27**, 75.

Reach, W. T. (1988), *Astrophys..J.*, **335**, 468.

Röser, S. and Staude, H.J. (1978). *Astron. Astrophys.*, **67**, 381.

Rowan-Robinson, M., Hughes, J., Vedi, K., and Walker, D. W. (1990), *M.N.R.A.S.*, **11**, 1.

Sykes, M. V. (1990). *Icarus*, **84**, 267.

Sykes, M. V., Greenberg, R., Dermott, S. F., Nicholson, P. D., Burns, J. A., and Gautier, T. N. (1989). In *Acteroids II*, eds. R. P. Binzel, T. Gehrels, and M. S. Matthews, (Tucson: U. of Arizona), p.336.

van de Hulst, H.C. (1957), *Light Scattering by Small Particles* (New York: Wiley).

Wiscombe, W.J. (1980). *Appl. Optics*, **19**, 1505.

3.0 THE CBSD POINT SOURCE BACKGROUND MODULE

3.1 Background

The emission from stellar point sources and other galactic "point-like" sources represents singly the most important source of *clutter* in the celestial background. This background is described by many catalogs of point sources.

Because the CBSD has been directed at the 2-30 μm spectral range, the most important point source catalog for the IR CBSD was the IRAS Point Source Catalog (PSC). The IRAS PSC, Version 2, encompasses ~246,000 sources, going down to about magnitude 5 in its Band 1 (at 12 μm). However, only about 159,000 of these sources have good quality flux data at 12 μm. The other 12 μm flux entries are upper limits for point sources which have been detected in one or more longer wavelength bands. Many of those may actually be little more than "knots" in the pervasive cirrus background.

Although the PSC is an excellent source of CBSD information, there are several important reasons why it does not satisfy the requirements for generalized IR backgrounds modeling:

- *The PSC samples the background for only two bands in the 2-30 μm region, and each of those spectral bands has a large spectral bandwidth.*

- *The IRAS 12 μm sensitivity limit (a few tenths of a Jansky) is at least 5-10 times higher than the CBSD objective.*

- *In much of the galactic plane, as well as several other regions (e.g. the Magellanic clouds), IRAS was confusion-limited; consequently, the IRAS PSC is complete only down to ~2 Jy in many regions.*

- *The IRAS spatial finesse of only a few arc-minutes is clearly insufficient for the CBSD requirement of a few arc-seconds.*

Figure 3-1 below vividly illustrates the IRAS confusion limitation, showing that there is an important region in the galactic plane for which the IRAS PSC does not include *any* 12 μm sources fainter than 0.5 Jansky.
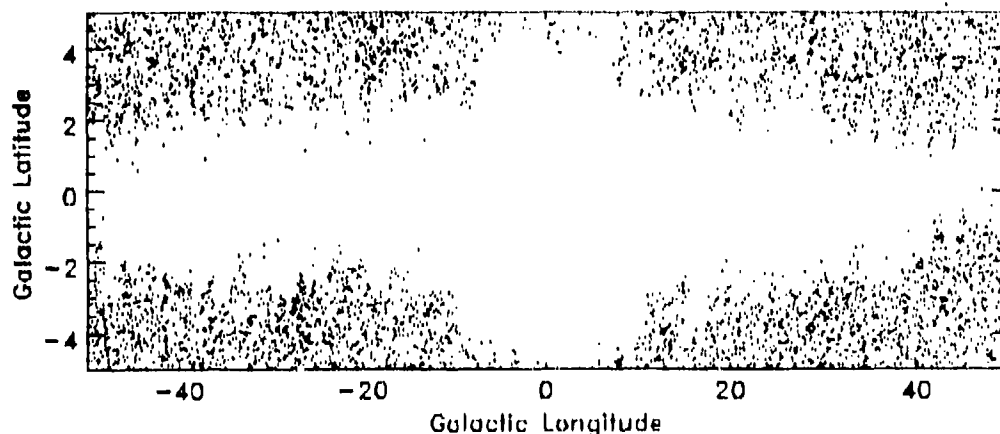
Figure 3-1.   Map of IRAS PSC Band 1 Sources Fainter than 0.5 Jansky

60

The Air Force Geophysics Laboratory (now the Geophysics Directorate of the Phillips Laboratory), in conjunction with the NASA Ames Research Center, supported and directed the development of an IR model of the point source sky which would be consistent with IRAS point source data but would not be subject to these limitations.

Developed by Jamieson Science & Engineering (JS&E) and initially delivered to the Air Force in early 1989, *SKY* comprises geometrically and physically realistic representations of the galactic disk, bulge, spheroid, spiral arms (including the "local arm"), molecular ring, and the extra-galactic sky. Each component was modeled in detail based upon existing information drawn from optical, infrared, radio continuum, and radio molecular line surveys. *SKY* provides a description of the infrared point source sky which comprises realism sufficient to match all relevant available source counts (predominantly IRAS).

SKY models each of the galaxy's geometric components as distributions of up to 87 different spectral classes, including 82 classes of stars, two classes each of planetary and reflection nebulae, and one of compact HII regions.

The statistical descriptions of point source distributions which are employed within *SKY* have been validated by Jamieson Science and Engineering, via comparison of *SKY* point source counts (versus 12 and 25 μm magnitudes) with the IRAS PSC, Faint Source Catalog (FSC), and Serendipitous Catalog (SSC). Figures 3-2a and 3-2b synopsize the 12 μm global comparisons with the PSC; in the unshaded zones, the agreement is said to be in the range of ±25%.

The quality of the validation results essentially verifies the formalism of the model code, the geometrical description of the galaxy, and the critical selections from the literature of absolute magnitudes, scale heights, and population densities for the many classes of celestial sources represented in it.

Although *SKY* does not itself generate scenes, it has been adopted as a major resource for CBSD scene modeling and generation.

> *SKY predicts, for any specified line of sight, the number of point sources per unit angular area per magnitude interval for each of the spectral classes.*

> *The greatest "limitation" of SKY is that each line of sight calculation requires, for example, 10-20 seconds on a SPARCstation. For scene generation addressing ~10^6 lines of sight, this is unacceptably slow.*

For each of the spectral classes contained within it, the *SKY* program also contains a spectral template and tables of absolute magnitudes for the J, H, K, [2.4], and the IRAS 12 and 25 μm bands. However, in the first deliveries of *SKY*, the spectral templates were derived solely from IRAS LRS (Low-Resolution Spectrometer) data. Accordingly, the initial *SKY* spectral templates were limited to the LRS's 7.67 - 22.74 μm spectral range.

Validation of NASA/Ames SKY Model

12 μm
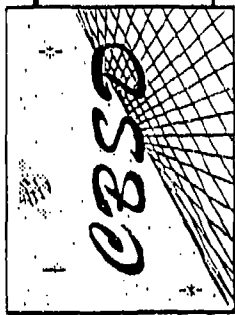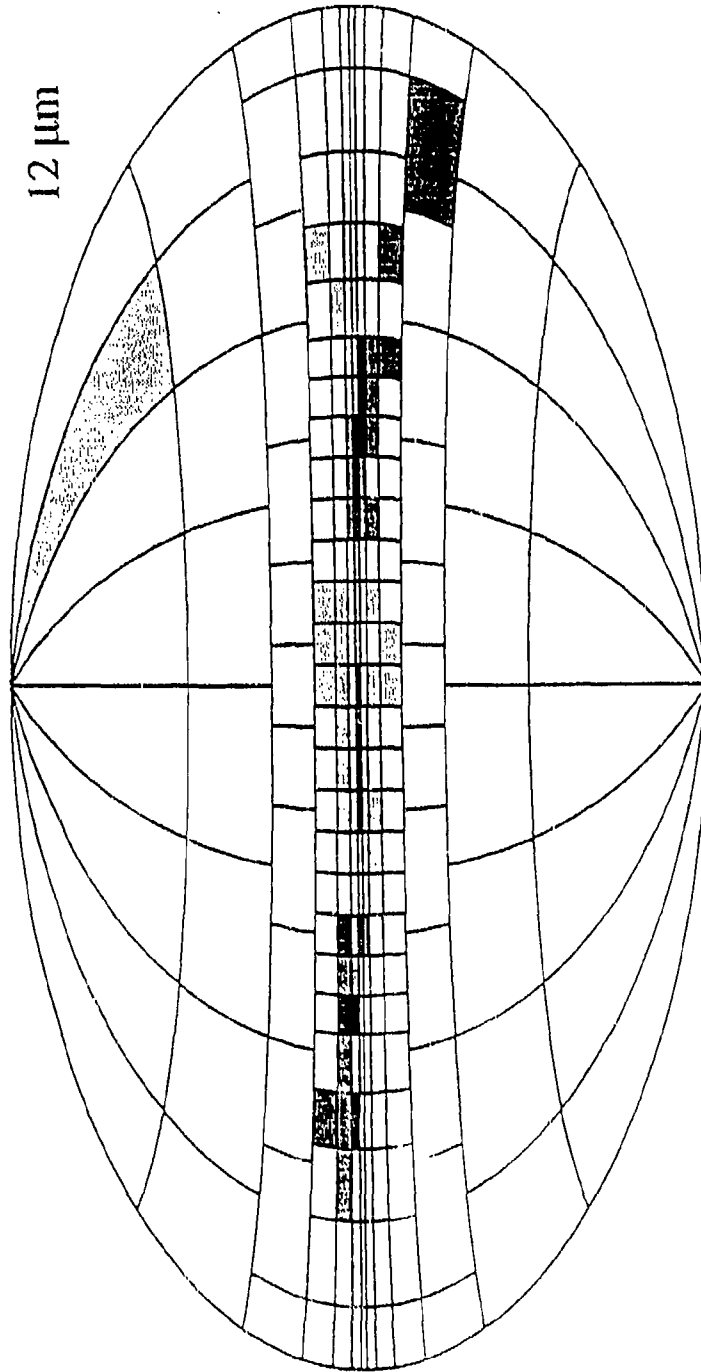
Black: PSC > 2*SKY   MdGry: PSC > 1.5*SKY   LtGry: PSC < SKY

Figure 3-2a.   All-Sky Galactic Map of SKY vs PSC 12 μm Comparison Differences

Validation of NASA/Ames SKY Model

12 μm
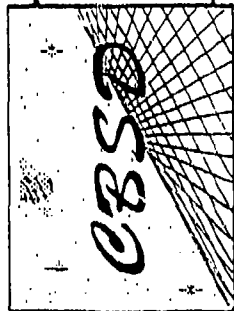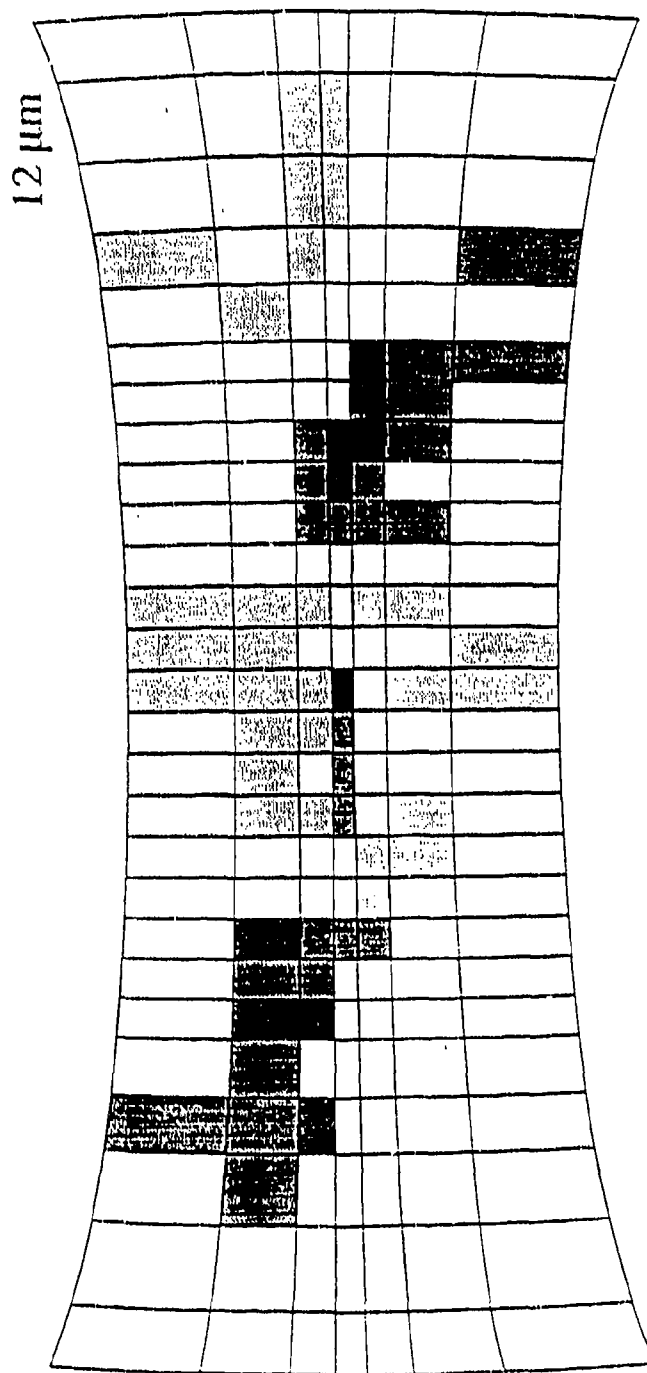
Black: PSC > 2*SKY   MdGry: PSC > 1.5*SKY   LtGry: PSC < SKY

Figure 3-2b.   Galactic Plane Map of SKY vs PSC 12 μm Comparison Differences

3.1.1 Two Different CBSD Approaches

As the CBSD developed, two distinctly different procedures for point source scene generation were used. In the first method, "on the fly" Monte Carlo statistics were employed to generate discrete point sources, in user-specified scenes, whose distribution and characteristics were guided by the SKY luminosity functions. In the second approach, a SKY-based synthetic point source catalog was generated with dial-a-wavelength capability. However, the actual one-time generation of the catalog made use of the initial CBSD point source scene generator (basically, to make one all-sky point source image which became the catalog). Therefore, in the following sections a brief overview of the first method will be provided so that the catalog generation can be better understood.

3.2 Initial CBSD Implementation

In order to achieve realistic execution times for the first CBSD point source modules, it was decided that SKY would be used to generate galactic coordinate "maps" of the distribution functions corresponding to binned magnitudes of each spectral class. If properly designed, sparsely sampled distribution maps can be accessed with very fast bi-linear interpolation methods to adequately represent the essence of SKY (its density distribution functions), and, ultimately, to guide the placing of discrete point sources for background scene generation.

Source brightness space was initially quantized into 17 astronomical magnitude "bins" ranging from magnitudes -1 to +15, in increments of one magnitude. (Note that an astronomical magnitude is defined such that a factor of ten in brightness corresponds to a difference of 2.5 astronomical magnitudes.) In these first CBSD point source modules, HII regions and nebulae (both reflection and planetary) were also treated as point sources, providing a total of 87 spectral classes.

Phenomenologically, this approach is equivalent to treating the galactic point source background as being made up of 1,479 different types of point sources: 87 spectral classes, each with 17 possible brightness sub-classes.

- *The adopted strategy called for generating a digital "library" of the 1,479 (i.e. 17 x 87) such maps, employing non-uniform sampling within the maps so that the galactic plane would be rather finely sampled while those regions far from the plane could be much more coarsely sampled.*

- *To arrive at optimal sampling intervals, the distribution functions were to be sampled finely enough such that bi-linear interpolation of the maps would be accurate to ~ ± 10%.*

- *After several experimental iterations, a final design of the Point Source Density Maps (PSDM's) resulted in a non-uniform sampling mesh which sampled the SKY luminosity functions at 31 galactic latitudes and 29 galactic longitudes - for a total of only 899 samples per PSDM.*

3.2.1 Spatial Quantization

Figure 3-3 illustrates the PSDM sampling grid which was adopted for the CBSD. The *SKY* point source distribution functions are discretely sampled at all the grid intersections, i.e. at 31 galactic latitudes and 29 galactic longitudes. *(Note that the space is clearly very over-sampled at high galactic latitudes. However, to simplify the computations driven by this sampling, it was convenient to have samples at the same set of longitude points for each latitude.)* The actual coordinates of the grid nodes are:

Galactic Latitude:

$0°, ±0.2°, ±0.4°, ±0.7°, ±1°, ±1½°, ±2°, ±3°, ±4°, ±5°, ±7½°, ±10°, ±15°, ±30°, ±45°, ±90°$

Galactic Longitude:

$0°, ±1, ±2½°, ±5°, ±10°, ±15°, ±20°, ±25°, ±30°, ±35°, ±45°, ±60°, ±90°, ±120°, ±180°$

For the galactic coordinates corresponding to each of the 899 nodes, one *SKY* run was made to compute the distribution function values for each of the 1,479 point source types. Thus, 899 *SKY* runs lead to development of 1,479 PSDM's.

Each of the 1,479 PSDM's is simply a data file containing a regularly ordered list of 899 point source density values (P_d = sources/deg^2). To minimize the total size of the 1,479 data files and to optimize I/O access to them, the density values are logarithmically compressed and stored as 2-byte integers in binary (unformatted) form. Each file is, therefore, $2 \times 899 = 1,798$ bytes in size. The complete PSDM data base for one "master" wavelength is $1,479 \times 1,798 = 2.65$ MBytes, a size which is both easily manageable and highly portable.

The character of some individual PSDM's is illustrated in Figures 3-4 and 3-5. Each Figure is a surface plot of the inner plane sections of the 6th and 12th magnitude PSDM's for one spectral class. Note that the ordinates are auto-scaled. These Figures provide a good "feel" for the nature of a few distribution functions, how they vary, and how they are sampled.

The procedure in which these PSDM's were used for point source scene generation was quite straightforward. For any given pixel, of a given size, in a scene, and for each of the 1,479 point source types, a point source density value was computed via bi-linear interpolation amongst the four nearest neighbors in the PSDM sampling grid. *(Note that the same one set of bi-linear interpolation coefficients can be employed for all 1,479 contributions to a given pixel.)*

The point source density value, P_d, was multiplied by the pixel size (i.e. IFOV) to get sources/pixel, P_p. If the interpolated sources/pixel value, P_p, was ≥ 1, then the flux from nint(P_p) sources was added to the pixel. If $P_p < 1$, then a random number, ξ, was drawn, $0 \leq \xi \leq 1$, and ξ was compared with P_p to decide whether to add the flux from one source to the pixel. Note that for most scenes, with reasonably small pixels, $P_p < 1$ is usually the case.

For each point source thus "generated," within a specified brightness magnitude "bin," a different random number was drawn to assign the source a brightness within its magnitude bin.
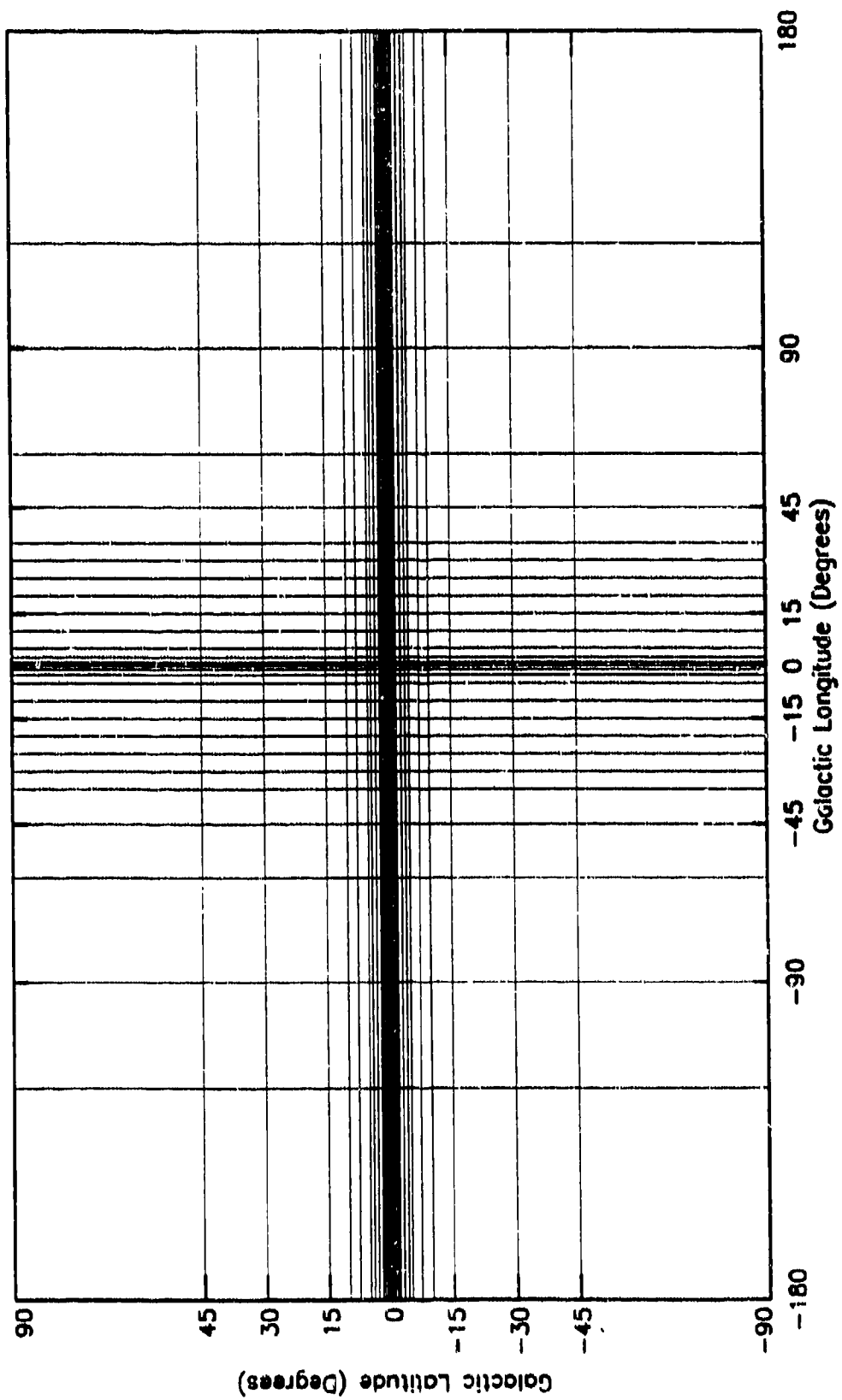
Figure 3-3.   The CBSD Point Source Density Map (PSDM) Sampling Grid
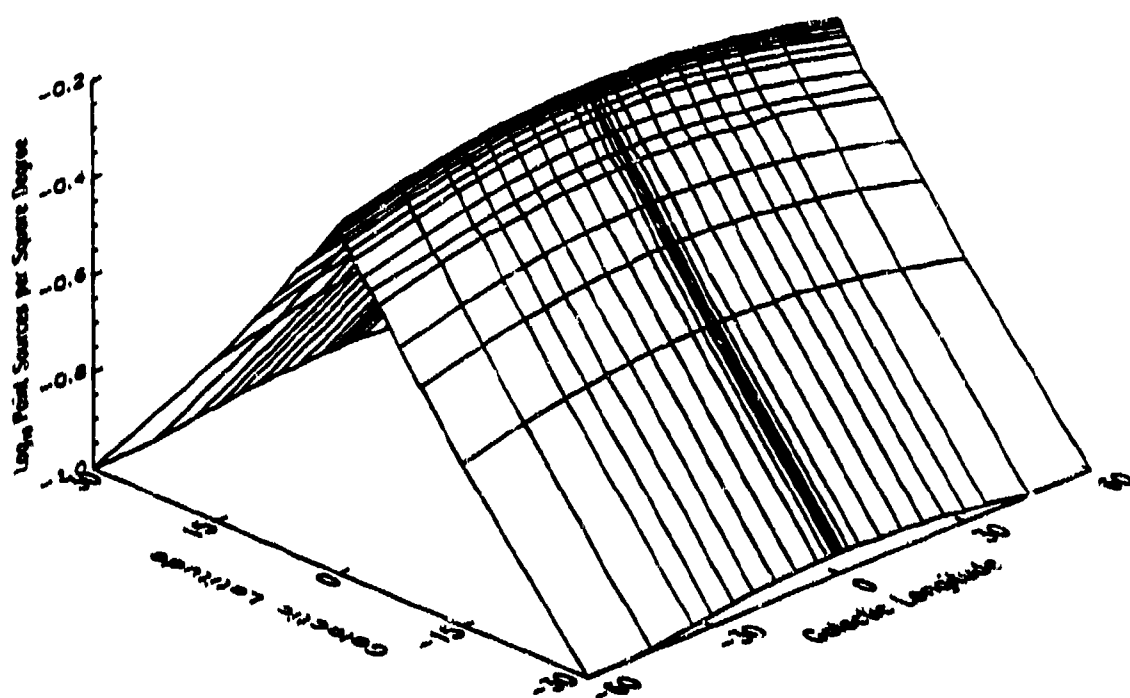
MO III 12μm Mag = 6 22
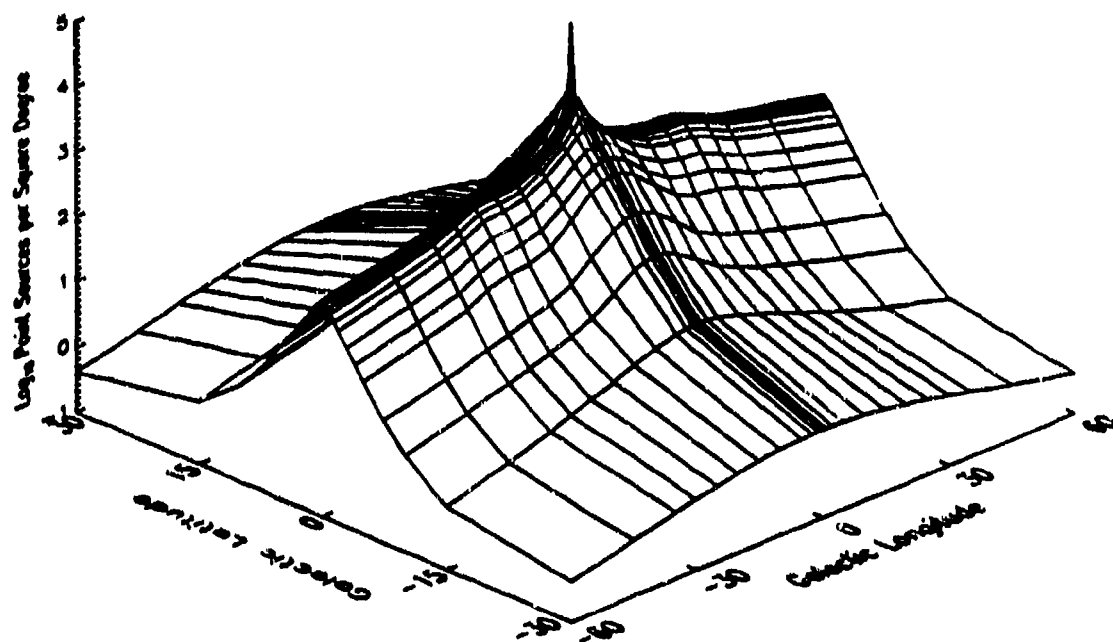
MO III 12μm Mag = 11

Figure 3-4. Two PSDM's for SKY Spectral Class 22 - Showing [12]=6 and [12]=11

67
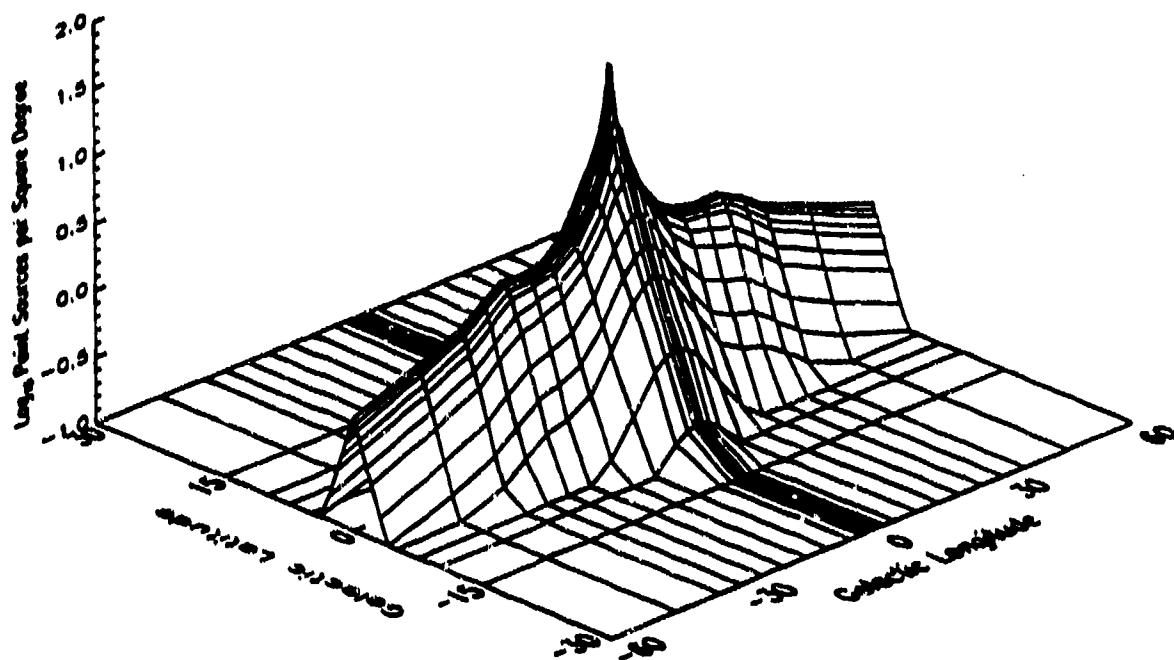
PN RED   12μm   Mag = 6   83
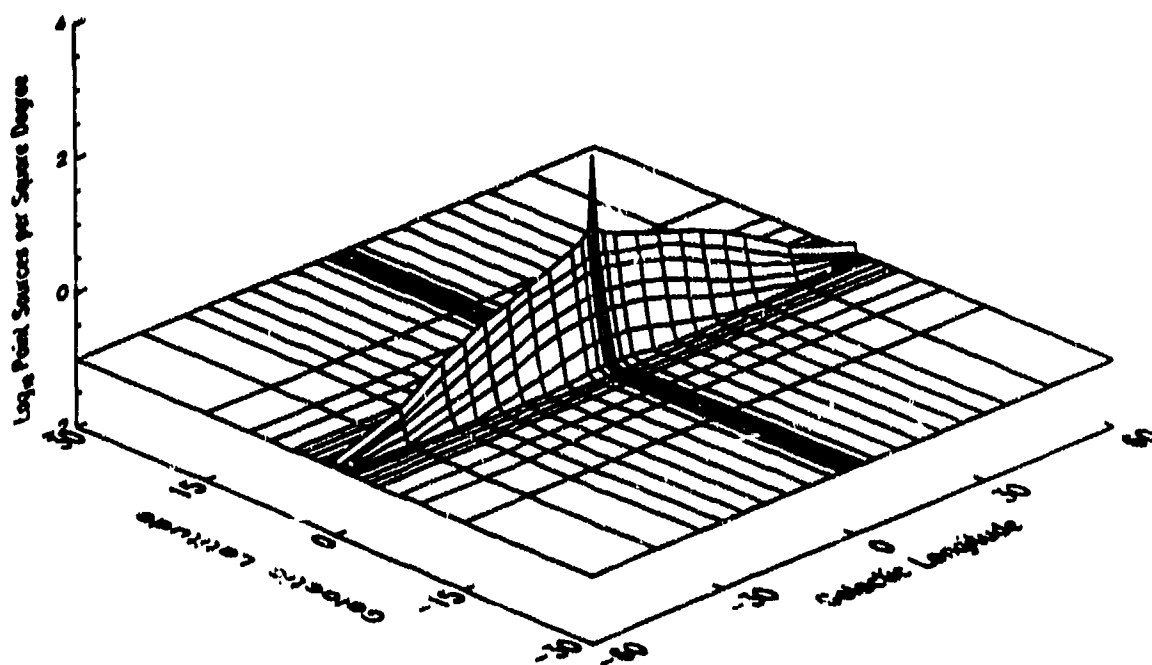
PN RED   12μm   Mag = 11

Figure 3-5.   Two PSDM's for SKY Spectral Class 83 - Showing [12]=6 and [12]=11

3.2.2 Spectral Brightness Treatment

The limited 7.7 - 22.7 μm LRS-based spectral range of the initial SKY spectral templates was inconsistent with the requirements imposed on the CBSD (particularly relative to SSGM support) for modeling and scene generation in the full 2 - 35 μm region.

> As a "stopgap" expedient measure, it was decided that the tables of absolute magnitudes for 2.4, 12, and 25 μm embedded within the SKY code would be employed as the spectral definitions for each of the 87 classes. From 2.4 to 25 μm, interpolation between the 2.4, 12, and 25 μm table values was used to assign spectral characteristics. From 2 - 2.4 μm and 25 - 35 μm, extrapolation was used.

> This approach would work satisfactorily if the spectral character of all sources was single-temperature Planckian in nature, and, in fact, was a rather reasonable approach for most of the 12 - 25 μm range.

> However, at wavelengths less than 12 μm the emission from these point sources becomes increasingly dominated by non-Planckian spectral line radiation. Consequently, the interpolation between 2.4 and 12 μm becomes increasingly less reliable below 12 μm. Above 25 μm the spectral character is frequently contaminated by the "infrared excess" associated with low-temperature thermal emission from massive circumstellar dust shells. Consequently, the reliance on extrapolation will oftern lead to an underestimate of flux above 25 μm.

> Thus, it was well understood that some errors would arise in both the interpolation between 2.4 and 12 μm and the extrapolation beyond 25 μm.

To increase the "realism" of the CBSD statistical point source scene generation module, it was decided to replace the above-described magnitude bins -1 and 0 with a list of the brightest IRAS PSC sources, so that the actual asterisms of the IR sky would be reproduced by CBSD.

> The 2,503 PSC sources with 12 μm IRAS intensities brighter than 28.3 Jy (i.e. [12] = 0), along with their IRAS 12 and 25 μm brightnesses, were made into a "mini-catalog" for CBSD scene generation. At arbitrary wavelengths in the 2-35 μm range, their intensities could be roughly estimated from the IRAS 12 and 25 μm data by a similar combination of interpolation and extrapolation as already described. Figure 3-6 illustrates the galactic distribution of those sources.

Figure 3-7 schematically illustrates all the elements of point source scene generation relied upon in the original CBSD point source modules.

CBSD Point Source Scene Descriptor

The 2503 Brightest (12μm) IRAS PSC Sources
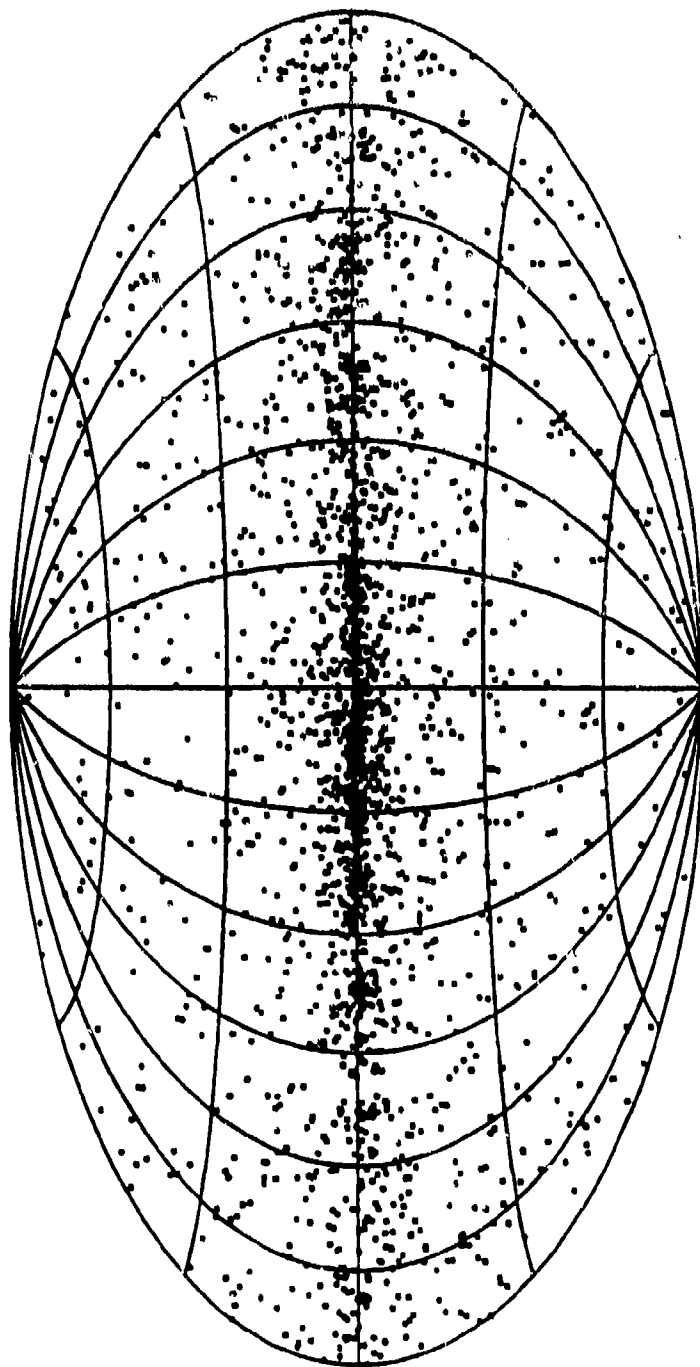
Figure 3-6.   Galactic Distribution of the Brightest IRAS 12 μm Sources

70
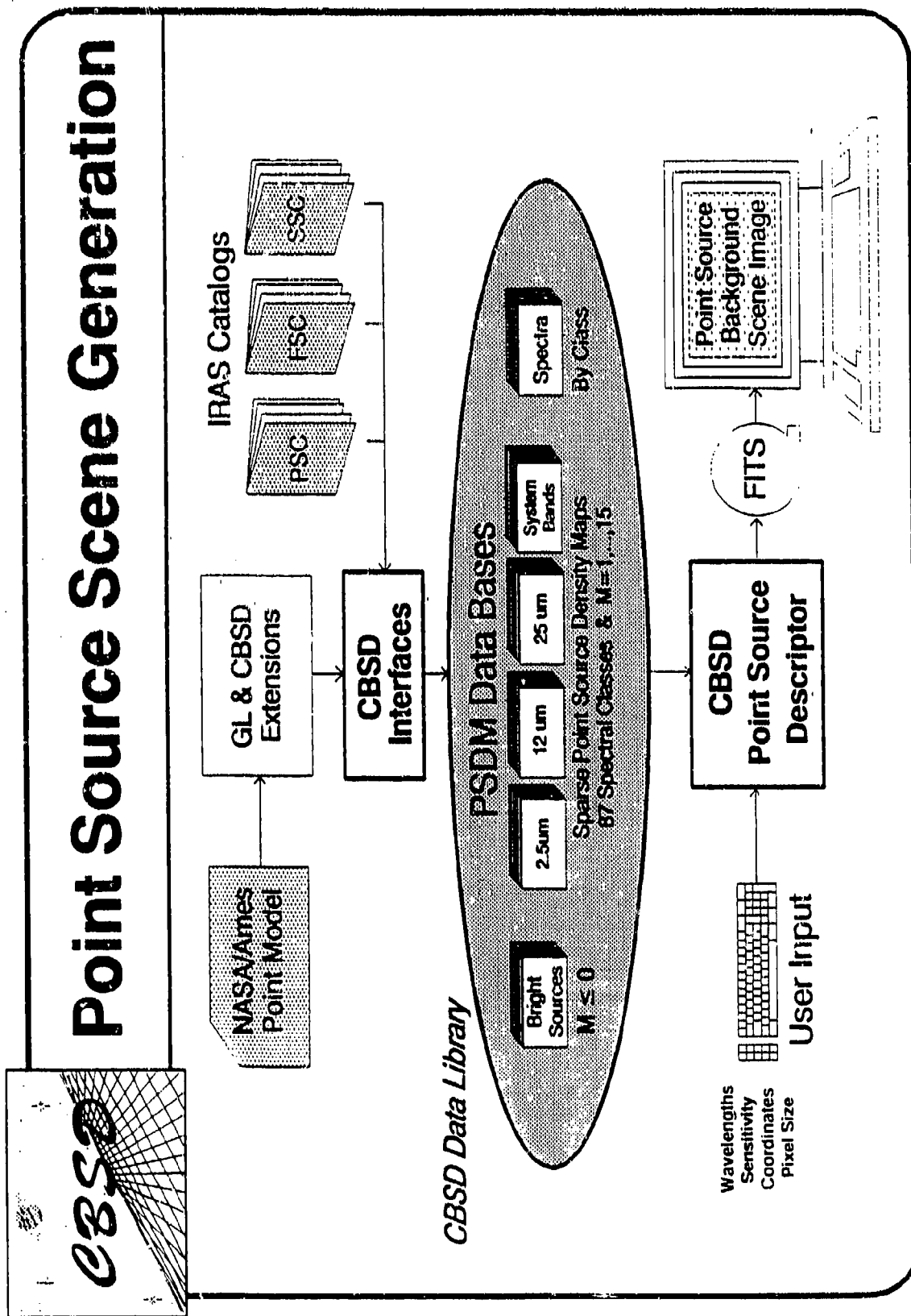
Figure 3-7. Overall Architecture of the Original CBSD Point Source Module

3.3   Current CBSD Implementation

Version 3 of *SKY* was delivered to the Air Force in 1991. It incorporated a library of spectral templates which covered the entire 2-35 μm range. Figures 3-8a and 3-8b illustrate a few of these newest templates. (A brief guide to Version 3 of the SKY model is attached as an Appendix to this report.) At the same time that the expanded spectral templates were becoming available, experience with CBSD was providing some important feedback.

1. For the dynamic tracking applications supported by SSGM, a much faster point source module was desired (e.g. a typical 512×512 point source scene required ~45 minutes on a SPARCstation).

2. An improved method for assuring multi-spectral point source scene coherence was desired; i.e. assuring that scenes generated at different wavelengths, but in the same region of the sky, were not just statistically consistent but contained *exactly* the same point sources at exactly the same locations.

3. For some sensor simulations, SSGM users wished to know details of the point source count and spatial distribution *within* scene pixels.

4. The spectral dependence of interstellar extinction was not satisfactorily accounted for in the initial CBSD IR point source modules.

3.3.1   The CBSD Galactic Point Source Catalog

The newest CBSD point source module employs a synthetic point source catalog, based on successful experience with a PSC-based point source module in the CBSD/PC, as well as the understanding that 7th magnitude modeling was adequate for the bulk of today's IR scene description requirements, . A fixed catalog of point sources based upon the *SKY* distribution functions addresses the above-listed concerns.

- *A catalog provides for extremely fast scene generation. No significant calculations are necessary to actually generate the sources once the catalog exists, and only very simple calculations are required to calculate the spectral brightnesses at user-specified wavelengths.*

- *Multi-spectral scene coherence is guaranteed, because exactly the same discrete point sources are used at all wavelengths.*

- *A user can always recover the details of point sources within a pixel, simply by referring back to the details in the catalog.*

- *Relatively straightforward MRC modifications to the SKY code enabled the generation of PSDM's which tabulated an LOS-averaged 12 μm interstellar extinction as well as a point source density. The only embedded approximation comes from the use of the simplifying assumption that all sources of a given type and a given brightness suffer the same extinction for a given line of sight.*

  This is, of course, equivalent to saying that all such sources are also at the same distance, certainly not true individually but probably statistically valid.

72
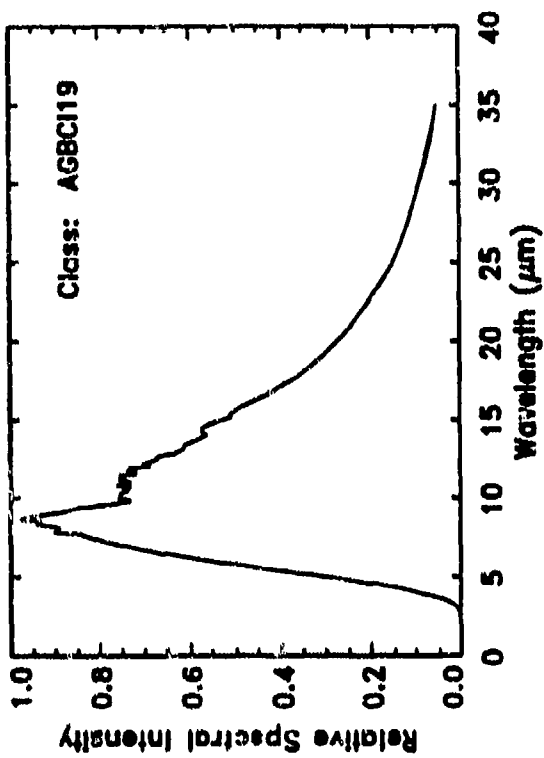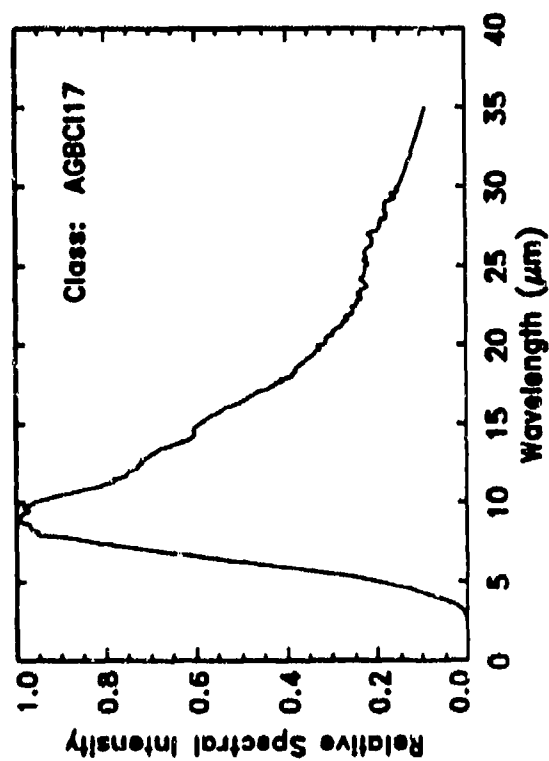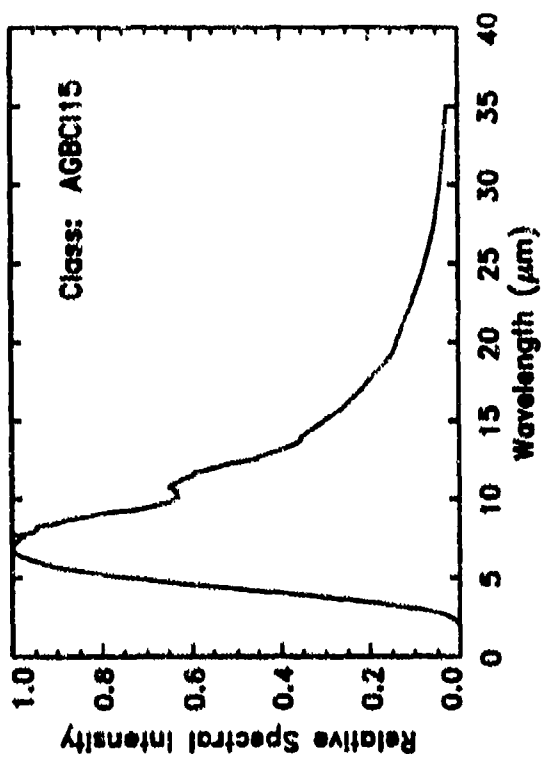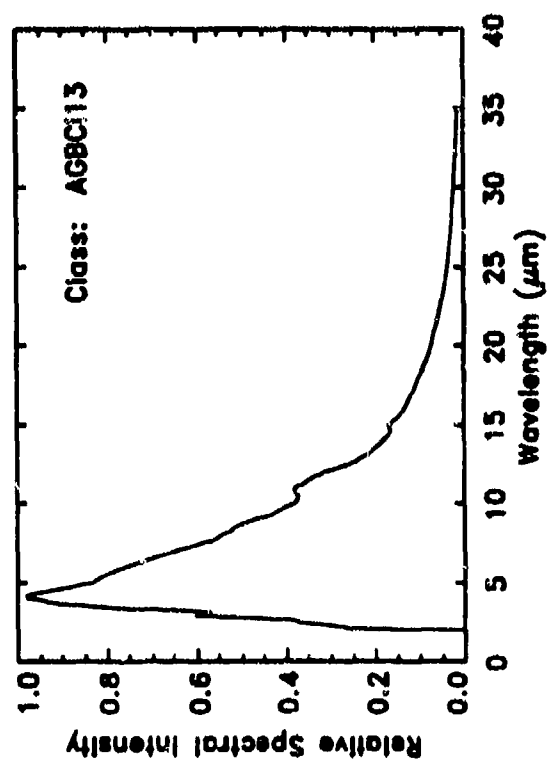
Figures 3-8a.   Sample SKY Version 3 Spectral Templates

73
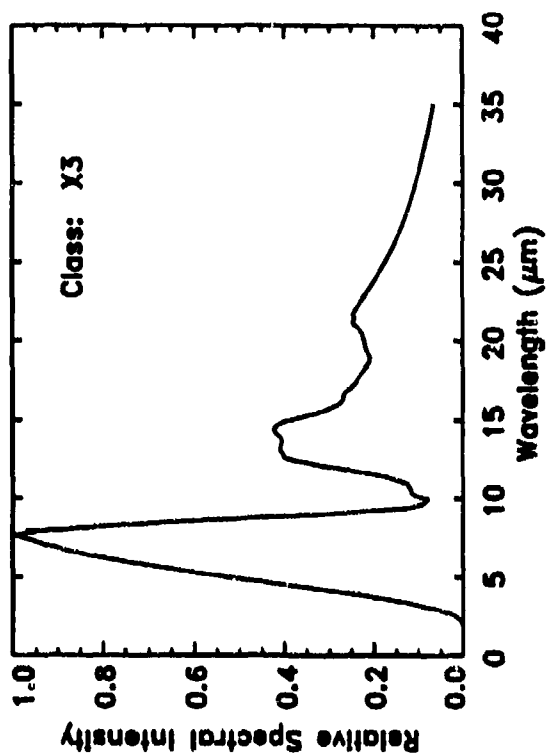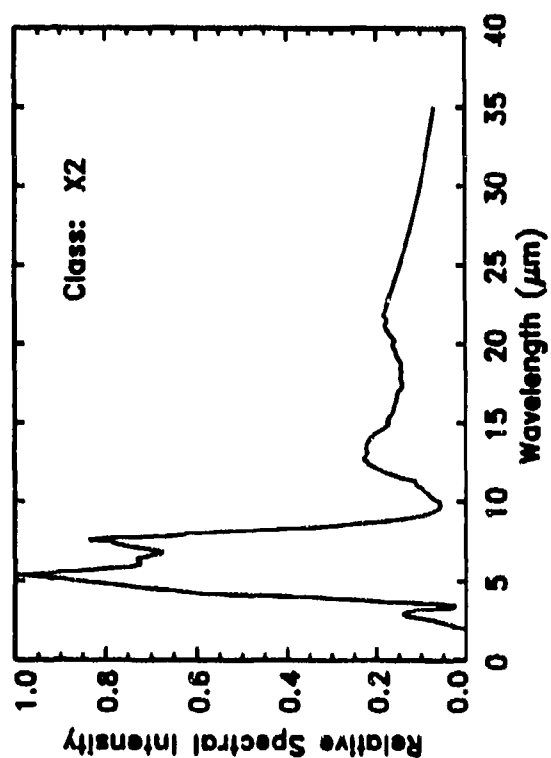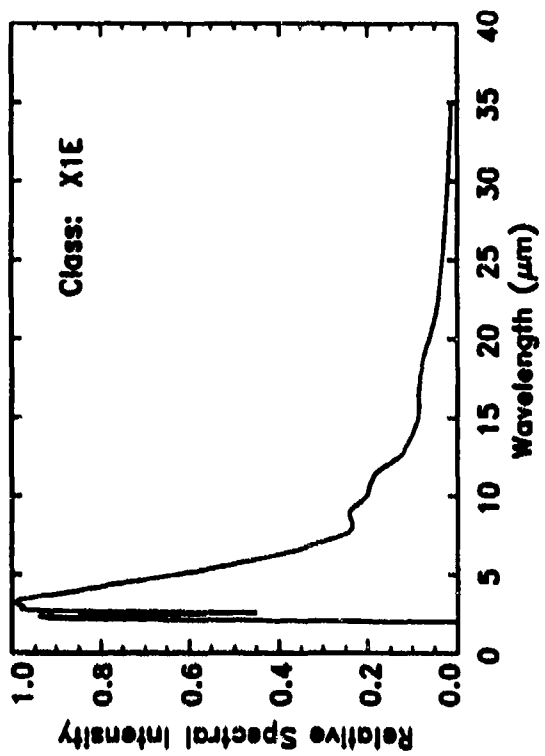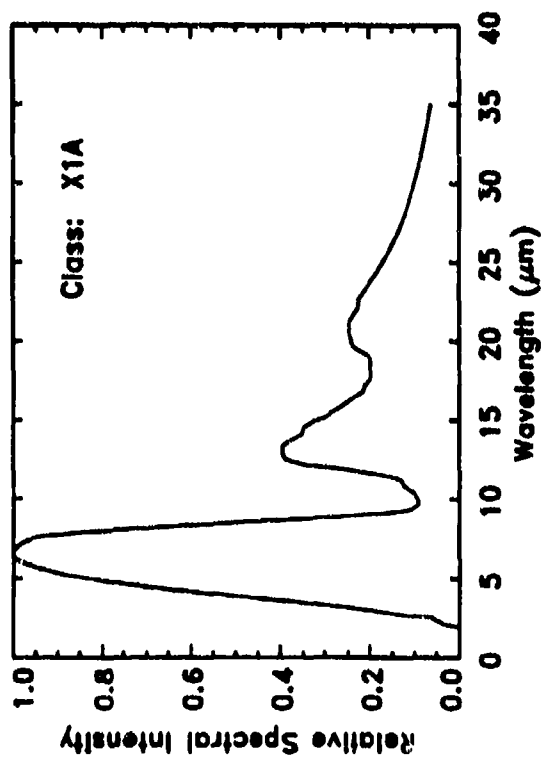
Figures 3-9b.   Sample SKY Version 3 Spectral Templates

74

This catalog was generated from a version of the previous CBSD module, which was updated to use maps generated from the newest *SKY* code and included tabulated values of LOS-averaged extinction. The SKY spectral extinction function employed for these calculations is shown below in Figure 3-9. Actual catalog generation was carried out very similarly to scene generation, except that the "scene" was galactic all-sky and non-uniform effective "pixel" sizes were used.
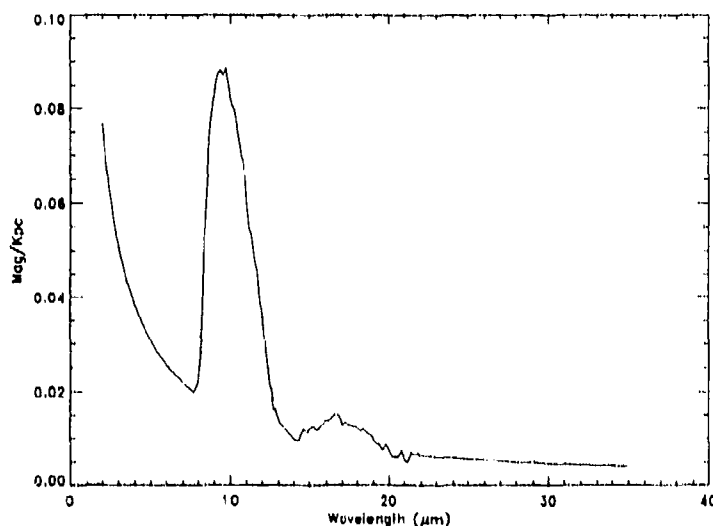
Figure 3-9. The Sky Spectral Extinction Function

3.3.2 Catalog Generation

Referring back to Figure 3-3, the "pixels" used for catalog generation were constructed by dividing each gridded zone into 100 equal size elements. The map in Figure 3-3, divided into 30 galactic latitude intervals and 28 galactic longitude intervals, encloses $30 \times 28 = 840$ zones. Each linear interval here was then sub-divided into 10 intervals. This ten-fold sub-division was done to ensure smooth transitions in source distribution between zones. Thus, the "target" scene for catalog generation had 84,000 "pixels."

Discrete sources were generated for each such "pixel," as described in 3.2.1, and then randomly "placed" within the pixel in order to produce the catalog. Of course, whereas normal scene generation sums the flux from all contributing sources into the pixel, here the "pixel" was simply a construct of convenience and the individual sources were tabulated into a list (i.e. the catalog) rather than accumulated into image elements.

In addition, because the new catalog was intended to be in celestial equatorial coordinates, while *SKY* operates in galactic coordinates, the new PSDM's were coupled to a coordinate projection correction in order to eliminate distribution artifacts when the source coordinates were converted from galactic to equatorial. The actual projection correction function is shown below in Figure 3-10. *(A preliminary version of the catalog, produced without using this projection correction, created point source clusters at the galactic poles for scenes generated*

75

in equatorial coordinates and also generally exhibited incorrect source count gradients away from the galactic plane.)
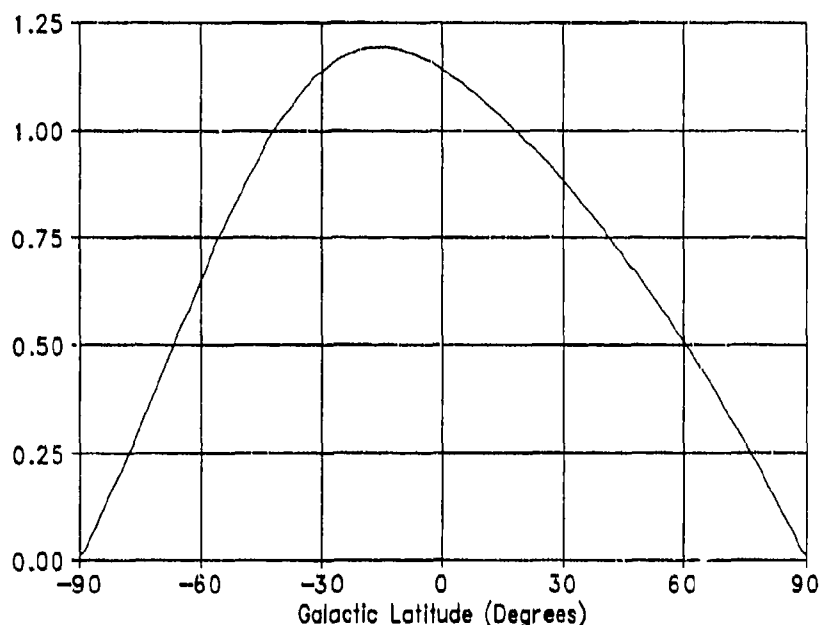
Figure 3-10.   Galactic → Equatorial Map Projection Correction

3.3.3   Catalog Characteristics

After translating the catalog coordinates from galactic to equatorial, the catalog list was sorted in Right Ascension and binned into 360 binary (unformatted) files, one file for each degree of R.A. The division into 360 files is a convenience for most anticipated applications, but some users may wish to work with fewer files. Because the entire catalog is R.A.-sorted, the 360 files may be easily catenated into however few files any particular user desires.

It was decided that the catalog would be generated for a 1 μm bandpass centered at 12 μm. There is a small but quantifiable extinction at 12 μm and all the SKY spectral templates have non-zero values at 12 μm. Therefore, by employing a 12 μm catalog, the SKY extinction function and spectral templates can be safely relied upon to achieve the desired "dial-a-wavelength" capability.

The current version of this R.A.-ordered catalog is complete down to 7th magnitude (for 12 μm) and contains ~1.18 million sources. For the ith source, the catalog entry is:

R.A.$_i$	Decl$_i$	M$_i$	X$_i$	K$_i$

where M_i contains the 12 μm brightness, X_i contains the 12 μm extinction, and K_i is the SKY spectral class of the ith source.

76

Note that the amount of extinction tabulated for a given source is also already accounted for in the tabulated 12 μm brightness. Extinction is tabulated solely as an aid in calculating the brightness of the source at wavelengths other than 12 μm.

Within the catalog, the Right Ascension and Declination coordinates are coded as IEEE 4-byte "reals" and have a precision of ~0.2 arc-seconds. The other entries are coded as 2-byte integers, where $M_i = 1000 \times [12]_i$ and $X_i = 1000 \times$ the 12μm extinction (in magnitudes). *(The resultant quantization error in brightness and extinction is only 0.0005 magnitude.)* Each point source entry, therefore, requires 14 bytes, and the complete catalog is about 16.5 MBytes in size.

This catalog, combined with the *SKY* 2-35 μm spectral templates and extinction function, makes it a simple matter to quickly generate a point source scene, for any part of the sky and for any spectral bandpass in the 2-35 μm range. Once a scene geometry is specified, the appropriate sources are extracted from the catalog, and their brightnesses over a user-specified spectral bandpass wavelength are computed via transformation from their tabulated 12 μm brightnesses. Point sources of a given *SKY* spectral class are wavelength-converted based upon bandpass integral ratios computed from the appropriate *SKY* spectral template and the *SKY* extinction function.

Figure 3-11, on the following page, illustrates the architectural approach employed for both the development and usage of the latest CBSD point source background modeling techniques.
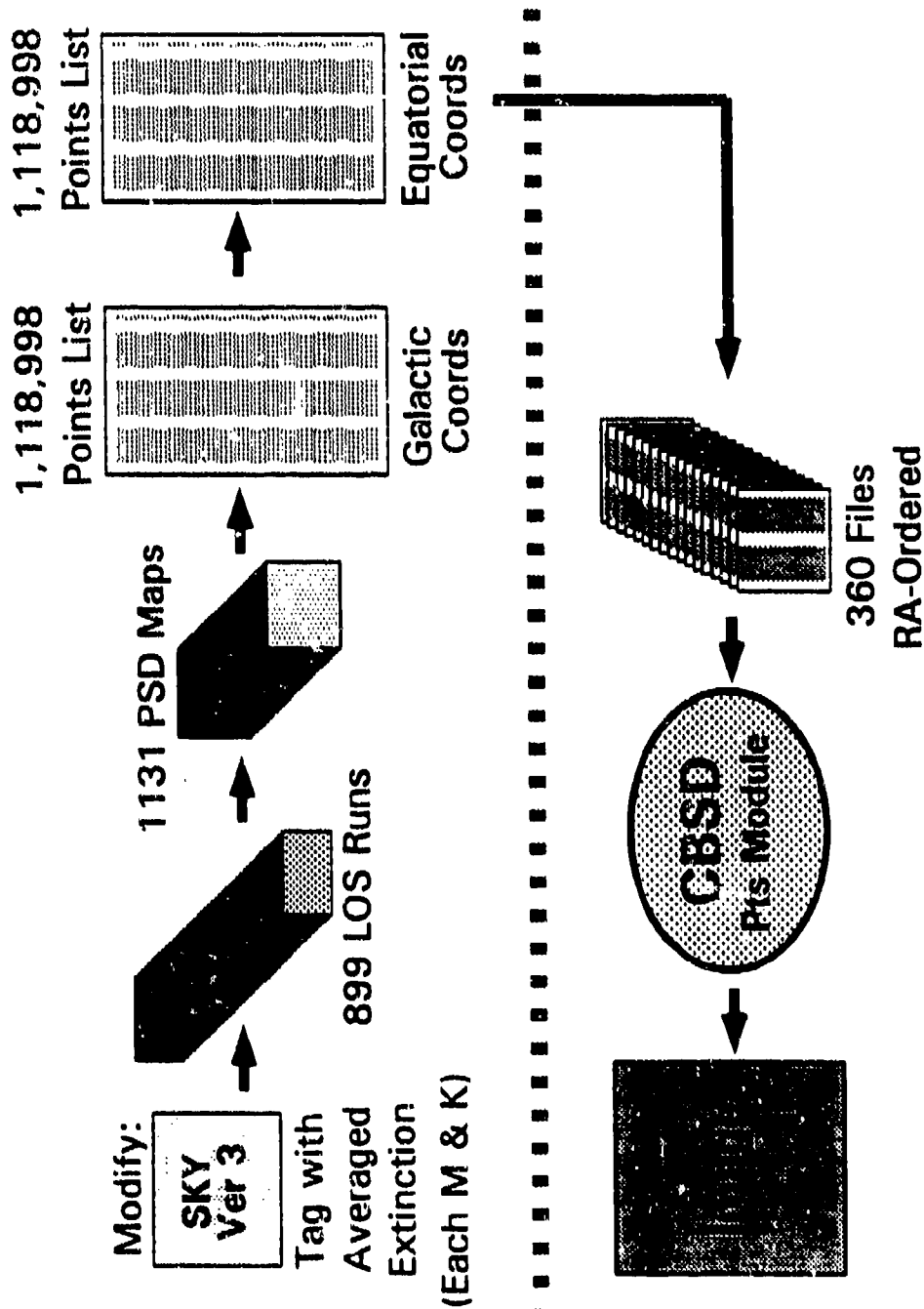
Figure 3-11.   Overall Architecture of the Newest CBSD Point Source Modeling Method

3.4　Use & Validation of the New Point Source Module

The newest catalog-based CBSD point source scene descriptor module has now been in use since July 1992, i.e. for approximately six months. Operational FORTRAN code, accessing the catalog and *SKY* spectral functions, has been developed for the CBSD/PC, PLEXUS, and the SSGM RAD-S programs. In addition to serving the normal requirements of these programs, the new point source module has been used to create simulations for the MSX satellite mission.

Although, for simplicity's sake, the initial CBSD/PC and PLEXUS modules currently generate a scene for only a 1 μm bandpass centered at the user-specified wavelength, the SSGM RAD-S module now generates scenes for arbitrarily-sized spectral bandpasses. User input to the CBSD and PLEXUS modules is extremely simple, being a file of only four parameters:

> Wavelength
> Right Ascension
> Declination
> Pixel Size (IFOV).

The module currently generates scenes of only one size: 256×256 pixels. (RAD-S, however, has been employed to generate scenes as large as several thousand pixels square.) The default projection for scene generation is gnomonic, although the user may select a rectangular projection via appending the single parameter "2" to the command line.

It is a simple matter to upgrade the CBSD module to generate any size scene over any spectral bandpass. Although the general introduction of these changes has purposely been delayed in order to establish a base of experience with a single piece of software, the upgrade prototype has been designed. For this more versatile module, the user inputs are comparably simple:

> Wavelength$_1$　　Wavelength$_2$　　Sp_File_Name
> Right Ascension
> Declination
> Pixel Size
> Image_Columns　　Image_Rows.

Wavelength$_1$ and Wavelength$_2$ are the user-specified wavelength limits for a spectral band, and Sp_File_Name, an optional input, is the name of an ASCII file containing the user's tabulated description of his spectral response function. If Sp_File_Name is not present, the CBSD module will assume a rectangular spectral response.

Note that this specific input file format will permit the expanded module to be fully compatible with the simpler module. If the input parameters *Wavelength$_2$*, *Sp_File_Name*, *Image_Columns*, and *Image_Rows* are not present, their absence will be detected by the code and the module will function identically to the earlier, simpler module.

For typical scenes, this newest CBSD point source module is 20-30 times faster than its predecessor, as well as being more accurate and versatile. The experience of the past six months has already been valuable in identifying several details of the catalog data base which can and should be improved upon.

The first of these details is related to a failure of the specific Monte Carlo approach employed, but only for cases of very small point source density. The manifestation of this failure is a slight under-population of the brightest sources (i.e. brighter than ~ [12] = 2) in scenes with fairly small pixels.

The second problem is the appearance of very slight striations, aligned to the galactic plane, in the point source distribution near the galactic center.

The causes of these problems, arising in both cases during actual generation of the catalog, are now well understood and will be addressed in the next catalog generation.

3.4.1 Validation Results

In addition, the CBSD point source model has now been validated via extensive comparison with the IRAS Point Source Catalog (PSC).

The first step in this phase of the validation was to generate all-sky 12 μm images in galactic coordinates, from both the IRAS Point Source Catalog (PSC) and the new CBSD statistical point source data base.

Both of these images were generated with pixels of 1 square degree. The images were generated in "real" numbers to maintain the large dynamic range present in the data. The images (and plots) are in normalized units of F_0 / deg^2, where F_0 is the flux from a 12 μm point source whose brightness is exactly zero magnitude (i.e. 28.3 Jy).

The integrated brightness plots in Figures 3-12, 3-13, and 3-14 compare averaged and smoothed "columns" of these images, for a full range of galactic longitudes. For a given galactic longitude, an average is made up from the column at that longitude and the 2 adjacent columns on either side (e.g. for a longitude of 45 degrees, the data at 43, 44, 45, 46, and 47 degrees is averaged). This averaged column is then convolved, in galactic latitude, with a triangle (FWHM = 3 degrees).

The reason for this type of data averaging and smoothing is to reduce the significance of the "spikiness" associated with very bright discrete sources.

As is evident in the Figures, the CBSD point source background model (and, implicitly, the NASA/Ames SKY model on which it is based), is statistically consistent with the IRAS PSC. The most noticeable and consistent difference in these comparisons shows up near GLat=0 in the GLon=0 plot, and is believed to be due to PSC deficiencies originating with "point source confusion" in the IRAS measurements.

Some comparisons have also been made, by MRC/Nashua and JSE scientists, between SSGM/CBSD results generated at MRC/Nashua and JSE-generated SKY results. The focus of this comparison is an IFOV=40 μrad (~8 arc-sec) scene ~2.5° square, located very close to the galactic center (actual coordinates: R.A. = 265.5°, Decl = -28.9°), generated for bands centered roughly at 12 and 25 μm.

Although SKY can not generate a scene *per se*, the JSE scientists modified SKY to generate log(N)-log(S) results for the specified region, and a log(N)-log(S) analysis was also done on the SSGM/CBSD scenes. The log(N)-log(S) results are shown in Figures 3-15 and 3-16.
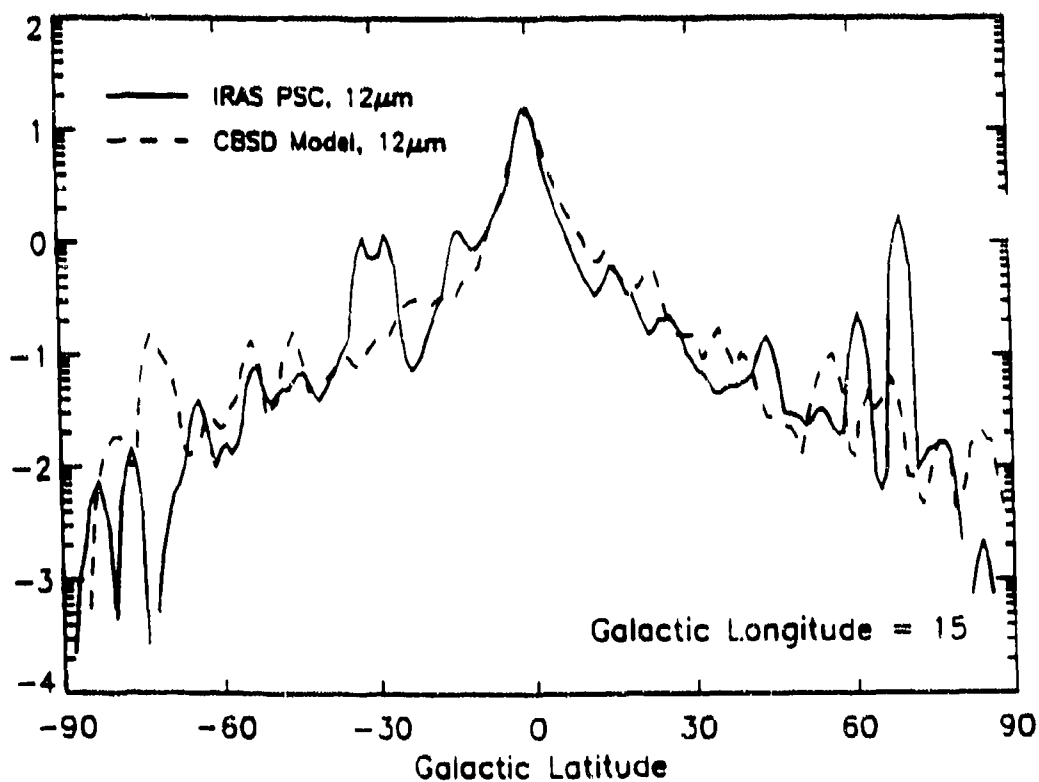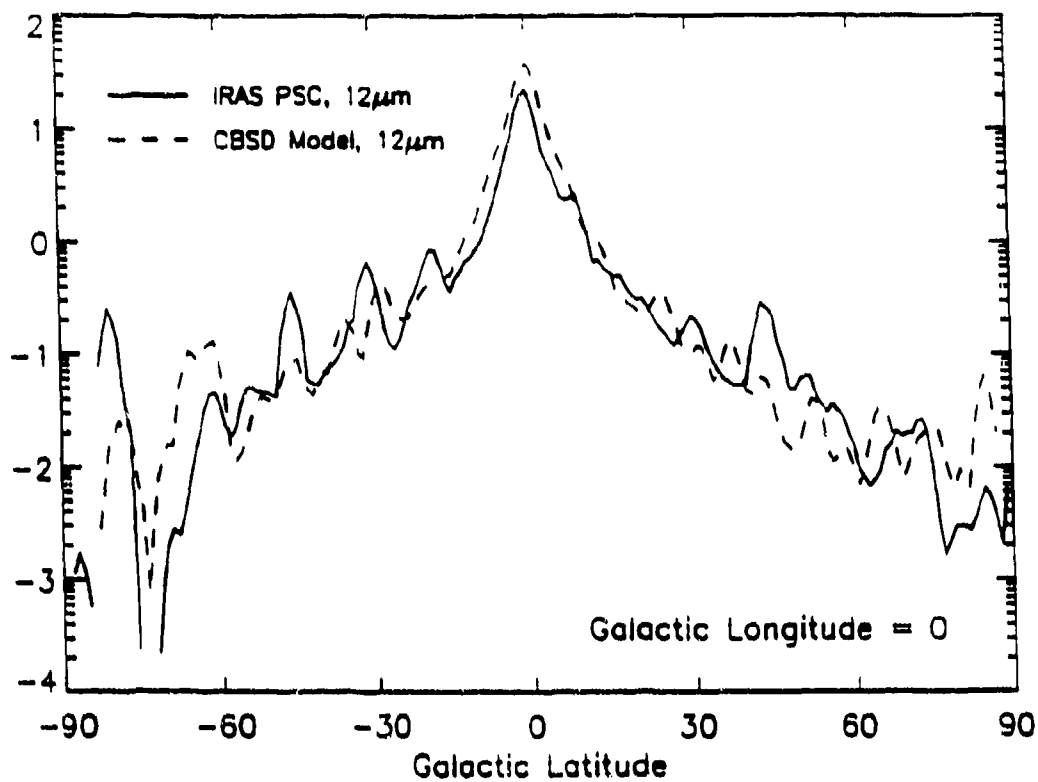
Figure 3-12. CBSD Compared to the 12 μm IRAS PSC at GLon=0 and GLon=15
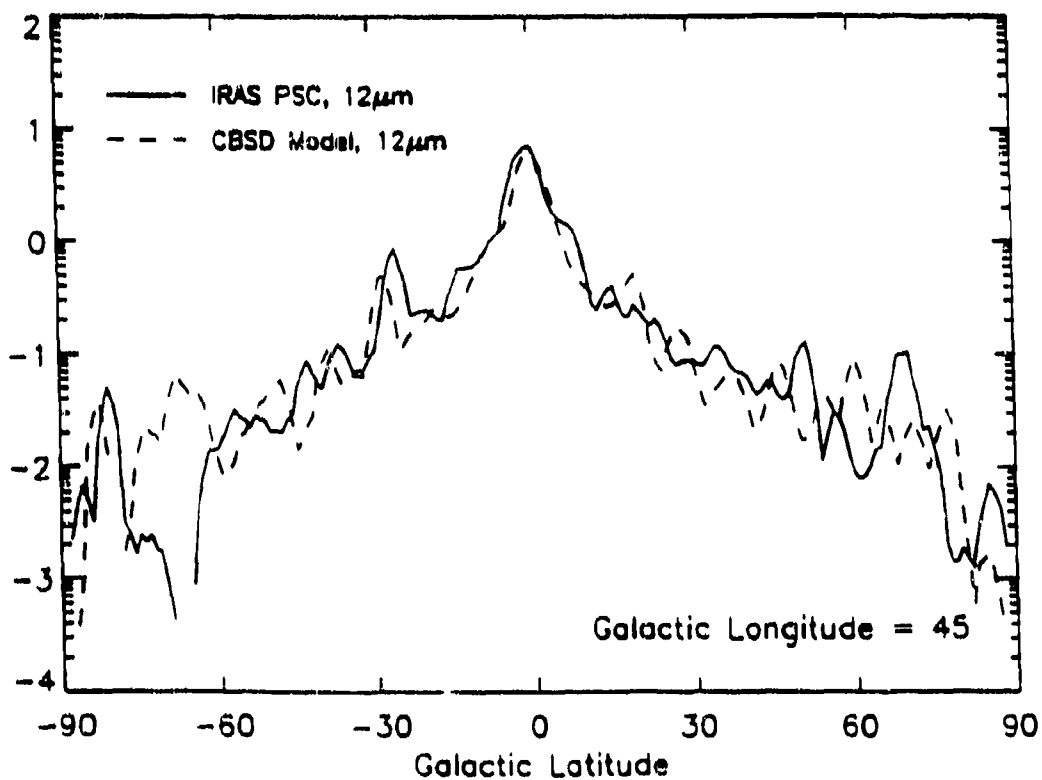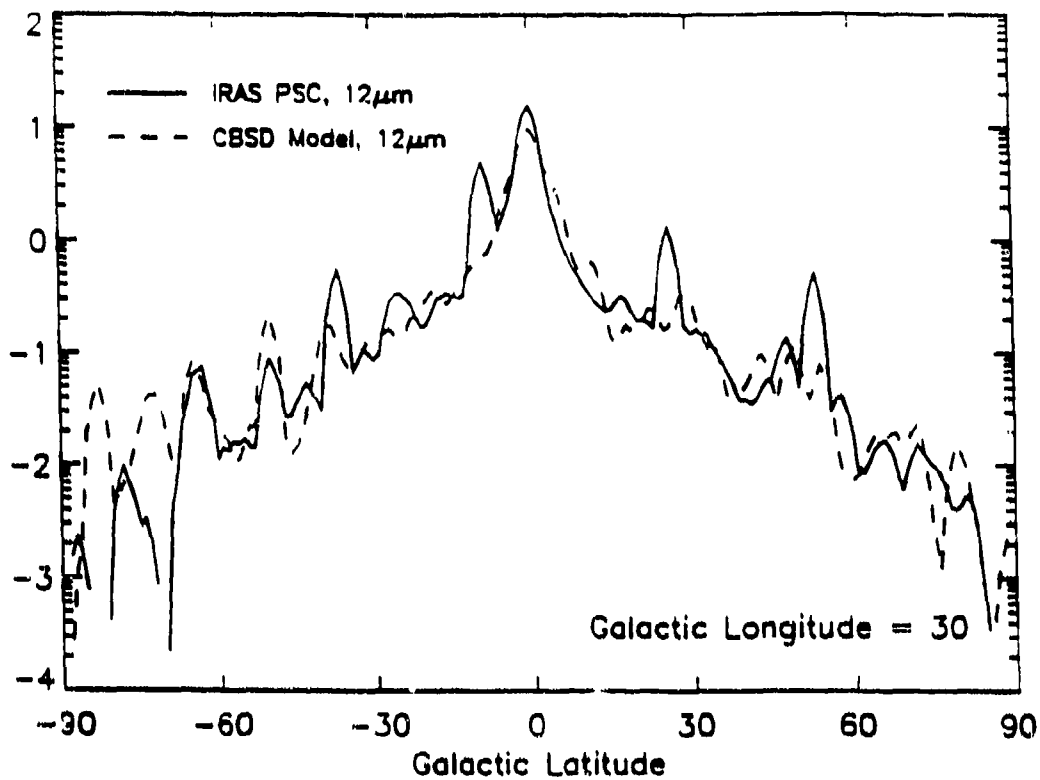
Figure 3-13. CBSD Compared to the 12 μm IRAS PSC at GLon = 30 and GLon = 45
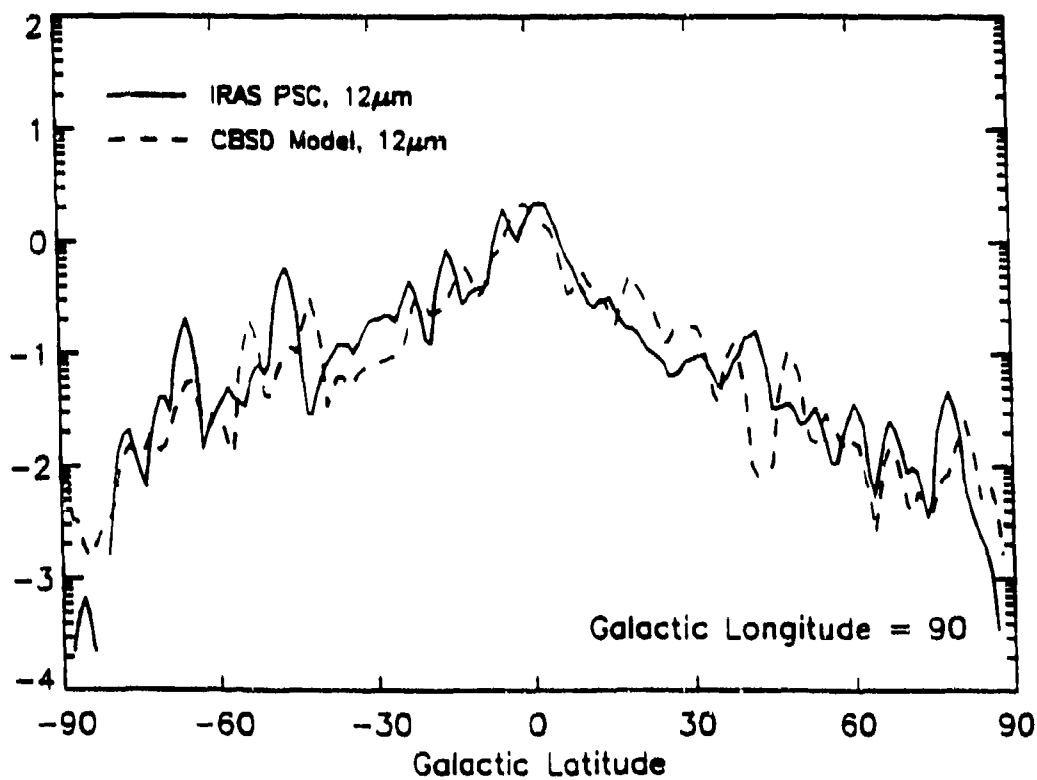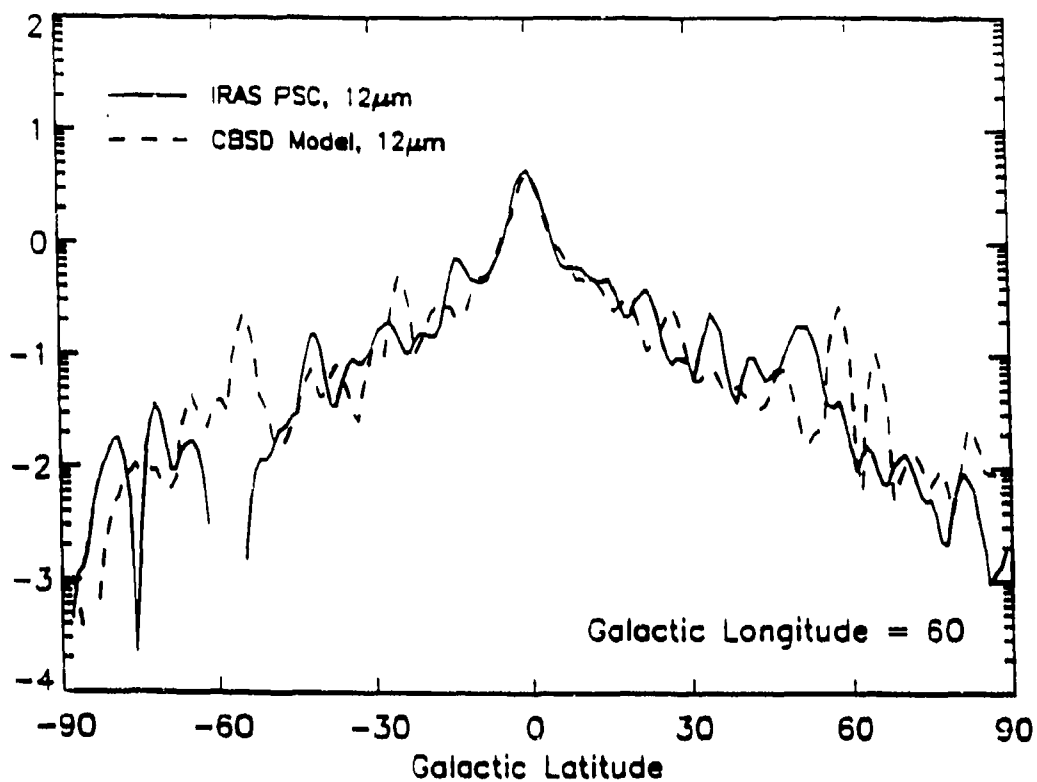
Figure 3-14. CBSD Compared to the 12 μm IRAS PSC at GLon=60 and GLon=90

BAND A
(8-15um Square, 1024x1024 Rotated)
JSE vs. MRC SkyModel Comparison
December 31, 1992

MRC

JSE

Number of Point Sources

Irradiance (w/cm²)
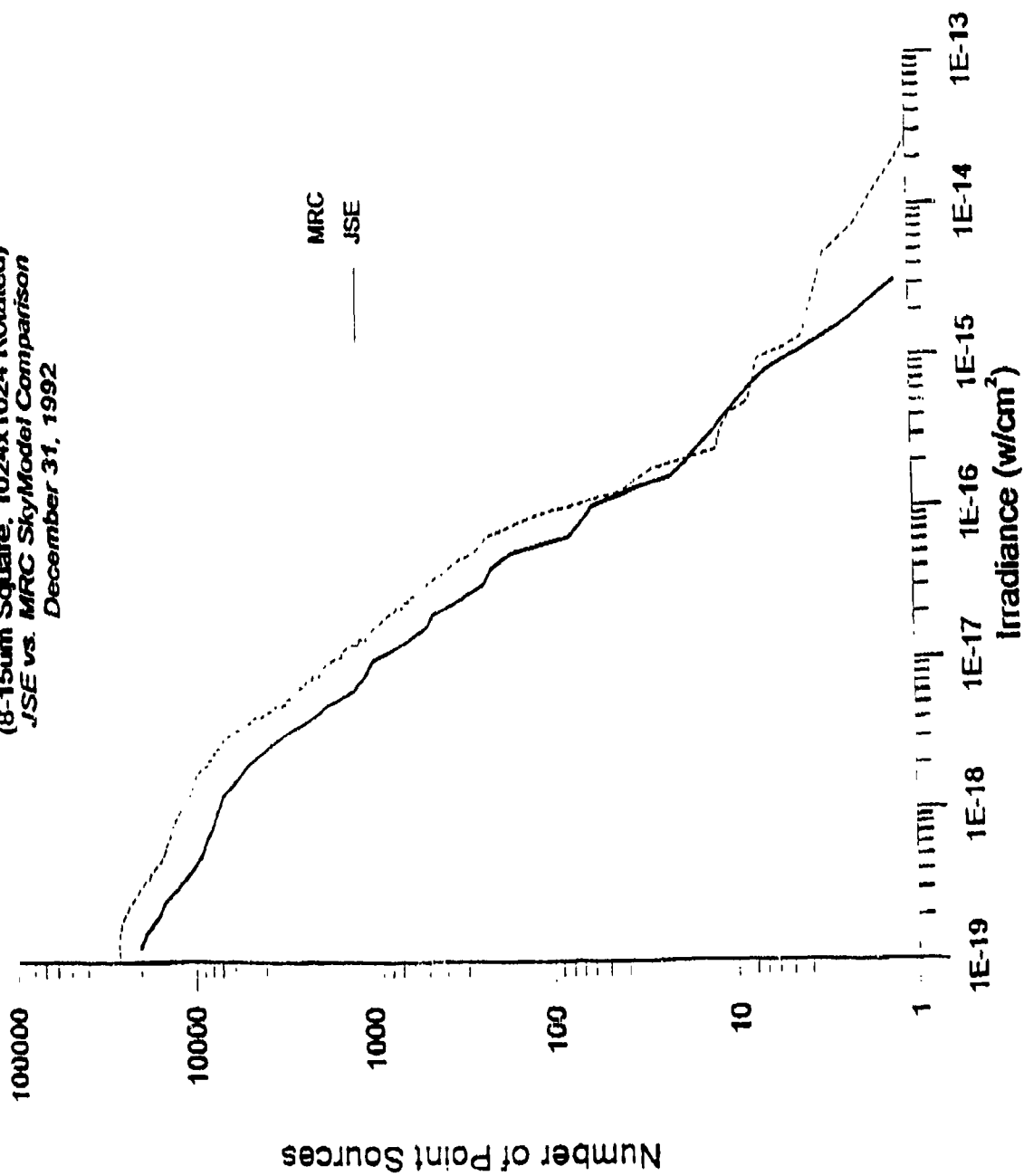
Figure 3-15. SKY vs CBSD *log(N) - log(S)* Comparison at 12 µm

BAND B
(18-29.5um Square, 1024x1024 Rotated)
JSE vs. MRC SkyModel Comparison
December 31, 1992
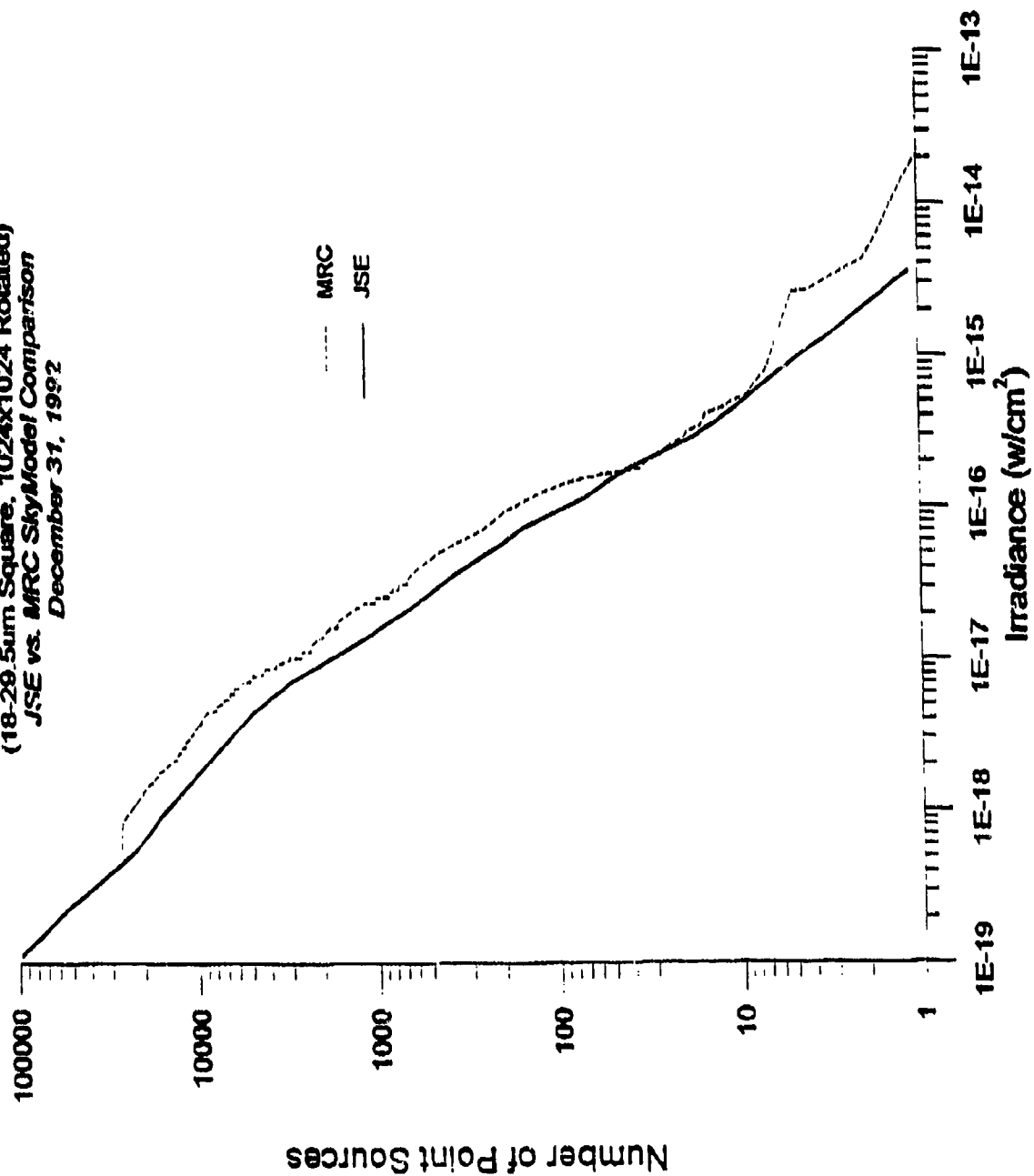
Figure 3-16. SKY vs CBSD $log(N)$-$log(S)$ Comparison at 25 µm

85

There are several obviously interesting characteristics of the comparison results:

First, and not so obvious on these plots, the total number of sources brighter than [12]=7 was very close to ~30,000 in both cases.

Second, the difference at the highest brightness levels is due to the fact that the SSGM scene employs the older CBSD PSC-based "bright star" mini-catalog for sources brighter than magnitude zero. Whereas the highest SKY brightness bin is at [12]=-1, the IRAS sources are distributed out to approximately [12]=-8.

Third, the CBSD under-population of bright stars shows up clearly here around the cumulative source count equals 10 level.

Fourth, there is a general displacement, by approximately a factor of ~1.7, of the SSGM/CBSD curves away from the JSE SKY curves in both spectral bands.

The only aspect of this which has not already been discussed, and, therefore, which is cause for some concern, is the factor of ~1.7 displacement between these results. At the present time, we have no explanation for this difference.

Looking back at the comparisons between CBSD and the IRAS PSC, it was apparent that the agreement was *excellent* at all locations along the galactic plane except right at the galactic center, where there was a factor of ~2× difference in integrated brightness. We believe that most (all ?) of that difference is due to the confusion limitation of the IRAS PSC near the galactic center. The excellent quality of the PSC comparison results makes the SKY - CBSD *log(N)-log(S)* differences even harder to understand.

The factor of ~1.7 is about half of a magnitude (i.e., ~1.58), possibly suggesting an ambiguity in the SKY - CBSD comparison based upon differences between JSE and MRC in how the SKY magnitude bins were assigned flux brightnesses. CBSD distributes sources uniformly within a magnitude bin, so the average brightness is about half a magnitude above the integer magnitude definition of the bin. We do not yet know anything about how the entirely new SKY *log(N)-log(S)* feature operates. An improved understanding of this apparent difference between SKY and CBSD in the region of the galactic center is still being pursued.

3.5   Recommended Extensions of Capability

Jamieson Science & Engineering is being contracted by the Air Force to extend the domain of SKY down to the near-UV and also to incorporate "patchiness" in the description of extinction within the galactic plane region. The CBSD point source module should be extended to fully incorporate the newest extensions to SKY as soon as they are considered by JS&E and the Air Force to be in stable, usable form.

We also believe it will be useful for the new synthetic catalog approach to preserve the major asterisms of the real sky. However, to use the brightest 2,503 IRAS sources (for example) in a manner consistent with the rest of the model necessitates a spectral classification of each of these sources. We recommend use of the full IRAS PSC description of these sources in conjunction with the spectral classification criteria originally used in SKY development to achieve this end. This same approach can be followed to incorporate the brightest mid-IR,

near-IR (e.g., from 2MASS), visible, and UV stars in a spectrally extended CBSD point source module.

4   CBSD COMPONENT MODULE CBAMP.

4.0   INTRODUCTION.

The CBSD Asteroid, Moon, and Planets code (CBAMP) generates images containing the asteroids, Moon, Sun, planets, and satellites of the planets. The images generated by the program CBAMP project the proper positions of these objects as well as their fluxes in the 2μm to 30μm wavelength region. The user specifies the field of view (Right Ascension and Declination), the IFOV (degrees per pixel), the central wavelength, bandwidth, the date and time of the observation, the observer's latitude, longitude, and altitude, and the time scale used. The remaining parts of this section introduce the concepts of Time Scales (Section 4.0.1) Coordinate Systems and Transformations (Section 4.0.2), the Theory of Orbits (4.0.3), the Reference Equinox and Precession (Section 4.0.4), and the Precession and Nutation Matrices (4.0.5). Section 4.1 discusses the methods used to obtain planetary positions and the reduction of these positions into apparent Right Ascension and Declination. Section 4.1.1 describes the planetary theory DE/LE-200 used for positions of all objects in the period 1959 to 2025. Section 4.1.2 presents the analytical theory VSOP87D that is used outside the DE/LE-200 range and Section 4.1.3 gives the lunar position theory ELP-2000/82 that is used outside the DE/LE-200 range for the Moon. Section 4.1.4 discusses the fit to the orbit of Pluto. Section 4.1.5 presents the conversion from heliocentric longitude, latitude and radius to apparent position as seen from Earth, and Section 4.1.6 gives the formalism for parallax. Section 4.2 discusses the planetary satellites. The asteroids are discussed in Section 4.3. Section 4.4 gives a detailed view of the methods used to calculate flux for the various objects. Section 4.5 is the CBAMP User Manual. Finally, Section 4.6 describes additional validation efforts for CBAMP giving sample inputs and comparing outputs to published data.

4.0.1   TIME SCALES.

CBAMP has been designed to give 2 arc-second position accuracy for solar system objects. To maintain such accuracy and to compare model predictions with observations, it is necessary to define the time scale used while recording the observations. In the astronomical community several time scales, which are based on different clock rates, are used to describe different events. Currently three different time scales can be specified in CBAMP: Terrestrial Dynamical Time (TDT), Universal Time (UT1), and Coordinated Universal Time (UTC).

Terrestrial Dynamical Time (TDT) is the common time scale used for calculating geocentric ephemerides, such as *The Astronomical Almanac*. TDT is independent of the Earth's rotation and is derived from Barycentric Dynamical Time (TDB), which is the time scale defined at the center of mass of the solar system. Differences between TDT and TDB arise from purely general relativistic effects and have an amplitude of less that 0.002 seconds of time. CBAMP reports both TDT and TDB but internally treats these times as the same with no loss in accuracy. In terms of astronomical systems a day is 86400 TDB seconds and a Julian century is 3υ525 days. The terms tropical year and Besselian epoch are no longer used in the general astronomical literature and are not supported by CBAMP.

The second time scale is Coordinated Universal Time (UTC). UTC is derived from atomic time signals given as International Atomic Time (TAI). The fundamental unit of time of TAI is the SI second, which is defined as the duration of 9192631770 periods of the radiation

corresponding to the transition between two hyperfine levels of the ground state of the Cesium 133 atom. UTC and TAI differ by an integral number of seconds, for example during all of 1988 and 1989 the difference was 24 seconds. UTC is also commonly referred to as clock time since it is the basis of the broadcast time standards and also forms the legal time system in most countries. The need for the difference between UTC and TAI arises in the definition in the last time scale used in CBAMP, UT1. A data file named DELTAAT.DAT is included with the CBAMP distribution. This ASCII text file can be updated to add the latest leap second information.

The Universal Time (UT) time scales are all based on the sidereal rate, the diurnal motion of stars, as observed at Greenwich, England; this is Greenwich Mean Sidereal Time (GMST). Universal Time refers to several different systems; a Universal Time scale directly determined from stellar observations is dependent on the observers geographic location; this is the UT0 system. UT1 is the time scale that is independent of the observers position and is obtained by removing the observed motion of the geographic pole. Finally, UT1 and UTC have been defined to be less than 1 second of time apart at any time. This definition causes certain astronomical events to have a fixed time. The Sun will always appear on the meridian at local noon, for example. This then is the requirement for the integral number of seconds difference between TAI and UTC. UTC must be maintained to within a second of sidereal time (UT1) by introducing *leap seconds*. The Earth's rotational rate is slowing due to tidal interaction between the Earth and Moon, which means that the sidereal rate is changing relative to TAI. Since the rate that the Earth is slowing down is not constant, the difference can only be obtained from observations. Hence, it is not possible to predict when a leap second has to be added, however, by convention they only occur on January 1 or June 1.

The need for these different time scales arises from the type of observation to be obtained and how the observations will be compared. If the observations are to be compared with ephemerides then TDT should be used. If the observations are obtained from a spacecraft linked to a standard time reference, then the time of observations are most likely given by UTC. CBAMP keeps track of the different time scales and automatically converts between the different systems. Internally, all times are converted into TDT and this forms the basis for all calculations.

4.0.2 COORDINATE SYSTEMS AND COORDINATE TRANSFORMATION.

When dealing with astronomical objects one is faced with several different coordinate systems and several seemingly discrepant methods of specifying the positions of objects in the solar system. In fact, these different systems have different physical meanings and, depending on the type of problem being solved, one will provide the numerically simplest method of solution. There are three possible frames of reference when solving for planetary (or any solar system objects') orbits. These are, heliocentric (Sun centered), geocentric (Earth centered), or planetocentric (planet centered). In each of the frames, the specified object is considered to be at the center of the coordinate system.

The second concern for the coordinate frames is the orientation of the coordinate system, which means the direction in which the primary axis points. Here, a simple convention is used; the positive *x* direction is taken to be the direction to the vernal equinox. The Earth's orbit about the Sun defines the plane of the ecliptic. The Earth's rotation axis is tilted at a roughly 23° angle to this plane. This tilt angle defines the Earth's obliquity and the Earth's

89

equator defines the equatorial plane. Viewed from the Earth, the Sun follows a path in the sky which crosses the Earth's equator twice each year; first from the southern hemisphere to the northern hemisphere in March of each year and then from the northern to southern hemisphere every September. The two crossings are termed the equinoxes, when the Sun is directly above the Earth's equator. The north-to-south crossing is the autumnal equinox and the south-to-north crossing is the vernal equinox.

The Earth's equator forms a second plane in the solar system, the equatorial plane. These two planes, ecliptic and equatorial, define the two principal coordinate systems of the solar system, both with principal axes tied to the vernal equinox. However, there is still a question of the center of the coordinate system. In astronomical literature it is common to measure solar system positions in one of the four coordinate systems:

1. geocentric ecliptic,
2. heliocentric ecliptic,
3. geocentric equatorial, or
4. heliocentric equatorial.

As an example of each we present in Table 4-1 the coordinates of the Sun and the Earth in the four frames for the date 29 October 1992 at 0h UT. There are slight differences in positions because the Earth-Moon barycenter (center of mass) is used instead of the physical center. However, you can see that the ecliptic frames are one in the same with only sign reversals due to the different centers. Likewise, the equatorial frames are the same except for the sign.

Table 4-1. Solar and Earth positions in each of the four reference frames.

	Sun			Earth		
	x	y	z	x	y	z
geocentric ecliptic	-0.804	-0.583	0.000	0	0	0
heliocentric ecliptic	0	0	0	0.805	0.581	0.000
geocentric equatorial	-0.804	-0.535	-0.232	0	0	0
heliocentric equatorial	0	0	0	0.807	0.538	0.233

Implicit in the positions stated above are that they are defined in a rectangular (x, y, z) coordinate system. A spherical system whose coordinates are longitude, latitude, and radius vector (distance) and whose symbols are (l, β, r) is also commonly used. The special case of geocentric equatorial spherical coordinates forms the basis for most astronomical catalogs and is known as Right Ascension, α, and Declination, δ.

The transformations among these coordinate systems may not always be obvious. Consider an object in heliocentric rectangular coordinates (x, y, z). The transformation to heliocentric spherical coordinates (l, β, r) is given by:

$$x = r \cos\beta \cos l \qquad y = r \cos\beta \sin l \qquad z = r \sin\beta \qquad (4\text{-}1)$$

To convert between heliocentric and geocentric, (X, Y, Z), systems we can use the transformation:

$$X = r\cos\beta\cos l - r_o\cos\beta_o\cos l_o$$
$$Y = r\cos\beta\sin l - r_o\cos\beta_o\sin l_o \qquad (4\text{-}2)$$
$$Z = r\sin\beta - r_o\sin\beta_o$$

or:

$$X = r\cos\beta\cos l - x_o \qquad Y = r\cos\beta\sin l - y_o \qquad Z = r\sin\beta - z_o \qquad (4\text{-}3)$$

where (x_o, y_o, z_o) and (l_o, β_o, r_o) refer to the Earth's heliocentric coordinates and (X, Y, Z) are the object's geocentric coordinates. And, to complete the set, the object's geocentric equatorial spherical coordinates (α, δ, R) or Right Ascension, α, and Declination, δ, are defined by:

$$X = R\cos\delta\cos\alpha \qquad Y = R\cos\delta\sin\alpha \qquad Z = R\sin\delta \qquad (4\text{-}4)$$

The transformation between heliocentric ecliptic spherical coordinates (l, β, r) and geocentric ecliptic spherical coordinates (L, B, R) is:

$$L = l + 180^\circ \qquad B = -\beta \qquad R = r \qquad (4\text{-}5)$$

which directly leads to the observations of Table 4-1:

$$X = -x \qquad Y = -y \qquad Z = -z \qquad (4\text{-}6)$$

The second set of transformations involves the conversion between ecliptic and equatorial systems. A required quantity is the Earth's obliquity, which changes with time. Section 4.0.4 discusses the calculation of the obliquity at any time. Once the obliquity, ε, is known the transformation between geocentric equatorial rectangular coordinates and geocentric ecliptic spherical coordinates is:

$$X = R\cos B\cos L$$
$$Y = R(\cos B\sin L\cos\varepsilon - \sin B\sin\varepsilon) \qquad (4\text{-}7)$$
$$Z = R(\cos B\sin L\sin\varepsilon + \sin B\cos\varepsilon)$$

The similar transformation for the heliocentric system is:

$$x = r\cos\beta\cos l$$
$$y = r(\cos\beta\sin l\cos\varepsilon - \sin\beta\sin\varepsilon) \qquad (4\text{-}8)$$
$$z = r(\cos\beta\sin l\sin\varepsilon + \sin\beta\cos\varepsilon)$$

These transformations are used throughout CBAMP in converting coordinate systems. Although not explicitly stated here, the inverse transforms are easily solved.

4.0.3 THEORY OF ORBITS.

Johannes Kepler was the first to demonstrate that the objects of the solar system move along elliptical orbits. Since that time it has been demonstrated that the elliptical orbits of Kepler are not appropriate in detail due to gravitational perturbations of the other objects in the solar system. The objects still roughly follow elliptical orbits, but the ellipses do not meet back on themselves and the line of apsides, and hence, the semi-major axis, seems to drift around the Sun, a process known as apsidal motion. Figure 4-1 shows a simplified orbit of an object about the Sun. At any time the orbit is defined by the inclination, i, to the plane of the ecliptic. The angle, ω, marks the argument of the perihelion (longitude of the closest approach of the object to the Sun) measured from the Vernal Equinox, in the plane of the ecliptic. The angle, Ω, is the longitude of the ascending node; that point on the orbit at which the object moves from below (south) of the ecliptic plane to north. The line of apsides is the intersection of the two planes and includes the line of the ascending node.
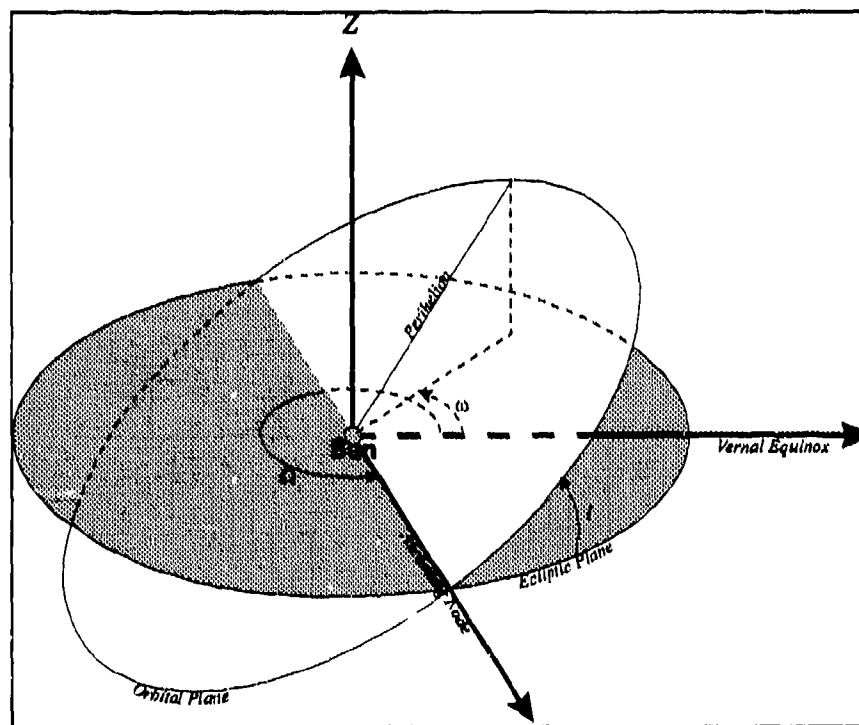
Figure 4-1. Simplified orbit showing longitude of ascending node, Ω, argument of the perihelion, ω, and orbital inclination, i, to the plane of the ecliptic.

Due to the perturbations of the other planets, the quantities i, ω, and Ω are complicated functions of time and positions of the other planets. In general there are three methods which can be used to determine an object's position. The three methods are:

1. numerical integration,
2. expansions of periodic terms, or
3. calculating the orbit from a set of orbital parameters.

CBAMP uses all three methods, or the results of the methods, in calculating planetary positions. Numerical integration has been used in the computation of the NASA JPL's DE/LE-200 ephemerides described in Section 4.1.1. CBAMP uses the results of the numerical integration in calculating the positions of the planets, the Sun, and the Moon for the years 1959 through 2025. Outside of that range CBAMP uses the analytical theory of VSOP87 which is a theory of motion generated from perturbation theory and orbital mechanics. The analytical theory generates sets of periodic terms for the planets. VSOP87 is described in Section 4.1.2. In this section, we present the calculation of an object's position using orbital parameters which gives insight into the methods used in DE/LE-200 and VSOP87. For the asteroids, the only method of calculating position is by use of orbital elements, and therefore, we will be describing the methods used in computing positions for the asteroids.

The solution for the equation of motion of an object undergoing a gravitational force can be found in any introductory text on classical mechanics (Marion 1965, Goldstein 1950, etc.). A key part of the solution is known as Kepler's equation, viz.:

$$E = M + e \sin E \qquad (4-9)$$

The definitions of the angles are best shown in Figure 4-2. In the figure, a planet, or any solar system object, is in an elliptical orbit of eccentricity, e, and semi-major axis a. A circle, whose radius is the same as that of the semi-major axis is circumscribed about the center, C, of the ellipse. The angle, v, the true anomaly, is the measure of the object's angular distance from closest approach to the Sun, the perihelion, and is defined as:

$$\tan\frac{v}{2} = \sqrt{\frac{1+e}{1-e}} \cdot \tan\frac{E}{2} \qquad (4-10)$$

The eccentric anomaly, E, is the angle from the center of the circle to the planet's position projected onto the circle, as seen in Figure 4-2 The mean anomaly, M, is the angular deviation of a fictitious object in a circular orbit (not shown) that has the same period as the object in the elliptical orbit. The mean anomaly is then the angular distance of the object in a circular orbit from the object's true perihelion. At any time, the radius vector, distance from the Sun, can be determined from:

$$r = a \cdot (1 - e \cdot \cos E) \qquad (4-11)$$

The orbital elements are provided by any number of astronomical observatories. However, since most of the solar system objects, the asteroids and comets have poorly determined orbits, the orbital elements are not sufficient to generate positions over long periods of time. In practice sets of osculating
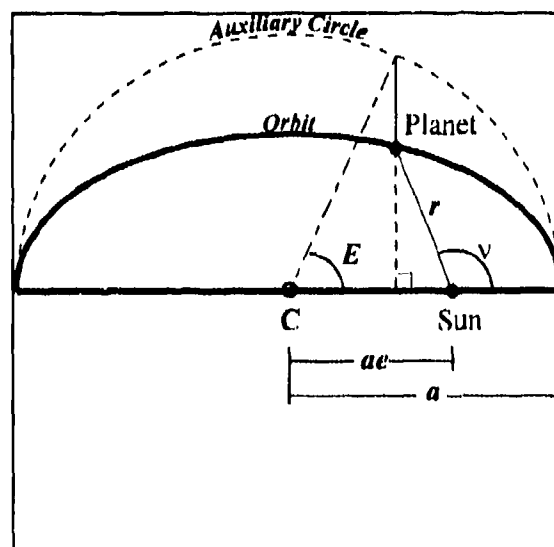
Figure 4-2. Planetary orbit showing true anomaly, v, and eccentric anomaly, E for an elliptical orbit of eccentricity e and semi-major axis a.

93

elements are distributed. The osculating elements are the elements of a body's orbit assuming an elliptical orbit at the instant the elements are defined. Therefore, a set of osculating elements has an associated epoch, and a lifetime. In general, the osculating (orbital) elements are:

a = semi-major axis, in AU
e = eccentricity,
i = inclination,
ω = argument of perihelion,
Ω = longitude of ascending node, and
M_O = mean anomaly at the Epoch of the osculating elements.

The mean motion, n, is a measure of the objects orbital velocity. If not distributed with the osculating elements it can be computed, in degrees per day (Seidelmann 1992, p.28):

$$n = \frac{0.9856076686}{a\sqrt{a}}$$

(4-12)

where the value, 0.9856076686, is the Gaussian gravitational constant in degrees. The Mean anomaly, M, can be determined from M_0 the Mean anomaly at the epoch of the osculating elements by:

$$M = (\text{TDT} - Epoch) \cdot n + M_o$$

(4-13)

The Eccentric anomaly, E, is then solved iteratively from Kepler's equation. The true anomaly, v, and the radius vector, r, are found as shown in the equations. The next step involves calculating a set of transformations which transform the position from the plane formed by the object's orbit into the heliocentric equatorial frame:

$$
\begin{aligned}
F &= \cos\Omega & P &= -\sin\Omega \cdot \cos i \\
G &= \sin\Omega \cdot \cos\varepsilon & Q &= \cos\Omega \cdot \cos i \cdot \cos\varepsilon - \sin i \cdot \sin\varepsilon \\
H &= \sin\Omega \cdot \sin\varepsilon & R &= \cos\Omega \cdot \cos i \cdot \sin\varepsilon + \sin i \cdot \cos\varepsilon
\end{aligned}
$$

(4-14)

$$
\begin{aligned}
A &= \tan^{-1}\frac{F}{P} & a' &= \sqrt{F^2 + P^2} \\
B &= \tan^{-1}\frac{G}{Q} & b' &= \sqrt{G^2 + Q^2} \\
C &= \tan^{-1}\frac{H}{R} & c' &= \sqrt{H^2 + R^2}
\end{aligned}
$$

(4-15)

From which we can now calculate the heliocentric rectangular equatorial coordinates:

$$x = r \cdot a' \cdot \sin(A + \omega + v)$$
$$y = r \cdot b' \cdot \sin(B + \omega + v) \qquad \text{(4-16)}$$
$$z = r \cdot c' \cdot \sin(C + \omega + v)$$

These definitions will be used throughout the rest of this document.

4.0.4 THE REFERENCE EQUINOX AND PRECESSION.

The Earth's obliquity changes with time which causes the vernal equinox to move with respect to the fixed stars. The motion of the vernal equinox, or equivalently the position of the north pole on the sky, is referred to as precession and must be accounted for when defining an object's position. Precession of the Earth is due to the fact that the Earth is not spherical. The flattening at the poles allows the Sun and the Moon to exert a net torque on the Earth. The torque is small and hence, the precession rate is long. The precessional period is ~26,000 years. Since the position of the vernal equinox changes on a daily basis, albeit slowly, it is customary in astronomy to define fixed times at which to measure the Earth's obliquity. By custom, these times occur every fifty years, such as 1850, 1900, 1950, 2000. Catalogs will state the positions of all astronomical objects (including stars) along with the equinox, for example, $(\alpha, \delta \ 1950)$ or $(\alpha_{2000}, \delta_{2000})$ etc.

Another important construct is the equinox of the observation, also stated as the equinox of date. The equinox of the observation records the position of the equinox at the time the observation is taken. The position of the object relative to the equinox of observation is known as the apparent position. The apparent position is normally used with certain high accuracy observations. Planetary ephemerides typically report the apparent coordinates of the planets. The CBAMP calculations are referenced to J2000.0 and the epoch of observation. CBAMP reports both the apparent (epoch of observations) and J2000.0 location of all objects.

In addition to the precession of the equinox there is an additional wobble in the Earth's tilt referred to as nutation. The nutation is a result of the varying gravitational forces of the Sun and Moon, due to their changing distances, which causes the net torque to vary. This is known as nutation and is a two component vector, one component directed toward (or away) from the pole and known as the nutation in obliquity and one at a right angle to the mean obliquity-nutation in obliquity plane, known as the nutation in longitude (Figure 4-3). In Figure 4-3, the Earth's mean precession is simplified as a circle. The Earth's rotation rate is ω. Imposed on the precession circle are small oscillations due to the gravitational action of the Sun and Moon acting on the figure of the Earth, the tidal forces. The mean obliquity is the position of the pole without accounting for nutation and is defined as:

$$\varepsilon_o = 23° 26' 21.448'' + 4680''.93 \cdot u - 1''.55 \cdot u^2$$
$$+ 1999''.25 \cdot u^3 - 51''.38 \cdot u^4 - 249''.67 \cdot u^5 - 39''.05 \cdot u^6 \qquad \text{(4-17)}$$
$$- 7''.12 \cdot u^7 + 27''.87 \cdot u^8 + 5'' \ 79 \cdot u^9 + 2''.45 \cdot u^{10}$$

95

where u is the number of Julian millennia from J2000.0 and TDT is the Terrestrial Dynamical Time of the observation:

$$u = \frac{TDT - 2451545}{3652500} \qquad (4\text{-}18)$$

The mean obliquity has an estimated error of 0".01 over the years AD 1000 to AD 3000 (Laskar 1986 also Meeus 1991). The true obliquity, ε, which includes the effects of nutation, is the sum of the mean obliquity plus the nutation in obliquity, $\Delta\varepsilon$:

$$\varepsilon = \varepsilon_o + \Delta\varepsilon \qquad (4\text{-}19)$$

The calculation of the nutation terms has been expanded into sums of periodic terms. The nutation terms (obliquity and longitude) come from the 1980 IAU Theory of Nutation Working Group with corrections by Herring (1987). The errors associated with the nutation terms are a few milli-arcseconds. To calculate the effects of nutation[1] begin by calculating the following angles, defining T as the number of Julian centuries from the standard epoch J2000.0:

$$T = \frac{(TDT - 2451545)}{36525} \qquad (4\text{-}20)$$

Mean Elongation of the Moon from the Sun (degrees),

$$D = 297.8503631 + 445267.11148 \cdot T - 0.0019142 \cdot T^2 + \frac{T^3}{189474} \qquad (4\text{-}21)$$

Mean Anomaly of the Sun (degrees),

$$M = 357.5277233 + 35999.05034 \cdot T - 0.0001603 \cdot T^2 + \frac{T^3}{300000} \qquad (4\text{-}22)$$

Mean Anomaly of the Moon (degrees),

$$M' = 134.9629814 + 477198.8673981 \cdot T + 0.0086972 \cdot T^2 + \frac{T^3}{56250} \qquad (4\text{-}23)$$

Moon's Argument of Latitude (degrees),

$$F = 93.2719103 + 483202.0175381 \cdot T - 0.00365825 \cdot T^2 + \frac{T^3}{327270} \qquad (4\text{-}24)$$

---

[1]In the astronomical definition of precession, nutation due to force free motion is already included. Nutation as defined here is the so called *astronomical nutation* due to irregular perturbations from the Sun, Moon, and planets.
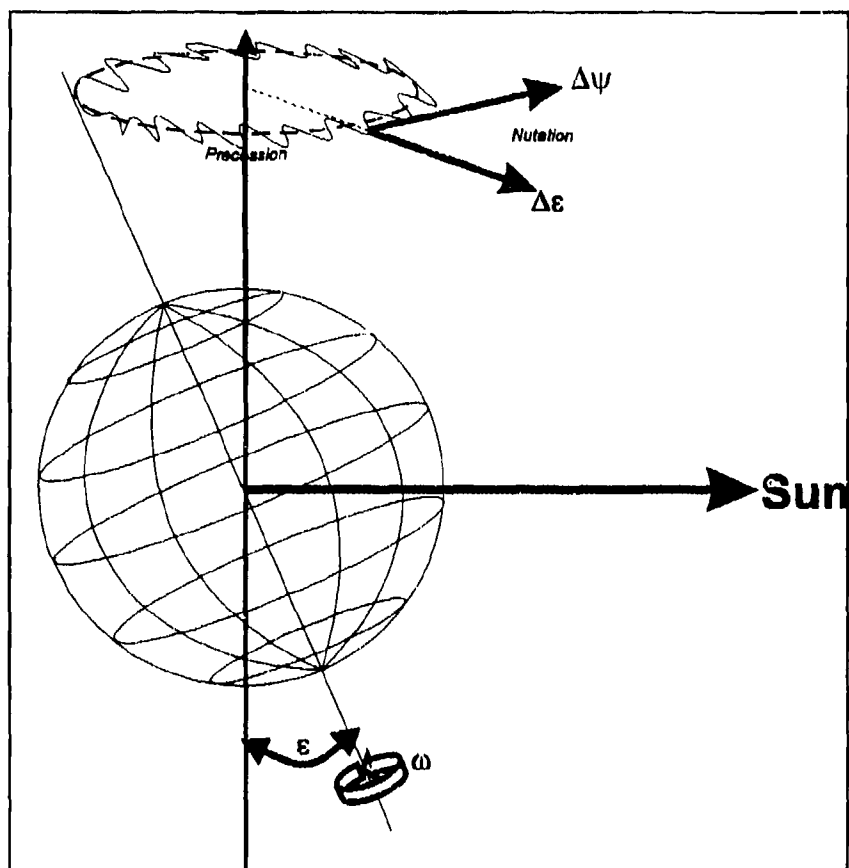
Figure 4-3: Schematic showing the effects of nutation and precession on the position of the Earth's north pole. The Earth's rotates at a rate, ω, once per day. The precession circle is completed in ~26,000 years. Nutation is the smaller, higher frequency wobble.

Ascending Node of the Moon's Orbit (degrees),

$$\Omega = 125.0445222 - 1934.1362608 \cdot T + 0.00207833 \cdot T'^2 + \frac{T'^4}{450000} \qquad (4\text{-}25)$$

Using the above definitions we form the angular components α and β as:

$$\alpha = i \cdot D + j \cdot M + k \cdot M' + m \cdot F + n \cdot \Omega$$
$$\beta = i' \cdot D + j' \cdot M + k' \cdot M' + m' \cdot F + n' \cdot \Omega \qquad (4\text{-}26)$$

The multipliers i, j, k, m, and n are given in Table 4-2 while the multipliers i', j', k', m', and n' are provided in Table 4-3. The angles α and β are then used as the arguments of cosine and sine series expansions. The IAU nutation series consists of 106 periodic terms and are presented in Table 4-2 as the coefficients $A^\Psi, B^\Psi, A^\varepsilon, B^\varepsilon$. The four correction terms in Table 4-3 are due to Herring and are the coefficients $C^\Psi, D^\Psi, C^\varepsilon, D^\varepsilon$. These two series have slightly

different forms as seen in the equations below. The complete nutation terms are then, the nutation in longitude:

$$\Delta\psi = 0''.0001 \cdot \sum_{i=1}^{106} (A_i^{\psi} + B_i^{\psi} \cdot T) \cdot \sin\alpha + 0''.00001 \cdot \sum_{i=1}^{4} \left\{ (C_i^{\psi} \cdot \sin\beta + D_i^{\psi} \cdot \cos\beta \right\} \qquad (4\text{-}27)$$

and the nutation in obliquity:

$$\Delta\varepsilon = 0''.0001 \cdot \sum_{i=1}^{106} (A_i^{\varepsilon} + B_i^{\varepsilon} \cdot T) \cdot \cos\alpha + 0''.00001 \cdot \sum_{i=1}^{4} \left\{ (C_i^{\varepsilon} \cdot \sin\beta + D_i^{\varepsilon} \cdot \cos\beta \right\} \qquad (4\text{-}28)$$

For each line in Table 4-2 compute the angle α of equation (4-26) and then sum the terms as indicted by equations (4-27) and (4-28). Likewise for Table 4-3, form the angle β and sum the terms formed.

4.0.5 THE PRECESSION AND NUTATION MATRICES.

Since precession and nutation can be decomposed into two rotations, the rectangular formalism of planetary positions lends itself well to the use of matrix algebra to apply the precession and nutation correction . Here we present the general precession between any two arbitrary dates. The precession equations calculate the amount of precession between two epochs *through* the standard equinox of J2000.0. Applying the Euler angle formalism to the rotations, we can define the following rotation angles (Yallop, *et al.* 1989):

$$\xi = (2306''.2181 + 1''.39656 \cdot t - 0''.000139 \cdot t^2) \cdot T$$
$$+ (0''.30188 - 0''.000344 \cdot t) \cdot T^2 + 0''.017998 \cdot T^3 \qquad (4\text{-}29)$$

$$z = (2306''.2181 + 1''.39656 \cdot t - 0''.000139 \cdot t^2) \cdot T$$
$$+ (1''.09468 + 0''.000066 \cdot t) \cdot T^2 + 0''.018203 \cdot T^3 \qquad (4\text{-}30)$$

$$\theta = (2004''.3109 + 0''.85330 \cdot t - 0''.000217 \cdot t^2) \cdot T$$
$$- (0''.42665 + 0''.000217 \cdot t) \cdot T^2 - 0''.041833 \cdot T^3 \qquad (4\text{-}31)$$

Where, T, is the time in Julian centuries between the time of observation (TDT), the final epoch, and some starting epoch:

$$T = \frac{\text{TDT} - \text{JD}_\bullet}{36525} \qquad (4\text{-}32)$$

and t is the time in Julian centuries between the starting epoch and J2000.0.

$$t = \frac{\text{JD}_\bullet - 2451545}{36525} \qquad (4\text{-}33)$$

If the starting epoch is the standard equinox of J2000.0 then $t = 0$.

98

Table 4-2. The 106 terms of the IAU nutation series.

Term	i	j	k	m	n	A^ψ	B^ψ	A^ε	B^ε	Term	i	j	k	m	n	A^ψ	B^ψ	A^ε	B^ε
1	0	0	0	0	1	-171996	-1742	92025	89	54	1	0	2	2	2	-8	0	3	0
2	0	0	0	0	2	2062	2	-895	5	55	1	0	0	2	0	6	0	0	0
3	-2	0	2	0	1	46	0	-24	0	56	2	0	2	-2	2	6	0	-3	0
4	2	0	-2	0	0	11	0	0	0	57	0	0	0	2	1	-6	0	3	0
5	-2	0	2	0	2	-3	0	1	0	58	0	0	2	2	1	-7	0	3	0
6	1	-1	0	-1	0	-3	0	0	0	59	1	0	2	-2	1	6	0	-3	0
7	0	-2	2	-2	1	-2	0	1	0	60	0	0	0	-2	1	-5	0	3	0
8	2	0	-2	0	1	1	0	0	0	61	1	-1	0	0	0	5	0	0	0
9	0	0	2	-2	2	-13187	-16	5736	-31	62	2	0	2	0	1	-5	0	3	0
10	0	1	0	0	0	1426	-34	54	-1	63	0	1	0	-2	0	-4	0	0	0
11	0	1	2	-2	2	-517	12	224	-6	64	1	0	-2	0	0	4	0	0	0
12	0	-1	2	-2	2	217	-5	-95	3	65	0	0	0	1	0	-4	0	0	0
13	0	0	2	-2	1	129	1	-70	0	66	1	1	0	0	0	-3	0	0	0
14	2	0	0	-2	0	48	0	1	0	67	1	0	2	0	0	3	0	0	0
15	0	0	2	-2	0	-22	0	0	0	68	1	-1	2	0	2	-3	0	1	0
16	0	2	0	0	0	17	-1	0	0	69	-1	-1	2	2	2	-3	0	1	0
17	0	1	0	0	1	-15	0	9	0	70	-2	0	0	0	1	-2	0	1	0
18	0	2	2	-2	2	-16	1	7	0	71	3	0	2	0	2	-3	0	1	0
19	0	-1	0	0	1	-12	0	6	0	72	0	-1	2	2	2	-3	0	1	0
20	-2	0	0	2	1	-6	0	3	0	73	1	1	2	0	2	2	0	-1	0
21	0	-1	2	-2	1	-5	0	3	0	74	-1	0	2	-2	1	-2	0	1	0
22	2	0	0	-2	1	4	0	-2	0	75	2	0	0	0	1	2	0	-1	0
23	0	1	2	-2	1	4	0	-2	0	76	1	0	0	0	2	-2	0	1	0
24	1	0	0	-1	0	-4	0	0	0	77	3	0	0	0	0	2	0	0	0
25	2	1	0	-2	0	1	0	0	0	78	0	0	2	1	2	2	0	-1	0
26	0	0	-2	2	1	1	0	0	0	79	-1	0	0	0	2	1	0	-1	0
27	0	1	-2	2	0	-1	0	0	0	80	1	0	0	-4	0	-1	0	0	0
28	0	1	0	0	2	1	0	0	0	81	-2	0	2	2	2	1	0	-1	0
29	-1	0	0	1	1	1	0	0	0	82	-1	0	2	4	2	-2	0	1	0
30	0	1	2	-2	0	-1	0	0	0	83	2	0	0	-4	0	-1	0	0	0
31	0	0	2	0	2	-2274	-2	977	-5	84	1	1	2	-2	2	1	0	-1	0
32	1	0	0	0	0	712	1	-7	0	85	1	0	2	2	1	-1	0	1	0
33	0	0	2	0	1	-386	-4	200	0	86	-2	0	2	4	2	-1	0	1	0
34	1	0	2	0	2	-301	0	129	-1	87	-1	0	4	0	2	1	0	0	0
35	1	0	0	-2	0	-158	0	-1	0	88	1	-1	0	-2	0	1	0	0	0
36	-1	0	2	0	2	123	0	-53	0	89	2	0	2	-2	1	1	0	-1	0
37	0	0	0	2	0	63	0	-2	0	90	2	0	2	2	2	-1	0	0	0
38	1	0	0	0	1	63	1	-33	0	91	1	0	0	2	1	-1	0	0	0
39	-1	0	0	0	1	-58	-1	32	0	92	0	0	4	-2	2	1	0	0	0
40	-1	0	2	2	2	-59	0	26	0	93	3	0	2	-2	2	1	0	0	0
41	1	0	2	0	1	-51	0	27	0	94	1	0	2	-2	0	-1	0	0	0
42	0	0	2	2	2	-38	0	16	0	95	0	1	2	0	1	1	0	0	0
43	2	0	0	0	0	29	0	-1	0	96	-1	-1	0	2	1	1	0	0	0
44	1	0	2	-2	2	29	0	-12	0	97	0	0	-2	0	1	-1	0	0	0
45	2	0	2	0	2	-31	0	13	0	98	0	0	2	-1	2	-1	0	0	0
46	0	0	2	0	0	26	0	-1	0	99	0	1	0	2	0	-1	0	0	0
47	-1	0	2	0	1	21	0	-10	0	100	1	0	-2	-2	0	-1	0	0	0
48	-1	0	0	2	1	16	0	-8	0	101	0	-1	2	0	1	-1	0	0	0
49	1	0	0	-2	1	-13	0	7	1	102	1	1	0	-2	1	-1	0	0	0
50	-1	0	2	2	1	-10	0	5	0	103	1	0	-2	2	0	-1	0	0	0
51	1	1	0	-2	0	-7	0	0	0	104	2	0	0	2	0	1	0	0	0
52	0	1	2	0	2	7	0	-3	0	105	0	0	2	4	2	-1	0	0	0
53	0	-1	2	0	2	-7	0	3	0	106	0	1	0	1	0	1	0	0	0

Table 4-3. The four correction terms due to Herring (1987).

Term	Argument					$\Delta\psi$		$\Delta\varepsilon$	
	l'	l'	k'	m'	n'	C_i^ψ	D_i^ψ	C_i^ε	D_i^ε
1	0	0	0	0	1	-725	417	224	213
2	0	1	0	0	0	523	61	-24	208
3	-2	0	0	2	-2	102	-118	-47	-41
4	0	0	0	2	2	-81	0	0	32

The precession matrix, P, is then defined as:

$$P = \begin{pmatrix} \cos\xi\cos\theta\cos z - \sin\xi\sin z & -\sin\xi\cos\theta\cos z - \cos\xi\sin z & -\sin\theta\cos z \\ \cos\xi\cos\theta\sin z + \sin\xi\cos z & -\sin\xi\cos\theta\sin z + \cos\xi\cos z & -\sin\theta\sin z \\ \cos\xi\sin\theta & -\sin\xi\sin\theta & \cos\theta \end{pmatrix} \quad (4\text{-}34)$$

Similarly the nutation matrix, N, can be formed using the nutation and obliquity terms developed in Section 4.0.3:

$$N = \begin{pmatrix} \cos\Delta\psi & -\sin\Delta\psi\cos\varepsilon_o & -\sin\Delta\psi\sin\varepsilon \\ \sin\Delta\psi\cos\varepsilon & \cos\Delta\psi\cos\varepsilon_o\cos\varepsilon + \sin\varepsilon_o\sin\varepsilon & \cos\Delta\psi\sin\varepsilon_o\cos\varepsilon - \cos\varepsilon_o\sin\varepsilon \\ \sin\Delta\psi\sin\varepsilon & \cos\Delta\psi\cos\varepsilon_o\sin\varepsilon - \sin\varepsilon_o\cos\varepsilon & \cos\Delta\psi\sin\varepsilon_o\sin\varepsilon + \cos\varepsilon_o\cos\varepsilon \end{pmatrix} \quad (4\text{-}35)$$

Then, any precession can be described as:

$$\begin{pmatrix} x' \\ y' \\ z' \end{pmatrix} = \begin{pmatrix} \cos\xi\cos\theta\cos z - \sin\xi\sin z & -\sin\xi\cos\theta\cos z - \cos\xi\sin z & -\sin\theta\cos z \\ \cos\xi\cos\theta\sin z + \sin\xi\cos z & -\sin\xi\cos\theta\sin z + \cos\xi\cos z & -\sin\theta\sin z \\ \cos\xi\sin\theta & -\sin\xi\sin\theta & \cos\theta \end{pmatrix} \begin{pmatrix} x \\ y \\ z \end{pmatrix} \quad (4\text{-}36)$$

And any correction for nutation is:

$$\begin{pmatrix} x' \\ y' \\ z' \end{pmatrix} = \begin{pmatrix} \cos\Delta\psi & -\sin\Delta\psi\cos\varepsilon_o & -\sin\Delta\psi\sin\varepsilon \\ \sin\Delta\psi\cos\varepsilon & \cos\Delta\psi\cos\varepsilon_o\cos\varepsilon + \sin\varepsilon_o\sin\varepsilon & \cos\Delta\psi\sin\varepsilon_o\cos\varepsilon - \cos\varepsilon_o\sin\varepsilon \\ \sin\Delta\psi\sin\varepsilon & \cos\Delta\psi\cos\varepsilon_o\sin\varepsilon - \sin\varepsilon_o\cos\varepsilon & \cos\Delta\psi\sin\varepsilon_o\sin\varepsilon + \cos\varepsilon_o\cos\varepsilon \end{pmatrix} \begin{pmatrix} x \\ y \\ z \end{pmatrix} \quad (4\text{-}37)$$

The two effects can easily be included into a single, precession-nutation matrix, R, as:

$$R = PN \quad (4\text{-}38)$$

4.1   THE SUN, MOON, AND PLANETS.

The positional accuracy of the Sun and the planets in CBAMP far exceeds the 2 arc-seconds requirement for CBSD. An ephemeris can be calculated in one of two different ways. The first method uses the NASA Jet Propulsion Laboratory ephemeris DE/LE-200. DE/LE-200 is a recognized standard in calculating planetary positions and is used by the Naval Observatory in the calculation of *The Astronomical Almanac*. The second uses the analytical planetary theory VSOP87 (Variations Séculaires des Orbites Planétaires) of Bretagnon and Francou (1988) as adapted by Meeus (1991) to calculate the positions of the Sun and planets out to Neptune.

The DE/LE-200 ephemeris is the preferred method when calculating planetary positions; however, there are a few drawbacks to using DE/LE-200. DE/LE-200 requires the use of a large database file which, as distributed, is 16 Megabytes of ASCII data. This file is around 4 Megabytes when condensed into its binary form. Another drawback is that the coverage is limited to the years 1959 to 2025. While this is clearly acceptable for Air Force requirements, it is anticipated that CBAMP will have a broader user base, i.e. the astronomical community. To allow the program CBAMP to have the largest possible number of users, the VSOP87 theory is also incorporated.   VSOP87 is an analytical model; however, with the implementation used in CBAMP it is of lower precision than DE/IE-200, but still within the 2 arc-second accuracy as will be shown below. VSOP87 is valid over a larger time span. In its reduced form, as used in CBAMP, the coverage should be a 1 arc-second accuracy covering 1000 years before and after the epoch J2000.0.

4.1.1   THE JPL DE/LE-200 EPHEMERIS.

The ephemerides DE/LE-200 (Seidelmann, 1992, Standish, 1985) is a numerical integration scheme using a variable-order, variable-step-size Adams method preceded by a least squares fit to the observational data. The observational data used in the least squares fitting consists of optical data, radar-ranging for Mercury and Venus, spacecraft range points consisting of Pioneer Mission to Jupiter, Mariner 9 orbiter of Mars, and Viking Landers on Mars, and the Lunar Laser Range data for the Moon. DE/LE-200 is not an analytical theory of planetary motion but it does include:

1.   The point mass interactions among the Moon, Sun, and planets,
2.   General relativity using an isotropic, parameterized post-Newtonian *n*-body metric,
3.   Newtonian perturbations of the asteroids Ceres, Pallas, Vesta, Iris, and Bamberga,
4.   Moon and Sun action on the figure of the Earth,
5.   Earth and Sun action on the figure of the Moon,
6.   Earth tide action on the Moon, and
7.   Physical libration of the Moon.

The ephemeris DE/LE-200 is aligned with the reference frame of J2000. In the *n*-body metric all dynamical quantities are expressed with respect to the solar-system barycenter.

The distributed ephemeris DE/LE-200 is not the numerical integration scheme but an interpolation routine based on runs of the integrator. For each object in the solar system the

coefficients of a polynomial are produced at a fixed interval of time. The time period for each object, called granule by JPL and the degree of the polynomial is given in Table 4-4.

Table 4-4. Granule lengths used in DE/LE-200

Body	Granule length (days)	Polynomial degree (N)
Mercury	8	13
Venus	16	9
Earth-Moon barycenter	16	12
Mars	32	10
Jupiter	32	7
Saturn	32	6
Uranus	32	5
Neptune	32	5
Pluto	32	5
Moon	4	12
Sun	16	10

Any function $f(t)$ has an approximate Nth-degree expansion in Chebyshev polynomials of:

$$f(t) \approx \sum_{n=0}^{N} a_n T_n(t)$$
(4-39)

and a derivative of:

$$\dot{f}(t) \approx \sum_{n=0}^{N} a_n \dot{T}_n(t)$$
(4-40)

For each heliocentric coordinate (x, y, z) and associated velocity $(\dot{x}, \dot{y}, \dot{z})$ a set of a_n have been determined with degree and length given in Table 4-3. In the procedure nine pairs of position and velocity values are obtained for each granule at equally spaced times -- two for the end points and seven interior points. The output is the set of a_n for the polynomial that is an exact fit to the end points of the positions and a least-squares fit to the interior positions.

4.1.2   THE ANALYTICAL THEORY VSOP87.

The VSOP87 (Variations Séculaires des Orbites Planétaires) of Bretagnon and Francou (1988) is an analytical representation of the orbits of the planets. VSOP87 and its predecessor VSOP82 (Bretagnon, 1982) is a complete theory of motion of all the planets, except Pluto. The theory retains perturbation corrections up to third order for Mercury, Venus, Earth, and Mars and up to sixth order for Jupiter, Saturn, Uranus, and Neptune. The VSOP theories use the positions generated by DE/LE-200 to build the set of integration constants. Six different variations of the VSOP87 exist, A through F, representing the solutions in different coordinate systems or different frames of reference. The D

102

representation of the VSOP87 provides the heliocentric spherical variables longitude, latitude, and radius vector reckoned to the mean ecliptic and equinox of the date of observation. Here positions are given by sets of periodic terms of the form:

$$A \cdot \sin(B + C \cdot u) \tag{4-41}$$

where u is the number of Julian millennia since J2000.0.

$$u = \frac{(TDT - 2451545)}{3652500} \tag{4-42}$$

For example, the heliocentric ecliptic longitude is given by:

$$L = L_0 + L_1 \cdot u + L_2 \cdot u^2 + L_3 \cdot u^4 + L_4 \cdot u^4 + L_5 \cdot u^5 \tag{4-43}$$

where each of the L_n terms are given by the series:

$$L_n = \sum_i A_i \cdot \cos(B_i + C_i \cdot u) \tag{4-44}$$

Table 4-5 gives the 20 terms which make up the L_2 term for the Earth. The L_0 term contains 64 terms, the L_1 contains 34 terms, etc. Table 4-6 gives the number of terms for each of the planets. The first column is the planet name, the second column identifies the longitude (L) latitude (B), or radius vector (R), the next five columns gives the number of terms in each series, e.g. L_0, B_1, R_2, etc.

Table 4-5. The 20 terms of the L_2 series for the Earth.

Term	A (10^{-8} radians)	B (radians)	C (radians)
1	52919	0	0
2	8720	1.0721	6283.0758
3	309	0.867	12566.152
4	27	0.05	3.52
5	16	5.19	26.30
6	16	3.68	155.42
7	10	0.76	18849.23
8	9	2.06	77713.77
9	7	0.83	775.52
10	5	4.66	1577.34
11	4	1.03	7.11
12	4	3.44	5573.14
13	3	5.14	796.30
14	3	6.05	5507.55
15	3	1.19	242.73
16	3	6.12	529.69
17	3	0.31	398.15
18	3	2.28	553.57
19	2	4.38	5223.69
20	2	3.75	0.98

The original VSOP87 theory gives positional accuracy to better than $0''.01$ encompassing 12,723 terms in order higher than 10^{-9} and with many more terms existing for higher order. By comparison, CBAMP uses a truncated form of this expansion (Meeus 1991) and retains

only 2,420 terms of order higher than 10^{-8}. CBAMP's truncated form retains approximately a 1" accuracy. Table 4-7 gives differences between CBAMP and *The Astronomical Almanac* for 24 January 1990. Table 4-8 gives the RMS error for the Right Ascension and Declination for 36 dates, 12 dates in each of the years 1989, 1990, and 1992.

Table 4-6. Numbers of terms used in the truncated VSOP87D theory.

		0	1	2	3	4	5
Mercury	L	38	16	10	8	6	1
	B	14	11	9	7	2	0
	R	13	8	7	5	0	0
Venus	L	24	12	8	3	3	1
	B	9	4	4	4	1	0
	R	12	3	3	1	1	0
Earth	L	64	34	20	7	3	1
	B	5	2	0	0	0	0
	R	40	10	6	2	1	0
Mars	L	69	46	33	12	8	2
	B	16	9	7	4	3	0
	R	45	27	11	6	4	0
Jupiter	L	64	61	57	39	19	5
	B	26	22	14	9	6	1
	R	46	43	36	28	15	7
Saturn	L	90	79	63	48	27	12
	B	34	32	29	21	12	2
	R	44	38	32	28	23	18
Uranus	L	91	57	35	18	4	0
	B	28	20	11	4	1	0
	R	59	35	18	10	2	0
Neptune	L	38	18	7	4	1	0
	B	17	13	6	4	1	0
	R	32	15	5	1	0	0

Table 4-7. Errors Associated with CBAMP Planetary Positions for 24 January 1990. Positions of the Sun, Moon, and planets are apparent except for Pluto which is the astrometric J2000.0 position.

True Obliquity	0".001	Mercury RA	-0^s.02	Saturn RA	0^s.00
Equation of the Equinox	0^s.001	Mercury Declination	0".1	Saturn Declination	-0".2
Solar Longitude	-0".06	Venus RA	0^s.00	Uranus RA	0^s.00
Solar Latitude	0".12	Venus Declination	0".1	Uranus Declination	0".0
Solar RA	0^s.07	Mars RA	0^s.02	Neptune RA	-0^s.03
Solar Declination	0".2	Mars Declination	0".4	Neptune Declination	-0".2
Lunar RA	0^s.2	Jupiter RA	0^s.05	Pluto RA	-0^s.01
Lunar Declination	0".	Jupiter Declination	0".1	Pluto Declination	-0".2

104

Table 4-8. Measured errors of VSOP87D compared to *The Astronomical Almanac*. The Moon's position was calculated using Chapront's ELP-2000/82 Lunar Theory.

	Mean error in Right Ascension (seconds of time)	Standard Deviation of Mean	Mean Error in Declination (seconds of arc)	Standard Deviation of Mean
Sun	-0.006	0.047	0.000	0.216
Moon	0.01	0.20	0.3	1.5
Mercury	-0.001	0.025	0.003	0.247
Venus	0.014	0.029	-0.050	0.186
Mars	0.003	0.040	0.064	0.322
Jupiter	0.025	0.025	0.108	0.290
Saturn	-0.015	0.026	0.119	0.182
Uranus	-0.012	0.015	-0.061	0.049
Neptune	0.030	0.016	0.131	0.067
Pluto	-0.012	0.004	-0.264	0.022

4.1.3 THE ELP-2000/82 LUNAR THEORY.

The DE/LE-200 option for calculating the position of the Moon can be overridden For these cases CBAMP uses a truncated form of Chapront's (1983, 1988) ELP-2000/82 lunar theory to obtain the lunar apparent position. This estimate, referenced to J2000.0, gives the position of the Moon to an accuracy of 10" in ecliptic longitude and 4" in ecliptic latitude spanning the years 1910 through 2110.

We begin by calculating, T, the number of Julian centuries from J2000.0:

$$T = \frac{(\text{TDT} - 2451545)}{36525} \qquad (4\text{-}45)$$

where again, TDT is the Terrestrial Dynamical Time of the observation. We then calculate the following angles (note that these angles have a slightly different form then used for the nutation series):

Moon's mean longitude (degrees),

$$L' = 218.3164591 + 481267.88134236 \cdot T - 0.0013268 \cdot T'^2 + \frac{T'^3}{538841} - \frac{T'^4}{65194000} \qquad (4\text{-}46)$$

Mean elongation of the Moon (degrees),

$$D = 297.8502042 + 445267.1115168 \cdot T - 0.0016300 \cdot T'^2 + \frac{T'^3}{545868} - \frac{T'^4}{113065000} \qquad (4\text{-}47)$$

Sun's mean anomaly (degrees),

$$M = 357.5291092 + 35999.0502909 \cdot T - 0.0001536 \cdot T^2 + \frac{T^3}{24490000}$$ (4-48)

Moon's mean anomaly (degrees),

$$M' = 134.9634114 + 477198.8676313 \cdot T + 0.0089970 \cdot T^2 + \frac{T^3}{69699} - \frac{T^4}{14712000}$$ (4-49)

Moon's argument of latitude (degrees),

$$F = 93.2720993 + 483202.0175273 \cdot T - 0.0034029 \cdot T^2 - \frac{T^3}{3526000} + \frac{T^4}{863310000}$$ (4-50)

Correction term due to Venus (dagrees),

$$A_1 = 119.75 + 131.849 \cdot T$$ (4-51)

Correction term due to Jupiter (degrees),

$$A_2 = 53.09 + 479264.290 \cdot T$$ (4-52)

Correction term due to the Earth's flattening (degrees),

$$A_3 = 313.45 + 481266.484 \cdot T$$ (4-53)

Earth's orbital eccentricity (degrees),

$$E = 1 - 0.002516 \cdot T - 0.0000074 \cdot T^2$$ (4-54)

The terms geocentric ecliptic longitude, latitude and radius vector, (l, β, r) are found from the series expansion:

$$l = L' + 3958 \cdot \sin A_1 + 1962 \cdot \sin(L' - F) + 318 \cdot \sin A_2$$
$$+ 10^{-6} \cdot \sum_m C_m^l \cdot E^{|j|} \cdot \sin(i \cdot D + j \cdot M + k \cdot M' + n \cdot F) + \Delta\psi$$ (4-55)

where the multipliers for the sine argument, $i, j, k,$ and n and the coefficients C_m^l are given in Table 4-9. The term, $\Delta\psi$, is the nutation in longitude as described in Section 4.0.2.

$$\beta = -2235 \cdot \sin L' + 382 \cdot \sin A_3 + 175 \cdot \sin(A_1 - F) + 175 \cdot \sin(A_1 + F)$$
$$+ 127 \cdot \sin(L' - M') - 115 \cdot \sin(L' + M')$$ (4-56)
$$+ 10^{-6} \cdot \sum_m B_m^l \cdot E^{|j|} \cdot \sin(i \cdot D + j \cdot M + k \cdot M' + n \cdot F)$$

The quantities l and β are in degrees while the radius vector, r, is defined in kilometers as:

$$r = 385000.56 + 10^{-3} \cdot \sum_m C_m^r \cdot E^{|j|} \cdot \cos(i \cdot D + j \cdot M + k \cdot M' + n \cdot F) \qquad (4\text{-}57)$$

Tables 4-9 and 4-10 present the 60 terms used for longitude, latitude, and radius vector for this implementation of ELP-2000/82. Following the methods put forth in Section 4.0.5 and Section 4.0.6 the longitude, latitude, and radius vector can be converted into Right Ascension and Declination and should include parallax effects.

Table 4-8 also gives the Moon's position as compared to *The Astronomical Almanac* over 36 dates in the years 1989, 1990, and 1992. The *Almanac* only reports the Right Ascension to 0.1 seconds of time and the Declination to 1 second of arc. While the mean position is within the 2 arc second requirement for CBSD, the standard deviation is quite large indicating some large deviations from the true position. This is due to the truncated form of Chapront's theory used.

4.1.4 A LEAST SQUARES FIT FOR PLUTO.

No analytical theory exists for the orbit of Pluto. The orbital period of Pluto is, roughly, 250 years. Discovered in 1930, with observations dating back to 1914, Pluto has completed less than a third of its orbit since the first observation. However, Meeus (1991) has constructed a series consisting of periodic terms based on a least squares fit to the observations for the epoch J2000.0. The terms include the perturbations of the eight major planets. This is an extension of the work of Goffin, Meeus, and Steyaert (1986) who performed a similar construction referenced to the epoch B1950.0. The resulting theory provides the position, in heliocentric ecliptic coordinates, spanning 1885-2099 to an accuracy of 0".6 in longitude, 0".2 in latitude, and 0.00002 AU for the radius vector.

Using T as the number of Julian centuries from the epoch J2000.0 the following angles are calculated:

$$\begin{aligned} J &= 34°.35 + 3034°.9057 \cdot T \\ S &= 50°.08 + 1222°.1138 \cdot T \\ P &= 238°.96 + 144°.9600 \cdot T \end{aligned} \qquad (4\text{-}58)$$

The longitude, l, latitude, β, and radius vector, r are then given by:

$$l = 238°.956785 + 144°.96 \cdot T + \sum_{n=1}^{43} (A_n^l \sin \alpha_n + B_n^l \cos \alpha_n) \qquad (4\text{-}59)$$

$$\beta = -3°.908202 + \sum_{n=1}^{43} (A_n^\beta \sin \alpha_n + B_n^\beta \cos \alpha_n) \qquad (4\text{-}60)$$

$$r = 40.7247248 + \sum_{n=1}^{43} (A_n^r \sin \alpha_n + B_n^r \cos \alpha_n) \qquad (4\text{-}61)$$

where the angle α_n is defined as:

$$\alpha_n = i \cdot J + j \cdot S + k \cdot P \qquad (4\text{-}62)$$

There are 43 terms which make up the series. The A and B coefficients for l, β, and r are given in Table 4-11. Table 4-8 shows the errors found for 36 positions of Pluto over the years 1989, 1990, and 1992.

4.1.5 CONVERSION TO APPARENT POSITION.

The DE/LE-200 theory returns the heliocentric rectangular ecliptic coordinates (x, y, z) of an object. The VSOP87D theory returns the heliocentric spherical ecliptic coordinates (l, β, r). Slightly different methods are used to convert these two formalisms of positions to apparent Right Ascension and Declination as seen from Earth. To convert the DE/LE-200 positions to apparent Right Ascension and Declination, we follow the steps outlined in *The Astronomical Almanac* as detailed by Seidelmann (1992). All DE/LE-200 calculations should be referenced to TDB (Barycentric Dynamical Time); however, since the difference between TDT and TDB is much less then a second, the time TDT are substituted in CBAMP (see Section 4.0.1). Using DE/LE-200 we calculate the Sun's barycentric position at time TDB, the Earth's position and velocity at time TDB, and the planet's Barycentric position at TDB:

$$\bar{S}_B(\text{TDB}) = \text{Solar Barycentric position,}$$
$$\bar{E}_B(\text{TDB}) = \text{Earth's Barycentric position,}$$
$$\dot{\bar{E}}_B(\text{TDB}) = \text{Earth's Barycentric velocity,}$$
$$\bar{Q}_B(\text{TDB}) = \text{Planet's Barycentric position,}$$

From which we form the geocentric vectors:

$$\bar{P} = \bar{Q}_B(\text{TDB} - \tau) - \bar{E}_B(\text{TDB})$$
$$\bar{E} = \bar{E}_B(\text{TDB}) - \bar{S}_B(\text{TDB}) \qquad (4\text{-}63)$$
$$\bar{Q} = \bar{Q}_B(\text{TDB} - \tau) - \bar{S}_B(\text{TDB} - \tau)$$

where τ is the light time between the planet and the Earth and must be solved iteratively by using equation (4-63) and:

$$c\tau = P + \left(\frac{2GM_o}{c^2}\right) \ln\left[\frac{(E + P + Q)}{(E - P + Q)}\right] \qquad (4\text{-}64)$$

where the constants have the following values:

G = Gravitational Constant = $3.986005 \cdot 10^{14}$ m^3/kg/s^2
M_o = Solar Mass = $1.9891 \cdot 10^{30}$ kg
c = velocity of light = 299792458 m/s

Table 4-9. Terms used for the ELP-2000/82 Lunar Theory, Longitude and Radius Vector.

No.	Argument				Longitude	Radius Vector
	i	j	k	n	C^l	C^r
1	0	0	1	0	6288774	-20905355
2	2	0	-1	0	1274027	-3699111
3	2	0	0	0	658314	-2955968
4	0	0	2	0	213618	-569925
5	0	1	0	0	-185116	48888
6	0	0	0	2	-114332	-3149
7	2	0	-2	0	58793	246158
8	2	-1	-1	0	57066	-152138
9	2	0	1	0	53322	-170733
10	2	-1	0	0	45758	-204586
11	0	1	-1	0	-40923	-129620
12	1	0	0	0	-34720	108743
13	0	1	1	0	-30383	104755
14	2	0	0	-2	15327	10321
15	0	0	1	2	-12528	0
16	0	0	1	-2	10980	79661
17	4	0	-1	0	10675	-34782
18	0	0	3	0	10034	-23210
19	4	0	-2	0	8548	-21636
20	2	1	-1	0	-7888	24208
21	2	1	0	0	-6766	30824
22	1	0	-1	0	-5163	-8379
23	1	1	0	0	4987	-16675
24	2	-1	1	0	4036	-12831
25	2	0	2	0	3994	-10445
26	4	0	0	0	3861	-11650
27	2	0	-3	0	3665	14403
28	0	1	-2	0	-2689	-7003
29	2	0	-1	2	-2602	0
30	2	-1	-2	0	2390	10056
31	1	0	1	0	-2348	6322
32	2	-2	0	0	2236	-9884
33	0	1	2	0	-2120	5751
34	0	2	0	0	-2069	0
35	2	-2	-1	0	2048	-4950
36	2	0	1	-2	-1773	4130
37	2	0	0	2	-1595	0
38	4	-1	-1	0	1215	-3958
39	0	0	2	2	-1110	0
40	3	0	-1	0	-892	3258
41	2	1	1	0	-810	2616
42	4	-1	-2	0	759	-1897
43	0	2	-1	0	-713	-2117
44	2	2	-1	0	-700	2354
45	2	1	-2	0	691	0
46	2	-1	0	-2	596	0
47	4	0	1	0	549	-1423
48	0	0	4	0	537	-1117
49	4	-1	0	0	520	-1571
50	1	0	-2	0	-487	-1739
51	2	1	0	-2	-399	0
52	0	0	2	-2	-381	-4421
53	1	1	1	0	351	0
54	3	0	-2	0	-340	0
55	4	0	-3	0	330	0
56	2	-1	2	0	327	0
57	0	2	1	0	-323	1165
58	1	1	-1	0	299	0
59	2	0	3	0	294	0
60	2	0	-1	-2	0	8752

109

Table 4-10. Latitude terms used for ELP-2000/82.

No.	Argument				Latitude
	I	j	k	n	C^β
1	0	0	0	1	5128122
2	0	0	1	1	280602
3	0	0	1	-1	277693
4	2	0	0	-1	173237
5	2	0	-1	1	55413
6	2	0	-1	-1	46271
7	2	0	0	1	32573
8	0	0	2	1	17198
9	2	0	1	-1	9266
10	0	0	2	-1	8822
11	2	-1	0	-1	8216
12	2	0	-2	-1	4324
13	2	0	1	1	4200
14	2	1	0	-1	-3359
15	2	-1	-1	1	2463
16	2	-1	0	1	2211
17	2	-1	-1	-1	2065
18	0	1	-1	-1	-1870
19	4	0	-1	-1	1828
20	0	1	0	1	-1794
21	0	0	0	3	-1749
22	0	1	-1	1	-1565
23	1	0	0	1	-1491
24	0	1	1	1	-1475
25	0	1	1	-1	-1410
26	0	1	0	-1	-1344
27	1	0	0	-1	-1335
28	0	0	3	1	1107
29	4	0	0	-1	1021
30	4	0	-1	1	833
31	0	0	1	-3	777
32	4	0	-2	1	671
33	2	0	0	-3	607
34	2	0	2	-1	596
35	2	-1	1	-1	491
36	2	0	-2	1	-451
37	0	0	3	-1	439
38	2	0	2	1	422
39	2	0	-3	-1	421
40	2	1	-1	1	-366
41	2	1	0	1	-351
42	4	0	0	1	331
43	2	-1	1	1	315
44	2	-2	0	-1	302
45	0	0	1	3	-283
46	2	1	1	-1	-229
47	1	1	0	-1	223
48	1	1	0	1	223
49	0	1	-2	-1	-220
50	2	1	-1	-1	-220
51	1	0	1	1	-185
52	2	-1	-2	-1	181
53	0	1	2	1	-177
54	4	0	-2	-1	176
55	4	-1	-1	-1	166
56	1	0	1	-1	-164
57	4	0	1	-1	132
58	1	0	-1	-1	-119
59	4	-1	0	-1	115
60	2	-2	0	1	107

Table 4-11. Periodic terms for the orbit of Pluto.

No.	Argument			Longitude		Latitude		Radius Vector	
	i	j	k	A^l	B^l	A^β	B^β	A^r	B^r
1	0	0	1	-19798886	19848454	-5453098	-14974876	66867334	68955876
2	0	0	2	897499	-4955707	3527363	1672673	-11826086	-333765
3	0	0	3	610820	1210521	-1050939	327763	1593657	-1439953
4	0	0	4	-341639	-189719	178691	-291925	-18948	482443
5	0	0	5	129027	-34863	18763	100448	-66634	-85576
6	0	0	6	-38215	31061	-30594	-25838	30841	-5765
7	0	1	-1	20349	-9886	4965	11263	-6140	22254
8	0	1	0	-4045	-4904	310	-132	4434	4443
9	0	1	1	-5885	-3238	2036	-947	-1518	641
10	0	1	2	-3812	3011	-2	-674	-5	792
11	0	1	3	-601	3468	-329	-563	518	518
12	0	2	-2	1237	463	-64	39	-13	-221
13	0	2	-1	1086	-911	-94	210	837	-494
14	0	2	0	595	-1229	-8	-160	-281	616
15	1	-1	0	2484	-485	-177	259	260	-395
16	1	-1	1	839	-1414	17	234	-191	-396
17	1	0	-3	-964	1059	582	-285	-3218	370
18	1	0	-2	-2303	-1038	-298	692	8019	-7869
19	1	0	-1	7049	747	157	201	105	45637
20	1	0	0	1179	-358	304	825	8623	8444
21	1	0	1	393	-63	-124	-29	-896	-801
22	1	0	2	111	-268	15	8	208	-122
23	1	0	3	-52	-154	7	15	-133	65
24	1	0	4	-78	-30	2	2	-16	1
25	1	1	-3	-34	-26	4	2	-22	7
26	1	1	-2	-43	1	3	0	-8	16
27	1	1	-1	-15	21	1	-1	2	9
28	1	1	0	-1	15	0	-2	12	5
29	1	1	1	4	7	1	0	1	-3
30	1	1	3	1	5	1	-1	1	0
31	2	0	-6	8	3	-2	-3	9	6
32	2	0	-5	-3	6	1	2	2	-1
33	2	0	-4	6	-13	-8	2	14	10
34	2	0	-3	10	22	10	-7	-65	12
35	2	0	-2	-57	-32	0	21	126	-233
36	2	0	-1	157	-46	8	5	270	1068
37	2	0	0	12	-18	13	16	254	155
38	2	0	1	-4	8	-2	-3	-26	-2
39	2	0	2	-5	0	0	0	7	0
40	2	0	3	3	4	0	1	-11	4
41	3	0	-2	-1	-1	0	1	4	-14
42	3	0	-1	6	-3	0	0	18	35
43	3	0	0	-1	-2	0	1	13	3

and therefore:

$$\frac{GM_o}{c^2} = 1476.53m = 9.87 \times 10^{-9} \, AU \tag{4-65}$$

The magnitudes of the vectors are given by:

$$P = \left|\vec{\mathbf{P}}\right| \qquad Q = \left|\vec{\mathbf{Q}}\right| \qquad E = \left|\vec{\mathbf{E}}\right| \tag{4-66}$$

Again, τ is solved iteratively using the above set of equations. Once τ has converged form the unit vectors:

$$\bar{p} = \frac{\bar{P}}{P} \qquad \bar{q} = \frac{\bar{Q}}{Q} \qquad \bar{e} = \frac{\bar{E}}{E} \qquad (4\text{-}67)$$

From which we can calculate the geocentric direction of the planet corrected for light deflection:

$$\bar{p}_1 = \bar{p} + \left(\frac{2GM_o}{c^2}E\right)\frac{\left((\bar{p}\cdot\bar{q})\bar{e} - (\bar{e}\cdot\bar{p})\bar{q}\right)}{(1 + \bar{q}\cdot\bar{e})} \qquad (4\text{-}68)$$

where the dots indicate scalar products. Next calculate the proper direction of the planet in the geocentric inertial frame that is moving with a velocity V:

$$\bar{p}_2 = \frac{\left\{\beta^{-1}\bar{p}_1 + \left[1 + \frac{\bar{p}_1\cdot\bar{V}}{(1+\beta^{-1})}\right]\bar{V}\right\}}{\left(1 + \bar{p}_1\cdot\bar{V}\right)} \qquad (4\text{-}69)$$

Where the velocity V is defined as:

$$\bar{V} = \frac{\dot{\bar{E}}_B}{c} \qquad \beta = \sqrt{(1-V^2)} \qquad (4\text{-}70)$$

To obtain the apparent position as seen by the observer, we must multiply by the Rotation matrix R:

$$\bar{p}_3 = R\bar{p}_2 \qquad (4\text{-}71)$$

Where R is the product of the precession, P, and the nutation, N, matrices of Section 4.0.5. In calculating the matrix R, $t=0$ since the starting epoch is the standard equinox J2000.0 and T has the usual definition of the number of Julian centuries from J2000.0.

$$T = \frac{(\text{TDT} - 2451545)}{36525} \qquad (4\text{-}72)$$

and . Finally, the Right Ascension and Declination are found from the components of $\bar{p}_3 = (x,y,z)$:

$$\alpha = \tan^{-1}\left(\frac{y}{x}\right) \qquad \delta = \sin^{-1}z \qquad (4\text{-}73)$$

112

One can find the Right Ascension and Declination when using VSOP87D by first converting from the heliocentric spherical coordinate system (l, β, r), to the rectangular (x, y, z) system as discussed in Section 4.0.2. This is simply:

$$x = r\cos\beta\cos l - r_o\cos\beta_o\cos l_o$$
$$y = r\cos\beta\sin l - r_o\cos\beta_o\sin l_o \qquad (4\text{-}74)$$
$$z = r\sin\beta - r_o\sin\beta_o$$

Where the subscript o indicates Earth's coordinates. We iteratively solve for the light time using equation (4-74), the methods of Section 4.1.2, and:

$$\tau = \frac{\Delta}{c} \qquad\qquad \Delta = \sqrt{x^2 + y^2 + z^2} \qquad (4\text{-}75)$$

With Δ being the Earth-Planet distance. Converting back to ecliptic longitude and latitude:

$$l = \tan^{-1}\left(\frac{y}{x}\right) \qquad (4\text{-}76)$$

$$\beta = \tan^{-1}\left(\frac{z}{\sqrt{x^2 + y^2}}\right) \qquad (4\text{-}77)$$

The correction for aberration effects can be included by using the terms:

$$\Delta l = \frac{-\kappa \cdot \cos(l_{Sun} - l) + e \cdot \kappa \cdot \cos(\pi - l)}{\cos\beta} \qquad (4\text{-}78)$$

$$\Delta\beta = -\kappa \cdot \sin\beta \cdot \left[\sin(l_{Sun} - l) - e \cdot \sin(\pi - l)\right] \qquad (4\text{-}79)$$

where l_{Sun} is the ecliptic longitude of the Sun and we use the definitions:

$$e = 0.016708617 - 0.000042037 \cdot T - 0.0000001236 \cdot T^2 \qquad (4\text{-}80)$$

$$\pi = 102°.93735 + 0°.71953 \cdot T + 0°.00046 \cdot T^2 \qquad (4\text{-}81)$$

and the aberration constant $\kappa = 20".49552$. Hence, to correct for nutation, $\Delta\Psi$ from Section 4.04, and aberration add the corrections to equations (4-76) and (4-77):

$$l_2 = l + \Delta l + \Delta\psi \qquad (4\text{-}82)$$

$$\beta_2 = \beta + \Delta\beta \qquad (4\text{-}83)$$

Finally, we can convert to apparent Right Ascension and Declination:

$$\alpha = \tan^{-1}\left(\frac{\sin l_2 \cdot \cos\varepsilon - \tan\beta_2 \cdot \sin\varepsilon}{\cos l_2}\right) \tag{4-84}$$

$$\delta = \sin^{-1}(\sin\beta_2 \cdot \cos\varepsilon + \cos\beta_2 \cdot \sin\varepsilon \cdot \sin l) \tag{4-85}$$

An alternative formalism for aberration in equatorial coordinates defines the correction in Right Ascension, $\Delta\alpha$, and Declination, $\Delta\delta$, as:

$$\Delta\alpha = -\kappa\,\frac{\cos\alpha \cdot \cos l_{Sun} \cdot \cos\varepsilon + \sin\alpha \cdot \sin l_{Sun}}{\cos\delta} + e \cdot \kappa\,\frac{\cos\alpha \cdot \cos\pi \cdot \cos\varepsilon + \sin\alpha \cdot \sin\pi}{\cos\delta} \tag{4-86}$$

$$\Delta\delta = -\kappa \cdot \left[\cos l_{Sun} \cdot \cos\varepsilon \cdot (\tan\varepsilon \cdot \cos\delta - \sin\alpha \cdot \sin\delta) + \cos\alpha \cdot \sin\delta \cdot \sin l_{Sun}\right]$$
$$+ e \cdot \kappa \cdot \left[\cos\pi \cdot \cos\varepsilon \cdot (\tan\varepsilon \cdot \cos\delta - \sin\alpha \cdot \sin\delta) + \cos\alpha \cdot \sin\delta \cdot \sin\pi\right] \tag{4-87}$$

Where the same definitions apply. Using equations (4-76) and (4-77) the apparent Right Ascension and Declination would then be:

$$\alpha = \tan^{-1}\left[\frac{\sin(l + \Delta\Psi) \cdot \cos\varepsilon - \tan\beta \cdot \sin\varepsilon}{\cos(l + \Delta\Psi)}\right] + \Delta\alpha \tag{4-88}$$

$$\delta = \sin^{-1}\left[\sin\beta \cdot \cos\varepsilon + \cos\beta \cdot \sin\varepsilon \cdot \sin(l + \Delta\Psi)\right] + \Delta\delta \tag{4-89}$$

This alternative form can be applied to any derivation of Right Ascension and Declination.

4.1.6   CORRECTION FOR PARALLAX.

The final correction applied to an object's position is a correction for parallax. All the coordinates computed so far are for the geocentric observer. An observer on, or above, the surface of the Earth, topocentric, views the celestial sphere from a slightly shifted perspective. The rigorous formulae for parallax (Meeus 1991) are:

$$\alpha' = \alpha + \Delta\alpha \tag{4-90}$$

$$\delta' = \tan^{-1}\left[\frac{(\sin\delta - \rho\sin\varphi'\sin\pi)\cos\Delta\alpha}{\cos\delta - \rho\cos\varphi'\sin\pi\cos H}\right] \tag{4-91}$$

114

where the correction in Right Ascension is defined as:

$$\Delta\alpha = \tan^{-1}\left[\frac{-\rho\cos\varphi'\sin\pi\sin H}{\cos\delta - \rho\cos\varphi'\sin\pi\cos H}\right] \qquad (4\text{-}92)$$

with:

α' = Right Ascension corrected for parallax,
δ' = Declination corrected for parallax,
H = geocentric Hour Angle of the object,
ρ = geocentric radius,
φ' = geocentric latitude of the observer, and
π = parallax angle.

The parallax angle for any object is defined as:

$$\sin\pi = \frac{8''.794}{\Delta} \qquad (4\text{-}93)$$

where the distance, Δ, is defined as the object distance from Earth in AU.

The Earth's shape is not a perfect sphere and is slightly flattened at the poles. We account for this by using the shape of the reference geoid as defined by the IAU in 1976:

$$\rho\sin\varphi' = \frac{b}{a}\sin u + \frac{h}{6378140}\sin\varphi$$

$$\rho\cos\varphi' = \cos u + \frac{h}{6378140}\cos\varphi \qquad (4\text{-}94)$$

with h being the observers height above sea level (meters) and φ is the observer's geographic latitude. The Earth's equatorial radius, a, polar radius, b, and flattening coefficient, f, are defined as:

$$a = 6378.14 \, km \qquad (4\text{-}95)$$

$$b = a(1 - f) \qquad (4\text{-}96)$$

$$f = \frac{1}{298.257} \qquad (4\text{-}97)$$

and the associated angle, u, is:

$$\tan u = \frac{b}{a}\tan\varphi \qquad (4\text{-}98)$$

115

The geocentric Hour Angle, H, is found from:

$$H = \theta_o - \phi - \alpha \qquad \text{(4-99)}$$

Where ϕ is the observers true longitude west of Greenwich and θ_o is the apparent sidereal time at Greenwich and is defined, in degrees, from:

$$\theta_o = 100.46061837 + 36000.770053608 \cdot T + 0.000387933 \cdot T^2 - \frac{T^{\prime 3}}{38710000} + \Delta\psi \cdot \cos\varepsilon \qquad \text{(4-100)}$$

This formalism works for an observer on the surface of the Earth or a satellite in orbit provided the altitude above mean sea level and the latitude and longitude of the observer are known.

4.2 PLANETARY SATELLITES.

The current version of CBAMP includes the positions of the four Galilean satellites, Io, Europa, Ganymede, and Callisto (Meeus 1991). Positions are reckoned from Jupiter in terms of Jupiter radii.

Define the number of days from J2000.0:

$$d = TDT - 2451545 \tag{4-101}$$

The argument for the long-period term of Jupiter's motion:

$$V = 172°.74 + 0°.00111588 \cdot d \tag{4-102}$$

The mean anomalies of Earth, M, and Jupiter, N:

$$M = 357°.529 + 0°.9856003 \cdot d$$
$$N = 20°.020 + 0°.0830853 \cdot d + 0°.329 \cdot \sin V \tag{4-103}$$

The difference between the mean heliocentric longitudes of Earth and Jupiter:

$$J = 66°.115 + 0°.9025179 \cdot d - 0°.329 \cdot \sin V \tag{4-104}$$

Equations of the center of the Earth, A, Jupiter, B, and a phase, K:

$$A = 1°.915 \cdot \sin M + 0°.020 \cdot \sin 2M$$
$$B = 5°.555 \cdot \sin N + 0°.168 \cdot \sin 2N \tag{4-105}$$
$$K = J + A - B$$

The radius vector of the Earth, R (AU), of Jupiter, r (AU), and the Earth-Jupiter Distance, Δ (AU) are then given as:

$$R = 1.00014 - 0.1671 \cdot \cos M - 0.00014 \cdot \cos 2M$$
$$r = 5.20872 - 0.25208 \cdot \cos N - 0.00611 \cdot \cos 2N \tag{4-106}$$
$$\Delta = \sqrt{r^2 + R^2 - 2 \cdot r \cdot R \cdot \cos K}$$

The phase angle of Jupiter is then:

$$\sin \psi = \frac{R}{\Delta} \cdot \sin K \tag{4-107}$$

The planetocentric declination of Earth is found from:

$$D_E = D_S - 2°.22 \cdot \sin \psi \cdot \cos(\lambda + 22°) - 1.30 \cdot \frac{r - \Delta}{\Delta} \cdot \sin(\lambda - 100°.5) \qquad (4\text{-}108)$$

Where the heliocentric longitude of Jupiter, λ, and the planetocentric position of the Sun, D_S, are defined as:

$$\lambda = 34°.25 + 0°.083091 \cdot d + 0°.329 \cdot \sin V + B \qquad (4\text{-}109)$$

$$\eta_S = 3°.12 \cdot \sin(\lambda + 42°.8) \qquad (4\text{-}110)$$

The approximate angles from inferior conjunction are:

$$u_1 = 163°.8067 + 203°.4058643 \cdot \left(d - \frac{\Delta}{173}\right) + \psi - B \qquad (4\text{-}111)$$

$$u_2 = 358°.418 + 101°.2916334 \cdot \left(d - \frac{\Delta}{173}\right) + \psi - B \qquad (4\text{-}112)$$

$$u_3 = 5°.7129 + 50°.2345179 \cdot \left(d - \frac{\Delta}{173}\right) + \psi - B \qquad (4\text{-}113)$$

$$u_4 = 224°.8151 + 21°.4879801 \cdot \left(d - \frac{\Delta}{173}\right) + \psi - B \qquad (4\text{-}114)$$

From which we can calculate the angles u as measured from the inferior conjunction with Jupiter as:

$$u_{Io} = u_1 + 0°.473 \cdot \sin 2(u_1 - u_2) \qquad (4\text{-}115)$$

$$u_{Europa} = u_2 + 1°.065 \cdot \sin 2(u_2 - u_3) \qquad (4\text{-}116)$$

$$u_{Ganymede} = u_3 + 0°.165 \cdot \sin\left\{331°.18 + 50°.310482 \cdot \left(d - \frac{\Delta}{173}\right)\right\} \qquad (4\text{-}117)$$

$$u_{Callisto} = u_4 + 0°.841 \cdot \sin\left\{87°.40 + 21°.569231 \cdot \left(d - \frac{\Delta}{173}\right)\right\} \qquad (4\text{-}118)$$

These angles include the effects of the other satellites: Io as perturbed by Europa, and Europa perturbed by Ganymede. Ganymede and Callisto's orbits are non-circular and these

effects are seen in the additional terms. The distances to the center of Jupiter for each of the satellites in terms of Jupiter radii are:

$$r_{Io} = 5.9073 - 0.0244 \cdot \cos 2(u_1 - u_2)$$ (4-119)

$$r_{Europa} = 9.3991 - 0.0882 \cdot \cos 2(u_2 - u_3)$$ (4-120)

$$r_{Ganymede} = 14.9924 - 0.0216 \cdot \cos\left\{331°.18 + 50°.310482 \cdot \left(d - \frac{\Delta}{173}\right)\right\}$$ (4-121)

$$r_{Callisto} = 26.3699 - 0.1935 \cdot \cos\left\{87°.40 + 21°.569231 \cdot \left(d - \frac{\Delta}{173}\right)\right\}$$ (4-122)

Finally, the rectangular displacement from Jupiter's center are calculated, again in Jupiter radii as:

$$X_{Io} = r_{Io} \cdot \sin u_{Io}$$
$$Y_{Io} = -r_{Io} \cdot \cos u_{Io} \cdot \sin D_E$$ (4-123)

$$X_{Europa} = r_{Europa} \cdot \sin u_{Europa}$$
$$Y_{Europa} = -r_{Europa} \cdot \cos u_{Europa} \cdot \sin D_E$$ (4-124)

$$X_{Ganymede} = r_{Ganymede} \cdot \sin u_{Ganymede}$$
$$Y_{Ganymede} = -r_{Ganymede} \cdot \cos u_{Ganymede} \cdot \sin D_E$$ (4-125)

$$X_{Callisto} = r_{Callisto} \cdot \sin u_{Callisto}$$
$$Y_{Callisto} = -r_{Callisto} \cdot \cos u_{Callisto} \cdot \sin D_E$$ (4-126)

These distances are converted to angles projected into the CBAMP image plane and overlaid on the image near Jupiter. Figure 4-4 shows an image containing Jupiter and the four satellites.
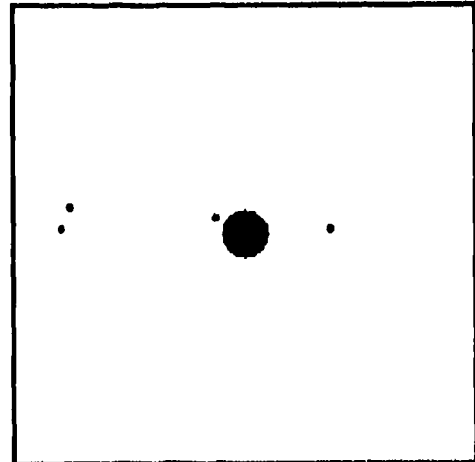
Figure 4-4. The satellites of Jupiter (enlarged for clarity) on 16.0 December 1992. From left to right Europa, Callisto, Ganymede, and Io.

119

4.3 ASTEROIDS.

Asteroids are numerous, moving, flux varying, celestial sources. In order to accurately portray the celestial background, one must be able to predict the location and flux for all previously cataloged asteroids plus produce an estimate of the total numbers to be expected as functions of location and flux at all wavelengths of interest. In order to arrive at the best possible estimate for these parameters, an updated version of the IRAS asteroid data base has recently been produced. This entailed reprocessing the raw IRAS data through essentially the same processing software used in creating the version of the IRAS asteroid data base currently available from the National Space Science Data Center, but using updated ground-based data and correcting several shortcomings in the original processing. These corrections included accounting for effects introduced by flux overestimation for low signal-to-noise sightings and correcting for the 12μm versus 25μm and 12μm versus 60μm albedo/diameter discrepancies.

Estimation of the total number of asteroids larger than a given, incompletely observed or currently unobservable size requires knowledge of the size-frequency distribution of the population. The question of the size-frequency distribution of the asteroids has long interested planetary scientists. Beginning in the 1980's the answer to this question became of more than academic interest. This was due to that fact that at wavelengths between 10 and 100μm asteroids are among the most numerous of bright celestial sources. With the advent of sensitive space telescopes, the radiation from these sources was recognized as being a significant component of the infrared sky.

IRAS used the fact that asteroids were moving sources of infrared radiation (relative to the "fixed stars") to avoid confusing them with other celestial infrared sources. This was accomplished by observing the same region of sky at intervals of weeks to months.

Future infrared satellites may be 100 to 1,000 times more sensitive than IRAS. In addition, they may operate primarily in a pointed, rather than all-sky-survey mode, and will therefore not be able to utilize the weeks and months confirmation strategy to weed out moving celestial sources. This problem is particularly acute for national defense satellites working at these wavelengths, where an assessment of the type of source (celestial versus man-made) must be made in near real-time. Here, a particular region of the sky will be observed over a short time scale searching for rapid motion.

The thermal spectra of asteroids in the middle part of the main asteroid belt peak between 10 and 20μm. The 25μm flux density observed by IRAS for the asteroid Ceres was about 850 Jy. Because Ceres is the largest asteroid (and, hence the brightest at 25μm), has a visual geometric albedo (p_H) near the middle of the range displayed by asteroids, and is located in the middle of the asteroid belt ($a = 2.7$ AU) it makes an ideal object from which to scale to smaller sizes.

Using 940 km as the diameter of Ceres and scaling down to 1 km allows us to estimate the 25μm flux expected from an asteroid of that size with a semi-major axis and visual geometric albedo corresponding to those for Ceres. Performing this calculation we find that such a 1 km asteroid would have a 25μm flux density of 0.74 mJy. The faintest 25μm sources in the IRAS Point Source Catalog have flux densities of about 170 mJy. Hence, IRAS was not troubled by 1 km main belt asteroids. A system 100 times more sensitive than IRAS, however, will routinely observe sources with flux densities on the order of 2 mJy; 1 km

asteroids are therefore a major source of concern to such systems, especially if such asteroids are numerous.

The present CBAMP includes known asteroids and calculates their fluxes. It does not attempt to compute and display the actual total number of asteroids which would be present in a real scene. The asteroid fluxes are determined using the "standard" thermal model (Lebofsky, et al., 1986). A size and a Bond albedo is determined from IRAS data or estimated depending on asteroid family. The family is determined by distance from the Sun, orbital inclination, and orbital eccentricity. Having determined to which asteroid group an asteroid belongs, the program randomly selects the geometric albedo for that object based on the albedo histogram, obtained from Dr. Mark Sykes, of group members.

Work is under way, using the as-yet-unpublished IRAS Minor Planet Survey (IMPS) data, to obtain a reliable asteroid size-frequency distribution. Preliminary results have been obtained by fitting a straight line to the log(Cumulative N) versus log(D) (in km) data for three different samples: all main belt (i.e., 2.06 < a <= 3.3 AU) asteroids, low albedo main belt asteroids, and moderate albedo main belt asteroids, are given in Table 4-12. The data used was restricted to log(D) bins between 1.5 and 2.1, inclusive. The form of the function fit to the data is given below:

$$\log(Cumulative\ N) = a + \{b \cdot \log(D)\} \tag{4-127}$$

Table 4-12. Size-Frequency Parameters for Main-Belt Asteroids.

Sample	Albedo Range	a	b	Corre. Coef.	Total Number with D> 1 km
All	0.01 - 0.35	5.49±0.10	-1.55±0.06	-0.997	310,000±74,000
Low p_H	0.01 - 0.10	5.32±0.10	-1.52±0.05	-0.997	210,000±48,000
Moderate p_H	0.01 - 0.35	5.03±0.14	-1.65±0.08	-0.995	110,000±35,000

These results indicate that there are about 300,000 asteroids in the main asteroid belt with diameters greater than 1 km. Asteroids inside the main belt (Aten's, Apollo's, Mars-crossers, and Hungaria group members) will contribute several thousand more and asteroids beyond the main belt (Cybele's, Hildas, and Trojans) about an additional 50%. Hence, the total number of asteroids with diameters greater than 1 km is on the order of 500,000.

Note that, due to incompleteness in the numbered asteroid population, this estimate represents a conservative lower limit. Other factors, for example a systematic flux overestimation for the smaller asteroids in the IRAS sample (which leads to an overestimation of their sizes), will also contribute to an underestimation of the total population with diameters greater than 1 km. The only factor which could result in a lower value is if there is another inflection (toward a shallower slope), similar to that which occurs near the 100 km size range, occurring at a diameter less than about 30 km, a region as yet very poorly sampled. However, it will require the next generation of Earth-orbiting infrared telescope, plus a significantly enhanced numbered population, to provide the data necessary to address this issue.

Reliable diameters are available for about half the known asteroids. From this sample one can compute the mean albedos for groups of asteroids found to have restricted ranges of albedos and then compute diameters for the remaining members of those groups using their known absolute magnitudes together with the adopted albedos. Groups of asteroids known to have restricted ranges of albedos include all taxonomic classes, most outer-belt asteroids, and many dynamical families. This procedure will permit determination of the range of albedos present among each such group and, thus, allow statistically reliable diameters to be determined for asteroids for which only visual data exist. For these asteroids the uncertainty in the albedos will be reduced to less than a factor of two compared with the potential range of a factor of ten.

Because size-frequency distributions differ for different asteroid orbital classes, e.g., among semi-major axis zones and Hirayama dynamical families, each such class requires a separate size-frequency distribution determination. Once a reliable size-frequency distribution is available for each significant asteroid orbital class, the different distributions can be summed to obtain the total number of asteroids with diameters greater than a given size. More importantly, for the CBSD application, one can use these results to generate orbital elements for each asteroid in each of the orbital element classes. Because the albedo range within each orbital class is much smaller than for the population as a whole, realistic albedos can also be assigned to each of these asteroids. The albedo together with the diameter then uniquely determines the absolute magnitude and, hence, the flux.

Generation of the statistical asteroid orbital element file, described in the preceding paragraph, will give us the ability to generate a scene containing all asteroids with fluxes above a given threshold using the same code presently used to predict the position and flux of known asteroids. The same can also be done for visual magnitudes using existing code which is used to generate ephemerides for ground-based telescopic observations. (A typical 1 km diameter main-belt asteroid has a visual magnitude of about 22.) In practice, the accuracy of this prediction is limited by the knowledge of the asteroid's color and the phase function at the particular wavelength.

Existing photometric data are sufficient to estimate the magnitude difference, with respect to the V band, for bands between 0.35 and 2.2μm. Refinement of these estimates and extension to shorter and longer wavelengths will be possible given data from the MSX UVISI and SPIRIT III experiments.

The orbital elements for the currently numbered population will be extended from the 4,559 at the present epoch of osculation, now in the CBSD, to the number known at the end of each year and at epochs of osculation between 1990 and 2000 AD. These orbital elements will be obtained as a special product, made at our request, by the International Astronomical Union's Minor Planet Center. This will enable us to accurately place (i.e., to within 1-to-2 arc-seconds) all known asteroids (currently numbering about 5,500) for any date between 1990 and 2000.

For CBAMP, 41 data files exist with names of the form J244xxxx.BIN. These contain the standard equinox B1950.0 osculating elements for the first 4,559 numbered asteroids on 200 day intervals starting at JD 2444400.0 (1970). The date of observation must fall within the 200 day interval of the file to provide an accurate position. The output log for CBAMP gives the number of days the elements are away from the osculating elements epochs. This is provided to the user as an indication of the accuracy with which the asteroids' positions have been calculated. The osculating elements produce positions that are most accurate when

the date is close to the epoch of the elements. The farther from the date the poorer the position determinations become. Date that are more than 200 days from the epoch of the osculating elements must be considered unreliable.

To proceed the elements must first be precessed from B1950.0/FK4 to J2000.0/FK5. The elements a and e are not dependent on the equinox chosen. Defining the initial system as i_o, ω_o, and Ω_o and the final elements as i, ω and Ω. We first define the angles

$$L' = 4°.50001688$$
$$L = 5°.19856209 \qquad \text{(4-128)}$$
$$J = 0°.00651966$$

Then the inclination, i, and the longitude of the ascending node, Ω, can be found from:

$$\cos i = \cos i_o \cdot \cos \eta + \sin i_o \cdot \sin \eta \cdot \cos(\Omega_o - \Pi)$$
$$\sin i \cdot \sin(\Omega - \Pi - p) = \sin i_o \cdot \sin(\Omega_o - \Pi) \qquad \text{(4-129)}$$
$$\sin i \cdot \cos(\Omega - \Pi - p) = -\sin \eta \cdot \cos i_o + \cos \eta \cdot \sin i_o \cdot \cos(\Omega_o - \Pi)$$

The new argument of perihelion, ω, is found from:

$$\omega = \omega_o + \Delta\omega$$
$$\sin i \cdot \sin \Delta\omega = -\sin \eta \cdot \sin(\Omega_o - \Pi) \qquad \text{(4-130)}$$
$$\sin i \cdot \cos \Delta\omega = \sin i_o \cdot \cos \eta - \cos i_o \cdot \sin \eta \cdot \cos(\Omega_o - \Pi)$$

Once the new osculating elements have been determined it is required to calculate the geocentric rectangular equatorial coordinates as described in Section 4.0.3 for the mean equator and equinox of J2000.0.

Using either VSOP87D or DE/LE-200 we can calculate the Sun's geocentric rectangular coordinates with which the Right Ascension, Declination, and Earth-object distance can be calculated:

$$\alpha = \tan^{-1} \frac{Y_{Sun} + y}{X_{Sun} + x} \qquad \text{(4-131)}$$

$$\Delta = \sqrt{(X_{Sun} + x)^2 + (Y_{Sun} + y)^2 + (Z_{Sun} + z)^2} \qquad \text{(4-132)}$$

$$\delta = \sin^{-1} \frac{Z_{Sun} + z}{\Delta} \qquad \text{(4-133)}$$

The position is precessed to the epoch of the observation and using the methodology set forth in Section 4.1.5 and 4.1.6 we can apply nutation, aberration, and parallax effects to the position to find the apparent position for a topocentric observer.

Table 4-13. Mean errors and standard deviations of the four brightest asteroids calculated from 27 comparisons during the years 1989, 1990, and 1992.

	Mean error in Right Ascension (seconds of time)	Standard Deviation of Mean	Mean Error in Declination (seconds of arc)	Standard Deviation of Mean
1 Ceres	-0.09	0.16	0.1	0.8
2 Pallas	0.03	0.06	-0.2	0.8
3 Juno	-0.03	0.06	-0.3	0.5
4 Vesta	0.07	0.08	0.2	0.6

Table 4-13 gives the mean errors in Right Ascension and Declination for 27 dates during 1989, 1990, and 1992 as compared with *The Astronomical Almanac*. The errors are calculated in the sense CBAMP minus *Almanac* and are for the geocentric astrometric positions for the equator and equinox of J2000.0. The Sun's position has been calculated using DE/LE-200. *The Astronomical Almanac* reports positions to 0.1 seconds of time in Right Ascension and 1 second of arc for Declination. The errors quoted in Table 4-13 are then well within the precession reported in the *Almanac*. Also, *The Astronomical Almanac* uses a single set of osculating elements for the entire year; CBAMP, on the other hand, uses elements 200 days apart. The positions, at least for these four asteroids, are well within the 2" requirement of CBSD. This demonstrates that the methodology used is basically correct and the accuracy of the position is determined by the accuracy of the osculating elements.

4.4 FLUX CALCULATIONS.

The flux from all objects in the solar system, other than the Sun, is composed of two components; thermal emission and reflected light:

$$L = L_{Thermal} + L_{Reflected} \tag{4-134}$$

The thermal component can be written as:

$$L_{Thermal} = f \cdot \varepsilon \cdot \left(\frac{4\pi \cdot hc}{\lambda^3}\right) \cdot \left(\frac{r}{R_{Geo}}\right)^2 \int_0^1 \frac{\mu}{\left(e^{\frac{hc}{\lambda k T_{\mu}^{0.25}}} - 1\right)} d\mu \tag{4-135}$$

Where:

f	= fraction of disk illuminated by Sun,
ε	= emissivity,
h	= Planck constant,
c	= speed of light,
λ	= central wavelength of passband,
μ	= $\cos(\phi)$ = angle from subsolar point to point of interest,
$T_{Subsolar}$	= temperature at the subsolar point, and
k	= Boltzmann's constant.

The disk fraction is simply:

$$f = \frac{1}{2}(1 + \cos \iota) \tag{4-136}$$

with:

$$\cos \iota = \frac{R_{Geo}^2 + R_{Sun}^2 - R_{Earth}^2}{2 R_{Geo} \cdot R_{Sun}} \tag{4-137}$$

Where:

R_{Geo} = true Geocentric distance of object,
R_{Sun} = heliocentric distance of object, and
R_{Earth} = true Earth-Sun distance.

The received flux for the scattering (reflected light) case can be written:

$$L_{Received} = \pi^2 \left(\frac{r_{Sun} \cdot r}{R_{Geo} \cdot R_{Sun}}\right)^2 \cdot \varepsilon \cdot S \cdot f \tag{4-138}$$

here:

r_{Sun} = radius of Sun,
r = radius of object, and
S = solar flux.

where the band limited solar flux is defined as:

$$S = \frac{\int_{\lambda_1}^{\lambda_2} B_\lambda(T) \cdot \phi(\lambda)\, d\lambda}{\int_{\lambda_1}^{\lambda_2} \phi(\lambda)\, d\lambda} \tag{4-139}$$

and:

$B_\lambda(T)$ = Blackbody function,
T = Solar surface temperature = 5770°K,
$\phi(\lambda)$ = bandpass response function,
λ_1 = bandpass short wavelength cutoff, and
λ_2 = bandpass long wavelength cutoff.

For this implementation of CBAMP we have assumed that

$$\phi(\lambda) = 1 \tag{4-140}$$

and therefore:

$$\int_{\lambda_1}^{\lambda_2} \phi(\lambda)\, d\lambda = \Delta\lambda = \lambda_2 - \lambda_1 \tag{4-141}$$

Lambertian scattering has also been assumed so:

$$L_{Reflected} = \frac{L_{Received}}{\pi} \tag{4-142}$$

When implementing the scattering for resolved objects we take the above scattering as the "full face" scattering and the phase correction is taken as 1. We divide the scattering intensity by the total number of resolvable pixels on the surface. When calculating the intensity at a point we take into consideration that we may not see the entire surface and include scattering only on the visible, sunlit side.

The temperature of the subsolar point ($T_{Subsolar}$) is defined for the moon and the asteroids as:

$$T_{Subsolar} = \left[\frac{(1-\alpha)F}{\varepsilon\sigma\eta R_{SUN}^2} \right]^{\frac{1}{4}} \tag{4-143}$$

126

with:

α = Bond albedo,
F = Solar constant at 1 A.U. = 0.1368 W/m²,
η = beaming parameter = 0.756,
ε = emissivity, and
σ = Stefan-Boltzmann constant.

For the Moon, when the surface element is shaded from the Sun, the dark side temperature is taken T_{Dark} = 90°K, as the surface temperature.

For the planets, the temperature is taken as the equilibrium temperature. These temperatures are presented in Table 4-14.

Table 4-14. Brightness temperatures used in CBAMP.

Planet	Brightness Temperature	Planet	Brightness Temperature
Mercury	620.0°K	Saturn	82.4°K [a]
Venus	250.0°K	Uranus	53.0°K
Mars	270.0°K	Neptune	50.2°K
Jupiter	109.5°K [a]	Pluto	57.5°K [b]

(a) Pearl and Conrath (1991).
(b) Aumann and Walker (1987).

For the moon the thermal flux is calculated at each point so we have for a given point on the surface:

$$L_{Thermal} = \varepsilon \cdot \left(\frac{hc}{\lambda^3}\right) \cdot \frac{1}{(e^{\frac{hc}{\lambda kT}} - 1)}$$ (4-144)

$$T = \begin{cases} T_{Dark} & \text{Dark side} \\ T_{Subsolar} \cdot \mu^{\frac{1}{4}} & \text{Sunlit side} \end{cases}$$ (4-145)

For the validation effort we have taken disk integrated observations in the 1μm to 30μm regions and run CBAMP for the same date and time. Disk integrated observations, however, are scarce for the planets closer to Earth. To date, we have compared CBAMP to observations of Uranus, Neptune, Pluto, and one asteroid Vundtia. Table 4-15 provides the fluxes predicated for Uranus by CBAMP versus observations for five dates over nearly 20 years. Table 4-16 has four observations of Neptune compared with the CBAMP predictions.

Table 4-15. Uranus observations and CBAMP estimates of fluxes.

Date	Wavelength (μm)	Bandwidth (μm)	Flux Density (W/cm²/μm/sr)	CBAMP (W/cm²/μm/sr)
22 May 1966[a]	20	7.5	8×10^{-18} W/cm²/μm	2.44×10^{-18} W/cm²/μm
31 May 1983[b]	32	5	7.99×10^{-8}	7.71×10^{-8}
30 Apr 1984[b]	32	5	6.15×10^{-8} 6.03×10^{-8}	7.71×10^{-8}
1 May 1984[b]	32	5	5.59×10^{-8} 5.81×10^{-8}	7.71×10^{-8}
20 June 1985[b]	21	8	0.933×10^{-8}	1.20×10^{-8}

(a) Low, F., (1966).
(b) Orton, G. S. et al. (1987).

Table 4-16. Neptune observations and CBAMP estimates of fluxes.

Date	Wavelength (μm)	Bandwidth (μm)	Flux density (W/cm²/μm/sr)	CBAMP (W/cm²/μm/sr)
31 May 1983[a]	32	5	11.91×10^{-8}	12.19×10^{-8}
30 Apr 1984[a]	32	5	10.78×10^{-8} 10.65×10^{-8}	12.20×10^{-8}
1 May 1984[a]	32	5	10.36×10^{-8} 12.63×10^{-8}	12.20×10^{-8}
20 June 1985[a]	21	8	2.165×10^{-8}	1.43×10^{-8}

(a) Orton, G. S. et al. (1987).

Table 4-17 gives magnitudes and fluxes of Pluto from Lebofsky, et al. (1979) and results of IRAS observations in 1983 (Aumann and Walker 1987). We have taken the magnitudes quoted in the Lebofsky, et al. paper and using their 0 magnitude flux and band parameters converted them into fluxes. The J, H, K, and L measurements correspond to standard passbands. The last column gives the estimate from CBAMP on the same date. There are four assumptions made which cause the mismatch between observed and modeled:

1. We have assumed that the Sun is a perfect blackbody,
2. Pluto is considered a single object, not a two body system,
3. We have not included Earth's atmosphere, and
4. We have assumed that each bandpass is square, i.e., we do not use a spectral response function.

The last two assumptions both cause an overestimate of the flux, as is seen in all but one data point.

Table **4-17**. Observations of Pluto and CBAMP flux comparisons.

Date	Wavelength (μm)	Bandwidth (μm)	Magnitude	Flux (W/cm^2/μm)	CBAMP (W/cm^2/μm)
16 May 1977 (a)	2.20 (K)	0.57	12.90±0.05	$2.99 \cdot 10^{-19}$	$5.04 \cdot 10^{-19}$
"	3.46 (L)	0.93	$3.4^{-.03}_{+.037}$	$3.25 \cdot 10^{-20}$	$1.05 \cdot 10^{-19}$
"	3.73	0.40	$3.35^{-.047}_{.088}$	$2.54 \cdot 10^{-20}$	$7.92 \cdot 10^{-20}$
27 May 1977 (a)	2.20 (K)	0.57	12.9±0.05	$2.99 \cdot 10^{-19}$	$4.99 \cdot 10^{-19}$
"	3.46 (L)	0.93	13.3 2σ	$3.56 \cdot 10^{-20}$	$1.04 \cdot 10^{-18}$
31 May 1978 (a)	1.22 (J)	0.27	12.76±0.04	$2.92 \cdot 10^{-19}$	$3.01 \cdot 10^{-18}$
"	2.00	0.058	12.12±0.20	$8.71 \cdot 10^{-19}$	$6.89 \cdot 10^{-19}$
"	2.20 (K)	0.57	12.87±0.02	$3.08 \cdot 10^{-19}$	$5.07 \cdot 10^{-19}$
"	2.20	0.084	12.86±0.17	$3.05 \cdot 10^{-19}$	$5.04 \cdot 10^{-19}$
"	2.35	0.072	14.01 2σ	$8.26 \cdot 10^{-20}$	$4.04 \cdot 10^{-19}$
1 June 1978 (a)	1.22 (J)	0.27	12.81±0.03	$2.79 \cdot 10^{-18}$	$3.00 \cdot 10^{-18}$
"	1.50	0.089	12.56±0.10	$1.57 \cdot 10^{-18}$	$1.68 \cdot 10^{-18}$
"	1.63 (H)	0.47	12.82±0.03	$9.09 \cdot 10^{-19}$	$1.32 \cdot 10^{-18}$
"	1.70	0.120	13.26±0.15	$5.16 \cdot 10^{-19}$	$1.15 \cdot 10^{-18}$
"	2.00	0.058	12.22±0.12	$7.95 \cdot 10^{-19}$	$6.89 \cdot 10^{-19}$
"	2.11	0.099	12.55±0.14	$4.80 \cdot 10^{-19}$	$5.78 \cdot 10^{-19}$
"	2.20 (K)	0.57	12.98±0.04	$2.78 \cdot 10^{-19}$	$5.07 \cdot 10^{-19}$
"	2.20	0.084	13.35±0.21	$1.94 \cdot 10^{-19}$	$5.03 \cdot 10^{-19}$
"	2.35	0.072	13.16 2σ	$1.81 \cdot 10^{-19}$	$4.04 \cdot 10^{-19}$
16 Aug 1983 (b)	12.00	7.00	N.A.	$<2 \cdot 10^{-20}$	$1.14 \cdot 10^{-21}$
"	25.00	11.15	N.A.	$1.93 \cdot 10^{-20}$	$2.38 \cdot 10^{-20}$

(a) Lebofsky, et al. (1979).
(b) Aumann and Walker (1987).

To validate the asteroid flux thermal model we have used IRAS observations of the asteroid Vundtia (635). Table 4-18 gives the results of the model versus observations for two dates.

Table **4-18**. Comparisons of flux predictions of 635 Vundtia with IRAS observations.

635 Vundtia	Flux (Jy) at 12μm predicated/observed	Flux (Jy) at 25μm predicated/observed
27.30833 Apr 1983	3.46/2.45	6.75/6.96
5.32639 May 1983	3.18/2.27	6.22/6.45

We note that the model over-predicts the observations at 12μm and under-predicts the model at 25μm. However, overall the fit is seen as reasonable considering that the actual IRAS passbands were not taken into account.

4.5 CBAMP USER'S MANUAL.

4.5.0 INTRODUCTION.

The latest release of CBAMP is Version 3.25, 9 February 1993.

There are three operational modes for CBAMP. These are:

1) Run the planetary ephemeris calculation using VSOP87D.
2) Run the planetary ephemeris calculation using JPL's DE/LE-200.
3) Run with or without the asteroid position calculations.

4.5.1 INSTALLATION.

To install CBAMP, copy all files from the distribution media (tape, floppy disk, etc.) into a subdirectory on your system. This subdirectory may have any name but the rest of this document assumes the subdirectory name of *cbamp*.

For the IBM compatible PC, an executable file cbamp.exe is included along with binary versions of the data files and the user can skip the compiling and conversion steps. CBAMP has been written is ANSI standard FORTRAN. However, not all compilers use the same semantics for defining OPEN statements and a few other procedures. We have identified as many differences between systems as we can and have written the code to allow easy configuration. There are five FORTRAN files distributed with CBAMP, these are:

    CBAMP1.FOR
    CBAMP2.FOR
    ASC2BIN.FOR
    EPH.FOR
    TESTEPH.FOR

The file CBAMP1.FOR contains the main body of the CBZODY code. CBAMP2.FOR contains the machine specific routines. The files ASC2BIN.FOR and EPH.FOR convert ASCII data into binary form to take up less disk space. The file TESTEPH.FOR tests the integrity of the JPL database.

> STEP1: In the file CBAMP1.FOR is a parameter called SLASH. This parameter sets up the naming conventions for the output data files. On PC and compatibles the SLASH parameter is set to backslash, '\', corresponding to directory naming conventions. For UNIX systems, however, the SLASH parameter must be set to '/', the forward slash. Comment out the one not used by your system and be sure the slash character used by your system has no comment.

> STEP 2: The file CBAMP2.FOR contains all the machine or compiler specific routines. These are EPHOPN, INPUT, IMOPEN, and INOPEN. The first corresponds to the statements used by the JPL routines. A parameter called IRECSZ defines the record length in direct access files. Comment out column 1 for the statement IRECSZ=IRECSZ*4 if your system has a record length of 4

bytes (a Silicon Graphics workstation is an example). For PC's, leave this statement uncommented. The next three routines correspond to all I/O functions. Comment out the lines not used by your system. If your system requires different calls you will have to make these changes yourself. All efforts will be made to include system configurations as soon as they are known.

STEP 3: Likewise, in the file EPH.FOR and TESTEPH.FOR change the IRECSZ comment to match your system configuration.

STEP 4: Compile all the codes using your native FORTRAN compiler. To aid PC users a file called CBAMP.MAK has been included which contains the calls for the 32-bit version of the Lahey FORTRAN compiler. To aid Sun/UNIX users a makefile has been included for CBAMP. Three additional make files, named mk2bin, mkeph, and mktest are provided for ASC2BIN, EPH, and TESTEPH respectively.

STEP 5: 41 files of the form j244xxxx.ast are located on the distribution medium. These are the asteroid database files. Using ASC2BIN convert these to binary. The conversion code will check the existence of each file before proceeding. It is possible to run the conversion program with only a single database file. This may be useful for systems short on space and where only a single or perhaps limited range of dates will be run.

STEP 6: Use the JPL conversion program EPH to convert the planetary database file EPHTAP. When completed a file called JPLEPH will be created. To test the integrity of the database run the code TESTEPH. It will report if your database is corrupt or suffers from other problems.

STEP 7: Edit the file IDIRNAME to match the subdirectory name where your source and data files are stored. A sample file for PC user's has been included. A sample UNIX IDIRNAME file would contain:

> /files2/pauln/cbamp/

STEP 8:Create a subdirectory called AMP by

> md amp

for PC users, or

> mkdir amp

for UNIX users. For UNIX systems this must be lower case.

STEP 9: A sample input file has been included. Run the CBAMP code by:

> CBAMP

Several output files will be created. CBAMP.LOG is the complete log file of the run. FLUX.LOG contains details of the planetary flux calculations and provides the output in several different units. The PIXEL.LOG file is a listing of all pixels in the image, the x, y coordinates, the RA and Dec., the flux in Jy and Jy/sr. The image file is stored in the subdirectory AMP under the name CBAMPIMG.xxx where xxx is the sequence 000 to 999. The full path must exist, CBAMP will not create subdirectories.

4.5.2 INPUTS.

All inputs are read from a file called CBAMP.INP. This file consists of nine lines:

LINE 1)	256 256	number of pixels in x (columns) and y (rows) directions
LINE 2)	12.0 1.0	central wavelength and bandwidth in microns.
LINE 3)	4.44,8,1992	fractional day, month, year of observation.
LINE 4)	71.1,42.5	observer's latitude and longitude on the earth's surface degrees. Latitude +90 is N, -90 is south. Longitude -180 to +180 where positive is West of Greenwich.
LINE 5)	0.00	Observer altitude above mean sea level, meters
LINE 6)	UTC	Time stamp. Accepted time stamps are UTC, TDT, and UT1.
LINE 7)	15.	Right Ascension of center of image in degrees or a keyword. Accepted keywords are SUN, MOON, MERCURY, VENUS, MARS, JUPITER, SATURN, URANUS, NEPTUNE, and PLUTO.
LINE 8)	0.	Declination of center of image in degrees. Ignored if keyword is used.
LINE 9)	0.06667	pixels size, degrees/pixel

All images have a 256 byte header.

To run the basic model type:

        CBAMP

at the command line·

4.5.3   FORCING THE VSOP87D THEORY.

By default CBAMP uses the DE/LE-200 ephemeris code as long as the file JPLEPH exists and as long as the range is within 1950 to 2035. If the file does not exist or if the date is outside of the 1950 to 2035 range the VSOP87D theory is used. The VSOP87D theory can be forced in the 1950 to 2035 range by typing:

        CBAMP 3

4.5.4 ELIMINATING THE ASTEROID CALCULATIONS.

By default CBAMP runs the asteroid position code. This is the recommended mode of operation; however, if a user requires a quick calculation on the position of the Sun or the planets, CBAMP can be run without the asteroid calculation. To avoid running the asteroid component of CBAMP modify the command line with a 2:

> CBAMP 2

4.5.5 USING VSOP87D AND NOT RUN THE ASTEROIDS.

To run VSOP87D and not run the asteroid module type:

> CBAMP 4

4.5.6 FLOATING POINT OUTPUT.

Like other CBSD component modules, CBAMP allows for the generation of a floating point (4-byte) image. Normal operation is to produce a byte (8-bit) image. To force a floating point output use any of the command line inputs with a negative value:

> CBAMP -1
> CBAMP -2
> etc.

4.5.7 CBAMP DATA FILES.

The program has a number of required input data files. These are the planetary elements for the VSOP87D theory:

EARTH.DAT	MARS.DAT	URANUS.DAT
MERCURY.DAT	JUPITER.DAT	NEPTUNE.DAT
VENUS.DAT	SATURN.DAT	PLUTO.DAT

The elements for the DE/LE-200 model:

> JPLEPH

A file containing the planets basic physical data (size, mass. etc.):

> PLANETS.DAT

A file containing the periodic terms for the Moon:

> MOON.DAT

A file containing the dates of leap seconds added to make UTC conform with UT1:

DELTAAT.DAT

This file may have to be hand edited since the dates that leap seconds occur cannot be predicted. The information is found in *The Astronomical Almanac* published by the Naval Observatory or a similar publication.

The remaining files deal with the asteroid database.

NAMES_HG.DAT   ALBPROB.DAT
AST1989.002   U891001.AST

Including 41 files of the type

J2xxxxxx.BIN

which have their names contained in the file

DATA.DAT

The files J2xxxxxx.BIN are the asteroid element database.

4.6 ADDITIONAL VALIDATION.

As additional tests of the model CBAMP we have run the code against various celestial events. In particular we have run dates and locations for total and annular eclipses and mutual planetary conjunctions. Figure 4-5 gives a 10μm image of the total eclipse of 20 January 1990 12 minutes before second contact and Table 4-19 gives the circumstances of the eclipse. Table 4-20 is the input file CBAMP.INP used to generate the image and Table 4-21 gives the output file CBAMP.LOG and Table 4-22 is the output file FLUX.LOG. Figure 4-6 gives a 10μm image of the annular eclipse of 6 January 1990 and Table 4-23 gives the circumstances. For these two images the time was taken from the circumstances along with the observer latitude and longitude.

Table 4-19. Circumstances of 22 July 1990 Total Solar Eclipse, from the *1990 Astronomical Almanac*.

Total Eclipse 22 July 1990	U.T. d h m	Longitude ° '	Latitude ° '
Eclipse Begins	July 22 00 40.0	+ 60 59.9	+43 28.2
Central Eclipse begins	July 22 01 53.4	+ 23 42.2	+59 46.6
Greatest eclipse	July 22 02 36.7 JD 2448094.60885	+142 25.1	+73 28.1
Central eclipse ends	July 22 04 11.2	- 138 52.2	+29 56.5
Eclipse ends	July 22 05 24.5	- 165 15.4	+11 22.8

Table 4-20. Input file CBAMP.INP for Figure 4-5.

```
256 256
10.00 1
22.10,7, 1990
73.46833333,142.418333333
0.0
UTC
Sun
-19.59515
0.0058593
```
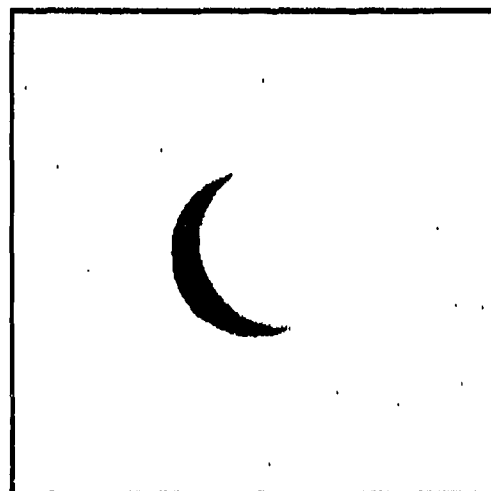

Figure 4-5. 22 July 1990 total solar eclipse 12 minutes before second contact.

135

Table 4-21. CBAMP.LOG file for the eclipse.

```
CBAMP - Version 3.19C - 10 November 1992
Image Size (columns,rows):   256   256
Wavelength (microns): 10.000
Coordinated Universal Time.
DATE:   22 July       1990
TIME:   2:24: 0.00000
 JD(UT1)    2448094.59998874
 JD(UTC)    2448094.60000000
 JD(TDT)    2448094.60065028
 JD(TDB)    2448094.60065026
 Using the DE/LE-200 Ephemeris Model.
 OBLIQUITY OF THE ECLIPTIC (DMS)    23   26  31.16944
 Nutation in obliquity (arc s)     5.29951
 Nutation in longitude (arc s)    14.74126
 EQUATION OF THE EQUINOX (sec)     0.90164
OBSERVER:
 Latitude (Degrees)       73.468
 Longitude (Degrees)      142.418
 Altitude above MSL (meters)           0.000
SUN DATA:
 Solar Longitude (DMS)  119   2 52.5739
 Solar Latitude  (DMS)    0   0  0.2206
 Solar Flux (Jy/sr) 1.4059E+17
           R.A.        DECLINATION
   App.    8   4 45.07    20 21  7.0
   J2000   8   5 18.12    20 19 21 8
   Parlx   8   4 45.08    20 21  0.1
 EARTH-SUN Distance (A.U.) = 1.016022
 ANGULAR DIAMETER OF SUN (ARC SECONDS)   = 1888.9
 Geocentric Rectangular coordinates of the Sun (X,Y,Z)
   For mean equator and equinox of J2000.0 (A.U.)
  -0.4953649   0.8138748   0.3528785
MOON DATA:
           R.A.        DECLINATION
   App.    8   4 15.4    21 10 28.
   J2000   8   4 48.7    21  8 50.
   Parlx   8   4 19.3    20 23 10.
 ANGULAR DIAMETER OF MOON (ARC SECONDS)   = 1942.8
 DISTANCE BETWEEN MOON-EARTH CENTERS (KM) = 369039.12
 FRACTION OF MOON ILLUMINATED  0.00
 MOONS PHASE ANGLE =179.2
 VISUAL MAGNITUDE OF THE MOON =      -2.1
 SUB-SOLAR TEMPERATURE OF MOON =   416.9
PLANET DATA:
```

PLANET		R.A.		DECLINATION	EARTH-PLANET DIST.	SUN-PLANET DIST.	PHASE ANGLE	FLUX (Jy/sr)
Pluto	15	8	4.55	-1 25 33.2	29.376	29.661	1.89	1.9016E+09
J2000	9	59	53.01	29 46 59.2				
Parlx	15	8	4.56	-1 25 33.5				
Neptune	18	55	3.33	-21 57 50.8	29.229	30.206	0.54	2.3667E+09
J2000	13	13	55.27	-6 13 38.2				
Parlx	18	55	3.33	-21 57 51.1				
Uranus	18	29	20.52	-23 35 58.2	18.472	19.416	1.14	5.6408E+09
J2000	12	49	44.70	-4 57 28.2				
Parlx	18	29	20.52	-23 35 58.5				
Saturn	19	32	48.25	-21 39 50.3	9.002	10.010	0.77	2.1981E+10
J2000	13	45	20.39	-10 16 51.8				
Parlx	19	32	48.25	-21 39 51.1				
Jupiter	7	43	51.01	21 32 30.5	6.235	5.224	0.98	2.1290E+11
J2000	1	54	33.93	11 29 47.4				
Parlx	7	43	51.01	21 32 29.4				
Mars	2	18	43.71	11 41 2.9	1.078	1.385	46.71	1.6410E+14
J2000	21	5	9.42	-19 42 44.7				
Parlx	2	18	43.55	11 40 55.3				
Venus	6	10	9.70	22 45 18.4	1.467	0.722	39.22	1.1209E+14
J2000	0	35	15.77	2 17 43.7				
Parlx	6	10	9.65	22 45 13.7				
Mercury	9	25	26.86	16 33 46.1	1.186	0.409	56.01	3.3831E+15
J2000	3	29	50.71	20 14 45.2				
Parlx	9	25	26.92	16 33 39.9				

FOUR BRIGHTEST SATELLITES OF JUPITER

NAME	RA			DEC			FLUX (Jy)
Io	7	43	55.1	21	32	31.	1.1270E-01
Parlx	7	43	55.1	21	32	29.	
Europa	7	43	43.2	21	32	31.	3.9632E-02
Parlx	7	43	43.2	21	32	29.	
Ganymede	7	43	53.3	21	32	31.	1.0308E+00
Parlx	7	43	53.3	21	32	29.	
Callisto	7	44	13.9	21	32	31.	1.6228E+00
Parlx	7	44	13.9	21	32	29.	

ASTEROID DATA:

Days from ephemeris: 94

FLUX JANSKY'S	ID	NAME		R ASCENSION H M SEC			DECLINATION D M SEC			RADIUS VECTOR	PHASE ANGLE
		Ceres	App.	9	14	1.18	22	59	27.50	3.517	
		Ceres	J2000	9	14	33.77	22	57	5.53		
		Pallas	App.	6	27	29.35	-1	34	34.16	2.997	
		Pallas	J2000	6	27	58.06	-1	34	57.01		
		Juno	App.	14	47	39.58	-2	5	44.85	3.014	
		Juno	J2000	14	48	8.94	-2	8	5.61		
		Vesta	App.	3	10	54.22	10	54	55.73	2.632	
		Vesta	J2000	3	11	25.08	10	57	2.94		
3.0083E-04	1097	Vicia		8	1	45.01	20	10	53.89	3.396	0.22
	1097		J2000	8	2	18.06	20	9	17.77		
	1097		Parlx	8	1	45.02	20	10	52.30		
5.9559E-04	2933	Amber		8	4	0.83	20	8	35.31	2.695	0.11
	2933		J2000	8	4	33.84	20	6	57.58		
	2933		Parlx	8	4	0.83	20	8	33.42		
1.0021E-06	3363	81EE10		8	1	52.84	20	27	55.67	2.502	0.28
	3363		J2000	8	2	25.94	20	26	19.46		
	3363		Parlx	8	1	52.84	20	27	53.68		
4.5124E-05	3563	81EO23		8	3	41.31	19	54	59.36	2.071	0.25
	3563		J2000	8	4	14.27	19	53	21.87		
	3563		Parlx	8	3	41.31	19	54	57.08		
1.0743E-05	3741	81EL33		8	2	6.14	20	11	1.68	2.869	0.23
	3741		J2000	8	2	39.18	20	9	25.31		
	3741		Parlx	8	2	6.14	20	10	59.07		
7.0533E-05	4476	83GU		8	4	38.90	20	53	27.99	3.030	0.18
	4476		J2000	8	5	12.06	20	51	49.82		
	4476		Parlx	8	4	38.90	20	53	26.27		
6.3265E-05	5365	87BJ2		8	2	2.52	19	56	13.85	2.183	0.36
	5365		J2000	8	2	35.51	19	54	37.52		
	5365		Parlx	8	2	2.52	19	56	11.65		
7.4832E-05	5899	98PZ1		8	7	21.40	20	37	3.74	3.529	0.19
	5899		J2000	8	7	54.48	20	35	23.66		
	5899		Parlx	8	7	21.40	20	37	2.20		
4.6315E-04	6414	2645PL		8	5	59.16	20	40	18.06	2.210	0.19
	6414		J2000	8	6	32.26	20	38	38.94		
	6414		Parlx	8	5	59.16	20	40	15.89		
4.5943E-05	6827	4070PL		8	6	57.21	20	17	42.36	2.265	0.23
	6827		J2000	8	7	30.22	20	16	2.56		
	6827		Parlx	8	6	57.22	20	17	40.22		
7.3613E-06	7544	6121PL		8	2	21.61	20	25	34.46	2.789	0.21
	7544		J2000	8	2	54.70	20	23	57.91		
	7544		Parlx	8	2	21.61	20	25	32.62		
7.2438E-07	8063	6878PL		8	4	35.23	19	41	10.51	2.847	0.24
	8063		J2000	8	5	8.14	19	39	32.38		
	8063		Parlx	8	4	35.24	19	41	8.68		
1.2544E-04	8269	1019T3		8	2	53.04	19	52	25.13	3.013	0.22
	8269		J2000	8	3	26.01	19	50	48.21		
	8269		Parlx	8	2	53.04	19	52	23.38		
4.2657E-05	8993	3748T3		8	7	47.16	20	51	54.57	3.468	0.25
	8993		J2000	8	8	20.29	20	50	14.19		
	8993		Parlx	8	7	47.17	20	51	53.02		

137

Table 4-22. Sample FLUX.LOG file

```
TDT      2448094.60065028
Pluto
 Brightness Temp.       40.0000000000000
 Thermal flux density (Jy)     0.509820368964781D-011
 Scattered flux density (Jy)     0.696188721148633D-003
 Phase angle (degrees)     1.89325647132860
 Radius (arcsecs)     0.704044323987063D-001
 Area (sr)     0.366015611406474D-012
 Number of pixels          1
 Total Flux density (Jy)     0.695998705459460D-003
 Total Flux (Jy/sr)     1901554698.13152
 Total Flux (w/cm2/um/sr)     0.570071756974296D-008
 Total Flux density (W/cm2/um)     0.208655162674510D-020
Neptune
 Brightness Temp.       50.2000000000000
 Thermal flux density (Jy)     0.454340507404328D-005
 Scattered flux density (Jy)     0.229625807532332
 Phase angle (degrees)     0.541922818929676
 Radius (arcsecs)     1.14626825215998
 Area (sr)     0.970224270486572D-010
 Number of pixels          1
 Total Flux density (Jy)     0.229625215284402
 Total Flux (Jy/sr)     2366723058.46610
 Total Flux (w/cm2/um/sr)     0.709525723102831D-008
 Total Flux density (W/cm2/um)     0.688399077088901D-018
Uranus
 Brightness Temp.       53.0000000000000
 Thermal flux density (Jy)     0.217058717464448D-004
 Scattered flux density (Jy)     1.49724137509036
 Phase angle (degrees)     1.13971804064361
 Radius (arcsecs)     1.89586737692684
 Area (sr)     0.265408919162602D-009
 Number of pixels          1
 Total Flux density (Jy)     1.49711497471238
 Total Flux (Jy/sr)     5640786223.14563
 Total Flux (w/cm2/um/sr)     0.169106516688936D-007
 Total Flux density (W/cm2/um)     0.448823778177632D-017
Saturn
 Brightness Temp.       82.4000000000000
 Thermal flux density (Jy)     12.7926836122152
 Scattered flux density (Jy)     124.309844123128
 Phase angle (degrees)     0.767221679158147
 Radius (arcsec )     9.19041863815230
 Area (sr)     0.623692031825353D-008
 Number of pixels          1
 Total Flux density (Jy)     137.096381977437
 Total Flux (Jy/sr)     21981422718.5488
 Total Flux (w/cm2/um/sr)     0.658986474713079D-007
 Total Flux density (W/cm2/um)     0.411004613359227D-015
Jupiter
 Brightness Temp.       109.500000000000
 Thermal flux density (Jy)     2569.64224690785
 Scattered flux density (Jy)     1349.07014457951
 Phase angle (degrees)     0.975562072420292
 Radius (arcsecs)     15.7876742025040
 Area (sr)     0.184050040607936D-007
 Number of pixels          1
 Total Flux density (Jy)     3918.42937898584
 Total Flux (Jy/sr)     212900163783.874
 Total Flux (w/cm2/um/sr)     0.638258634093702D-006
 Total Flux density (W/cm2/um)     0.117471527523312D-013
Mars
 Brightness Temp.       270.000000000000
 Thermal flux density (Jy)     269171.600433755
 Scattered flux density (Jy)     1710.91624950816
 Phase angle (degrees)     46.7071885634044
 Radius (arcsecs)     4.34076467281507
 Area (sr)     0.139133621730503D-008
 Number of pixels          1
 Total Flux density (Jy)     228316.991271046
 Total Flux (Jy/sr)     164099078591721.
 Total Flux (w/cm2/um/sr)     0.491956612654730D-003
```

```
      Total Flux density (W/cm2/um)      0.684477120163116D-012
Venus
  Brightness Temp.      250.000000000000
  Thermal flux density (Jy)       301366.896141059
  Scattered flux density (Jy)       348.244143546246
  Phase angle (degrees)      39.2205230679900
  Radius (arcsecs)      5.68749747999088
  Area (sr)      0.238859237075329D-008
  Number of pixels             1
  Total Flux density (Jy)       267729.652588476
  Total Flux (Jy/sr)      112086790474024.
  Total Flux (w/cm2/um/sr)      0.336027744255386D-003
  Total Flux density (W/cm2/um)      0.802633306289853D-012
Mercury
  Brightness Temp.      620.000000000000
  Thermal flux density (Jy)      2565725.03299845
  Scattered flux density (Jy)       9078.71003626154
  Phase angle (degrees)      56.0092279319746
  Radius (arcsecs)      2.83454484941957
  Area (sr)      0.593288967238636D-009
  Number of pixels             1
  Total Flux density (Jy)      2007135.95493436
  Total Flux (Jy/sr)      0.338306637366987D+016
  Total Flux (w/cm2/um/sr)      0.101421778373964D-001
  Total Flux density (W/cm2/um)      0.601724221469948D-011
```

Table 4-23. Circumstances of 4-5 January 1992 Total Solar Eclipse, from the *1992 Astronomical Almanac.*

Annular Eclipse 4-5 January 1992	U.T. d h m	Longitude ° '	Latitude ° '
Eclipse Begins	January 4 20 03.6	+151 38.1	+ 3 08.6
Central Eclipse begins	January 4 21 16.0	+137 07.3	+11 32.7
Greatest eclipse	January 4 23 14.7 JD 24448626.4685590107	- 167 27.2	+ 1 58.9
Central eclipse ends	January 5 00 53.1	- 117 45.2	+32 53.2
Eclipse ends	January 5 02 05.6	- 131 16.4	+24 42.5

Table 4-24. Input file CBAMP.INP for Figure 4-6.

```
256 256
10.00 1
4.9685590107,1, 1992
1.981666666,-167.453333333
0.0
UTC
Sun
-19.59515
0.0058593
```

Figure 4-7 gives a 2μm image of a mutual planetary occultation which occurred on 12-13 September 1170 as reported by the monk Gervase of Canterbury (Sinnott 1992). Table 4-25 is the input file used to generate Figure 4-7. Here Mars is seen to pass in front of the planet Jupiter. The observer is placed in London and the appearance is just as the planets rise above the horizon.
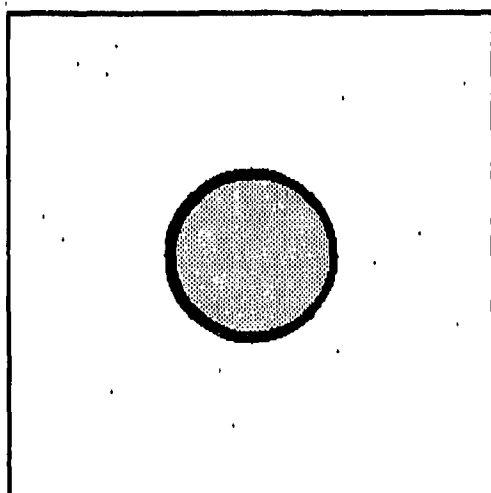
Figure 4-6. Annular eclipse of 4 January 1992 at mid eclipse.

Table 4-25. Input file CBAMP.INP for Figure 4-7.

```
256 256
2. 1.
12.85,9, 1170
52.,0.0
0.0
TDT
JUPITER
-19.59515
0.0005
```
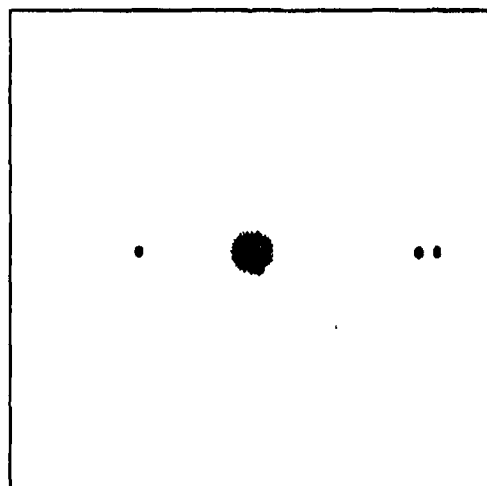

Figure 4-7. Mutual planetary occultation involving Mars and Jupiter in 1170.

Finally, the most recent mutual planetary occultation visible from Earth occurred on 3 January 1818. Figure 4-8 gives an L band (3.6μm) view of this occurrence and Table 4-26 is the input file.

Table 4-26. Input file CBAMP.INP for Figure 4-8.

```
256 256
3.6  0.70
3.91,1, 1818
52.,0.0
0.0
TDT
Jupiter
-19.59515
0.00015
```
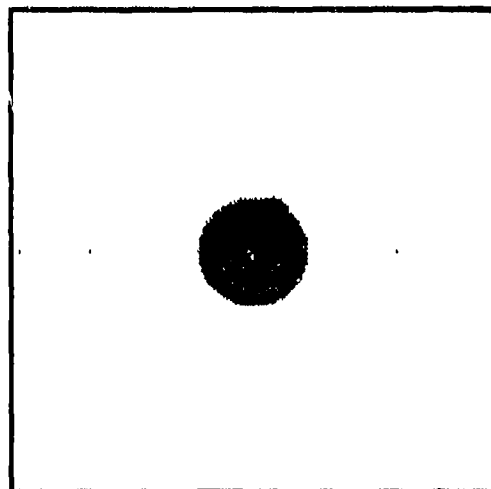

Figure 4-8. Mutual planetary occultation involving Venus and Jupiter on 3 January 1818, the most recent such occurrence visible from Earth.

141

4.7   REFERENCES

Aumann, H. H. and Walker, R. G. (1987), *Astronomical Journal*, **94**, 1088.

Bretagnon, P. (1982), *Astro. Astrophy.*, **114**, 278.

Bretagnon, P. and Francou, G. (1988), *Astron. Astrophy.* **202**, 309.

Chapront-Touze, M. and Chapront, J. (1983), *Astron. Astrophy.*, **124**, 50.

Chapront-Touze, M. and Chapront, J. (1988), *Astron. Astrophy.*, **190**, 346.

Goffin, E., Meeus, J., and Steyaert, C. (1986), *Astron. Astrophy.*, **155**, 323.

Goldstein, Herbert (1950), "Classical Mechanics", [Addison-Wesley, Reading, MA].

Herring, T.A. (1987), "Herrings Correction to the IAU 1980 Nutation Series", *BIH Annual Report for 1987* D-106.

Laskar, J. (1986), *Astronomy And Astrophysics*, **157**, 68.

Lebofsky, L. A., Rieke, G. H., and Lebofsky, M. J. (1979), *Icarus*, **37**, 554.

Lebofsky, L. A., Matson, D. L., Veeder, G. J., and Tedesco, E. F. (1986), in IPAC Report "Infrared Astronomical Satellite Asteroid and Comet Survey", ed. D. L. Matson.

Low, F. (1966), *Astrophysical Journal Letters*, **146**, 326.

Marion, Jerry B. (1965), "Classical Dynamics of Particles and Systems", [Academic Press, New York].

Meeus, J. (1991), "Astronomical Algorithms", [William Bell, Richmond, VA].

Orton, G. S., Baines, K. H., Bergstralh, J. T., Brown, R. H., Caldwell, J., and Tokunaga, A. T. (1987), *Icarus*, **69**, 230.

Pearl, J.C. and Conrath, B.J., (1991), *Journal of Geophysical Research, Supplement*, **96**, 18,921.

Seidelmann, P. K. (1992), "Supplement to the Astronomical Almanac", [University Science Books, Mill Valley, CA].

Sinnott, R. W. (1992), *Sky & Telescope, August*, 207.

Standish, E. M. (1985), *Astronomy And Astrophysics*, **233**, 252.

Yallop, B. D., Hohenkerk, C. Y., Smith, C. A., Kaplan, G.H., Huges, J.A., and Seidelmann, P.K. (1989), *Astronomical Journal*, **97**, 274.

5   THE INFRARED CIRRUS

5.0   INTRODUCTION

The 1983 mission of the Infrared Astronomical Satellite (IRAS) afforded an unprecedented view of the mid- and far infrared celestial emission over the entire sky. During its 10 month survey of the sky in four broad wavelength bands centered at 12, 25, 60 and 100µm, IRAS revealed an infrared background that was highly structured. The dominant components of the observed background included the broad diffuse emission associated with the Zodiacal plane, the Zodiacal dust bands, which are associated with the debris of asteroid collisions, diffuse emission associated with the Milky Way, and the highly structured, filamentary emission that has become known as the infrared cirrus.

During the past four years, we have carried out extensive investigations of the various infrared background components under contracts with the National Aeronautics and Space Administration and the United States Air Force Phillips Laboratory. The objective of these studies, which were based largely on the data collected by IRAS, has been to characterize the background components over a range of wavelengths and spatial scales, and to probe their physical properties. Per the terms of our contract with Mission Research Corp., SC-0014-88-0002, we have provided the results of these studies to MRC and consulted with them on the phenomenological validity of their models of the various infrared background components constructed for the Celestial Background Scene Descriptor (CBSD). We have given particular attention to the spatial and spectral characteristics of the infrared cirrus.

Of the many remarkable discoveries made by IRAS during its ten month mission, one of the most unexpected was that of highly structured diffuse emission that dominated the 100µm images of the sky. The similarity of these filamentary structures to terrestrial clouds led to their becoming known as the "infrared cirrus." While the cirrus is most prominent at 100µm, close examination of the IRAS image data revealed that the cirrus was also visible at the shorter wavelengths, although at much lower surface brightness and at lower contrast to the background. Low et al. (1984) determined from the 60-100µm colors of the cirrus that the infrared emission originated in clouds of dust in interstellar space that are emitting in thermal equilibrium with the ambient interstellar radiation field. It is the ubiquity of these diffuse interstellar clouds that compels us to characterize accurately their spatial and spectral properties. The filamentary cirrus clouds can be found over virtually the entire sky, and thus can affect any skyward looking detector system that operates at thermal infrared wavelengths.

Under contracts with NASA and the Air Force Phillips Lab, we have carried out a program to characterize the spatial distribution and physical composition of the infrared-emitting interstellar cirrus clouds. The program had several goals: 1) to develop an enhanced image database based on the IRAS Skyflux maps; 2) to probe the spatial distribution of the cirrus background both phenomenologically and in a quantitative manner using spatial Fourier Analysis; and 3) to examine the spectral properties of the cirrus with the objectives of understanding the empirical relationship between the 12 and 100µm emission and modeling the infrared emission from selected cirrus regions. We summarize the major findings of our cirrus investigations in the sections below.

5.1 DEVELOPING ENHANCED "CIRRUS MAPS"

Our investigations of the infrared emission from the cirrus background were based primarily on the IRAS Skyflux maps. The IRAS Skyflux database consists of three sets of 2-dimensional maps constructed from the three separate HCONs, or sky coverages, made by the satellite. Each HCON's data set is comprised of 12, 25, 60 and 100μm maps covering 16.5x16.5 deg^2, with 2'/pixel effective resolution. In principle, the images from the three HCON's could be added together to improve the signal-to-noise of the faint cirrus emission, particularly in the 12 and 25μm data where the cirrus emission is exceedingly faint. Unfortunately, the raw Skyflux plates are dominated by strong background emission from the Zodiacal plane and linear, fixed-pattern artifacts which are the result of background offset and gain variations in individual IRAS detectors. The intensity and geometry of these background and noise features not only mask the small-scale structure of the faint cirrus emission, they also differ significantly between the three HCONs, thus making coaddition impossible. Therefore, to assess accurately the spatial and spectral characteristics of the cirrus emission, particularly at the shorter wavelengths where the cirrus appears at very low contrast, it was necessary to develop techniques to eliminate these various noise and background features in the IRAS Skyflux maps.

5.1.1 IMAGE DESTRIPING AND DEWAVING.

The most prominent fixed pattern noise features present in the raw Skyflux data are high spatial frequency linear artifacts known as the image "stripes." The stripes are oriented along the satellite's scan direction and can be several pixels wide. There is also a lower frequency, lower intensity component of the stripes that is known as "waves." The wave features can have widths of 40 - 50 Skyflux pixels. Complicating removal of the stripes and waves is the fact that on high ecliptic latitude Skyflux images, there are usually groups of stripes and waves running in several directions because of the satellite's scan angles converged toward the ecliptic poles.

An image-based "destriping" and "dewaving" procedure for the raw Skyflux maps was developed at the University of Arizona. This procedure was designed to exploit the large linear coherence of the stripes and waves to generate a high signal-to-noise "stripe map." This map is then subtracted from the raw Skyflux image to leave a destriped image. Because the stripe map could be examined independently from the sky image, it was possible to "tune" the procedure to avoid removing true astronomical features. Custom software routines to carry out this procedure were written under the environment of the Image Reduction and Analysis Facility (IRAF) of the National Optical Astronomy Observatories. The steps involved in the destriping procedure are listed in Table 5-1.

Removal of the lower spatial frequency waves was accomplished using a procedure that was completely analogous to the destriping procedure. The primary difference between the two was that the dewaver utilizes larger filter bandpasses, as would be expected from the relative spatial scales of the stripes and waves.

144

TABLE 5-1. Image Plane Destriping Procedure.

A.	Rotate the raw Skyflux image such that the stripes run horizontally.
B.	Median filter the image in one-dimension along the stripes. This eliminates the signatures of real celestial sources such as stars, galaxies and small-scale modulations in the cirrus. The critical feature of this step is selecting the pixel bandpass of the filter.
C.	Run a one-dimensional "min-max" filter orthogonal to the stripe direction (along each column). This filter searches for subsequent minima and maxima associated with the stripe pattern, and evaluates the average between them. A spline fit is made to this average along each column, and the individual fits are combined to form a two-dimensional stripe map. This procedure filters out the true broad structure in the sky background, and leaves a stripe map with zero net intensity.
D.	Subtract the stripe map from the raw image to produce a destriped Skyflux map with the radiometric information intact.

5.1.2. COMPARATIVE ANALYSES OF IMAGE PLANE AND FOURIER DESTRIPERS.

A destriping procedure for the raw IRAS Skyflux maps was also developed by Mission Research Corporation during the course of this program. The fundamental difference between the Arizona, and MRC destripers was that the latter operated on the Fourier transform of the Skyflux maps. Both destripers appeared to do an adequate job of removing the stripe artifacts and each produces aesthetically pleasing cleaned images. However, it was most important to gauge how well the radiometric and structural integrity of the infrared background features are preserved through the processing. To this end, we carried out a comparative analysis of the two procedures. This performance evaluation was submitted as part of CBSD Annual Report No. 1, under Air Force contract No. F19628-88-C-0014. We summarize the results briefly here.

The performance of the three destripers was tested by comparing the raw and processed 12, 25, 60 and 100μm images of IRAS Skyflux plate 96 ($\alpha=01^h00^m$ $\delta=+0°00'$). Plate 96 was chosen as the test bed since it contains prominent cirrus and well-defined stripes that run in only a single direction. The raw Skyflux images were destriped using the Arizona and MRC software packages. The intensity along 24 equally spaced columns in the raw and destriped images was then extracted parallel to the stripe direction so that residual stripe noise would not effect the comparison. Finally, the ratio of the raw image intensity to that in each of the destriped image columns was then formed. In Figures 5-1 and 5-2 are shown the ratios along a column near the center of the images. A perfect destriper would produce a mean intensity ratio of unity along each of the extracted columns. Deviations from unity imply that the destriping procedures alter the radiometry of the maps and introduce or suppress real structure. Qualitative examination of the raw-to-destriped intensity ratios along each column indicate that the ratio of the raw-to-destriped image intensity occasionally exceeds unity for all of the destriper results. In the case of the Steward image-based destriper, this is probably a result of using a median filter to smooth the stripes, thus leading to slight overestimation of the strip intensity in certain locations. The reason for the over-correction in the Fourier

145
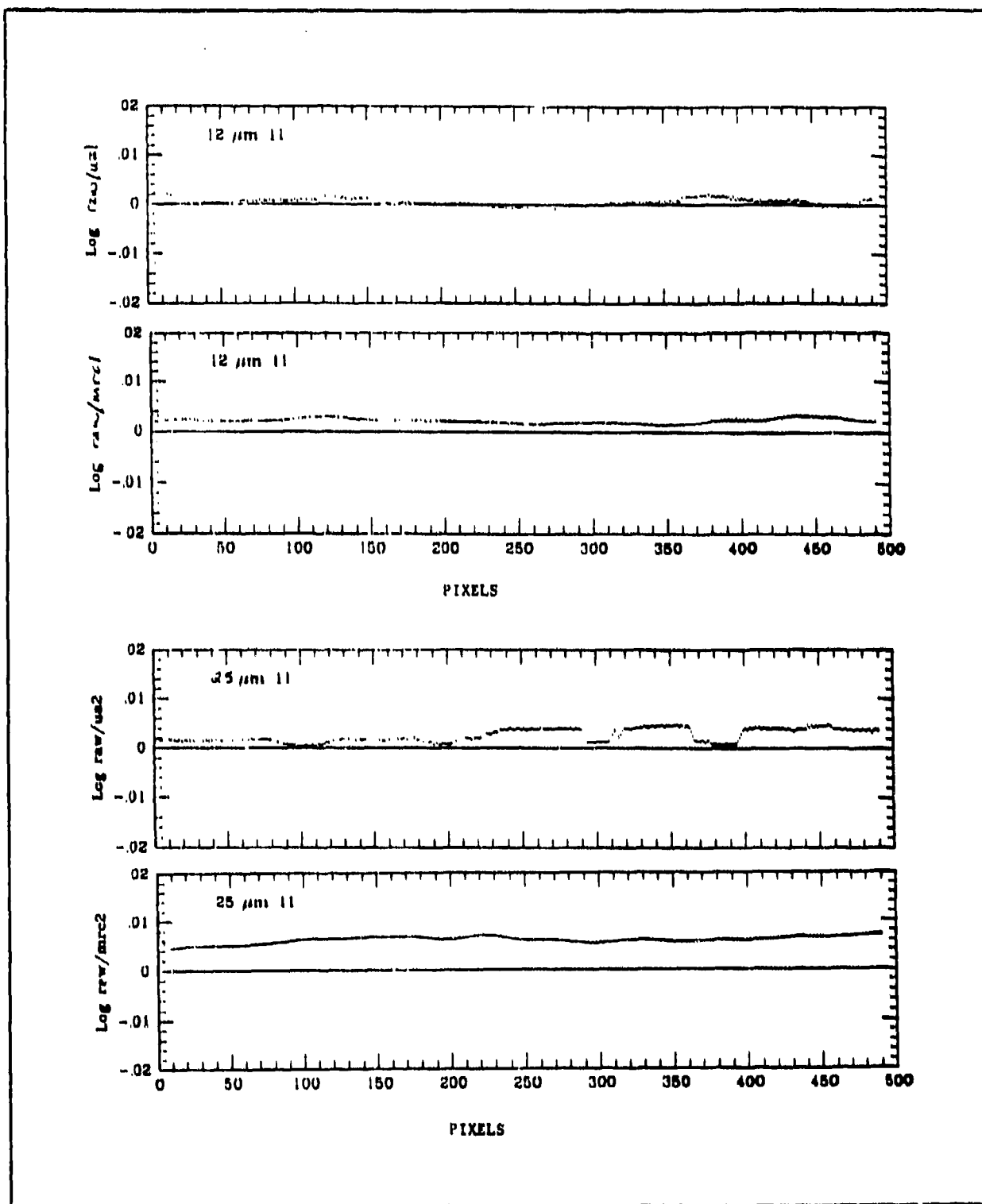
Figure 5-1. (top) The ratio of the raw-to-destriped pixel values along a column of the 12μm IRAS Skyflux plate 96 for the UA destriped (upper) and MRC destriper (lower). (bottom) The pixel ratios from the destriped 25μm images.
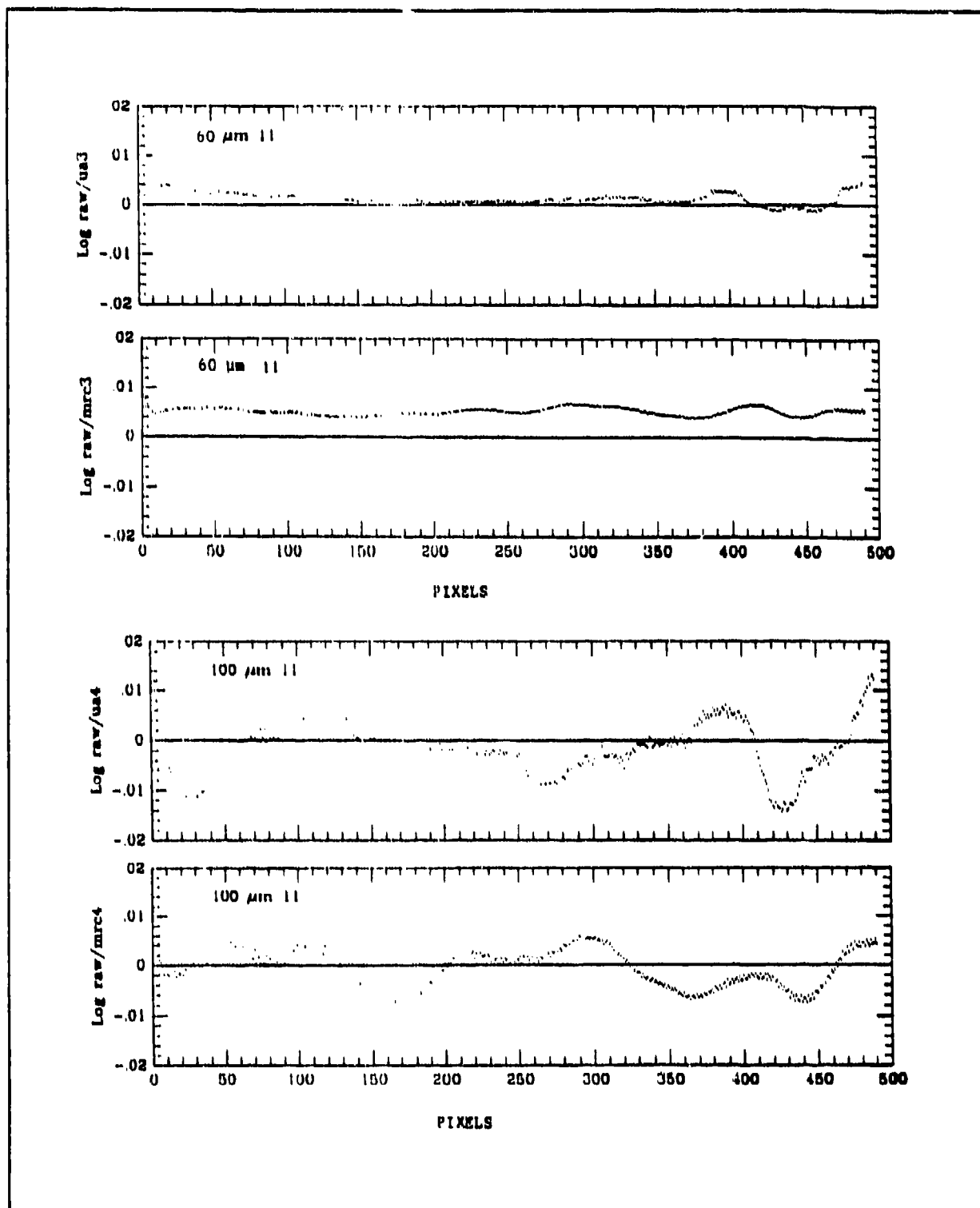
Figure 5-2. (top) The ratio of the raw-to-destriped pixel values along a column of the 60µm IRAS Skyflux plate 96 for the UA destriped (upper) and MRC destriper (lower). (bottom) The pixel ratios from the destriped 100µm images.
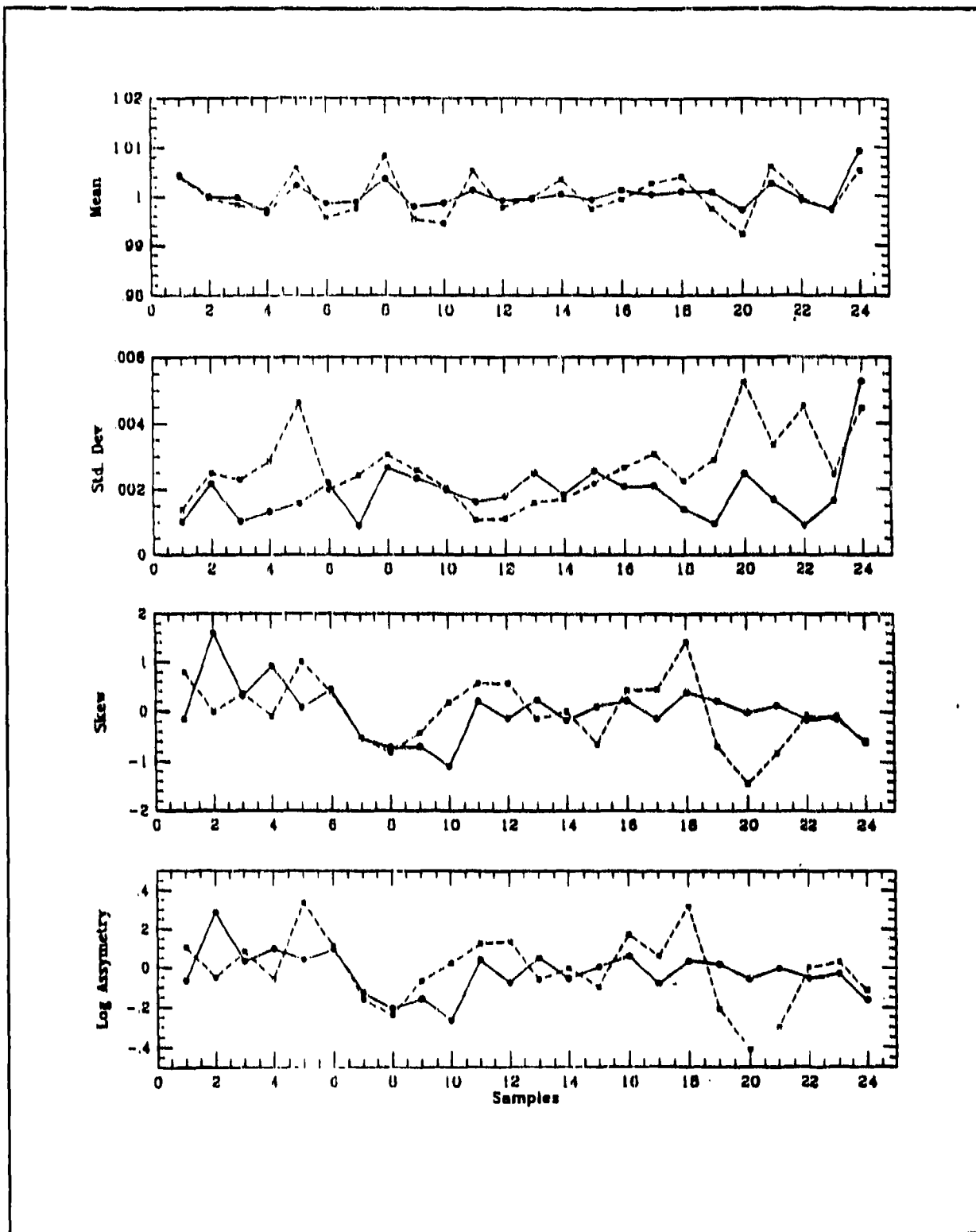
Figure 5-3. The mean, standard deviation, skewness and asymmetry of the distribution of raw-to-destriped pixel ratios values along 24 columns in the 12µm IRAS Skyflux plate 96.

148
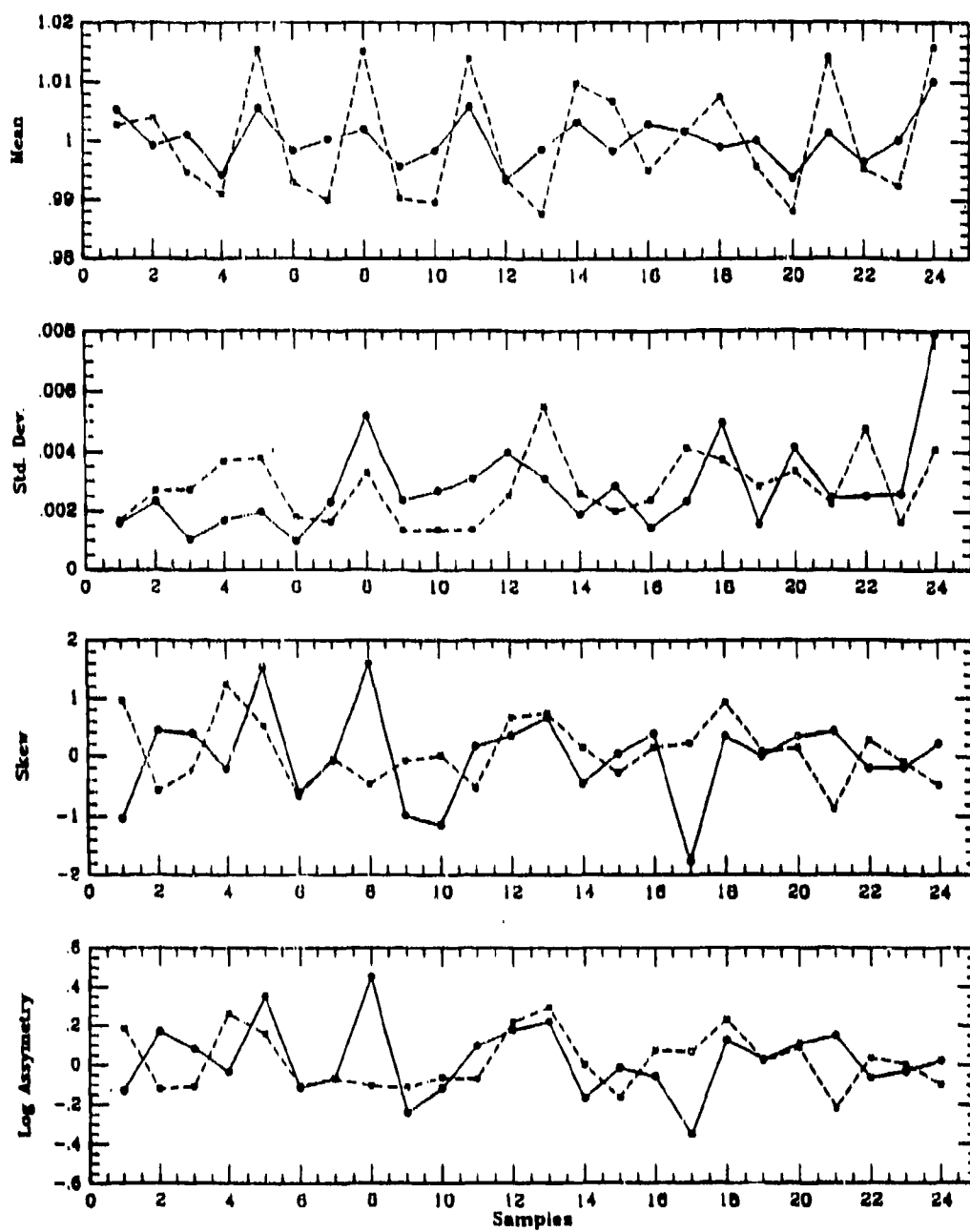
Figure 5-4. The mean, standard deviation, skewness and asymmetry of the distribution of raw-to-destriped pixol ratios values along 24 columns in the 25μm IRAS Skyflux plate 96.

149
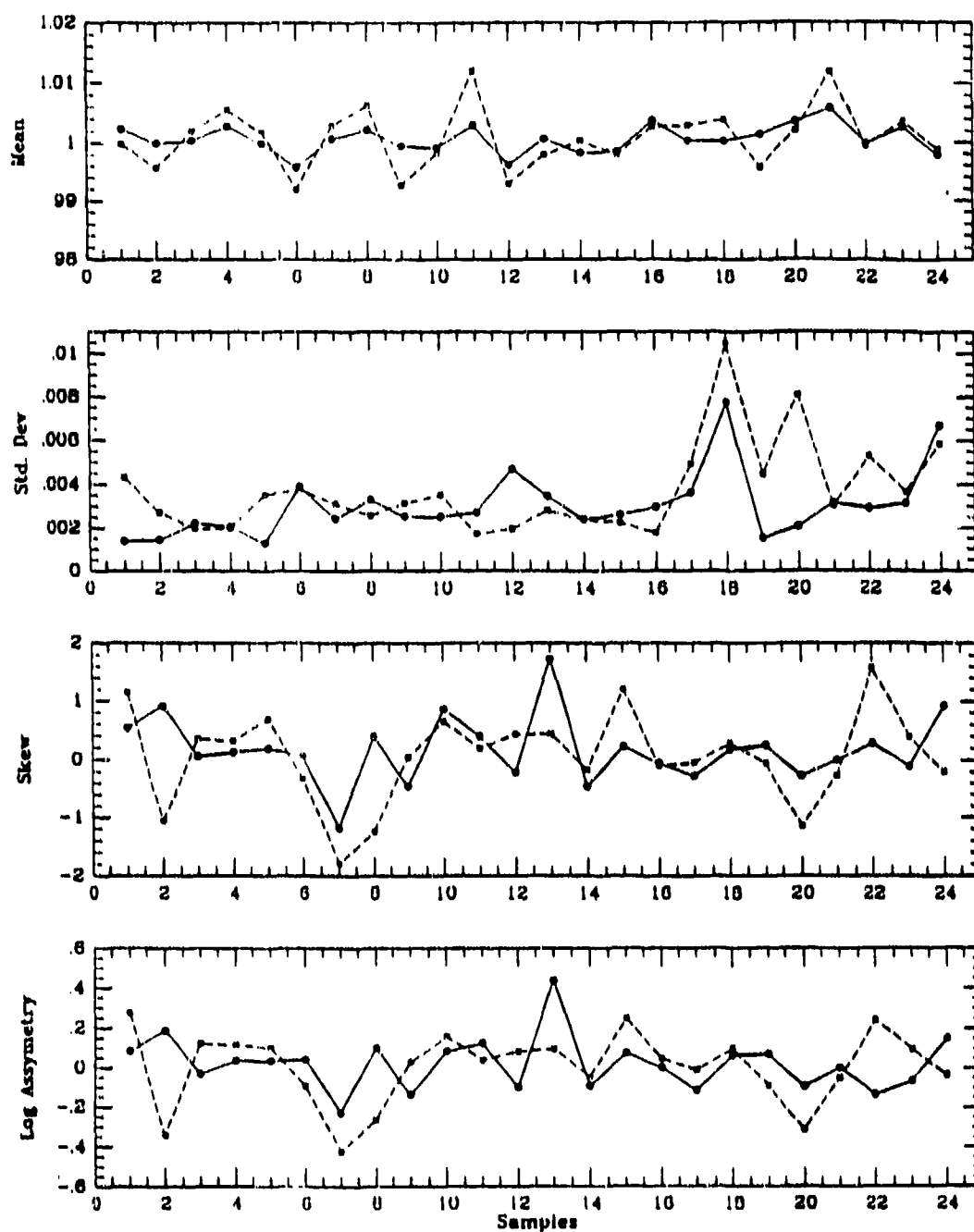
Figure 5-5. The mean, standard deviation, skewness and asymmetry of the distribution of raw-to-destriped pixel ratios values along 24 columns in the 60μm IRAS Skyflux plate 96.

150

Figure 5-6. The mean, standard deviation, skewness and asymmetry of the distribution of raw-to-destriped pixel ratios values along 24 columns in the 100µm IRAS Skyflux plate 96.
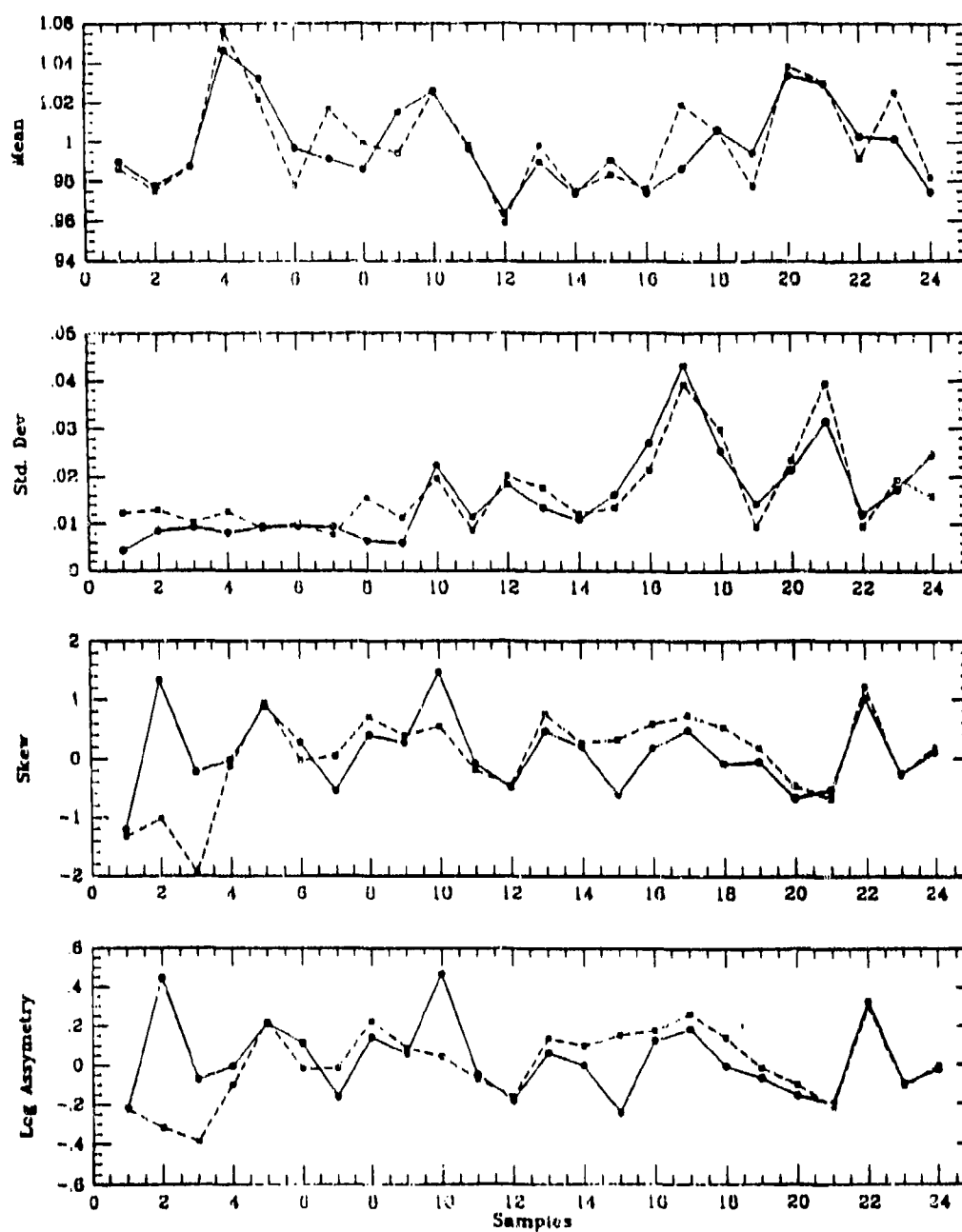
151

destriper is not obvious. In addition, each of the destripers produce a "roll-off" at the edges of the images. However, the roll-off is much more severe in the Fourier process than in the image plane destriper.

A more quantitative assessment of the two destripers was made by examining the distribution of the raw-to-destriped intensity ratios along each column. Histograms of the distributions generally had considerable breadth, and were frequently centered at values less than unity. The location of the central peak of the distributions, the width and the asymmetry provide measures of the effects of the destripers. These quantities are simply the first, second and third statistical moments of the distributions, better known as the mean, standard deviation and skewness of the distributions. The statistical moments were evaluated along each column of ratios for the 12, 25, 60 and 100µm images, as was an additional parameter, the asymmetry of the distributions. The asymmetry was defined to be the standard deviation from the mean of all points greater than the mean divided by the standard deviation of all points less than the mean. If the width of the distributions is 20% greater on the right side than on the left, then the asymmetry has a value of 1.20. A perfectly symmetrical distribution has asymmetry = 1.0.

The moments of the distributions show that neither the image-plane destriper nor the Fourier destriper seriously compromises the radiometric properties of the Skyflux maps. The mean values of the raw-to-destriped intensity ratios at 12, 25 and 60µm indicate that the destripers remove at most 2% of the total power in the images, and generally the value is less than 1%. At 100µm, the corrections range as high as ~6%, indicating that both destripers have a difficult time dealing with the bright 100µm cirrus structures. The range in standard deviations of the distributions show that all of the destripers introduce surface brightness variations of less than 0.5% at 12, 25 and 60µm. The variations at 100µm are typically ~1% with excursions as high as 4%. The skewness and asymmetry of the distribution of the ratios indicate that the surface brightness variations introduced by the destripers all tend to be negative, in the sense that the destripers tend to suppress structure in the background.

5.1.3. BROAD ZODIACAL EMISSION REMOVAL.

The broad zodiacal background was removed from the destriped Skyflux maps using an empirical method rather than a global model of the Zodiacal emission. This approach avoided the uncertainties in shape and zero points associated with the theoretical models, as well as errors introduced by real small-scale deviations from the smooth distributions used to model the background. For 12, 25 and 60µm Skyflux plates, a two-dimensional, third-order Chebyshev polynomial was fit to the image; the fits were of sufficiently low order to model only the trends in the broad background, and effectively to ignore small-scale brightness deviations. The background fits were then subtracted from the destriped Skyflux maps, yielding a "flat-fielded" image. The broad Zodiacal emission was not removed from 100µm images because bright cirrus complexes with scale sizes comparable to the image size tend to be integrated into the empirical fit and thus suppressed in the final product.

152

5.1.4. CO-ADDING THE THREE HCONs

Once the fixed pattern artifacts were cleaned from the Skyflux maps and the broad Zodiacal background was removed from the 12, 25 and 60μm images, data from the three HCONs was coadded. In addition to improving the signal-to-noise of the faintest cirrus emission in the images, coaddition also "filled in gaps" since regions of the sky that may have been missed in one HCON were frequently scanned in another.
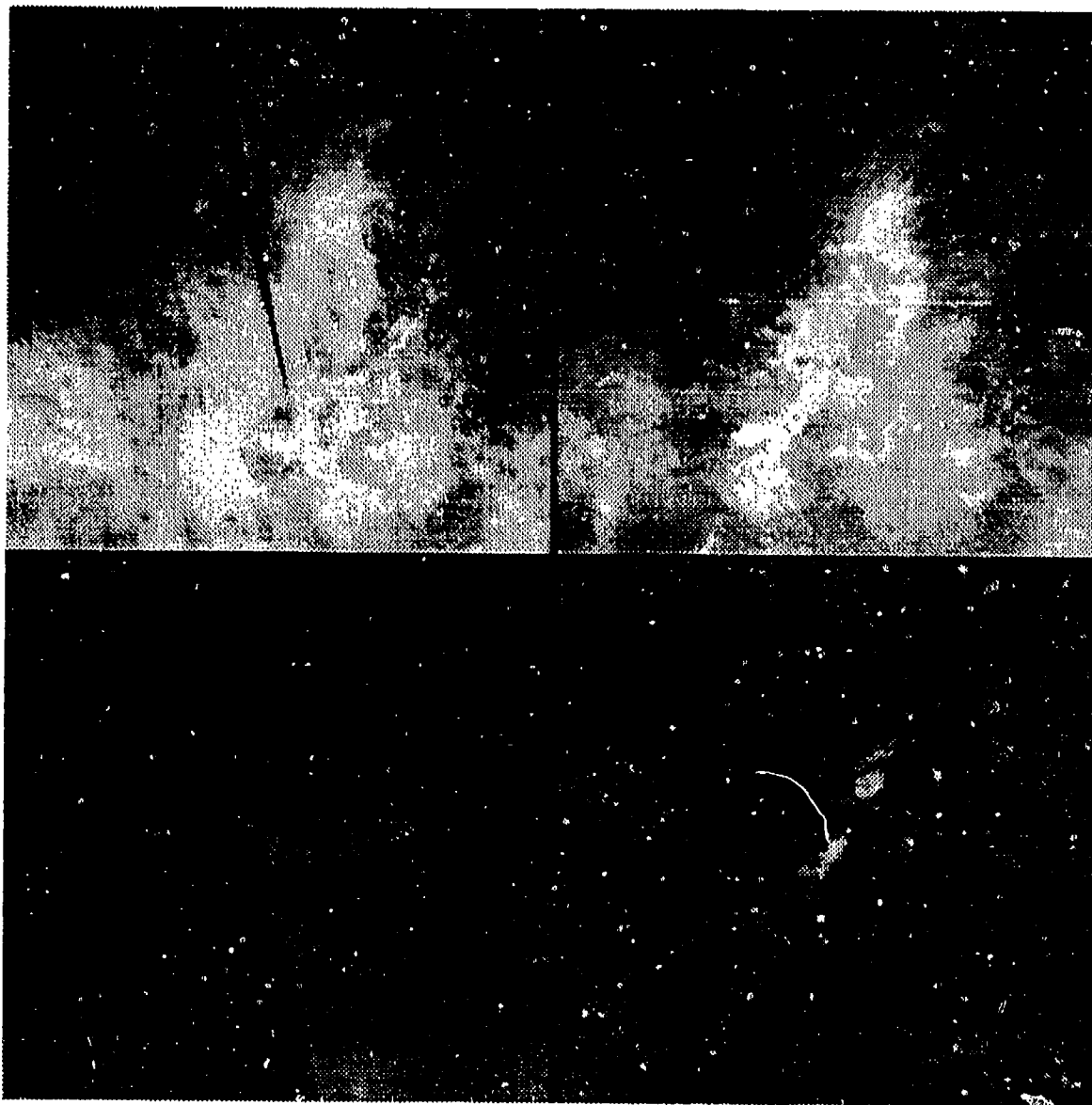
Figure 5-7. The raw HCON 1 IRAS Skyflux plate 99 maps at 100μm (top left) and 12μm (bottom left). The fully processed, 3 HCON coadded images are shown on the right.

153

In Figure 5-7 are shown the raw 12 and 100μm maps of HCON 1 Skyflux plate 99 (α = 4^h00^m, δ = +0°00') along with the fully processed, three-HCON-coadded versions of the images. The stripes have been removed from both maps to a high degree of accuracy and the coadding has provided full coverage of the field. Although the cirrus emission was quite bright even in the raw 100μm map, stripe removal allows detailed analysis to be made of the small-scale structure of the cloud. A much more striking improvement was made in the 12μm map where the bright stripes and strong gradient due to the Zodiacal background makes the very faint cirrus emission as well as faint point sources in the raw image virtually invisible. Some aliasing due to the median filtering can be seen in the cleaned 12μm map, although it is at a very low level. Essentially all of the faint structure visible in the cleaned image is real, as can be seen by close comparison with the distribution of the emission in the cleaned 100μm image.

5.2 SPATIAL CHARACTERISTICS OF THE INFRARED CIRRUS BACKGROUND.

At high galactic latitudes, the emission from interstellar infrared cirrus clouds is the dominant fixed pattern background at wavelengths of $100\mu m < \lambda < 300\mu m$, and it and the cirrus contribute significantly to the total background in the range $10\mu m < \lambda < 100\mu m$. Fast-scanning infrared detection systems that will be able to discriminate quickly between objects projected onto the sky must do so against the backdrop of the highly modulated cirrus emission. Therefore, it is essential that the characteristic spatial distribution of the cirrus emission be well understood.

Figure 5-8. A Galactic Aitoff projection of the high galactic latitude $100\mu m$ sky. This image was constructed from our enhanced IRAS Skyflux database.

5.2.1 LARGE SCALE CIRRUS MAPS.

The distribution of the infrared cirrus clouds on the largest scales was investigated by assembling destriped, dewaved and Zody-subtracted Skyflux maps into large-area mosaics. Software to generate these mosaics was developed at Steward Observatory using custom routines written under the IRAF IMFORT package. The general mosaic procedure begins by copying a "key" Skyflux image into the center of the output image and then maps up to 24 additional cleaned images into the projected equatorial gnomonic coordinate system of the "key" image. The resulting seamless large-scale maps preserve the full 2 arc-minute resolution and radiometry of the original images.

Upon the release of the IRAS Sky Survey Atlas images (ISSA) in 1991, the Steward Observatory Mosaic Software was adapted to operate on those images. In addition to running the software in-house at Steward Observatory, R. Cutri installed the Software at the Infrared Processing and Analysis Center in Pasadena for general use by the Astronomical community.

The final step in the generation of large scale cirrus maps was to combine the large Skyflux (or ISSA) mosaic images into full-sky maps. Because the cirrus is a galactic phenomenon,

we chose to generate these maps in Galactic Aitoff projections. Again, custom software routines were developed that reprojected individual 75°x75° mosaics into Galactic Aitoff coordinates, and then combined the pieces into all-sky maps. Figure 5-8 shows the high galactic latitude sky ($|b| > 20°$) at 100μm, as assembled from cleaned HCON 1 Skyflux images. There are several gaps in the high latitude map due to the incomplete sky coverage of IRAS. The jagged edges bordering the Galactic Plane region result when individual mosaic sections that are square in equatorial coordinates are remapped into the Aitoff projection.

5.2.2 GLOBAL DISTRIBUTION OF THE INFRARED CIRRUS.

Inspection of even individual Skyflux maps reveals that the infrared cirrus appears to be organized in complexes ranging in size from a few degrees to tens of degrees. However, the perceived size of cirrus complexes is strongly biased by the format in which they are viewed. Until one examines sensitive enhanced all-sky maps, such as the image in Figure 5-8, the true extent and morphology of the major cirrus complexes cannot be appreciated.

The projected surface density of infrared cirrus emission is strongly concentrated towards the Galactic Plane. This concentration implies that the scale height of the cirrus clouds is relatively small. If one assumes that the density of cirrus is roughly constant throughout the Galactic disk and the characteristic distance to prominent cirrus is 100-200pc (e.g., Magnani, Blitz and Mundy 1985; Heiles, Reach and Koo 1988; Herter, Shupe and Chernoff 1990), then the scale height must be ≤100pc. Although the bright cirrus emission is mostly confined to the vicinity of the Plane, there are numerous bright features at high galactic latitudes such as the cirrus knot visible in Figure 5-8 near the south Galactic pole. In addition to the bright cirrus complexes, there is considerable low surface brightness emission over virtually the entire sky. Emission from the faint ambient cirrus is typically 100-1000 times fainter than the peak 100μm intensity within the brighter complexes. It is likely that there is *no* line of sight from the Earth that does not pass through some cirrus clouds. It should be noted that most of the faint cirrus emission became apparent only after the Skyflux maps were cleaned and multiple HCONs were coadded.

The most common morphological structures observed in the high latitude cirrus are long arcuate filaments. The most prominent of these is the well-known North Celestial Polar (NCP) loop that extends up out of the Galactic plane. This feature was first discovered in the HI survey maps of Heiles (1976). Several long linear features are visible in the vicinity of the Magellanic Clouds. These filaments were actually first observed by de Vaucouleurs (1960) in very deep optical photographic plates, and there was conjecture that they might by tidal tails associated with the Large Magellanic Cloud. The large-scale infrared map shows that those features are actually part of the large cirrus complex to the right of the LMC, and they are associated with the Milky Way. Several previously unknown arcs or loops are also visible in Figure 5-8 below the Galactic plane slightly to the left of the NCP Loop. The complex structures in this region appear to be the superposition of 3-4 loops of emitting material. HI dynamical studies of the NCP loop (Meyerdiecks et al. 1991) suggest that the loop is actually a cylinder of gas and dust that is expanding at ~20 km/sec. The driving force behind the expansion is at present unknown, but may be a supernova or a hot stellar wind.

5.2.3 THE SPATIAL CHARACTERISTICS OF THE CIRRUS FROM IRAS SKYFLUX DATA.

In areas of both luminous and faint infrared cirrus emission there appear to be modulations in the surface brightness down to the 2 arc-minute resolution of the IRAS Skyflux maps. To characterize how the power of the infrared emission from the cirrus is distributed in spatial frequency space we carried out a Fourier spectral analyses of prominent cirrus features. These investigations involved evaluation of the one- and two-dimensional power spectra of selected cirrus complexes, and determination of the characteristic spectral slopes and variations in the slopes among the sample.

As part of the work undertaken for Air Force contract F19628-88-C-0014, we selected 24 cleaned IRAS Skyflux cirrus maps that contained prominent 100μm cirrus structures for power spectral analysis. While short wavelength (12μm) emission is visible in many Skyflux maps, there are very few fields in which the emission is of sufficiently high signal-to-noise to enable meaningful power spectra to be evaluated. Consequently, only four 12μm maps were selected for this study. The corresponding 100μm maps for these fields were included so that the relative power distributions at the two wavelengths could be compared.

Before evaluating the power spectrum of each of the selected Skyflux maps, the value of the mean intensity over the entire image was subtracted from each pixel, thus minimizing the zero frequency "spike" in Fourier space. Two-dimensional power spectra were evaluated using the STSDAS Fourier analysis packages within IRAF. Only those parts of the images that were free from artifacts or processing anomalies were utilized. This resulted in slightly different sized images going into each Fourier transform, and thus slightly different spectral resolutions for each power spectrum. No filtering or appodization was used. Most of the power spectra were dominated by strong low frequency peaks extending in the cardinal directions. These features are likely produced by the broad zodiacal emission, which was not removed from the 100μm images, and which may have been imperfectly removed from the 12μm maps. A portion of the very low frequency power was likely produced by the abrupt truncation of the images and the lack of appodization; despite having subtracted out total power in the image space, the images behave somewhat like rectangle functions which transform into sinc functions. Also apparent in many of the spectra were linear artifacts due to residual low level "stripes" in the images, left over from the cleaning process.

The first result of note is that the power spectra of most of the fields in this study exhibited strong azimuthal or angular symmetry over scales extending from near the DC level out to the Nyquist limit (0.25 arc-minutes^{-1}). This result was somewhat surprising since visual inspection of the Skyflux maps reveals large coherent spatial structures such as ridges and arcs. A few of the cirrus complexes did exhibit asymmetric spectra. However, the unusual structure in all of these spectra correlates with the presence of very bright, compact structure in the images, such as bright galaxies and luminous HII region/molecular cloud complexes.

Radial profiles through each of the 2-d power spectra were extracted in two orthogonal directions (20° and 110°). The profiles from most of the 100μm spectra could be well approximated over much of the spatial frequency range by single power law functions of the form $P \propto f^{\alpha}$. However, some of the spectra exhibited steepening with increasing frequency. This curvature, which was quite pronounced in a few cases, likely results from the contribution of point sources to the power spectrum (see below). In most of the cirrus complexes, the 20° and 110° profiles were virtually identical. When there were discrepancies between the profiles, the differences could be quite large at a given spatial frequency,

157

although the differences tended to be isolated to relatively narrow frequency ranges. The remaining sections of the spectra usually agreed quite well, further suggesting that, while coherent structure such as linear features may exist in some clouds, that coherence does not extend over all spatial scales.

The profiles of the power spectra of the 12μm Skyflux maps all exhibited fairly strong curvature that was the result of strong point source contamination. Because stars are the dominant sources of emission in the 12μm Skyflux maps, rather than extended cirrus which dominates at 100μm, it follows that point sources will also dominate power spectra. However, because the power spectra of the 12μm maps were observed to rise towards low frequencies, the emission from the cirrus still contributes a measurable fraction of the power. The most efficient means of recovering the pure cirrus power spectrum in the 12μm Skyflux maps was found to be two-dimensional median filtering in image space using a 7x7 pixel (14x14 arc-minutes) window. However, such filtering necessarily reduced the effective spatial resolution of the maps, and by suppressing point sources it also suppressed power over a broad range of frequencies. To estimate the effect of the filtering, we created artificial images that contained pure background noise similar to that in 12μm maps, and images containing the noise background along with a distribution of point sources having a number and brightness distribution similar to those measured in selected Skyflux maps. By comparing the power spectral profiles of the pure noise background image, the noise+stars image, and the median filtered image, we found that while the filtering effectively removes the point source contribution, it actually suppresses power down to 0.04 arc-minutes^{-1}, which is nearly half the spatial frequency of the window size (1/14' ~ 0.07 arc-minutes^{-1}). It should also be noted that median filtering the 12μm Skyflux images removed virtually all of the azimuthal asymmetries observed in the spectra of the non-filtered maps. This implies that the bulk of the asymmetry seen in the two-dimensional power spectra arises from structure on small spatial scales, either in the form of bright compact sources or small-scale cirrus filaments.

To characterize the slopes of the cirrus power spectra, power law functions were fit to the extracted radial spectral profiles of the filtered 12μm and unfiltered 100μm data in the frequency ranges 0.01-0.025 arc-minutes^{-1}, 0.025-0.063 arc-minutes^{-1}, 0.063-0.01 arc-minutes^{-1}, and 0.01-0.02 arc-minutes^{-1}. The distribution of power law indices, α, in each frequency regime for the images are shown in the histograms in Figure 5-9. In the figure, the entries for those spectra which qualitatively appeared to show the least high frequency curvature (e.g., point source contamination) are indicated by filled squares. We believe that the large dispersion in the distribution of 100μm slopes reflects the relatively poor signal-to-noise of the spectra, since no azimuthal averaging was employed for that data, rather than real variations in the characteristic spectral shapes. The average power law indices in each spectral regime were evaluated for the 12μm spectra, and for both the full set of 100μm spectra and the least-curved subset of 100μm spectra, and they are listed in Table 5-2. At low spatial frequencies (<0.063 arc-minutes^{-1}) the 12 and 100μm power spectral slopes agree fairly well, indicating that a value of α ~ -2.9 to -3.0 accurately describes both the distribution of the hot and cold cirrus components. At higher frequencies the 12μm spectra offer no valid slope information because of the effects of filtering. As a class, the 100μm spectra steepen towards higher frequencies most likely because of the contribution of point-like non-cirrus sources in the images.
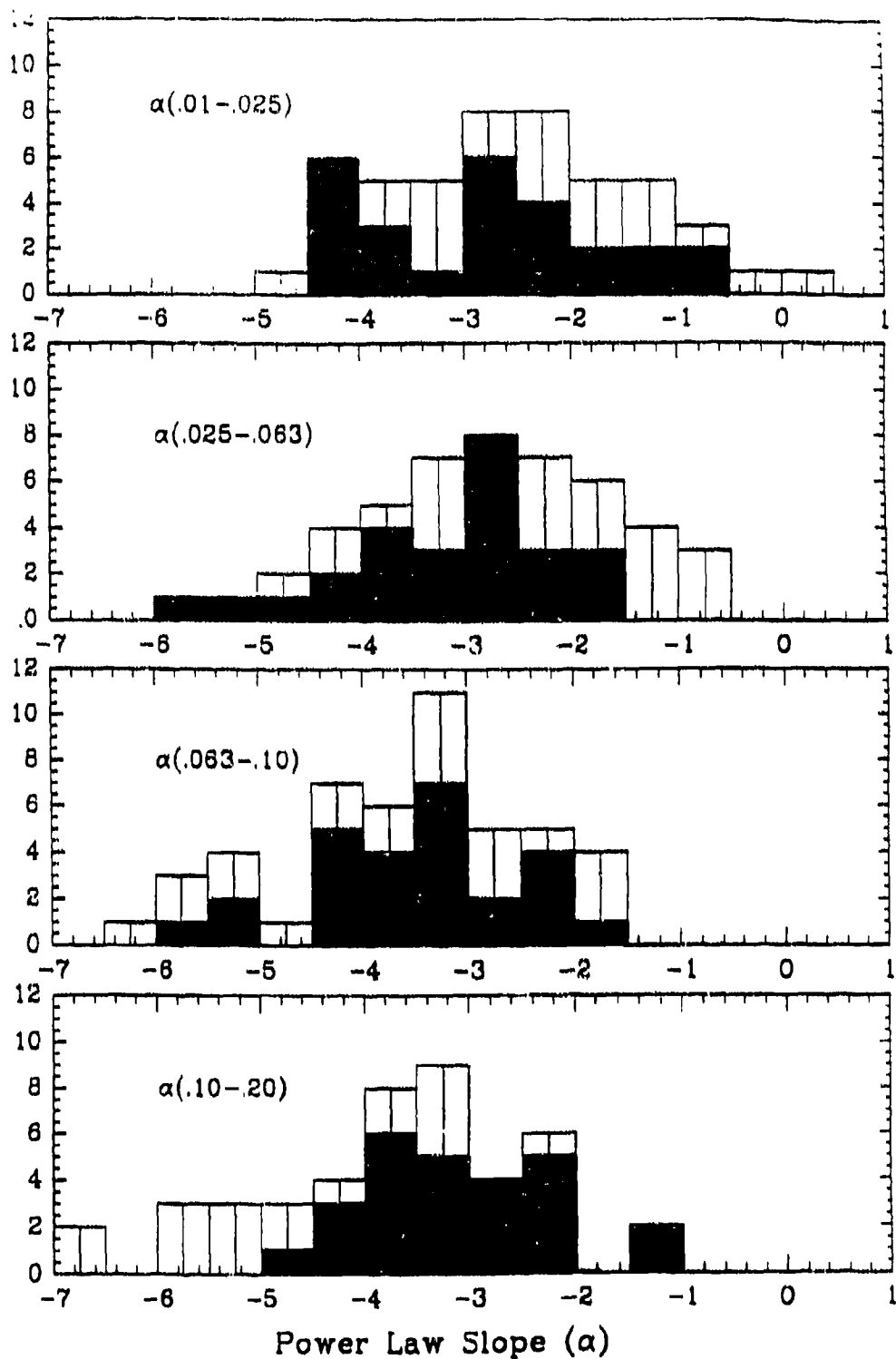
Figure 5-9. The distribution of power law slopes fit to the 100μm power spectral cross-sections shown in Figures 5-2 and 5-3. Slopes are shown for fits made in the spatial frequency ranges of (a) 0.01-0.025 arc-minutes^{-1}, (b) 0.025-0.063 arc-minutes^{-1}, (c) 0.063-0.10 arc-minutes^{-1}, and (d) -.10-0.20 arc-minutes^{-1}. The slopes of the spectra which qualitatively appeared to show the least amount of curvature are denoted by filled squares. Note, the large dispersion in the fit slopes, and the trend toward steeper slopes with increasing frequency range.

159

5.2.4. PROBING HIGHER SPATIAL FREQUENCIES WITH IRAS POINTED OBSERVATION DATA.

The quality of the power spectral data presented above is ultimately limited by the 2' resolution of the IRAS Skyflux maps and the point source contamination. In virtually all cases, the declining spectra merge with the noise in frequency space slightly above the Nyquist frequency. This is particularly apparent in the 12μm data because the surface brightness of the cirrus emission is so low. As part of our contract work for MRC, we attempted to obtain an improved measure of power at higher frequencies by utilizing data from the Pointed Observations of IRAS.

The Pointed Observations were carried out by repeatedly scanning the IRAS detector array over small regions (1-3 deg^2) of the sky at rates 2-8 times slower than that used in the all-sky survey. The slower scans resulted in much higher spatial sampling rates which, in turn, yielded better resolution than survey mode observations. Data samples were obtained on scales of 8-30 arc-seconds at 100μm and 2-8 arc-seconds at 12μm. However, the practical limit to the resolution available from any IRAS data is ~3-5 arc-seconds because of the wobble induced in the satellite due to the free-play in the gyroscope bearing (gyro pivotal clearance). Multiple scans and slower rates also resulted in longer net integration times than typical survey observations, and the Pointed Observations achieved sensitivities 3-7 time better than the survey mode. This would hopefully improve the signal-to-noise of cirrus detections at 12μm.

The major limitation in using the Pointed Observations for this application is that, of course, none were intentionally targeted at bright cirrus regions. However, we were able to identify a number of scans which serendipitously covered regions with reasonably high surface brightness 100μm cirrus emission. We obtained Calibrated Reconstructed Detector Data (CRDD) for several of those observations, and here we present the analysis for the three which cover the brightest regions of cirrus, BS63, SY52 and DF16. As an example of the improved resolution offered by the Pointed Observations, Figure 5-10 compares a single column of data from the 100μm IRAS Skyflux map 171 to the corresponding co-added scans of the BS63 Pointed Observation CRDD from a single 100μm detector. Much more detail is visible in the CRDD data, and the contrast in features is greatly enhanced. The difference in surface brightness between the Skyflux and CRDD scans is a result of larger effective area of the Skyflux beam as well as calibration differences between the two data sets.

In Figures 5-11 and 5-12 are shown the co-added 12, 25 60 and 100μm single detector scan data for the BS63 and SY52 Pointed Observations. For each field, three sets of scans are given, representing three separate "rows" of detectors seen by sources as they scanned across the IRAS focal plane. Referencing the schematic of the IRAS focal plane shown in Beichman et al. (1985), the three detector sets are: 47, 39, 31 and 55 which are small, "edge" detectors located at the bottom of the figure; 23, 16, 8 and 1 located just inboard the preceding edge detectors; and 54, 46, 11 and 62 which are the "edge" detectors. Use of the edge detectors has the benefit that these were generally the most sensitive because their smaller angular size resulted in their seeing fewer background photons. While the cirrus emission is prominent in the 60 and 100μm scans shown in the above Figures, it is still at a very low contrast in the short wavelength data, despite the improved sensitivity of the Pointed Observations. In addition, structural features in the cirrus emission can be seen to vary substantially across the focal plane.

160
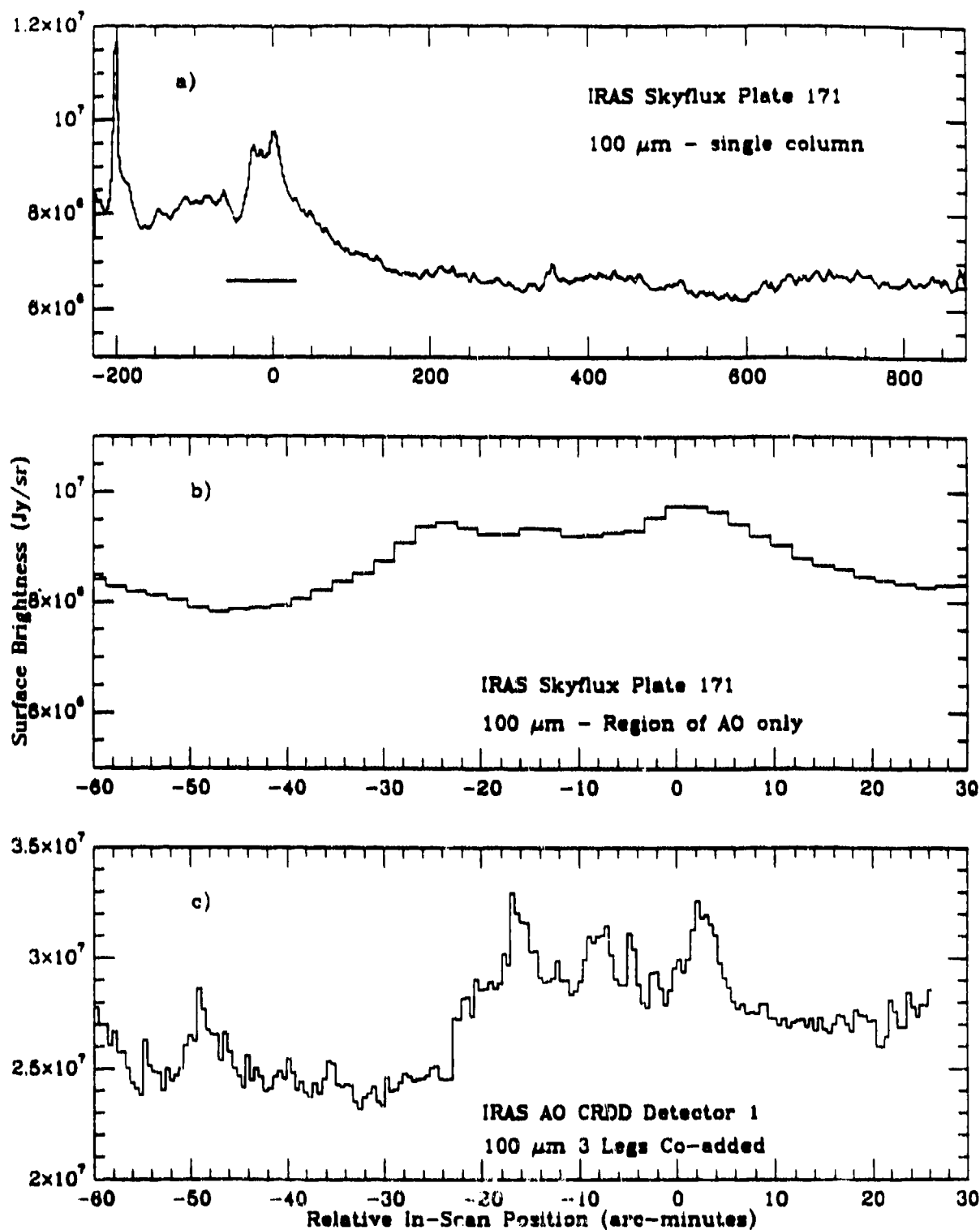
Figure 5-10. A comparison of the spatial resolution and sensitivity of IRAS Skyflux and Pointed Observation data. (a) A slice taken through IRAS Skyflux plate 171. (b) An enlargement of the Skyflux data in the region serendipitously covered by a Pointed Observations. (c) The Pointed Observation single detector data in the cirrus cloud.

161

Figures 5-13 to 5-15 illustrate the one-dimensional power spectra for each detectors' data in the BS63 and SY52 fields. Also included are the spectra for the DF16 Pointed Observations field. As for the Skyflux data, the power spectra were evaluated by first subtracting the average intensity for each from each pixel in the scan. Although it is apparent that the Pointed Observation data are severely limited by signal-to-noise, 100µm power spectral information is available up to spatial frequencies of ~0.005 arc-seconds⁻¹, which is a slight improvement over the Skyflux data. More importantly, because individual scans of the Pointed Observation data can be examined, non-cirrus sources can be selectively removed without suppressing the small scale structure in the cirrus. At 12, 25 and 60µm, no significant sign of power can be seen above the noise limits. The power spectra of detectors 16 and 23 (25 and 12µm) in the SY52 field illustrate the familiar signature of the point sources detected in the scans shown in Figure 5-12b. In addition, a peak is present in the 25µm spectrum, which is produced by the periodic noise seen in the raw scan (this noise is likely due to crosstalk between detector 16 and one of the onboard clocks).

If the assumption is made that the spatial power distributions will be similar across the cirrus field covered by the Pointed Observation, some improvement is possible by co-adding scans in frequency space. As shown in the Skyflux data, this assumption is typically correct, however there are exceptions in which the power distribution can be asymmetric. Figures 5-16 to 5-18 show the co-added power spectra for the three Pointed Observation fields. The shape and level of the spectra from each field is remarkably consistent within each IRAS band. At 100µm, the spectra can be coarsely fit with an average power law of slope ~-1.9 which becomes indistinguishable from the noise below ~0.006 arc-seconds⁻¹. When the correction for a one-dimension to two-dimension Fourier transform is made ($\alpha(2d) \sim \alpha(1d)-1$: Guatier et al. 1992), this slope agrees well with the average low frequency slopes of the 100µm Skyflux spectra listed in Table 5-2. This similarity suggests that the high frequency spectral curvature observed in the Skyflux data is virtually all due to the point source contribution. The co-added 12µm spectra show little useful information.
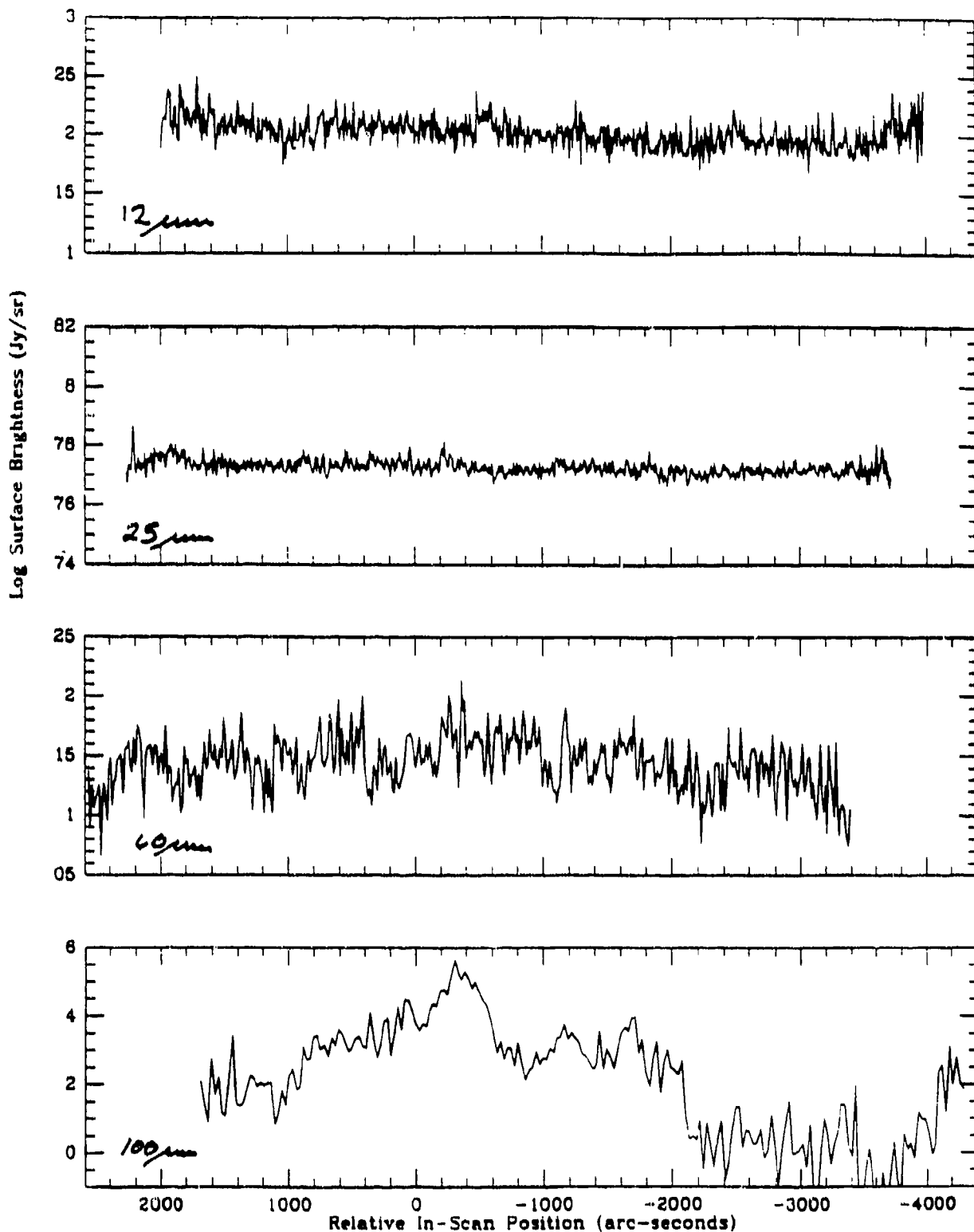
Figure 5-11a. The co-added single detector data from the Pointed Observation BS63. Descending from the top are the 12μm data from detector 47, the 25μm data from detector 39, the 60μm data from detector 31, and the 100μm data from detector 55.

163
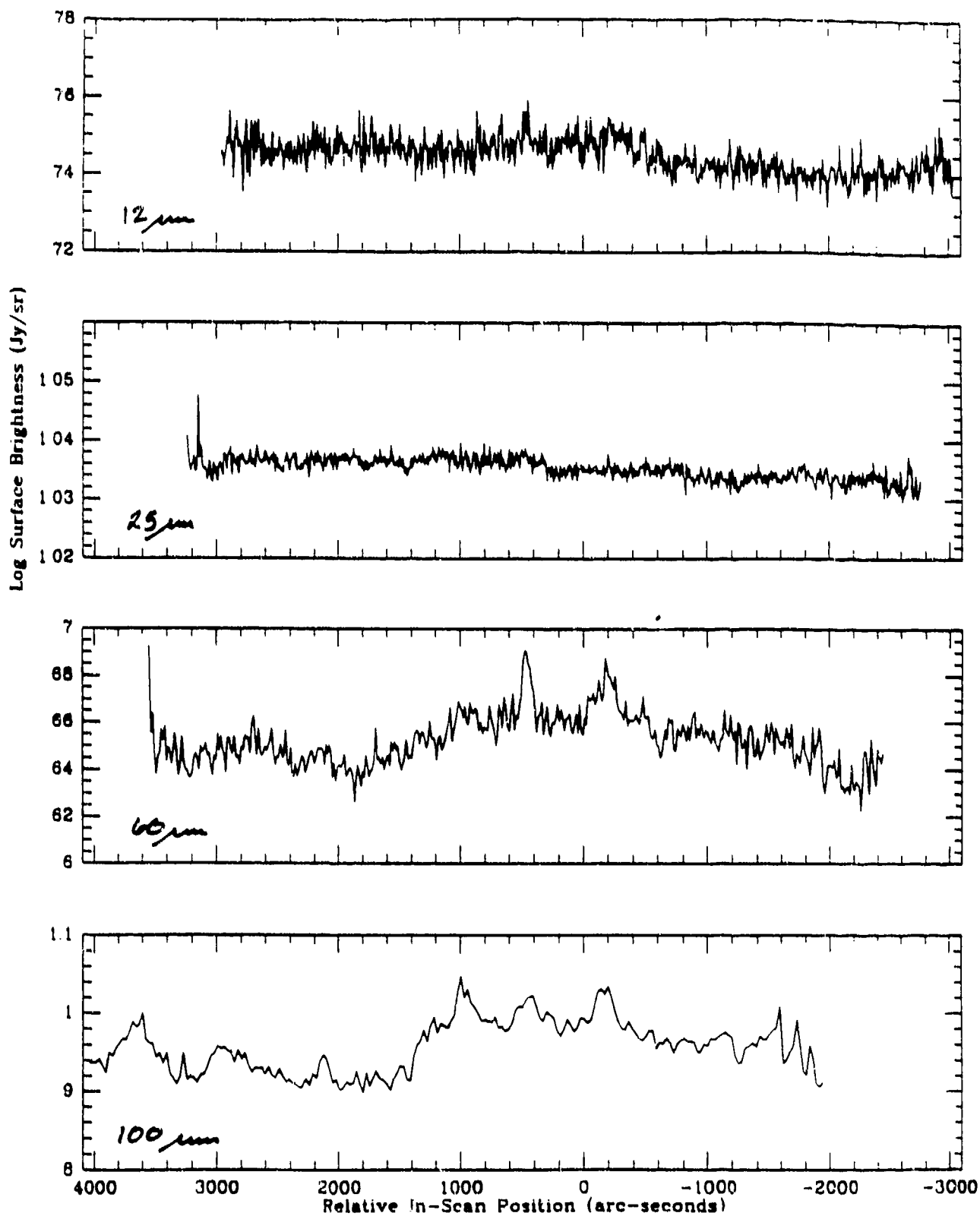
Figure 5-11b. The same as Figure 5-11a, but for detectors 23 (12μm), 16 (25μm), 8 (60μm), and 1 (100μm).

164
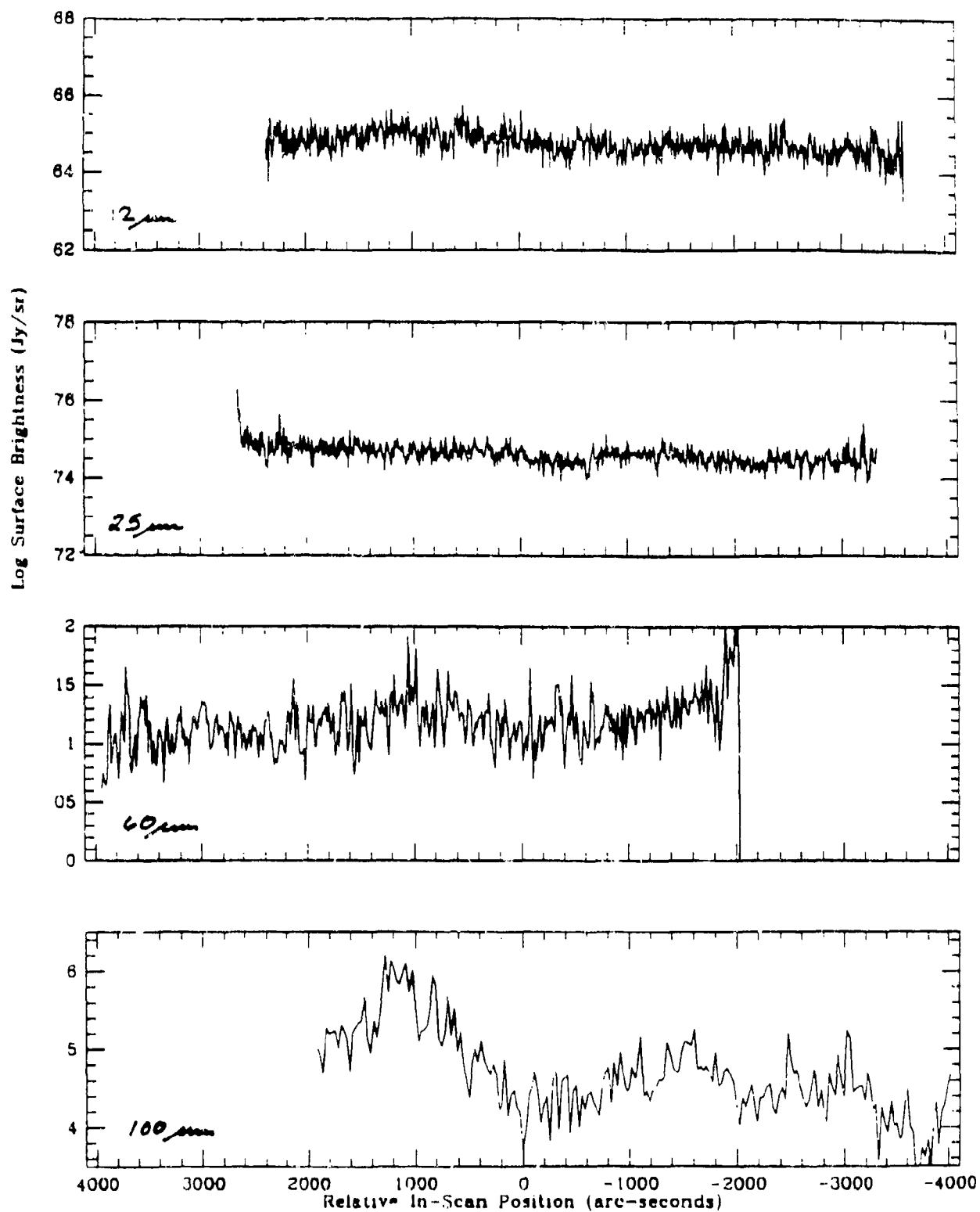
Figure 5-11c. The same as Figure 5-11a, but for detectors 54 (12µm), 46 (25µm), 11 (60µm), and 62 (100µm).

165
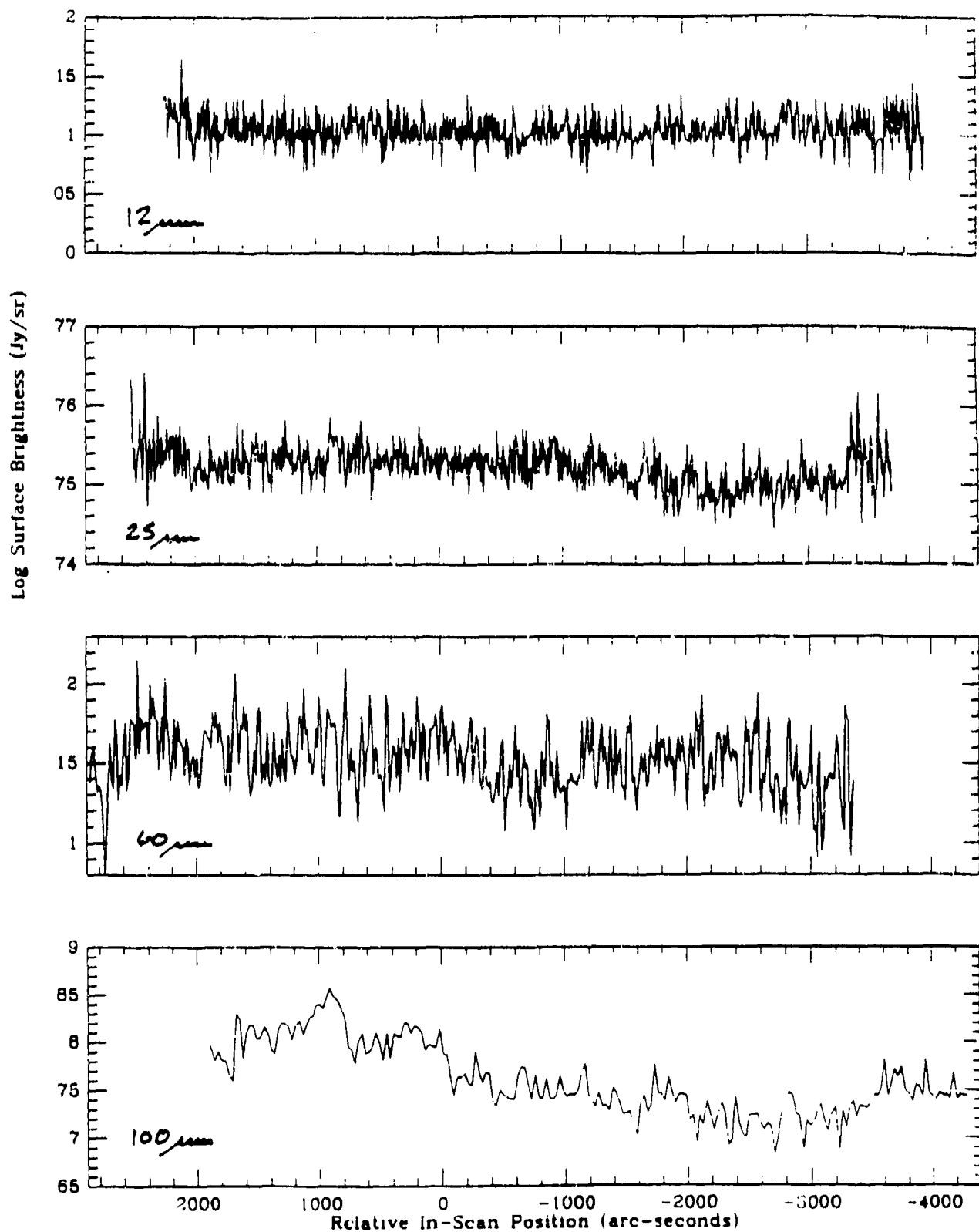
Figure 5-12a. The co-added single detector data from the Pointed Observation SY52. Descending from the top are the 12μm data from detector 47, the 25μm data from detector 39, the 60μm data from detector 31, and the 100μm data from detector 55.
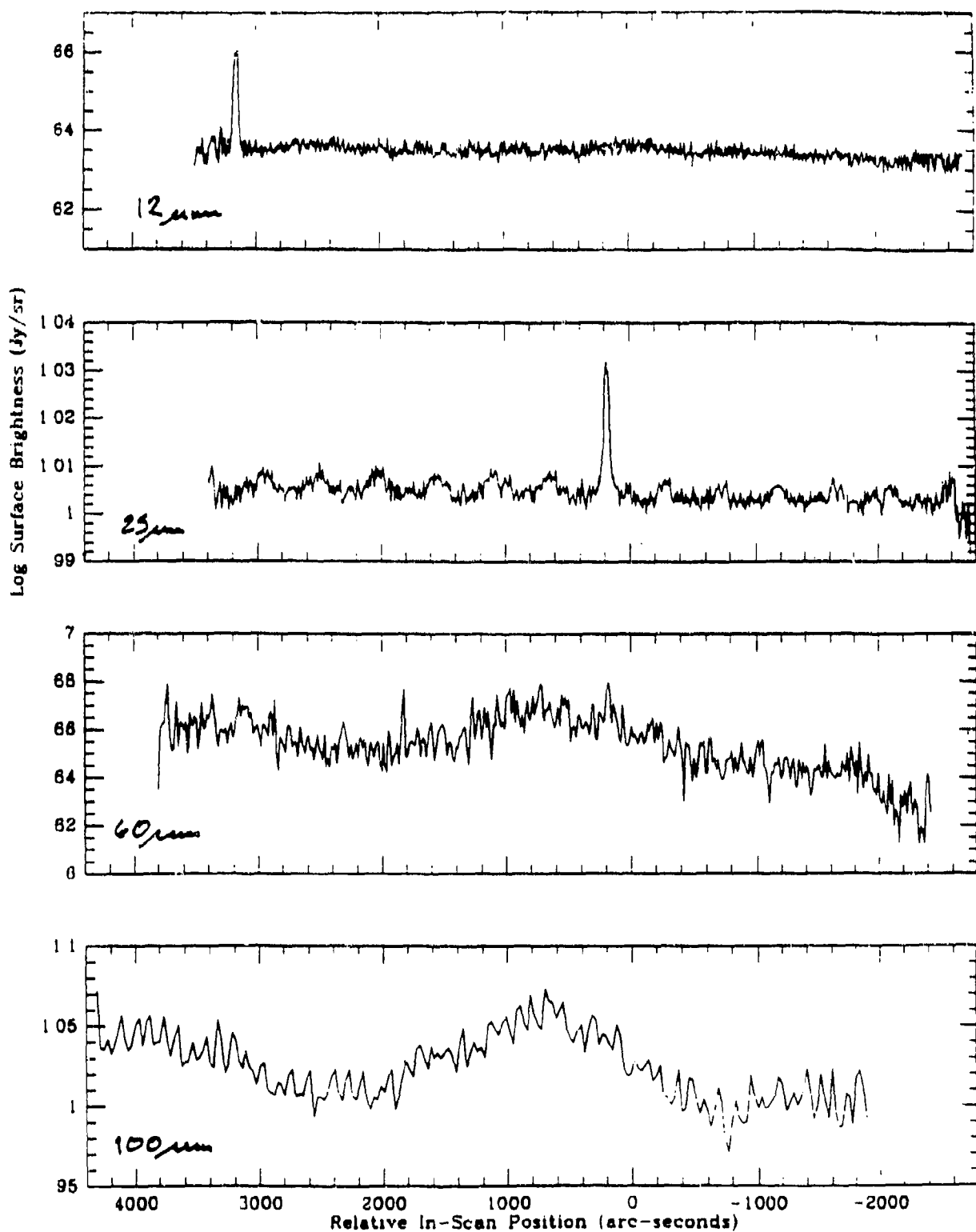
Figure 5-12b. The same as Figure 5-12a, but for detectors 23 (12µm), 16 (25µm), 8 (60µm), and 1 (100µm). Notice the two point sources detected at 12 and 25µm, and the periodic noise signal in the 25µm data.

167
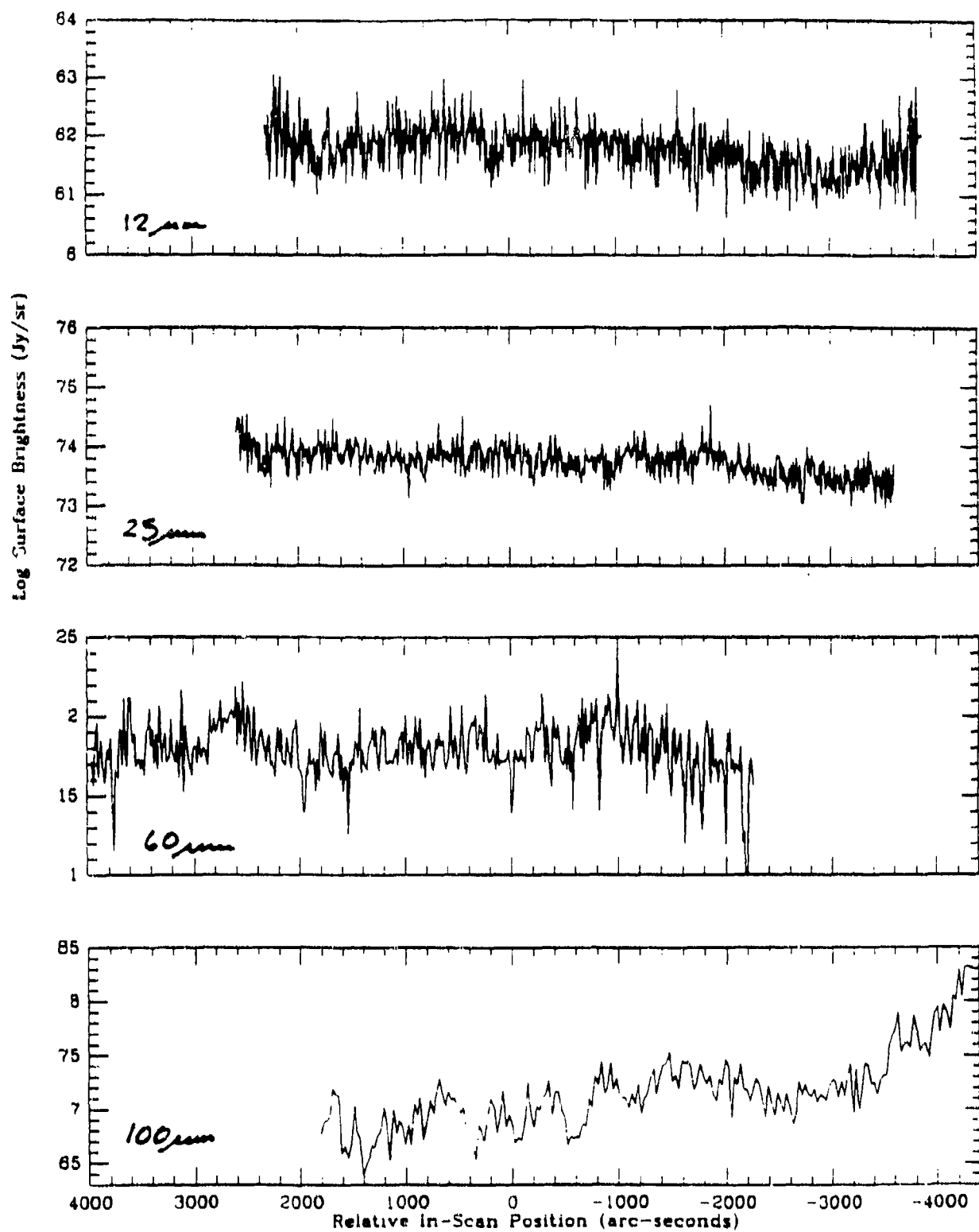
Figure 5-12c. The same as Figure 5-12a, but for detectors 54 (12μm), 46 (25μm), 11 (60μm), and 62 (100μm).

168
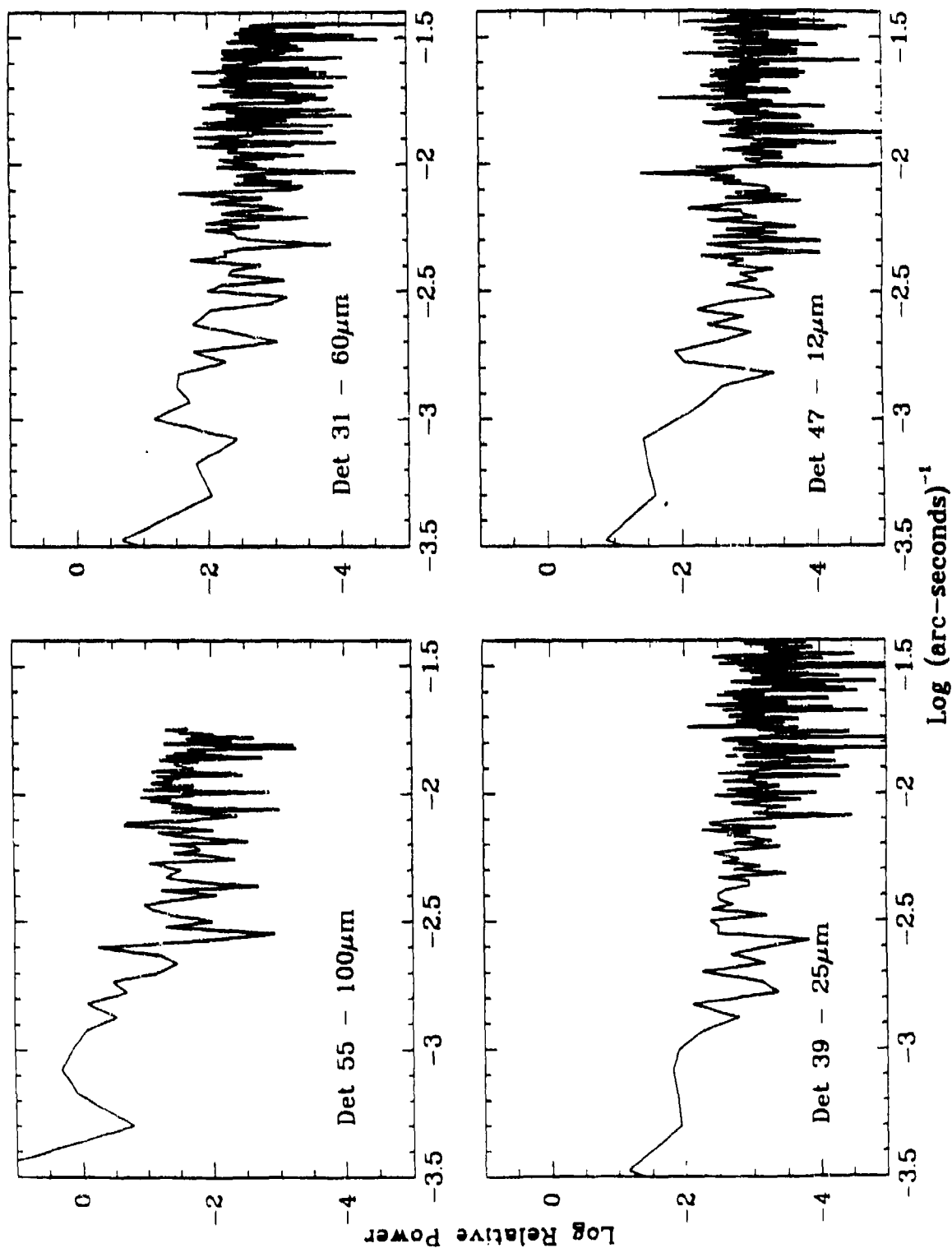
Figure 5-13a. The one-dimensional power spectra for each of the single detector scan data in Pointed Observation BS63 shown in Figure 5-11a.

169
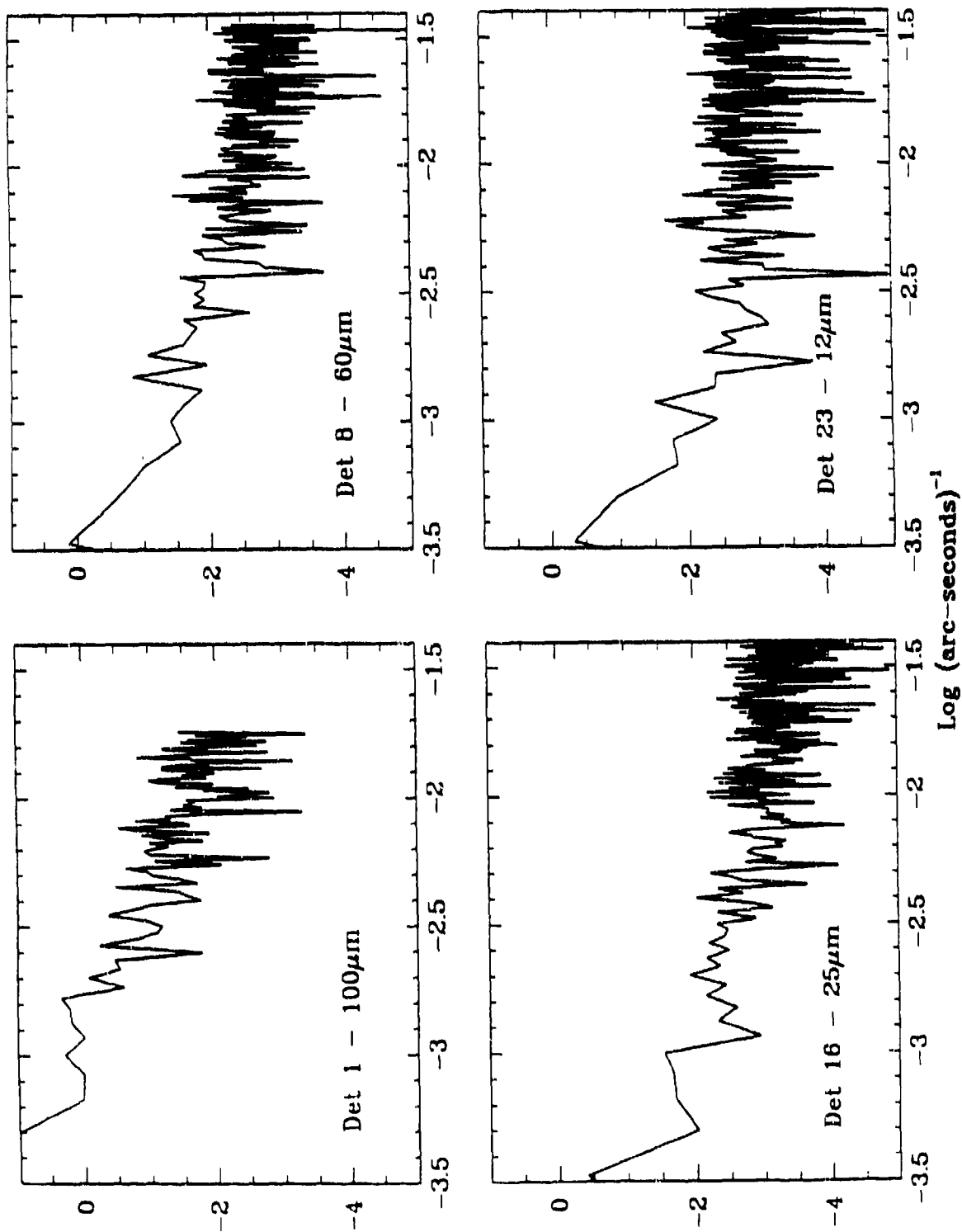
Figure 5-13b. The one-dimensional power spectra for each of the single detector scan data in Pointed Observation BS63 shown in Figure 5-11b.
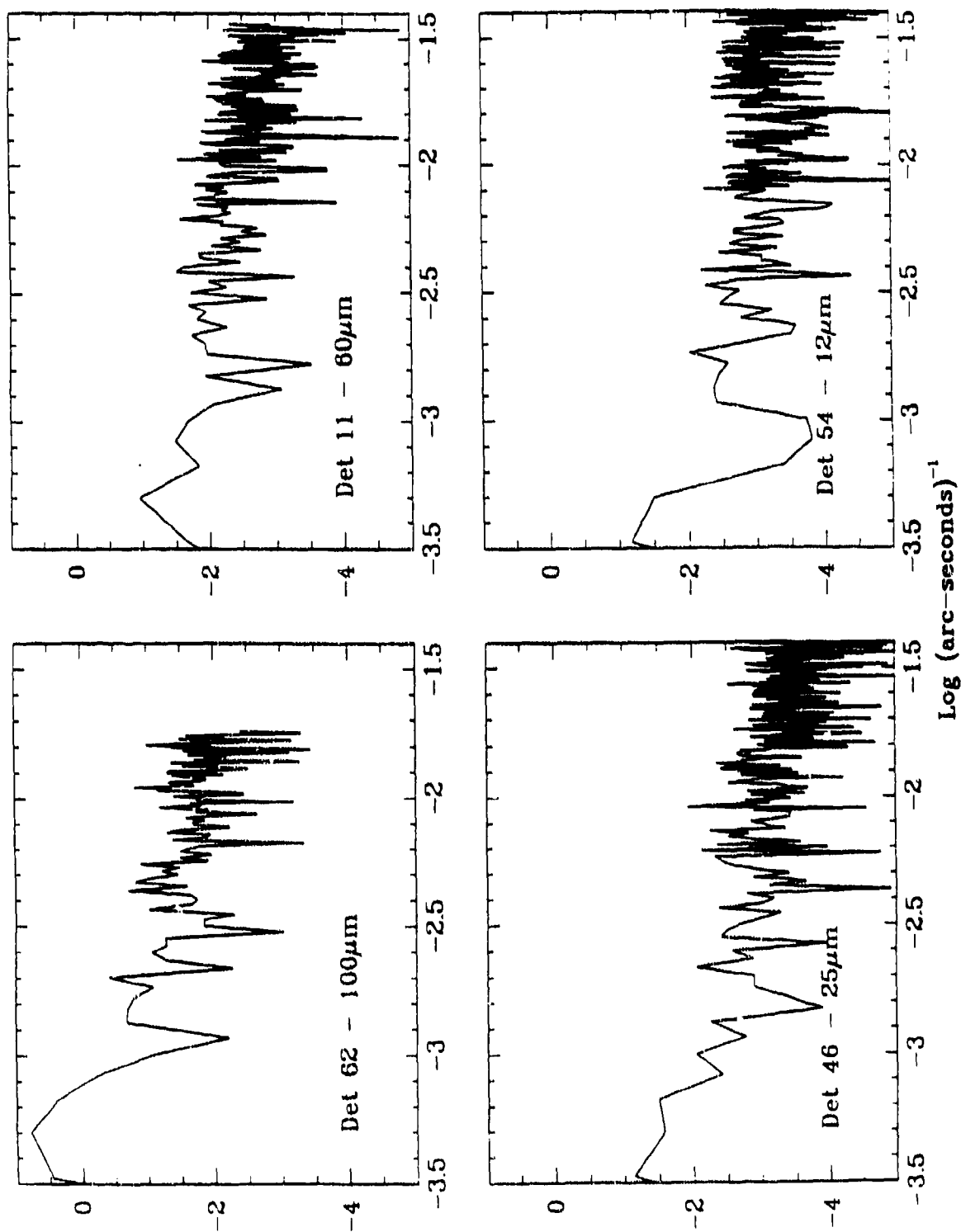
Figure 5-13c. The one-dimensional power spectra for each of the single detector scan data in Pointed Observation BS63 shown in Figure 5-11c.
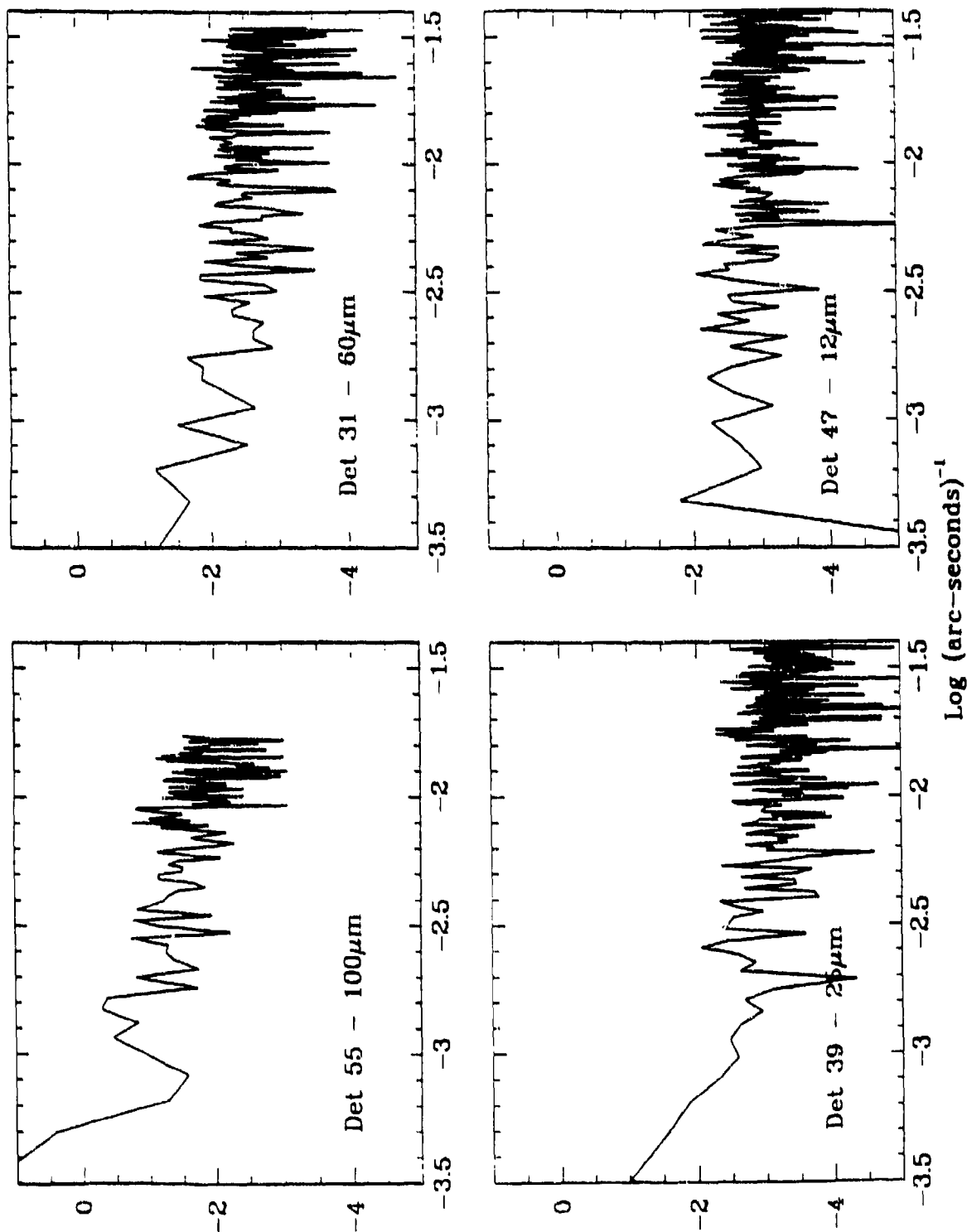
Figure 5-14a. The one-dimensional power spectra for each of the single detector scan data in Pointed Observation SY52 shown in Figure 5-12a.
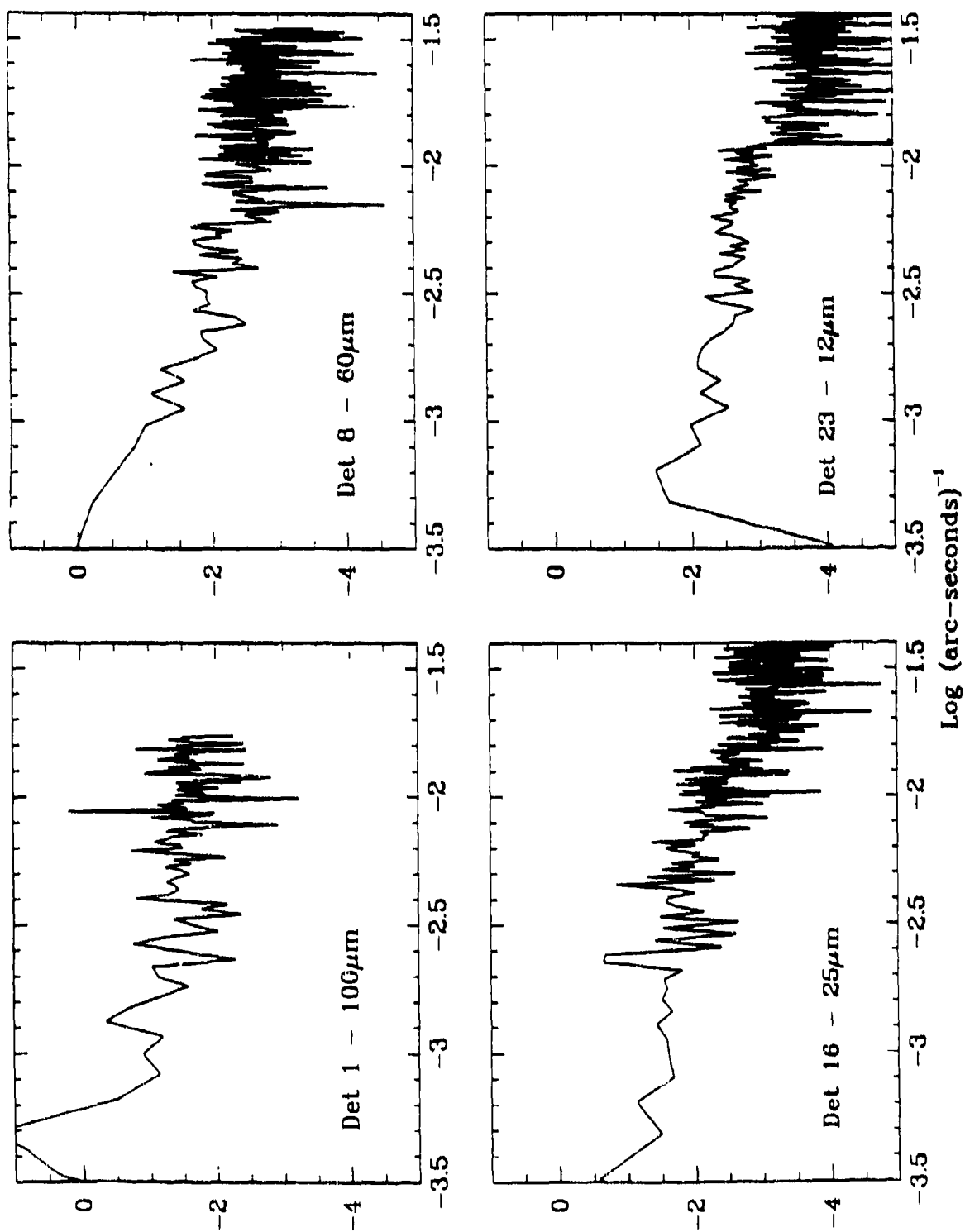
Figure 5-14b. The one-dimensional power spectra for each of the single detector scan data in Pointed Observation SY52 shown in Figure 5-12b.

173
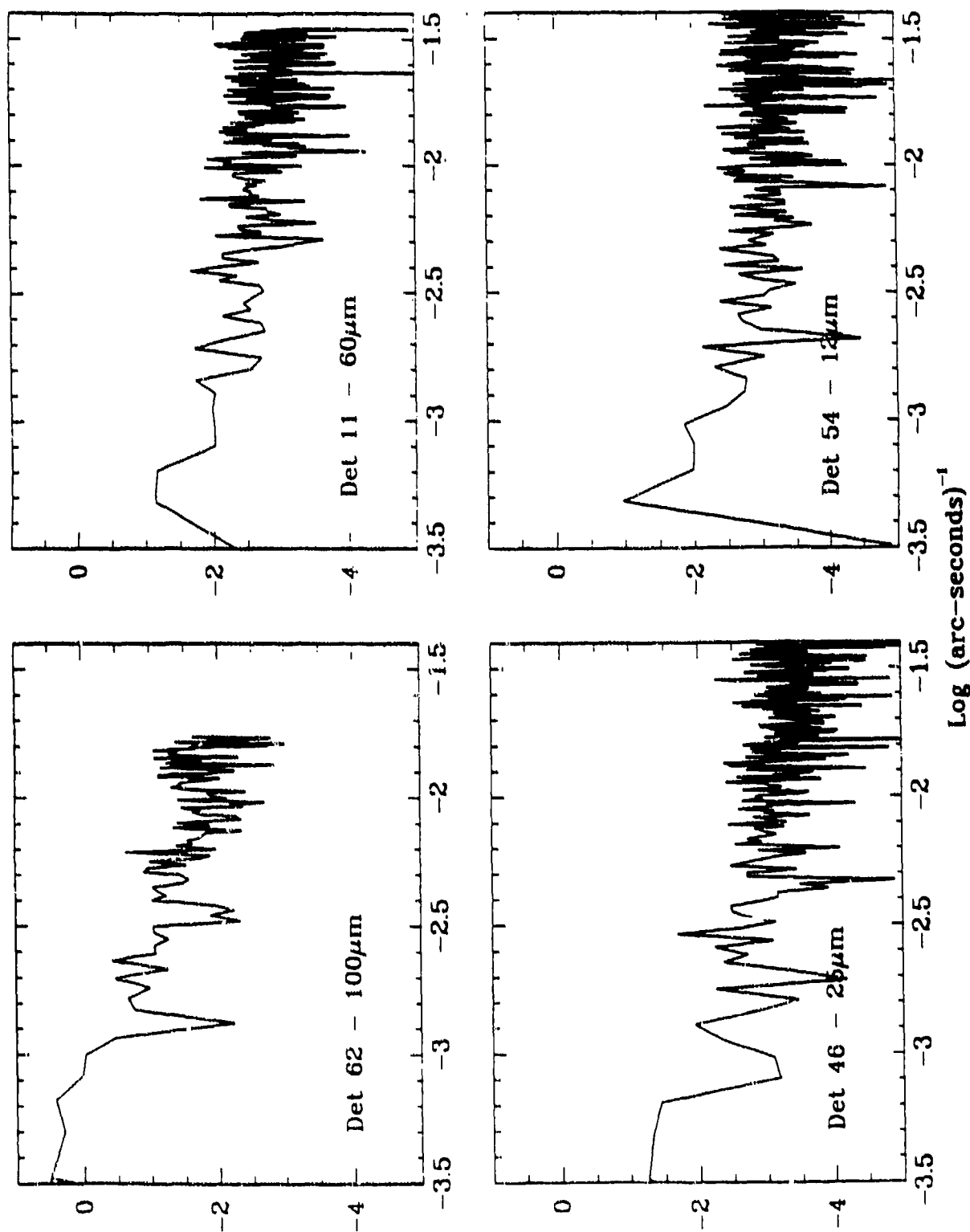
Figure 5-14c. The one-dimensional power spectra for each of the single detector scan data in Pointed Observation SY52 shown in Figure 5-12c.

174
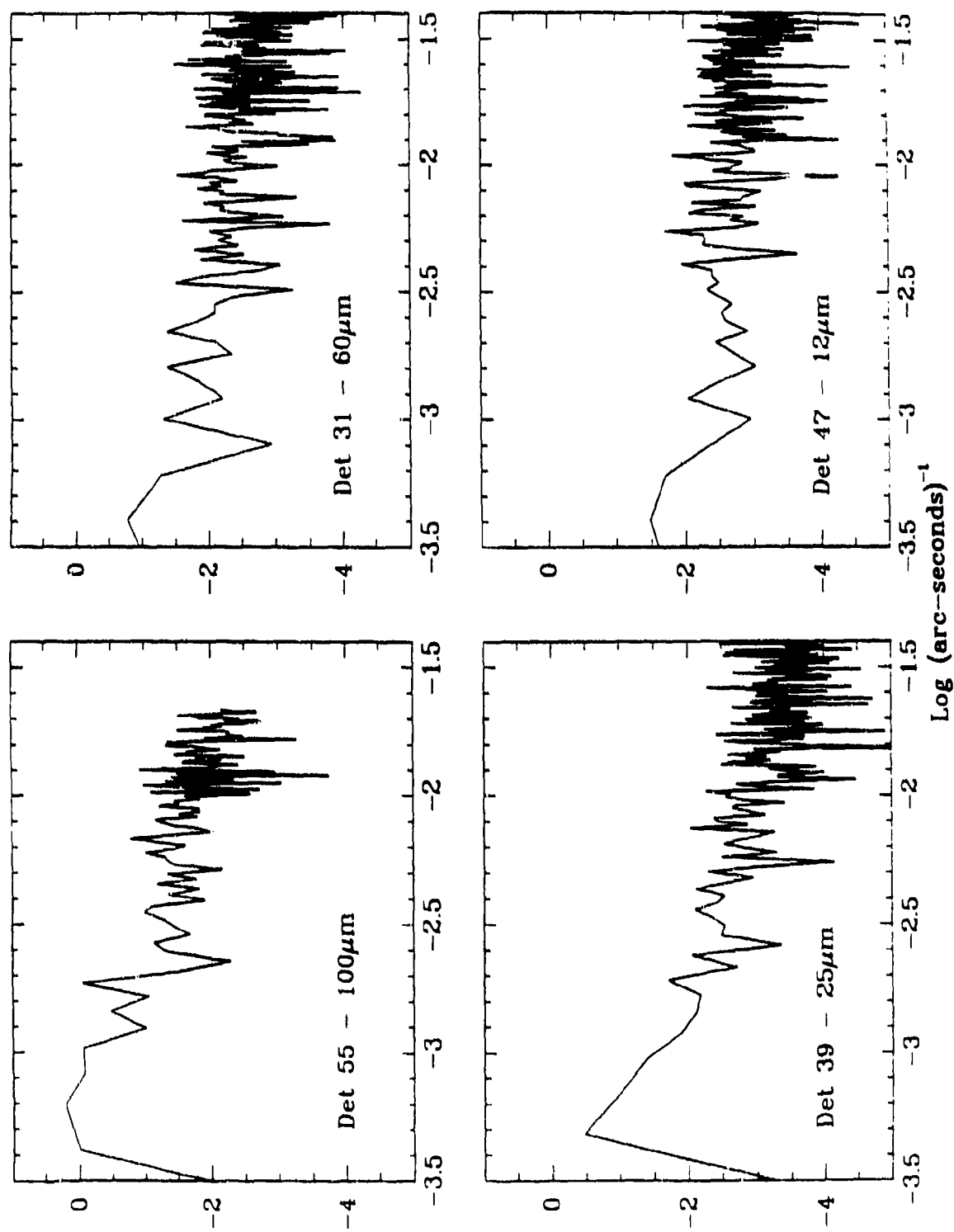
Figure 5-15a. The one-dimensional power spectra of the scan data of Pointed Observation DF16 for detectors 1, 8, 16, and 23. The raw scan data are not shown.

175
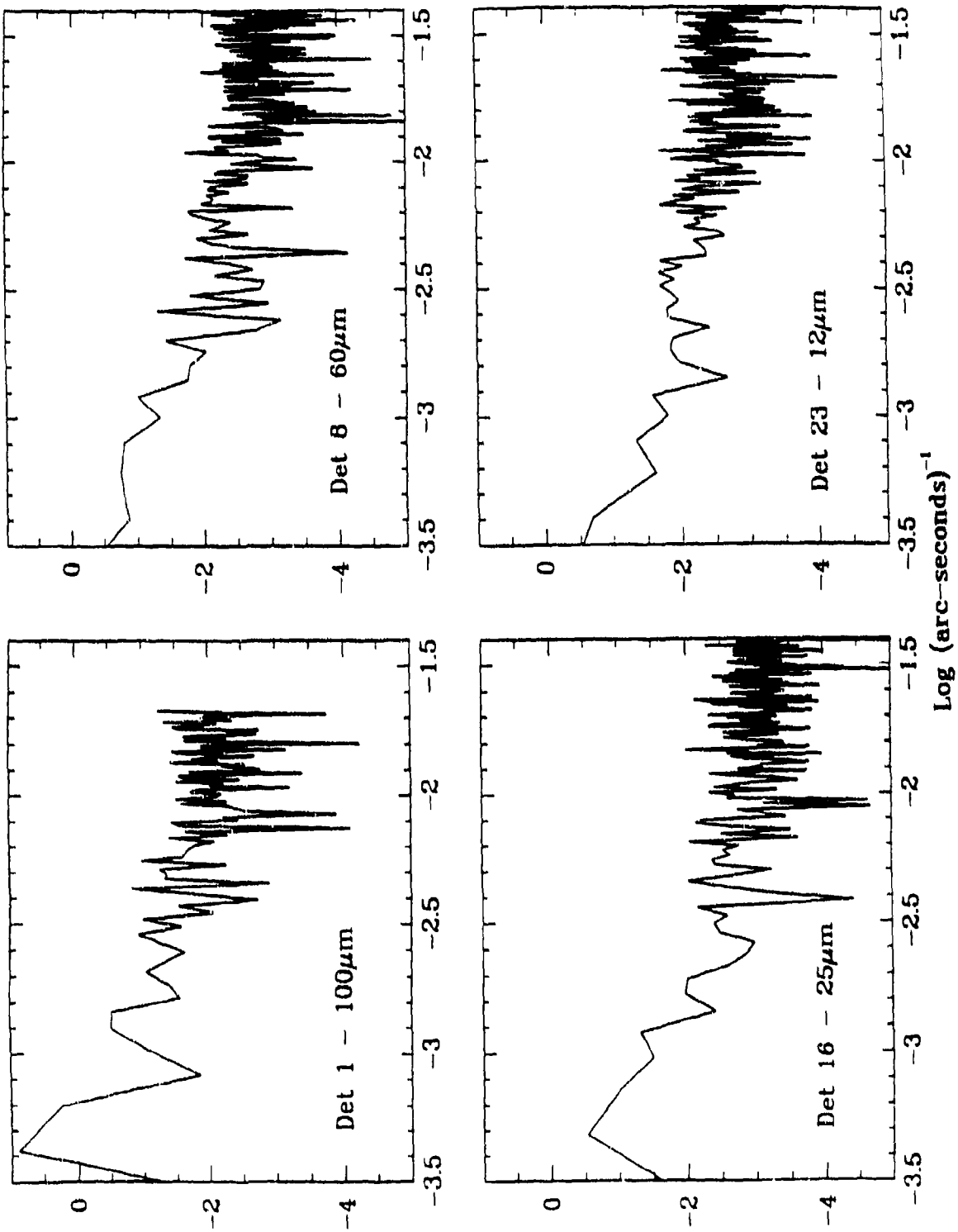
Figure 5-15b. The one-dimensional power spectra of the scan data of Pointed Observation DF16 for detectors 55, 31, 39, and 47. The raw scan data are not shown.

176
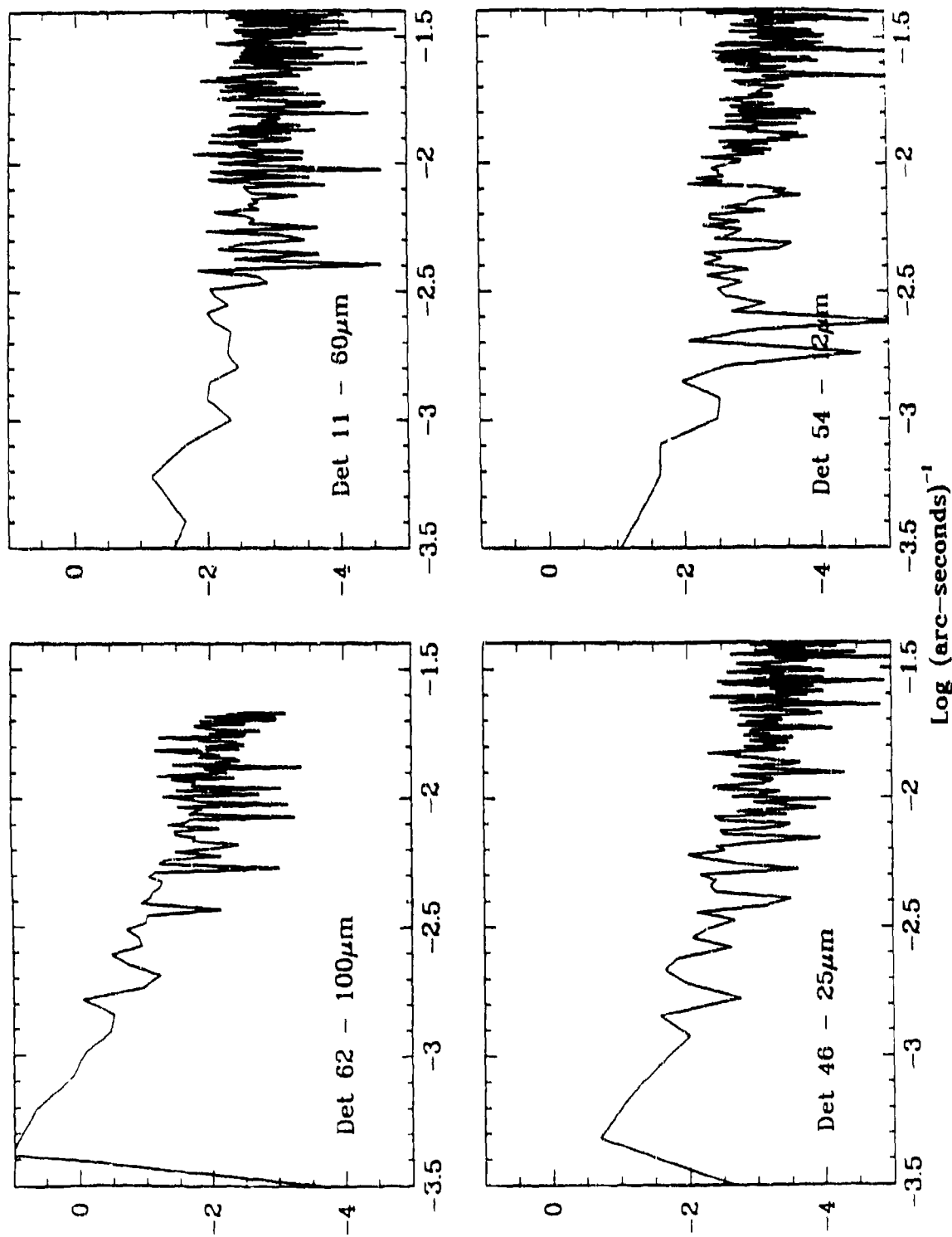
Figure 5-15c. The one-dimensional power spectra of the scan data of Pointed Observation DF16 for detectors 62, 11, 46, and 54. The raw scan data are not shown.
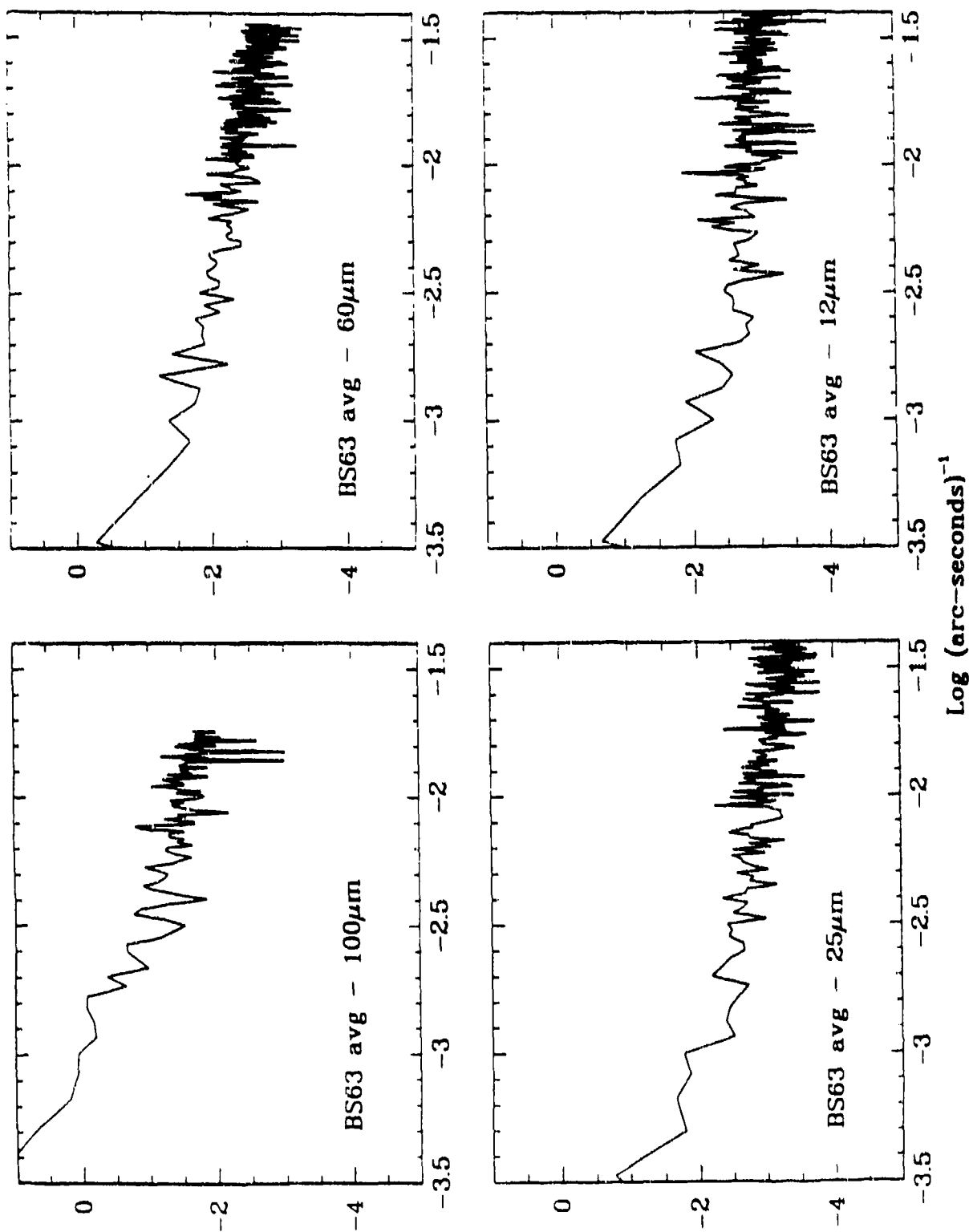
Figure 5-16. The average one-dimensional power spectra for BS63. The power spectra of three individual 12, 25, 60, and 100μm detector data have been averaged to produce these.
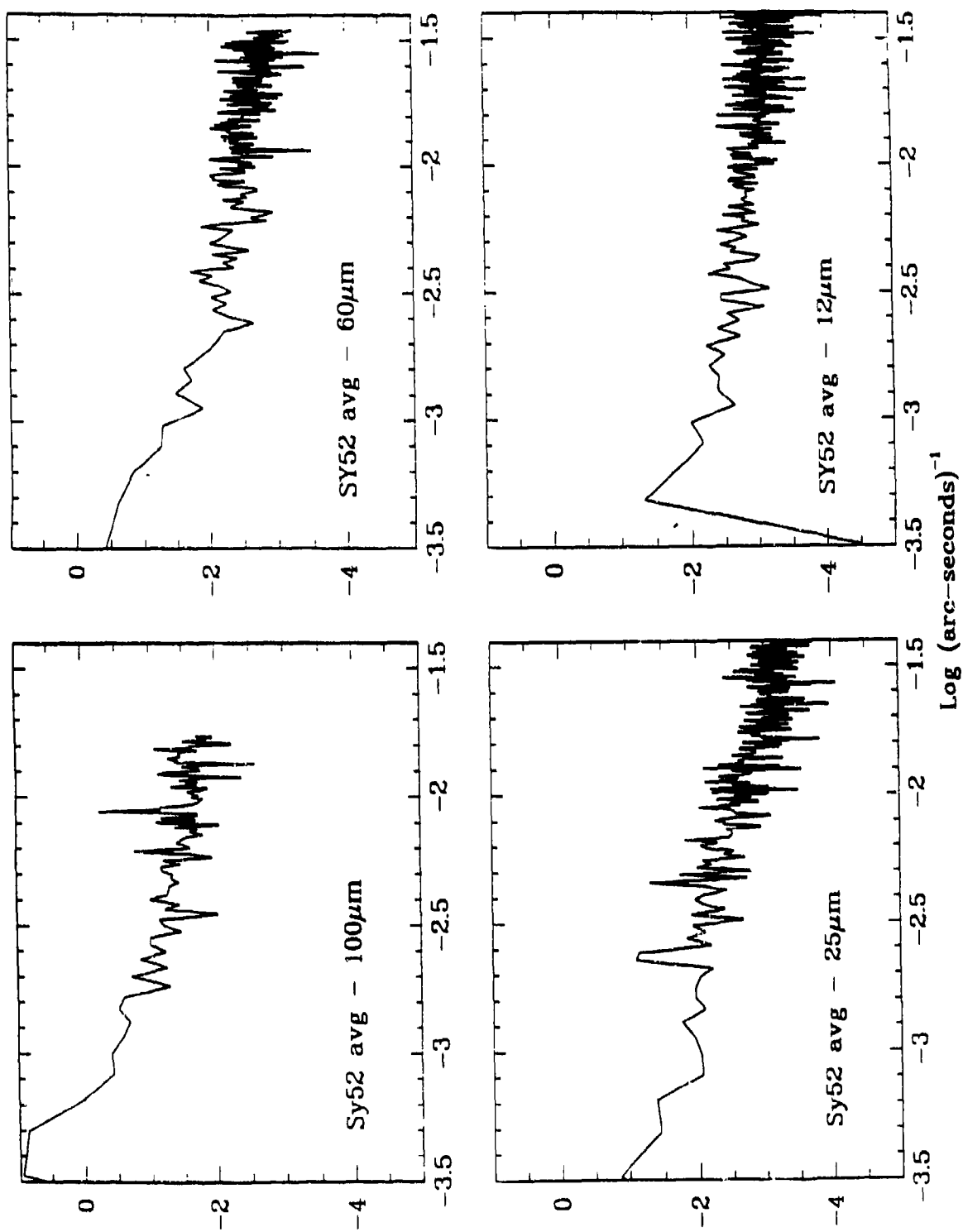
Figure 5-17. The average one-dimensional power spectra for SY52. The power spectra of three individual 12, 25, 60, and 100μm detector data have been averaged to produce these.

179
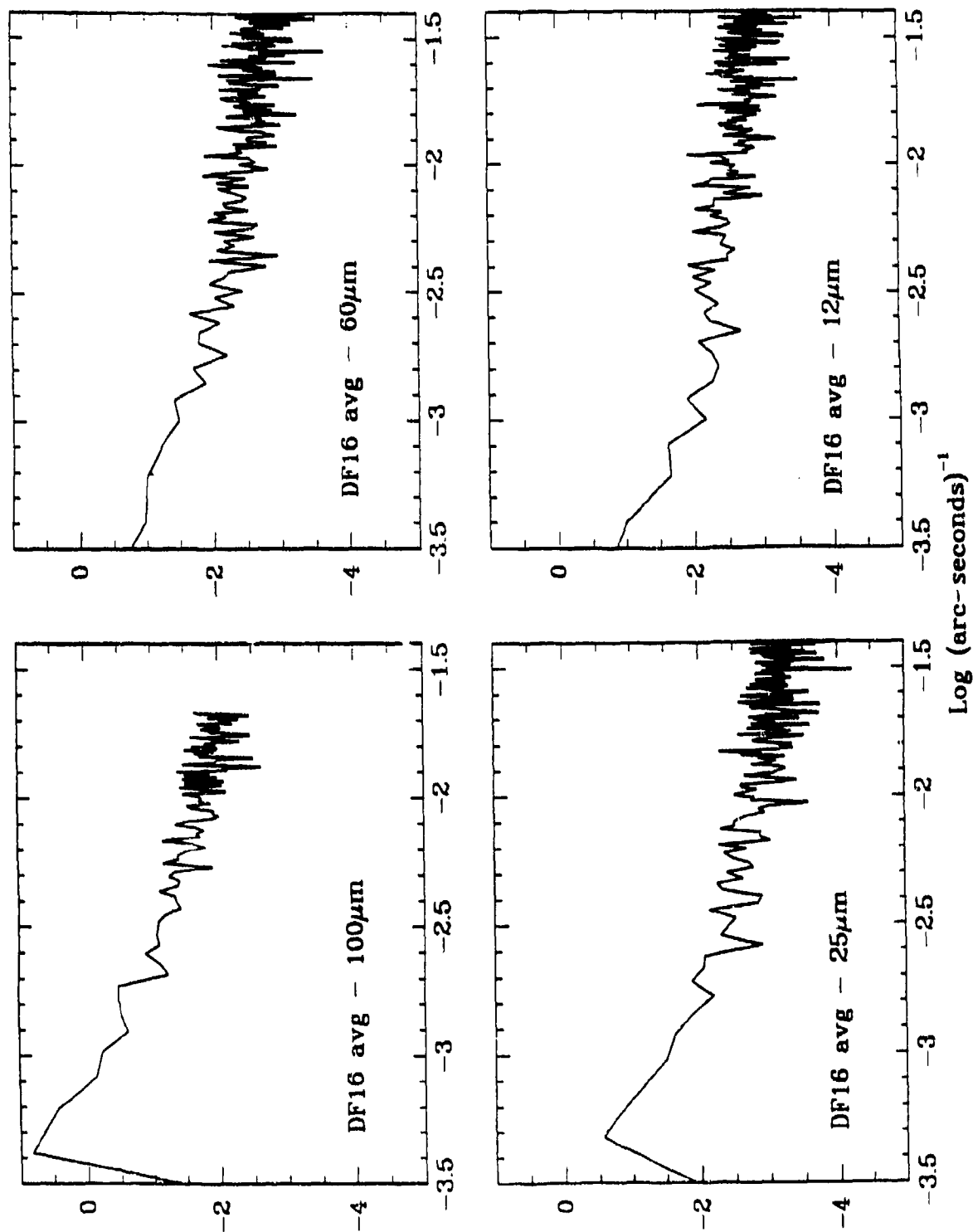
Figure 5-18. The average one-dimensional power spectra for DF16. The power spectra of three individual 12, 25, 60, and 100µm detector data have been averaged to produce these.

Table 5-2. Mean Power Spectral Slopes

	Spectral Range (arc-minutes^{-1})			
	0.01 - 0.025	0.025 - 0.063	0.063 - 0.10	0.10 - 0.20
Skyflux Data:				
$<\alpha(100)>$	-2.5±0.2	-2.8±0.2	-3.7±0.2	-4.1±0.3
$<\alpha(100)>$[a]	-2.9±0.2	-3.2±0.2	-3.6±0.2	-3.1±0.2
$<\alpha(12)>$[b]	-2.7±0.4	-3.2±0.1	...	...
Pointed Observations:				
$<\alpha(100)>$[c]	...	...	-2.9±0.3	-2.9±0.3
Optical CCD Imaging:	0.60 - 0.76 arc-minutes^{-1}			
$<\alpha(0.5)>$[d]	~-3.2			

Notes:

[a] Mean spectral indices for the set of 100μm power spectra exhibiting the least amount of curvature.

[b] No valid high frequency slopes are available for the 12μm spectra because of spatial median filtering of the images.

[c] Spectral slope from Pointed Observations one-dimensional power spectra corrected to two dimensions ($\alpha(2d) \sim \alpha(1d)-1$).

[d] Slope of the two-dimensional power spectra of a cirrus cloud observed at 5000Å .

5.2.5 SUMMARY OF THE FOURIER ANALYSES.

Fourier analysis has yielded a number of quantitative results concerning the characteristic spatial distribution of the infrared cirrus.

- The two-dimensional power spectra of 12μm IRAS Skyflux maps are dominated by the influence of stars in the maps. The power spectra of the 100μm cirrus fields are also influenced by point sources, although to a much smaller degree. Two dimensional median filtering of the 12μm maps can suppress the contribution of the point sources, but such filtering produces artifacts which must be taken into account.

- The two-dimensional power spectra of most 12 and 100μm cirrus fields are azimuthally symmetrical, indicating that the spatial power is distributed homogeneously. That is, the spatial structure of the cirrus is generally not coherent over large spatial scales.

- In 20% of the fields studied, the two-dimensional power spectra exhibit some asymmetries. However, these asymmetries extend over relatively small ranges in spatial frequencies. This suggests that although certain coherent cirrus

structures can be present, such as large linear features, the bulk of the cirrus structure is distributed with no preferred spatial orientation. At least some of the asymmetries observed in the power spectra may be caused by the presence of discrete, compact non-cirrus sources.

- At frequencies below ~0.05 arc-minutes^{-1}, both the 12 and 100µm two dimensional power spectra typically have power law slopes, α, of -2.9 to -3.0. Above 0.05 arc-minutes^{-1}, the slopes of the 100µm steepen to values of ~-3.3 to -3.5. Although we cannot rule out the that steepening is indicative of the small-scale structure of the cirrus, analysis of the Pointed Observation data strongly suggest that the curvature is caused by the contribution of point sources in the images. Because of the compromising effects of median filtering, the high frequency behavior of the 12µm spectra is unknown.

- Because only moderately bright cirrus was serendipitously scanned during the Pointed Observations of IRAS, the cirrus data and resulting power spectra are of relatively low signal-to-noise. The ability to verify that point sources are not present in the scan allows much higher confidence to be placed on the interpretation of the power spectral slopes at the highest frequencies. For the three brightest cirrus regions covered by Pointed Observations, the slopes of the 100µm power spectra up to spatial frequencies of ~0.2 arc-minutes^{-1} agree well with the lower frequency slopes observed in the Skyflux data (α~-2.9). The hot cirrus emission is too faint in these areas to produce useful power spectral information.

These analyses point out the strengths and limitations of the IRAS Skyflux maps and Pointed Observations database for studies of the spatial power distribution of the cirrus. The Skyflux maps cover essentially the entire sky so regions of the brightest cirrus emission may be selected for study. The individual scans of Pointed Observations, although limited in spatial coverage, can be screened for point sources. If all non-cirrus sources, including stars, galaxies and compact HII regions and molecular clouds, could be selectively removed from the two-dimensional Skyflux maps, uncontaminated power spectra could be accumulated. However, we suggest that a better data set to employ for spatial power studies of the cirrus may be the IRAS Survey CRDD. CRDD scans for selected regions covering the brightest cirrus complexes can be selected. As with the Pointed Observation data, these individual scans can be selectively filtered for non-cirrus sources and then combined into two-dimensional images, thus alleviating many of the problems incurred in post-processing the existing Skyflux maps.

5.2.6. THE PROSPECT OF HIGH SPATIAL RESOLUTION STUDIES OF THE CIRRUS USING OPTICAL IMAGING.

As is apparent from the preceding discussions, analysis of the small-scale spatial structure of the cirrus is severely limited by the moderate resolution of the IRAS data and the very low surface brightness of the emission at the shorter wavelengths. An alternative means of probing the cirrus at the resolution required by the CBSD is through very deep optical imaging. Low (1984) was the first to note that the 100µm emission matched the morphology of the optical nebulosity seen in deep blue Schmidt plates of the region around M81 and M82 taken by Sandage (1975). Subsequent investigations have shown that many cirrus regions are visible at optical wavelengths (e.g., de Vries and Le Poole 1985; Guhathakurta and

182

Tyson 1989; Paley et al. 1991). Despite the fact that the optical emission from the cirrus is exceedingly faint, because modern optical CCD detectors have very low noise characteristics and very small pixel sizes, optical observations may ultimately prove to be the best, if not only way to measure the very small-scale structure in this background component.

To assess the use of optical imaging as a probe of the fine spatial structure of the cirrus, we have carried out a pilot program of very deep CCD photometric imaging in B, V, R and I bands of several infrared cirrus clouds (e.g., Guhathakurta, Cutri, van Gorkom and Knapp 1990). An example of the quality of data obtained in this program is shown in Figure 5-19. This 7'x7' V-band image of an infrared-selected cirrus field at 10^h38^m and $+83°58'$ was obtained at the Steward Observatory 2.3m telescope, and was constructed from 20 three minute exposures, each of which was slightly offset relative to the center of the field. The faintest emission visible in the image has a surface brightness of $\mu_V \sim 27$ mag arc-second^{-2}. Detailed structure is apparent down to the scale of a few pixels, or 2 - 3 arc-seconds. A practical problem with utilizing optical images is that the measured high frequency power is dominated by compact sources such as stars and galaxies. Fortunately, such sources can be removed using any of several different techniques, as shown in Figure 5-19. Figure 5-20 shows the azimuthally-averaged two-dimensional power spectra of the cleaned 1038+8358 V-band cirrus field and that of the 14°x14° area surrounding the field at 100μm. The visual spectrum has a slope of $\alpha \sim -3.2$ in the range 0.010 to 0.126 arc-seconds^{-1}, which is consistent with the 100μm slope as well as the global 12 and 100μm slopes discussed above. The V-band power spectrum in Figure 20 represents the highest resolution information on the spatial-intensity distribution of the cirrus currently in existence.
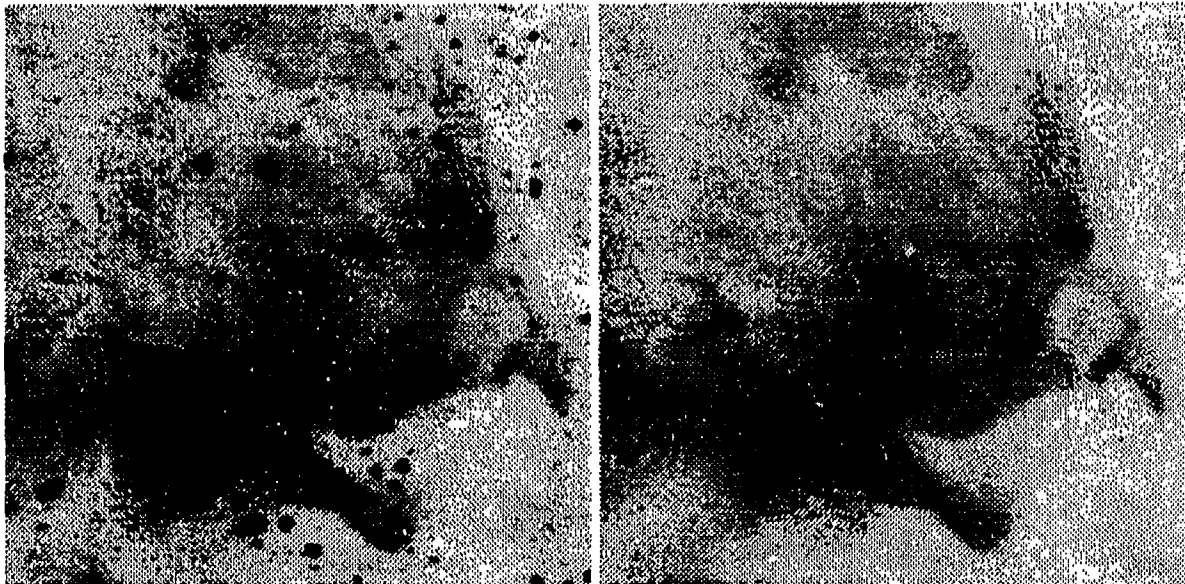
Figure 5-19. The V-band image of the infrared cirrus field 1039+8358 obtained at the Steward Observatory 2.3m telescope. (right) the V-band image after point sources were removed. Both images cover an area of 7'x7'.

A critical assumption that must be validated if the optical emission is to be used as a probe of the small-scale structure of the infrared cirrus for the CBSD is that the optical light accurately traces the distribution of the infrared emitting material. We shall see in the following section that the infrared emission at different wavelengths and the infrared and optical emission are

frequently distributed differently over large scales. However, if the dust grains that produce the optical and infrared emission are governed by similar dynamics within the clouds, then the manner in which the different grain species are spatially distributed can be expected to be similar although not spatially coincident.

## 5.3. SPECTRAL CHARACTERISTICS OF THE INFRARED CIRRUS BACKGROUND.

Because the requirements of the CBSD extend beyond the resolution and wavelength coverage of the IRAS data, it is necessary to extrapolate the properties of the infrared cirrus background to the desired spatial and spectral regimes. This extrapolation must be based on a sound physical understanding of the interstellar cirrus clouds as developed from the IRAS data. In this section, we discuss efforts to characterize the spectral properties of the cirrus and to develop physical models of the infrared emission.

5.3.1 RELATIONSHIP BETWEEN THE 12 AND 100µm CIRRUS EMISSION.

The 12 and 25µm emission from the cirrus clouds has the most direct bearing on the CBSD requirements. However, as was discussed in Section 8, the very low surface brightness of the short wavelength cirrus emission makes it difficult to characterize its spatial properties. If the spatial and spectral relationship between the 12 and 100µm cirrus emission is sufficiently uniform, then it might be possible to use the much brighter 100µm emission as a tracer of the shorter wavelength light.

Some of the highest surface brightness 12µm cirrus emission is found in the prominent cirrus complex covering the north celestial pole (IRAS Skyflux plate 1). To investigate the relationship between the short and long wavelength emission from the cirrus, we generated "color" maps of the region using our enhanced Skyflux plates. This procedure involved first subtracting a mean sky background level from each image and then binning each image 4x4 to improve the signal-to-noise and reduce the influence of point sources. The color maps were constructed by dividing pairs of binned, sky-subtracted images: 100/60µm, 25/12µm and 100/12µm. Color values (ratios) were recorded in a pixel only if there were detections at the wavelengths of both images, otherwise the ratio was entered as zero.

In Figure 5-21 are shown the 100/60µm, 25/12µm and 100/12µm color distributions of the north celestial pole cirrus complex. The ratio of 100 to 60µm surface brightness is remarkably uniform over the cloud, with a median value of I_{100}/I_{60}=11.2 and an RMS dispersion of ~11. This ratio corresponds to a color temperature of 23°K and the dispersion implies a color range of only about 8 - 9°K. Low et al. (1984) for nd that this temperature is approximately the equilibrium temperature that would be achieved by a mixture of silicate and graphite dust grains exposed to the ambient interstellar radiation field. The median 25/12µm brightness ratio in the NCP cloud is ~1.0 with an RMS dispersion of 1.1, corresponding to a color temperature of ~300°K and a range of approximately 150 - 600°K. These very high temperatures are clearly not consistent with those deduced from the longer wavelength emission. Draine and Anderson (1985) first noted the excess short wavelength emission from the cirrus and proposed that it originated in very small dust grains that were transiently heated upon absorption of ultraviolet photons. They successfully modeled the far infrared energy distribution of several cirrus clouds using a population of grains with radii ranging from 0.2 to 0.003µm in which the proportion of the smallest grains (a < 0.01µm) is elevated relative to the "standard" size distribution of interstellar grains reported by Mathis, Rumpl and Nordsieck (1977). Desert, Boulanger and Puget (1990) have suggested that at least a portion of the 12µm cirrus emission may arise due to fluorescence in macro-molecules such as polycyclic aromatic hydrocarbons (PAHs).
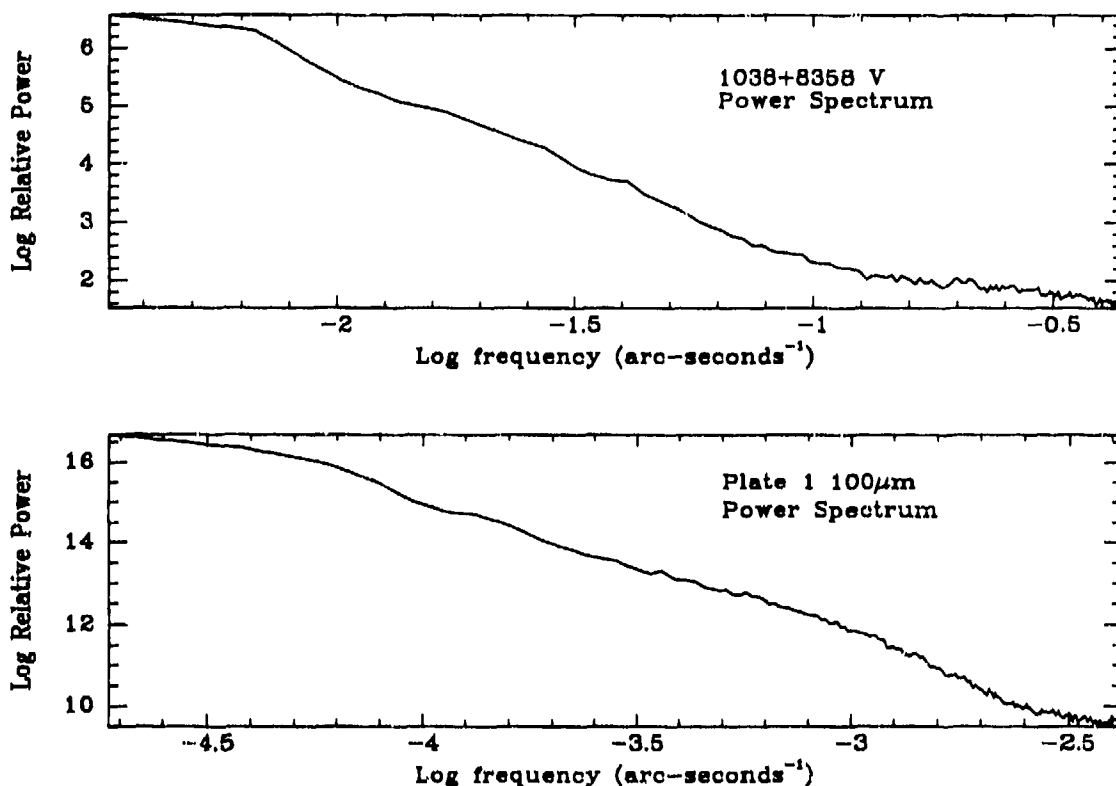
Figure 5-20. (top) The spatial power spectrum of the clean V-band cirrus image shown in Figure 5-16. (bottom) The power spectrum of the 100μm field surrounding 1038+8358.

The 100/60μm and 25/12μm colors are surprisingly uniform throughout of the NCP cloud, as evidenced by the relatively small dispersions in the color distributions. The variation in the 100/12μm color is quite large, however. The 100/12μm surface brightness ratio in the NCP cloud ranges from values as low as ~7 to as much as 300, representing real color variations of more than a factor of 40. These variations are not random throughout the cloud, but are spatially coherent. From a practical standpoint, the large range in 100/12μm surface brightness means that it will not be possible, in general, to trace the fainter 12μm emission with the brighter 100μm light. Physically, the color gradients imply there must be significant spatial variations in the dust grain populations throughout the cloud. It is unlikely that the color variations could be due to local anisotropies in the radiation field or optical depth variations because both the 100/60 and 25/12μm colors are relatively uniform across the cloud.
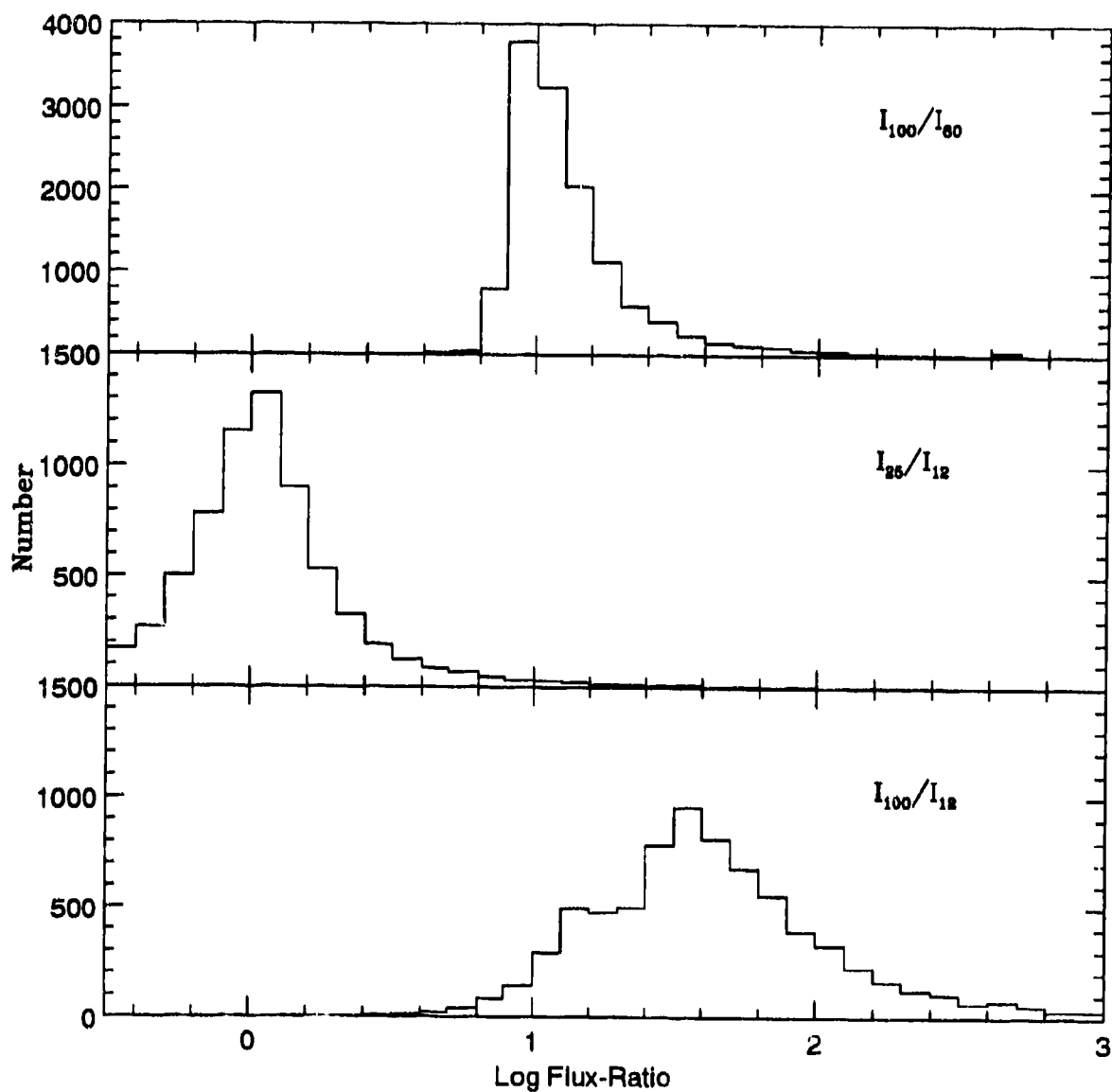
Figure 5-21. The distribution of colors in the North Celestial Pole cirrus field (Skyflux plate 1).

5.3.2 THE INFRARED AND OPTICAL PROPERTIES OF A SAMPLE OF COMPACT CIRRUS SOURCES.

An in-depth analysis of the emission from a selection of bright, compact $100\mu m$ cirrus sources constituted the major portion of Elizabeth Paley's Master's Thesis at the University of Arizona. This work has since been published in the *Astrophysical Journal* (Paley et al. 1991)

and we have appended a reprint of that article to this report. Here, we summarize the basic findings of that paper.

The objective of this work was to identify and study the properties of a sample of relatively compact, isolated cirrus condensations. Candidate sources were selected from the IRAS Point Source Catalog (PSC) with the following criteria: a) detected only at 100µm, b) $F_{100} \geq$ 2.5Jy and c) $|b|>40°$. Of the 170 PSC sources with these attributes, 19 were identified with galaxies, planetary nebulae or solar system objects. Examination of the 151 remaining sources on the Skyflux maps showed them to be tight condensations within larger cirrus complexes. Virtually all of these knots were also visible in the 60µm IRAS maps. It is likely that 60µm fluxes were not included in the PSC because these sources were marginally resolved by IRAS. The locations of the cirrus sources were also examined on the National Geographic/Palomar Observatory (POSS) and European Southern Observatory (ESO) Sky Survey plates. 119 of the 151 cirrus clouds were visible on the blue, red or both plates as faint, diffuse nebulosities.

Improved infrared surface brightness measures were obtained for a subset of the brightest 29 sources in the cirrus sample using IRAS ADDSCAN and two-dimensional survey co-added data. All of the sources had measurable emission at 60µm, and 11 were also detected at 12 and/or 25µm. The infrared spectral energy distributions of the 3 or 4-band detected sources (Figure 5 in Paley et al.) illustrate the presence of the excess 12 and 25µm emission that was discussed in the preceding section, and suggest that the cirrus emission must be composed of *at least* two thermal components. We used a simple two-temperature dust model to estimate the physical temperatures of these two components and their luminosities. Emissivities proportional to $\lambda^{-1.5}$ were assumed for the grains in each component, reflecting a mixture of silicate and graphite. The average physical temperature found for the 60-100µm or warm dust component was found to be 22.8±0.3°K, and that for the 12-25µm or "hot" dust was 173±8°K. The very small dispersion in the temperature of the warm dust components implies that the temperature is virtually identical in these clouds which lie in very different regions of the sky. This suggests that there is only a single type of warm dust particle that accounts for the bulk of the observed luminosity in these clouds. The ratio of the energy emitted from the hot component to that from the warm component ranges from ≤0.17 to 0.60, indicating that the amount of hot dust relative to the warm dust varies considerably from cloud-to-cloud. This is not too surprising considering the large 12-100µm color variations seen in a single cloud (c.f. 5.3.1).

A qualitative assessment of the optical brightness and color of the cirrus sources was made by examining the Sky Survey plates. The diffuse blue nebulosity associated with the cirrus sources presumably arises due to scattering of interstellar radiation field photons by the dust grains. Therefore, there should be a close correlation between the surface brightness of blue and 100µm light. We found a significant range in the ratio of blue-to-100µm emission from cloud-to-cloud and within cloud complexes. The complex relationship between the scattered blue light and the infrared emission suggests that there may be a population of dust grains in the cirrus that scatter and radiate very efficiently, and are therefore too cold to have been detected by IRAS. Such a "cold" grain component would have to have a characteristic temperature of <15°K. The existence of cold grains has since been corroborated by Wright et al. (1991) who reported that the spectrum of the integrated galactic emission observed by COBE could be fit by a combination of two blackbodies, one with a temperature of 20.4°K and one at ~5°K. Ironically, the only way to map the distribution of the cold grains may be with optical imaging.

Surprisingly, several of the cirrus clouds appeared brighter on the red Sky Survey plates than on the blue, suggesting that there is excess red emission associated with the cirrus. Guhathakurta and Tyson (1989) measured the optical surface brightness of several cirrus clouds from deep CCD images and found colors that were too red to be explained by classical scattering processes alone. The B-V and V-R colors they measured were similar to the red colors observed in several bright galactic reflection nebulae (Witt and Schild 1988). In those nebulae, the colors are believed to result from a broad luminescence feature of very small hydrogenated amorphous carbon grains (HACs). If the HAC particles are the small grains responsible for the 12 and 25μm emission from the cirrus, then one might expect there to be a correlation between red optical colors and the proportion of the hot grains in the clouds. No such correlation was observed in our data.

5.4 REFERENCES

Beichman, C.A., Neugebauer, G., Habing, H.J., Clegg, P.E. and Chester, T.J. (1985). *IRAS Catalogs and Atlases Explanatory Supplement*, U.S. Government Printing Office.

Desert, F.-X., Boulanger, F. and Puget, J.L. (1990). *Astron. Astrophys.*, **237**, 215.

Draine, B.T and Anderson, N. (1985). *ApJ*, **292**, 494.

Gautier, T.N., Boulanger, F., Perault, M. and Puget, J.L. (1992). *AJ*, **103**, 1313.

Guhathakurta, P. and Tyson, J.A. (1989). *ApJ*, **356**, 773.

Guhathakurta, P., Cutri, R.M., van Gorkom, J.H. and Knapp, G.R. (1990). *BAAS*, **23**, 1245.

Heiles, C. (1976). *Astron. Astrophys. Supplement*, **46**, 333.

Heiles, C., Reach, W.T. and Koo, B.-C. (1988). *ApJ*, **332**, 313.

Herter, T., Shupe, D.L. and Chernoff, D.F. (1990). *ApJ*, **352**, 149.

Low, F.J. (1984). Invited talk, American Astronomical Society meeting, Baltimore, *BAAS*, **16**, 5111.

Low, F.J. *et al.* (1984). *ApJLett*, **278**, L19.

Magnani, L., Blitz, L. and Mundy, L. (1985). *ApJ*, **295**, 402.

Mathis, J.S., Rumpl, W. and Nordsieck, K.H. (1977). *ApJ*, **217**, 425.

Meyerdiecks, H., Heithausen, H. and Reif, K. (1991). *Astron. Astrophys.*, **245**, 247.

Paley, E.S., Low, F.J., McGraw, J.T., Cutri, R.M. and Rix, H.-W. (1991). *ApJ*, **376**, 335.

Sandage, A. (1975). *AJ*, **81**, 954.

de Vaucouleurs, G. (1960). *The Observatory*, **80**, 106.

de Vries, C.P. and Le Poole, R.S. (1985). *Astron. Astrophys.*, **145**, L7.

Witt, A. and Schild, R.E. (1988). *ApJ*, **325**, 837.

Wright, E.L. *et al.* (1991). *ApJ*, **381**, 200.

6 THE COMPOSITE IMAGE MODULE

To form composite images a module has been created called COMPOSE. Compose takes two CBSD image object files and sums the two images. The code has been made general enough to take any of the three file type (HDR0, HDR1, and HDR2) as input or output. Different file type can easily be mixed. Also the code will accept either of the two current Intensity units, either Jy/sr or $W/cm^2/\mu m/sr$. The program is interactive, the user answers prompts at the command line. An illustration of a typical dialog is given b   .w. User inputs are underlined.

While COMPOSE is not intended to be anything other than a "quick look", it does incorporate the following features:

- The code provides a complete report of what it finds and is intended to allow the user to customize the final image.

- Scaling parameters are provided to allow the enhancement of certain image features for display purposes.

- If the wavelengths in the two images do not agree or if the wavelength is zero, the user will be prompted to input a value in microns.

- The user is prompted for the units type because the CBSD does not give a uniform string value.

- The user has the option of writing a CBSD header on the image or no header at all. It may be useful to ignore the header if the images are to be used in commercial packages. A converter to the Tagged Image File Format (TIFF) is also available.

- An option is provided to allow the user to force a minimum value. This allows the user to set a minimum threshold. The dynamic range of a composite image can easily span more than 8-bits regardless of which scaling type is selected. This again, allows the user to enhance certain features. If this option is selected the user is prompted for a minimum (threshold) value.

- The user has the option to select how the data are encoded into the image file. Either a linear scale corresponding to HDR1 can be selected (LIN), a logarithmic scale corresponding to HDR2 (LOG), or automatically select the image scaling (AUT) is possible. Also, no scaling can be selected (FLT) and a real, 4-byte, HDR0, floating point numbers are written to the file.

Below are the sample input images along with the output composite image.

Table 6-1. Input file for CBAMP.

```
256 256
10.00 1
19.5,10, 1992
42.5,72.3
0.0
TDT
Sun
-19.59515
0.0234375
```

Table 6-2. Input file for CBZODY.

```
256 256
10.
19,10,1992
12,0,0.0
42.5,72.3
0.0
0.0234375
204.43975
-10.172388
1
```
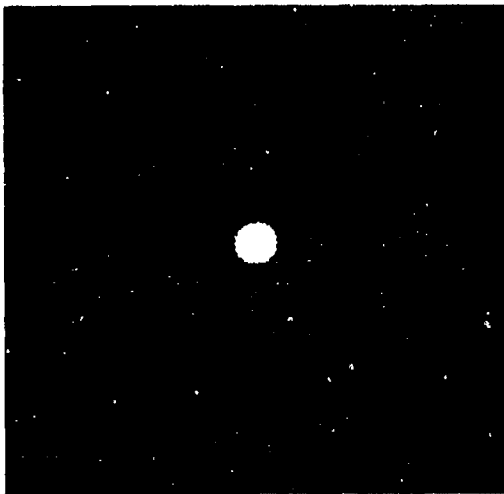

Figure 6-1. Output file from CBAMP using inputs of Table 6-1.
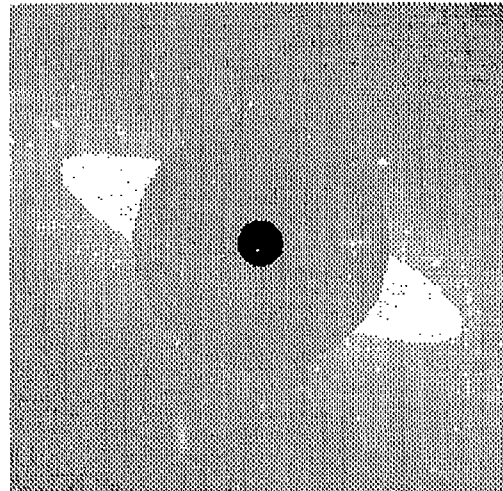
Figure 6-2. Output file from CBZODY using the inputs of Table 6-2.

192

Table 6-3. Sample run of COMPOSE.

```
Input first file name: CBAMPIMG.017
Input first scale factor: 1
Input second file name: CBZ55IMG.017
Input second scale factor: 1
Input output file name: TEST
Write CBSD File Header (Y/N): Y
Input image description:  cbamp + cbzody
Image 1
 Image size: col,rows            256          256
 JD      2448915.00000000
 CBSD Header information:
  Type  HDR2
  Description   SMPA Gnom SU                   235Ast
  bzero,bscale     0.100000E-03   0.646195E-01
  xzero,xscale     207.440       -0.234375E-01
  yzero,yscale     -13.1724       0.234375E-01
 Central wavelength       10.0000000000000
 Image 1 Intensity units    Jansky/sr
 Input units type:
  1=Jansky/sr
  2=W/cm2/um
==> 1
Image 2
 Image size: col,rows            256          256
 JD      2448915.00000000
 CBSD Header information:
  Type  HDR2
  Description   CBSD/PC ZODY(Brd+Bnd) 10/19/1992
  bzero,bscale     259971.        0.178466E-01
  xzero,xscale     207.440       -0.234375E-01
  yzero,yscale     -13.1724       0.234375E-01
 Central wavelength       10.0000000000000
 Image 1 Intensity units    Jansky/sr
 Input units type:
  1=Jansky/sr
  2=W/cm2/um
==> 1
Output units type:
  1=Jansky/sr
  2=W/cm2/um
==> 1
units              1
 1          1    1.00000000000000
 2          1    1.00000000000000
 Min and Max Image 1          0.000000000000000
3005840359424.00
 Min and Max Image 2          0.000000000000000
8870728704.00000
 Min and Max for the pair    259970.781250000
3005840359424.00
Do you want to force a minimum (Y/N): n
Linear, Log scaling, Auto, or Real (LIN/LOG/AUT/FLT): AUT
```

193

Figure 6-3. Combined output of CBAMP and CBZODY using the COMPOSE module.

7.0 SUMMARY

The preceding chapters speak for themselves: some excellent work has been done here, some highly valuable new tools have been created, and knowledge has been advanced.

The CBSD development program covered by this Final Report has been a notable success. Whereas the atmospheric models distributed by the Air Force Phillips Laboratory now have a lineage of several decades of development effort, the CBSD has been completely developed over a very short 3½ year period.

At MRC/Nashua, we are proud of this achievement. Clearly, we are much more intimately familiar with all the troubles we struggled with and the turmoil we encountered (and, yes, created too !) during this process than anyone on the outside possibly can be. Yet, we can also recognize that this has been a remarkably productive development effort. The models described in this report are now respectably solid and mature, and are in routine use for a variety of applications. Although they will continue to be refined and extended, they are able to be distributed now without great apprehension and they address important problems.

In retrospect, we also realize that the adjunct CBSD/PC development has been a valuable "forcing function" for much of the progress made. Not only have phenomenologically sound models been developed and validated, they have also been subject to considerable optimization effort to make them run fast ! A fast-running model will always experience more usage than a slow-running model. Somewhat to our own surprise, we see that we ourselves have benefited during much of these development cycles by having fast-running models to support us.

This program could not have been nearly so successful without the far-ranging collaborative support of Drs. Stephan D. Price and Frank O. Clark at the Air Force Phillips Laboratory. Both were bountiful sources of creative ideas, constructive criticism, and sound technical direction.

We must also acknowledge the invaluable support of many people at the JPL/CalTech *Infrared Processing and Analysis Center* (IPAC). We were not only the beneficiaries of abundant technical consultation support from many scientists there, but we were also frequently given pre-release access to new IRAS data products and even to some data sets which were not generally releasable.

APPENDIX A: IMAGE PROJECTIONS.

In the various CBSD modules three different projections can be specified, however, the set is not common to all modules. The projections are:

1. Rectangular,
2. Gnomonic, and
3. Mollweide.

Most of the definitions are for Right Ascension and Declination, by they apply equally to ecliptic and Sun centered ecliptic coordinates.

A.1 Rectangular.

The rectangular projection is the simpliest of all projections with sets of parallel and right angle lines. In CBSD we use the following definition for rectangular converted from a spherical coordinate system for an image of N_x (columns) by N_y (rows).

$$x = (\lambda - \lambda_o)\cos\varphi_o$$
$$y = \varphi$$

(A-1)

where:

λ = longitude,

λ_o = central (reference) longitude,

φ = latitude, and

φ_o = central (reference) latitude.

The central longitude and latitude are taken to be the center of the image and the x and y values are taken as displacements from the center of the image. The x and y values are converted to pixel coordinates by.

$$line = \frac{N_y}{2} + \text{Int}(y)$$

$$sample = \frac{N_x}{2} + \text{Int}(x)$$

(A-2)
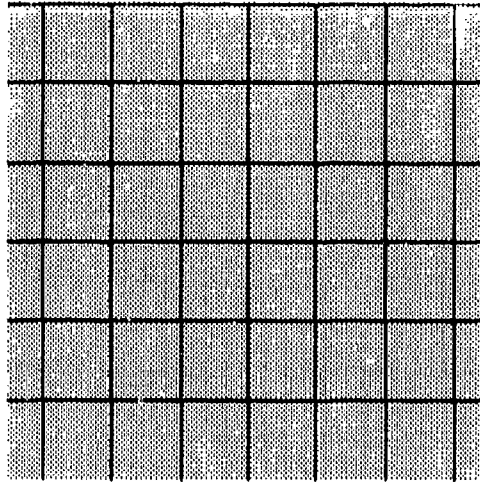
Figure A-1. Grid lines associated with the rectangular projection.

A.2 Gnomonic

The Gnomonic projection is the perspective of the globe from the center onto a plane tangent to the surface.

$$k' = \frac{1}{\cos c}$$
$$\cos c = \sin \varphi_o \cdot \sin \varphi + \cos \varphi_o \cdot \cos \varphi \cdot \cos(\lambda - \lambda_o)$$
(A-3)

and then:

$$x = k' \cdot \cos \varphi \cdot \sin(\lambda - \lambda_o)$$
$$y = k' \cdot [\cos \varphi_o \cdot \sin \varphi - \sin \varphi_o \cdot \cos \varphi \cdot \cos(\lambda - \lambda_o)]$$
(A-4)

λ = longitude,

λ_o = central (reference) longitude,

φ = latitude, and

φ_o = central (reference) latitude.

197

where again to convert to pixels:

$$line = \frac{N_y}{2} + \text{Int}(y)$$

$$sample = \frac{N_x}{2} + \text{Int}(x)$$

(A-5)
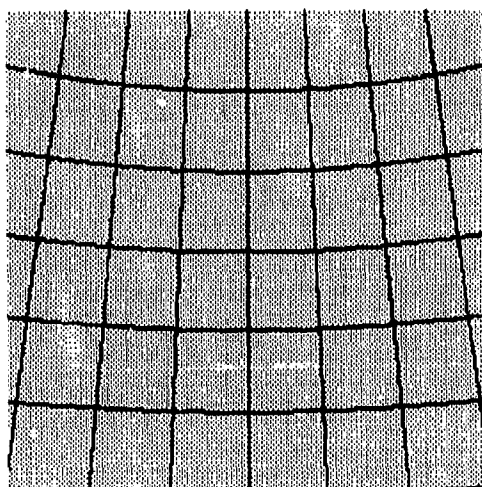
Figure A-2. Grid line associated with gnomonic projection.

A.3 MOLLWEIDE

The Mollweide projection is an equal-area, pseudocylindrial projection of the Earth within an ellipse. It has been termed Homalographic oe Homolographic. The parallels of latitude are straight line, but are not equally spaced, while the longitude lines are ellipses which meet at the poles.

$$x = (8^{\frac{1}{2}}/_\pi) \cdot (\lambda - \lambda_o) \cdot \cos\theta$$

$$y = 2^{\frac{1}{2}} \cdot \sin\theta$$

(A-6)

where the parametric angle θ is defined by:

$$2\theta + \sin 2\theta = \pi \cdot \sin\varphi$$

(A-7)

We have the usual definitions.

λ = longitude,

λ_o = central (reference) longitude,

φ = latitude, and

φ_o = central (reference) latitude.

In pixel coordinates

$$line = \frac{N_y}{2} + \text{Int}(y)$$

(A-8)

$$sample = \frac{N_x}{2} + \text{Int}(x)$$
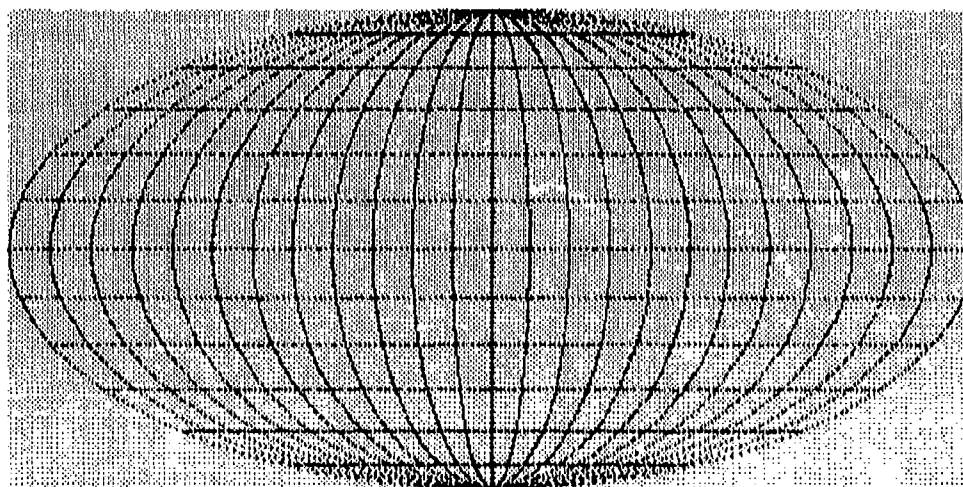
Figure A-3. Grid lines associated with the Mollweide all-sky projection.

199

APPENDIX B: CBSD HEADER FORMAT.

Table B-1 presents Version 2.2 of the CBSD Image Header format. New to Version 2.2 are:

1. HDR0, and
2. the DATA_MIN and DATA_MAX fields.

The HDR0 identification allows for the generation of 4-byte, floating point images. When using HDR0 BZERO is set to 0.0 and BSCALE is set to 1.0. The fields DATA_MIN and DATA_MAX were added for porgaming convience. No longer is it necessary to search through the image find the minimim and maximum values.

Table B-1. CBSD Image Data Object Header Format--Version 2.2.

Bytes	Variable	Size	Description
1:4	HDR	4-byte string	Header identification, either: HDR0 (4-byte real image), HDR1 (1-byte integer image), or HDR2 (1-byte integer image).
5:6	NCOLS	2-byte integer	Number of image columns.
7:8	NROWS	2-byte integer	Number of image rows.
9:10	KWAVE1	2-byte integer	Starting wavelength x 100.
11:12	KWAVE2	2-byte integer	Ending wavelength x 100.
13:16	KJULIN	4-byte integer	Julian Date x 100.
17:20	BZERO	4-byte real	Intensity of 0 byte pixels.
21:24	BSCALE	4-byte real	Intensity scale factor: for HDR0: Intensity = Image Value for HDR1: Intensity = BZERO+BSCALE*(Image Byte Value) for HDR2: Intensity = BZERO*10**(BSCALE*Image Byte Value).
25:28	DATA_MIN	4-byte real	Minimum data value with units set by ITYPE.
28:32	DATA_MAX	4-byte real	Maximum data value with units set by ITYPE.
33:36	XZERO	4-byte real	X coordinate of the lower left pixel.
37:40	XSCALE	4-byte real	X increment of the image space: (True X-coord) = XZERO + XSCALE*NCOL where the left edge corresponds to NCOL=0.
41:44	VERSION	4-byte string	Version number. Example 2.20. If this field is blank it is a version before 2.2
45:56	---	12-bytes	Reserved.
57:60	YZERO	4-byte real	Y coordinate of the lower left pixel.
61:64	YSCALE	4-byte real	Y increment of the image space: (True Y-coord) = YZERO + YSCALE*NROW where the top edge corresponds to NROW=0.
65:128	---	64-bytes	Reserved.
129:144	ITYPE	16-byte string	Name for Intensity units (Jy/sr) or (W/cm2/um/sr).
145:160	XTYPE	16-byte string	Name for X-axis type.
161:176	YTYPE	16-byte string	Name for Y-axis type.
177:224	---	48-bytes	Reserved.
225:256	IMDSC	32-byte string	Data description.

POINT SOURCE MODEL OF THE MID-INFRARED SKY: VERSION 3

This program is designed to model the point source sky in the mid-infrared. It has been compared with the IRAS 12 and 25 μm observations, and, by using a library of complete 2.0–35.00μm low-resolution spectra, we have expanded the wavelength coverage of the model so that it can operate through any arbitrary filter lying entirely within this wavelength.

The model consists of two broad components:

1. GALACTIC

The Galactic section of the program is within the main body of the program. The Galaxy is assumed to be made up of 5 components:

- An exponential disk, comprising both young and old populations, exponential in both the R and z directions, and truncated at a distance R_{max}. The disk is axisymmetric. All types of star are assumed to have the same radial scale length; younger, more massive stars are assumed to have smaller scale heights than the older stars.

- Spiral arms—these represent the non-axisymmetric disk component—they are assumed to consist of young, massive stars. A four arm logarithmic spiral has been used to represent the arms.

- Molecular Ring—this is an axisymmetric disk-like component introduced to represent an over-density of IRAS sources coincident with the molecular ring. A Gaussian function, peaking at R_{ring} has been used to represent this component.

- Bulge—an axisymmetric, moderately flattened component, concentrated in the region within $\sim 0.25R_0$ of the Galactic center. This has been represented by $\rho = \rho_0 x^{-1.8} \exp(-x^3)$, where $x = \sqrt{r^2 + k^2 z^2}/R_B$, k is the axial ratio, and R_B is the "bulge radius". The bulge is assumed to consist only of old stars, but the bulge does contain high metallicity stars, meaning that high infrared luminosities can occur in AGB stars.

- Halo—an axisymmetric, slightly flattened diffuse component, considered to be made up of old metal poor stars. This is the component described by the de Vaucouleurs $r^{\frac{1}{4}}$ law. Because of the complex nature of the deprojection of this law, the density has been calculated by means of a lookup table HALO.DAT.

203

Extinction is included at all relevant wavelengths and the dust causing the extinction is assumed to have a distribution exponential in both R and z, with an extinction of 0.08 mag kpc^{-1} at K in the solar neighborhood. The following are some of the general parameters that have been used:

- $R_0 = 8.5$ kpc   —the Galactocentric distance

- $R_{max} = 15.0$ kpc   —the disk truncation distance

- $R_{ring} = 0.45R_0$ —the ring radius

- $R_B = 2.0$ kpc   —the bulge "radius"

- $R_e = 2.8$ kpc   —the halo effective radius

- $h = 3.5$ kpc   —the disk scale length

- $\rho_{halo} = 0.002\rho_{disk}$ in the solar neighborhood

- $[12] = 4.034 - 2.5\log_{10}(S_{12})$ —definition of the 12 μm magnitude

- $[25] = 2.444 - 2.5\log_{10}(S_{25})$ —definition of the 25 μm magnitude

- $[60] = 0.490 - 2.5\log_{10}(S_{60})$ —definition of the 60 μm magnitude

- note that these magnitudes are color corrected as for a hot (10000 K) star, and S_λ is an IRAS PSC flux expressed as a flux density in Janskys by assuming that $\lambda F_\lambda = const.$

The Galactic section of the program works by assuming that the Galaxy consists of ntype different types of source. [In this version of the program, ntype = 87.] Each type of source is represented by an absolute magnitude, a dispersion in absolute magnitude, a local density, and a scale height. There are also corresponding numerical "masks", describing whether each type of source is present in a particular component.

The basic algorithm that has been used consists of looking along a ray, starting at the sun, and stepping along the ray until the "edge" of the Galaxy is reached. At each step, the volume (assuming an area of 1 square degree) is calculated, and the contribution from each component calculated and added to count buffers. To facilitate looking at extended areas, an option is included which instructs the program to look at a grid of areas specified by the user. An example of this will be given later. This is desirable for comparison with IRAS data since in general, an area of much larger than 1 square degree must be used. At each point along each ray, the total line-of-sight extinction is calculated and the apparent brightness of each source diminished by the appropriate amount.

2. EXTRAGALACTIC

The extragalactic point source sky has been modeled by assuming that the galaxies are homogeneously distributed. This part of the calculation is performed in the subroutine GALAXIES.FOR. The calculation starts by assuming a 60 μm luminosity function of the form given by Soifer *et al.* [*Ap. J.*, **320**, 238]. This luminosity function has been split into four components (blue galaxies, red galaxies, seyferts and quasars) and corresponding [12]−[25] and [25]−[60] colors and standard deviations in color determined, along with a representative complete spectrum for each of these four classes of galaxy. The 12 and 25 μm luminosity functions (and if necessary the luminosity function through an arbitrary filter) are then simply calculated by transforming the 60 μm luminosity function.

The calculation is again performed by integrating along a ray. Since the galaxies are assumed to be homogeneously distributed, only one ray is ever necessary, and the result is scaled to the appropriate area passed from the main program. At each step along the ray, the contribution from each magnitude interval of the luminosity function is calculated, and added to the count buffers. The integration through space includes cosmological effects (but no evolution) and the following assumptions have been made: cosmological constant $\Lambda_0 = 0$; $\Omega_0 = 1$; Hubble constant $H_0 = 75$ km s^{-1}Mpc^{-1}. The result is not sensitive to choice of Ω_0 unless magnitudes very much fainter than IRAS are used. The integration starts at redshift $z = 5 \times 10^{-6}$ (i.e. $D = 20$ kpc) and stops at $z = 5.0$.

There is still controversy about luminosity evolution of galaxies. Further, the near-infrared colors of galaxies are not yet fully-determined; therefore, the model is designed not to permit calculation of the extragalactic contribution for broadband wavelengths shortward of 12 μm, nor for custom filters with effective wavelengths less than 5.0 μm.

NON-STANDARD FILTERS

Filters with non-standard bandpasses within the 2.0–35.0 μm wavelength scale are dealt with as follows. Firstly, the user must have a file with the transmission at each of the nwav wavelengths [note that nwav=331.] Such a file can be produced with the auxiliary program INTLRS.FOR, an example of the use of which will be given later. The main program, when asked to process a non-standard filter, calls the subroutine SPECIAL.FOR. This subroutine takes as input from the main program an array of absolute 12 μm magnitudes. There are ntype magnitudes in this array. The subroutine

then obtains the characteristic spectrum for each of the ntype sources from the auxiliary file LIBRARY.DAT for the Galactic sources, or GALAXY_LIBRARY.DAT for the extragalactic sources. The subroutine then calibrates each of the nwav spectra to F_λ units (W m^{-2} μm^{-1}), based on the input absolute magnitude. It then integrates the flux through the specified bandpass. For convenience, an effective wavelength for the filter is determined (assuming $\lambda F_\lambda = const$) and a corresponding magnitude scale defined. The subroutine returns an array of "magnitudes" through the special filter, along with the new transformation back to in-band flux. In the final output, the user always has the option of either in-band flux or magnitude. Throughout the integrations along the line-of-sight, magnitudes are always used.

Note that INTLRS.FOR resides in a different subdirectory from the main programs SKY.FOR and SPECIAL.FOR. Consequently, after running INTLRS.FOR to generate the customized response file, be sure to move this file to the upper level directory, [.model].

DETAILS OF THE DIRECTORIES AND FILES

The following files are supplied:

SKY.FOR	the main program
SKY.EXE	executable form of SKY
SPECIAL.FOR	the subroutine which deals with the non-standard filters
GALAXIES.FOR	the subroutine which performs the galaxy integration
BREAKDOWN.DAT	the breakdown of extragalactic sources into the 4 types
LINK.COM	a command file to compile and link the program
SETUP.COM	command file to setup logical names
INTLRS.FOR	program to define user's filter at the nwav wavelengths
INTLRS.EXE	executable form of INTLRS
LIBRARY.DAT	galactic source spectral library
GALAXY_LIBRARY.DAT	extragalactic source spectral library
LIBRARY.FOR	program which creates *LIBRARY.DAT
LIBRARY.EXE	executable form of LIBRARY
*.AVE	91 spectra used by LIBRARY.FOR
EXTINCT.DAT	representation of interstellar extinction from 2.0–35.0 μm
HALO.DAT	lookup table for the $r^{\frac{1}{4}}$ law
TABLE.FOR	program that creates HALO.DAT
TABLE.EXE	executable form of TABLE
POLINT.FOR	subroutine called by TABLE
QROMB.FOR	subroutine called by POLINT
MAKE.COM	a command file to compile and link the programs to create the halo lookup table
TRAPZD.FOR	subroutine called by POLINT
LUMA.FOR	standalone subsection of SKY.FOR for Galactic sources
LUMA.EXE	executable form of LUMA
GALZA.FOR	standalone form of GALAXIES.FOR for extragalactic so urces
GALZA.EXE	executable form of GALZA
EXPLAIN.TEX	this file (actually in LATEX)

The organization of directories (with sizes in VAX blocks) in account USER is as follows:

Directory [USER.MODEL]

```
EXPLAIN.TEX;1    53/54
GALAXY.DIR;1     1/3
LINK.COM;1       2/3
LRS.DIR;1        1/1
LUMA.EXE;1       165/165
LUMA.FOR;1       115/117
NORM.DIR;1       1/3
SETUP.COM;1      1/3
SKY.EXE;1        167/168
SKY.FOR;1        117/117
SPECIAL.FOR;1    19/21
```

Directory [USER.MODEL.GALAXY]

```
BREAKDOWN.DAT;1    17/18
GALAXIES.FOR;1     26/27
GALZA.EXE;1        132/132
GALZA.FOR;1        45/45
```

Directory [USER.MODEL.NORM]

```
HALO.DAT;1      4/6
MAKE.COM;1      1/6
POLINT.FOR;1    2/6
QROMB.FOR;1     1/6
TABLE.EXE;1     11/12
TABLE.FOR;1     3/6
TRAPZD.FOR;1    1/6
```

Directory [USER.MODEL.LRS]

```
EXTINCT.DAT;1           6/6
GALAXY_LIBRARY.DAT;1    11/12
INTLRS.EXE;1            12/12
INTLRS.FOR;1            15/15
LIB.DIR;1               7/9
LIBRARY.DAT;1           226/228
```

Directory [USER.MODEL.LRS.LIB]

A25V.AVE;1	6/6	AGBC01.AVE;1	6/6	AGBC03.AVE;1	6/6
AGBC05.AVE;1	6/6	AGBC07.AVE;1	6/6	AGBC09.AVE;1	6/6
AGBC11.AVE;1	6/6	AGBC13.AVE;1	6/6	AGBC15.AVE;1	6/6
AGBC17.AVE;1	6/6	AGBC19.AVE;1	6/6	AGBC21.AVE;1	6/6
AGBC23.AVE;1	6/6	AGBC25.AVE;1	6/6	AGBCI01.AVE;1	6/6
AGBCI03.AVE;1	6/6	AGBCI05.AVE;1	6/6	AGBCI07.AVE;1	6/6
AGBCI09.AVE;1	6/6	AGBCI11.AVE;1	6/6	AGBCI13.AVE;1	6/6
AGBCI15.AVE;1	6/6	AGBCI17.AVE;1	6/6	AGBCI19.AVE;1	6/6
AGBCI21.AVE;1	6/6	AGBCI23.AVE;1	6/6	AGBCI25.AVE;1	6/6
AGBCI27.AVE;1	6/6	AGBCI29.AVE;1	6/6	AGBCI31.AVE;1	6/6
AGBM01.AVE;1	6/6	AGBM03.AVE;1	6/6	AGBM05.AVE;1	6/6
AGBM07.AVE;1	6/6	AGBM09.AVE;1	6/6	AGBM11.AVE;1	6/6
AGBM13.AVE;1	6/6	AGBM15.AVE;1	6/6	AGBM17.AVE;1	6/6
AGBM19.AVE;1	6/6	AGBM21.AVE;1	6/6	AGBM23.AVE;1	6/6
AGBM25.AVE;1	6/6	AGI.AVE;1	6/6	B01V.AVE;1	6/6
B23V.AVE;1	6/6	B5V.AVE;1	6/6	B8A0V.AVE;1	6/6
F05V.AVE;1	6/6	F8G2G.AVE;1	6/6	F8V.AVE;1	6/6
G02V.AVE;1	6/6	G5G.AVE;1	6/6	G5V.AVE;1	6/6
G8G.AVE;1	6/6	G8K3V.AVE;1	6/6	HIIREG.AVE;1	6/6
K01G.AVE;1	6/6	K23G.AVE;1	6/6	K45G.AVE;1	6/6
K45V.AVE;1	6/6	KM2I.AVE;1	6/6	LIBRARY.EXE;1	9/9
LIBRARY.FOR;1	6/6	M01V.AVE;1	6/6	M0G.AVE;1	6/6
M1G.AVE;1	6/6	M23V.AVE;1	6/6	M2G.AVE;1	6/6
M34I.AVE;1	6/6	M3G.AVE;1	6/6	M45V.AVE;1	6/6
M4G.AVE;1	6/6	M5G.AVE;1	6/6	M6G.AVE;1	6/6
M7G.AVE;1	6/6	MLATEV.AVE;1	6/6	NORMAL1.AVE;1	6/6
NORMAL2.AVE;1	6/6	PNBLUE.AVE;1	6/6	PNRED.AVE;1	6/6
QUASAR.AVE;1	6/6	RNBLUE.AVE;1	6/6	RNRED.AVE;1	6/6
SEYFERT.AVE;1	6/6	TTAURI.AVE;1	6/6	X1A.AVE;1	6/6
X1E.AVE;1	6/6	X2.AVE;1	6/6	X3.AVE;1	6/6
X4.AVE;1	6/6	X5.AVE;1	6/6	YG0B.AVE;1	6/6

For a VAX running the VMS operating system, simply mimicking this directory and file structure will result in a clone of the new version of the Model at the user's VAX site. This same structure and organization is now established in the IRAF account on the AFGL VAX machine.

Note that the executable is linked with the MONGO87 plotting package. The executable provided will work in a limited manner (for example using device=3 for a Tektronix); if the site where the program is to be installed has MONGO87, it is recommended that the executable be relinked—otherwise, the last part of the subroutine MONGOPLOT within SKY.FOR could be modified to make use of the locally preferred plotting package. Change the calling directory in which your own MONGO87 resides in the routine LINK.COM.

211

RUNNING THE PROGRAM

The following are examples of the use of SKY.EXE.

```
$ set default disk:[user.model]
$ @setup
$ r sky
Integrate over area?  N             (case of a small area)
Enter galactic latitude:  30            (in degrees)
Enter galactic longitude:  30           (in degrees)
Enter passband - 1=B, 2=V, 3=J, 4=H, 5=K, 6=2.4um, 7=12um, 8=25um, 9=other:  7
Should the y-axis be cumulative?  - <cr>=y:  Y
Should the x-axis show magnitudes?  - <cr>=y:  Y
Enter device number (3 = Tektronix, 6 = Sun Window, 12 = Falco, -5 = LaserWriter (portrait),-6
= LaserWriter (landscape), 0 = quit):  0
output files SKY.LOG and SKY.OUT have been created
$ r sky
Integrate over area?  Y           (case of a large area)
Enter limits of galactic latitude:  60 90
Enter limits of galactic longitude:  0 180
Enter incremental steps in lat and long:  5 30          be sensible here!  Enter passband
- 1=B, 2=V, 3=J, 4=H, 5=K, 6=2.4um, 7=12um, 8=25um, 9=other:  7
Should the y-axis be cumulative?  - <cr>=y:
Should the x-axis show magnitudes?  - <cr>=y:
Enter device number (3 = Tektronix, 6 = Sun Window, 12 = Falco, -5 = LaserWriter (portrait),-6
= LaserWriter (landscape), 0 = quit):  -6
output files SKY.LOG and SKY.OUT have been created
Do you wish to plot observed points?  - <cr>=y:
to compare model to existing data in that area
Enter name of file containing the data:  FILE.EXT
plot is now made
More plotting?  - <cr>=y, a=change axes:  A
Should the y-axis be cumulative?  - <cr>=y:  N            use differential
Should the x-axis show magnitudes?  - <cr>=y:  N          want flux
Enter device number (3 = Tektronix, 6 = Sun Window, 12 = Falco, -5 = LaserWriter (portrait),-6
= LaserWriter (landscape), 0 = quit):  3
extra output file SKY.OUT (differential/flux) is created
Do you wish to plot observed points?  - <cr>=y:  N
plot is now made
More plotting?  - <cr>=y, a=change axes:  N
$ r sky
Integrate over area?  N             (use of a non-standard filter)
Enter galactic latitude:  30
Enter galactic longitude:  30
Enter passband - 1=B, 2=V, 3=J, 4=H, 5=K, 6=2.4um, 7=12um, 8=25um, 9=other:  9
Enter name of file containing system response.  The file must contain
331 values matching the spectral wavelengths:  [.LRS]FILTER.DAT
```

```
Should the y-axis be cumulative?  - <cr>=y:
Should the x-axis show magnitudes?  - <cr>=y:  N
Enter device number (3 = Tektronix, 6 = Sun Window, 12 = Falco, -5 = LaserWriter (portrait),-6
= LaserWriter (landscape), 0 = quit):  -6
output files SKY.LOG and SKY.OUT have been created
```

The output file SKY.LOG has a detailed listing of the contribution from each type of source at a range of magnitudes. The file SKY.OUT contains the magnitude/log flux in the first column and the log number (cumulative/differential) in the second, depending upon the response to the prompts when running the program. The lower portion of SKY.LOG includes the surface brightness output: a table of cumulative flux and equivalent cumulative magnitude vs. x-axis magnitude for the zone area calculated; and a second pair of columns detailing the same quantities but now per square degree.

The contents of the two columns of SKY.OUT are summarized in the table below:

	MAGNITUDE	FLUX
CUMULATIVE	mag / $\log_{10} N$	$\log_{10}$ *Flux* (Wm^{-2}) / $\log_{10} N$
DIFFERENTIAL	mag / $\log_{10} N$ (mag^{-1})	$\log_{10}$ *Flux* (Wm^{-2}) / $\log_{10} N$ (dex^{-1})

INTLRS.EXE is self documenting, and should not cause any problems when executed.

SKY.EXE takes approximately 6–8 CPU seconds per ray on a VAX 8600 computer. This CPU time varies with direction; longer times are required for directions close to the Galactic center. In addition, the extragalactic component, which is calculated once each time the program is run, takes approximately 22 CPU seconds.

LUMA.EXE is a subsection of SKY.EXE for calculating the Galactic components only. This will probably be useful for studying fields close to the Galactic plane, where the extragalactic contribution will be relatively insignificant.

GALZA.EXE is a standalone form of the subroutine GALAXIES.FOR which calculates the extragalactic component. This subroutine assumes that the Galactic absorption is zero. For any region away from the plane, this assumption is valid. However, more caution is required in the plane. For example, there is expected to be over 1 mag of extinction between us and the Galactic Center at 12 μm. The amount of extinction decreases rapidly with latitude. The extinction is the reason that GALZA and LUMA were merged to form SKY. Note that the usage of GALZA and LUMA is similar to SKY .

Note that SKY and LUMA require input in Galactic coordinates. These are defined (by the IAU) as:

$$\sin b = \sin \delta \cos 62.6° - \cos \delta \sin(\alpha - 282.25°) \sin 62.6°, \qquad (1)$$

$$\cos b \sin(l - 33°) = \cos \delta \sin(\alpha - 282.25°) \cos 62.6° + \sin \delta \sin 62.6°, \qquad (2)$$

$$\cos b \cos(l - 33°) = \cos \delta \cos(\alpha - 282.25°), \qquad (3)$$

where l is the galactic longitude, b is the galactic latitude, and α and δ are the right ascension and declination respectively, for equinox 1950.0.

HOW WELL DOES THE MODEL WORK?

A detailed discussion of the model's performance at 12 and 25 μm, across the entire sky, is included in the paper by Wainscoat et al. (1990, shortly to be submitted to The Astrophysical Journal). We can plausibly attribute the deficient predictions of the model to one or more of the following causes:

- Our representation of the spiral arms as both homogeneously populated and symmetrically distributed about the plane of the Galaxy is overly simplistic.

- Accurate color characterization of the metal-rich stars of the bulge is still problematic.

- The extragalactic sky is also not homogeneous, although the effects of clustering are at a much lower level than the former two causes.